ARL-TR-9148 • Feb 2021

DEVCOM ARMY RESEARCH LABORATORY

A Dodecahedral Model for Alveoli. Part I. Theory and Numerical Methods

by Alan D Freed, Shahla Zamani, Sandipan Paul, and John D Clayton

NOTICES

Disclaimers

The findings in this report are not to be construed as an official Department of the Army position unless so designated by other authorized documents.

Citation of manufacturer's or trade names does not constitute an official endorsement or approval of the use thereof.

Destroy this report when it is no longer needed. Do not return it to the originator.

ARL-TR-9148 • Feb 2021

A Dodecahedral Model for Alveoli. Part I. Theory and Numerical Methods

Alan D Freed and John D Clayton
Weapons and Materials Research Directorate, DEVCOM Army Research Laboratory

Shahla Zamani and Sandipan Paul
Texas A&M University

REPORT DOCUMENTATION PAGE

Form Approved
OMB No. 0704-0188

1. REPORT DATE *(DD-MM-YYYY)*
February 2021

2. REPORT TYPE
Technical Report

3. DATES COVERED (From - To)
June 2019–January 2021

4. TITLE AND SUBTITLE
A Dodecahedral Model for Alveoli. Part I. Theory and Numerical Methods

5a. CONTRACT NUMBER

5b. GRANT NUMBER

5c. PROGRAM ELEMENT NUMBER

6. AUTHOR(S)
Alan D Freed, Shahla Zamani, Sandipan Paul, and John D Clayton

5d. PROJECT NUMBER

5e. TASK NUMBER

5f. WORK UNIT NUMBER

7. PERFORMING ORGANIZATION NAME(S) AND ADDRESS(ES)
DEVCOM Army Research Laboratory
ATTN: FCDD-RLW-PC
Aberdeen Proving Ground, MD 21005-5066

8. PERFORMING ORGANIZATION REPORT NUMBER
ARL-TR-9148

9. SPONSORING/MONITORING AGENCY NAME(S) AND ADDRESS(ES)

10. SPONSOR/MONITOR'S ACRONYM(S)

11. SPONSOR/MONITOR'S REPORT NUMBER(S)

12. DISTRIBUTION/AVAILABILITY STATEMENT
Approved for public release; distribution is unlimited.

13. SUPPLEMENTARY NOTES
primary authors' email: <afreed@tamu.edu> and <john.d.clayton1.civ@mail.mil>. ORCID accounts: 0000-0002-3492-0628 (ADF), 0000-0002-9477-9136 (SZ), 0000-0003-1445-6896 (SP), and 0000-0003-4107-6282 (JDC).

14. ABSTRACT
The dodecahedron is introduced as a model for alveoli. Its geometric properties are derived in detail with regard to its three geometric features: 1D septal chords, 2D septal membranes, and the 3D alveolar sac. The kinematics are derived for us to model a deforming dodecahedron, including the shape functions needed for interpolating each geometry. Constitutive models are derived that are suitable for describing the thermomechanical response for the structural constituents of an alveolus: its septal chords, its permeable membranes, and its volume. Numerical methods are advanced for solving first- and second-order ordinary differential equations (ODEs) and spatial integrations along a bar, across a pentagon, and throughout a tetrahedron using Gaussian quadrature schemes designed for each geometry. A variational formulation is used to create our structural modeling of an alveolus. Constitutive equations suitable for modeling biological tissues are derived from thermodynamics using the theory of implicit elasticity, presented in an appendix.

15. SUBJECT TERMS
nonlinear elasticity, structural mechanics, soft tissue mechanics, biomechanics, lung, dodecahedron, finite elements

16. SECURITY CLASSIFICATION OF:			**17. LIMITATION OF ABSTRACT**	**18. NUMBER OF PAGES**	**19a. NAME OF RESPONSIBLE PERSON**
a. REPORT	**b. ABSTRACT**	**c. THIS PAGE**			John D Clayton
Unclassified	Unclassified	Unclassified	UU	233	**19b. TELEPHONE NUMBER (Include area code)** 410-278-6146

Standard Form 298 (Rev. 8/98)
Prescribed by ANSI Std. Z39.18

Contents

List of Figures

List of Tables

Acknowledgments

Prof Alan D Freed acknowledges support of a Joint Faculty Appointment with the US Army Combat Capabilities Development (DEVCOM) Army Research Laboratory (ARL). Shahla Zamani and Sandipan Paul acknowledge support from a Cooperative Agreement funded by the DEVCOM Army Research Laboratory. John D Clayton acknowledges support of ARL. Prof JN Reddy is the Program Manager for research performed at Texas A&M University by Shahla Zamani and Sandipan Paul. Dr Michael Kleinberger is the Cooperative Agreement Manager, and Dr John Clayton is the Technical Manager for this contract. Insightful conversations from a clinical perspective regarding behind armor blunt trauma (BABT) with Dr David G Mohler MD at Stanford Health Care are gratefully acknowledged.

1. Introduction

Injuries that occur after a non-penetrating ballistic projectile impacts a Soldier wearing personal protective equipment (PPE) are referred to as behind armor blunt trauma (BABT). The kinetic energy from such an impact is absorbed by the Soldier's PPE and the bony and soft tissues of the Soldier beneath.[1–3] Standards have been written to which PPE have been designed since 1972. Verification is through experiments where, typically, a suit of body armor is placed over a "body" subjected to a ballistic impact from a projectile fired by a weapon, all in accordance with a standard. Current practice is to use clay (usually Roma Plastilina No. 1 clay) as a surrogate for the human body in these tests.[4] Injuries that occur from a rapidly increasing overpressure (e.g., shockwaves from an explosion) are denoted as primary blast injuries (PBI).[5] Blast lung injury (BLI) refers to PBI experienced by the lung.[6] Dynamic blunt thoracic trauma can also occur in nonmilitary settings (e.g., automobile accidents), and PBI likewise may occur irrespective of the presence of PPE.

A principal objective of an internal US Army Combat Capabilities Development Command (DEVCOM) Army Research Laboratory (ARL)–Weapons and Materials Research Directorate (WMRD) project, *Modeling Large Deformations and Stress Wave Mechanics in Soft Biological Tissue*, is to develop accurate material models for the human body that are also efficient in their finite element implementation, thereby facilitating the study of BABT and PBI in an effort to improve the designs of PPE. This is a 6.1 research project whose hand-off to a 6.2 development team at project's end will aid Army engineers in their design of improved PPE by allowing them to run in-silico BABT tests to complement their actual in-field testing.

The DEVCOM Army Research Laboratory-WMRD *Modeling Large Deformations and Stress Wave Mechanics in Soft Biological Tissue* project has three primary objectives: *i*) new material models, *ii*) new experiments, and *iii*) new trauma metrics. Lung has been selected as the soft tissue of interest for this study. What are sought are models and metrics whose parameters are physical and unique, and whose numeric implementation will be efficient and stable. Continuum thermodynamic models for lung tissue and a trauma metric are being developed (Clayton, Freed, and co-authors[7–13] and this document). The work done under this sub-project, *A Dodecahedral Model for Alveoli*, complements its parent project, *Modeling Large Defor-*

mations and Stress Wave Mechanics in Soft Biological Tissue, with regard to the first and third objectives of this ARL-WMRD program. The models being developed are expected to be improvements over those currently supplied by `LS-DYNA` in their materials library that, e.g., have been used to study shock waves traversing a human torso not wearing body armor, cf. Fig. 1.

BABT and BLI manifest at the microscopic level of alveoli, which make up the parenchyma, i.e., the spongy tissue of lung that composes around 90% of lung by volume, cf. Fig. 2, there being some 500 million alveoli in a typical human lung. Most damage occurs just beneath the visceral pleural, as seen in Fig. 3, and is thought to be a consequence of the large disparity in wave speeds between solid tissues ($\sim$1,500 m/s) and the spongy parenchyma ($\sim$30–40 m/s).[15] The objective of this work is to develop a mechanistic multi-scale model that is capable of describing the deformation and damage that occur at an alveolar level, caused by a shock wave traveling through the parenchyma, induced through either a blast or a ballistic impact to a Soldier's PPE. In-silico experiments done using this microscopic model are to be used to "inform" our macroscopic model in those areas where actual lung experiments are difficult, if not impossible, to perform.

This is the first full-length report for the project *A Dodecahedral Model for Alveoli*. This first report discusses theoretical foundations and numerical techniques for interrogating the dodecahedral response. A second report describing results of numerical calculations is anticipated in the next 12 months.

1.1 Problem Statement

Pulmonary contusion is one of the most common thoracic soft-tissue injuries caused by blunt trauma, with a mortality rate of 10%–25%.[16] Damage to lungs is the main cause of morbidity following high-level blast exposures.[17] Lung laceration is also common and debilitating.[18] Existing constitutive models for lung tissue have been developed from limited static test data, e.g., Fung, Vawter *et al*.[19–21] These models, and others developed since then, omit relevant physics pertinent to blast and ballistic impacts required to assess BLI and BABT, respectively. They also require cumbersome optimization protocols to fit non-unique parameter sets,[22,23] and/or are not validated against independent data.[24] Better lung models suitable for dynamic analysis are needed so that the Army can design improved PPE to better protect Soldiers.

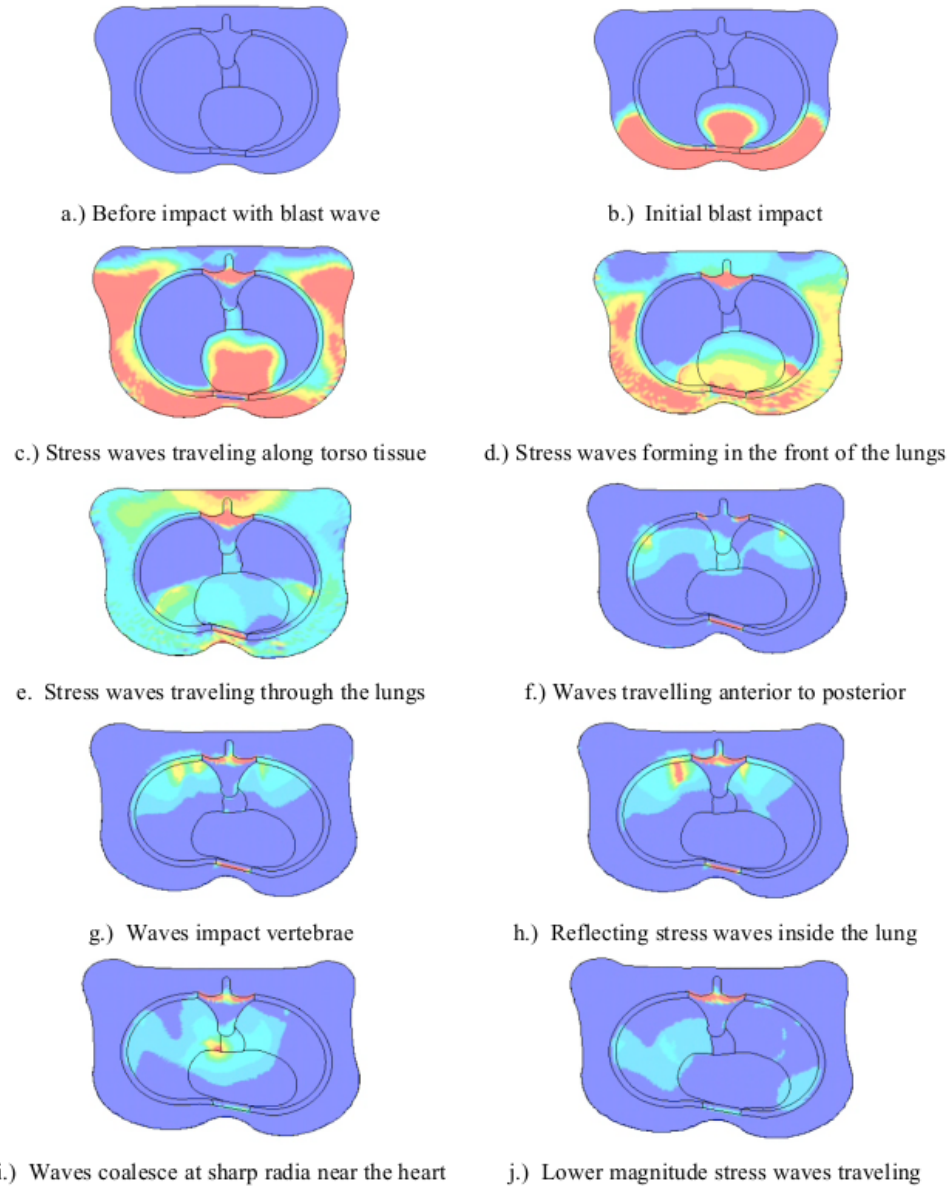

Fig. 1 Finite element analysis done using `LS-DYNA` to model shock waves traversing a cross-sectional slice of a human torso. Material models from the `LS-DYNA` library of available models were used.[14]

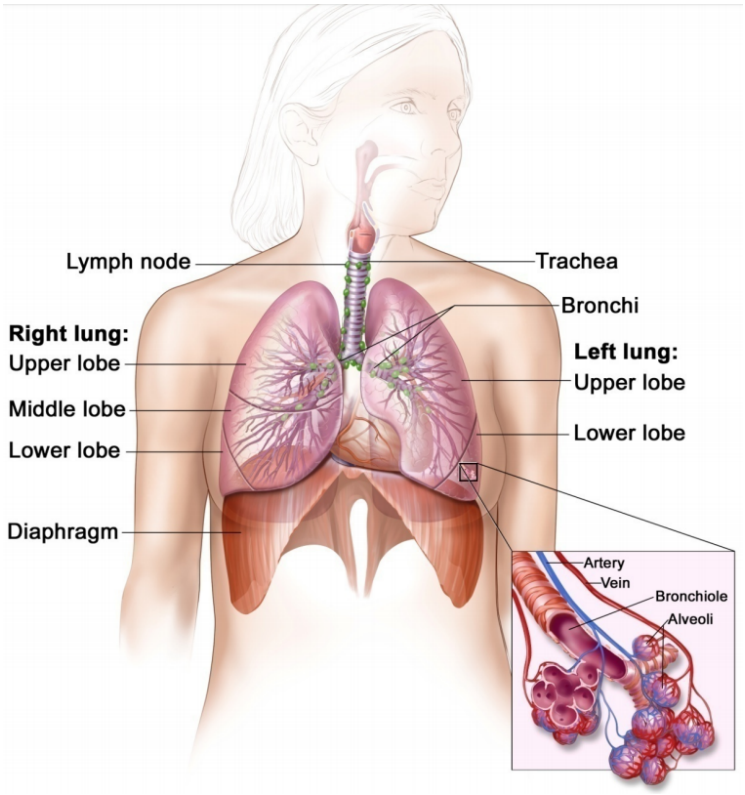

Fig. 2 A medical drawing of the respiratory system[14]

Fig. 3 Lungs excised from animals (most likely ovine) who expired from blast injury[15]

The primary objective of the ARL-WMRD project *Modeling Large Deformations and Stress Wave Mechanics in Soft Biological Tissue* is to develop such models for deformation and damage/injury assessment. These are continuum models derived from thermodynamics that utilize internal state variables to account for the irreversible aspects of response.[8,9] Models (both macroscopic and microscopic) are specifically sought whose parameters are physical and whose parameterization is straightforward. Characterization of the parameters in a model requires experimental data. This presents an enormous challenge, one that is being addressed in this ARL-WMRD project through other university collaborators.

Performing experiments for the purpose of model characterization is extremely difficult when it comes to modeling lung. Lung is a structure; parenchyma is a material. Therefore, one would normally choose to test the parenchyma, and from these data extract one's model parameters but, because of its spongy nature, we are challenged to do so in a physically meaningful way. Consequently, one typically tests whole lungs, or lobes thereof, and from these structural experiments we are tasked to extract material parameters through an inverse analysis. An alternative approach whereby one could, in principle, acquire parameters for the continuum models being developed at ARL-WMRD would be to homogenize a microscopic structural response for the alveoli of the parenchyma. The work presented here addresses this approach in our modeling of deformation, damage, and injury in alveolar structures.

Our approach is also advantageous for understanding the influence of microstructure on the higher-scale continuum properties. Curve fitting to macroscopic data alone does not provide such insight. This multi-scale approach can also be used to determine properties for regimes (stress/strain/strain-rate histories) that cannot be reached experimentally, due to limitations in testing facilities, capabilities, or sufficient animal/human tissue availability.

The narrative that follows seeks to develop two material models for lung: one for mechanical deformation and the other for damage/injury/trauma. Models are sought whose parameters have physical interpretation. Ideally, they will enhance our understanding of the deformation and damage mechanisms at play during BABT and BLI. Specifically, they will describe how alveoli respond to pressure-waves and/or shear-waves as these wave fronts pass through them. This modeling will be accomplished by constructing a multi-scale model connecting the parenchyma (macro)

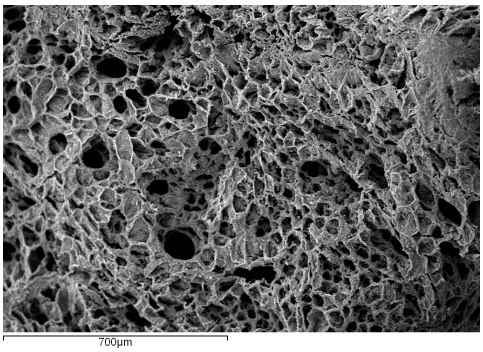

(a) Magnification at 100X. This is Fig. 5 in Freed *et al*.[25]

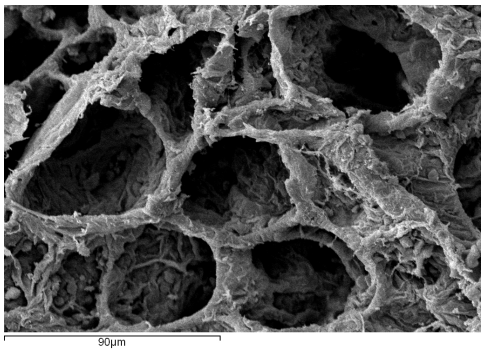

(b) Magnification at 750X. This is Fig. 7 in Freed *et al*.[25]

Fig. 4 Scanning electron microscopy photographs from a sectioned rat lung. The alveolar diameter in rat lung is about one quarter the alveolar diameter in human lung.

and alveolar (micro) levels. In-silico experiments can then be done on the alveolar structural model, whose homogenized response can serve as an aid in the characterization of ARL's continuum models. These ARL-WMRD continuum models are being designed to perform efficiently in their implementation in finite element codes. This will allow for BABT and BLI analyses to be done during the design of future PPE with an ultimate goal of saving Soldiers' lives.

The primary purpose of this work is to provide a microscopic model for lung tissue that can be used as an aid in the parameterization of a macroscopic model for lung that will be reasonably accurate yet efficient to run in full torso finite element analyses[13] to study BABT and BLI for the purpose of improving PPE. Secondarily, the alveolar-level model will provide stand-alone information that will increase our fundamental understanding of the thermomechanical response of lung parenchyma to dynamic loading.

1.2 Approach

Figure 4 shows micrographs from a rat lung taken at different magnifications. In the lower-resolution image, one sees numerous alveoli that became exposed because of the sectioning process. Also present are several alveolar ducts that connect individual alveoli to a bronchial tree. In the higher-resolution image we observe the faceted structure of these alveoli, wherein one can see the septal chords and membranes, the latter being traversed by capillaries through which gas exchange occurs. Gas exchange is not modeled here.

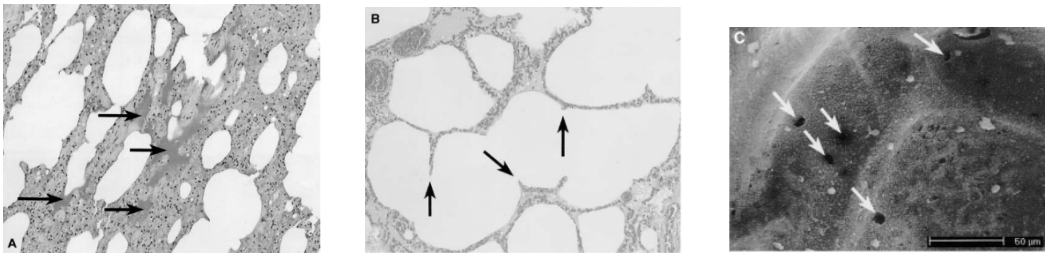

(a) Immunohistochemical staining for hemoglobin showing edema fluid buildups (arrows) caused by blast injury.

(b) Histopathology image showing tearing of septal membranes (arrows) caused by blast injury.

(c) Electron microscope image showing perforations (arrows) of the alveolar wall caused by blast injury.

Fig. 5 Local injury mechanisms in blast lung. All images from Tsokos *et al*.[26]

Alveolar geometry is modeled here as a dodecahedron, i.e., a soccer-ball like structure comprising 12 pentagonal facets bordered by 30 septal cords that are connected at 20 vertices. Each vertex links three neighboring cords of the alveolus with a fourth chord from a neighboring alveolus. BABT and BLI can occur through multiple mechanisms, e.g., tearing of septal cords and/or alveolar membranes, and in more severe cases, rupturing of capillaries can also happen causing interstitial fluids and blood to leak into neighboring alveoli, all illustrated in Fig. 5. Our dodecahedral model for alveoli is capable of capturing these trauma events.

Conjecture. *A microscopic strain field, measured at the scale of alveoli, is the same as its macroscopic strain field in which it resides, measured at the scale of parenchyma. The motion is affine, and the local motion is homogeneous.*

This hypothesis was tested and confirmed in an experimental study done by Butler *et al*.[27] where they used light scattering to study changes in geometry of the septal planes in alveoli, from which they concluded: "the microscopic strain field does not differ significantly from the macroscopic field." We employ this hypothesis by taking the deformation gradient from, say, a Gauss point in a finite element model of lung, e.g., from a Gauss point associated with Fig. 1, and imposing it as a far-field deformation onto our dodecahedral model of an alveolus. From this kinematic input we arrive at an upper bound on the macroscopic stress/stiffness response, akin to a Voigt approximation,[28,29] through a homogenization of the microscopic forces created within our structural model for an alveolus.

The authors of a recent review article on alveolar strain finished by writing:

> "In general, computational mechanics approaches to determine function in a healthy or diseased lung have proven to be useful in explaining or measuring observations that are not captured by imaging modalities. However, for these models to fully explain complex physiological mechanical events, appropriate mechanical properties, boundary conditions, and mechanical loads must be identified. Moreover, validation of such computational models, which is an essential component of any computational mechanics approach, remains to be a challenge in the analysis of soft tissue mechanics."
>
> Roan & Waters[30] (p. L633)

In this research we set out to develop a constitutive framework for alveolar mechanics, fully cognizant of the aforementioned challenges. Our objectives are different from those of prior studies in alveolar mechanics in that we seek to describe the response/injury of a human lung that has been subjected to a stress wave propagating across the thorax region caused by an impact from either a blunt object or a blast wave. Consequently, some important aspects in the modeling of a breathing lung are thought to be less impactful here, e.g., the effect of surfactant in keeping alveoli from collapsing at the end of expiration.

As a foundation, we adopt the guideline:

> "Constitutive equations are phenomenological. They are regarded as empirical by experimenters, and axiomatic by mathematicians. In biomechanics, we often try to derive them on the basis of microstructure ... in order to gain a better understanding, or to get some guidance to the mathematical form."
>
> Y.-C. Fung[31] (p. 431)

The approach adopted here is to use the geometry of a dodecahedron as a *micro*scopic mechanical model for alveoli, whose far-field response to mechanical stimuli, in accordance with our Conjecture on p. 7, will be used to inform the development of a *macro*scopic mechanical model for parenchyma,[9] the predominant tissue in lung. This is deemed necessary because of the complex porous structure of parenchyma, as compared with the homogeneous structure of rubbery elastic solids whose theories have historically been employed to model parenchyma.[19,20,32,33] The complementary continuum (macroscopic) model for parenchyma[7,9,11–13] is implemented into finite element codes with an end objective of providing a numerical

tool that can be used by Army engineers in their efforts to develop improved and more effective designs for a Soldier's PPE.

1.3 Organization

This document is organized in the following manner. Section 2 introduces the dodecahedron as a model for alveoli. Its geometric properties are derived in detail with regards to its three geometric features: 1D septal chords, 2D septal membranes, and 3D alveolar sacs. Section 3 develops the kinematics required for us to model a deforming dodecahedron, again focusing on the 1D chords, 2D membranes, and the 3D volume within, including the shape functions needed for interpolating each geometry. Section 4 derives constitutive models suitable for describing the thermomechanical response for the structural constituents of an alveolus: its septal chords, its permeable membranes, and its volume. Section 5 presents numerical methods used for solving first- and second-order, ordinary, differential equations (ODEs) and spatial integrations along a bar, across a pentagon, and throughout a tetrahedron using Gaussian quadrature schemes designed for each geometry. Section 6 describes a variational formulation used to create our structural modeling of an alveolus, which consists of three separate models: one consisting of septal chords, another consisting of septal membranes, and the third consisting of alveolar volume. Forces at the vertices are summed and homogenized for return to the macroscopic solver. Constitutive equations suitable for modeling biological tissues are derived from thermodynamics using the theory of implicit elasticity, and are presented in the Appendix.

2. Dodecahedra: A Model for Alveoli

Typical alveoli are 14 sided polyhedra with one face normally being open as a mouth to an alveolar duct, and whose septal membranes typically become flat at transpulmonary pressures as low as 2 cm H_2O.[34] To capture the microstructural features of lung, researchers have modeled both alveoli and alveolar ducts, as seen in Fig. 4; we only address alveoli here. One of three different geometric shapes is usually employed when modeling an alveolus: a dodecahedron introduced by Frankus and Lee[35] in 1974, a rhombic dodecahedron introduced by de Ryk *et al*.[36] in 2007, and a truncated octahedron, i.e., a tetrakaidecahedron, introduced by Dale *et al*.[37] in 1980. The dodecahedron and rhombic dodecahedron are both 12 sided polyhedra with faces being pentagons and rhombuses, respectively. A tetrakaidecahedron is a pair of pyramids stacked bottom to bottom, forming an octahedron, whose six points are then removed. The end result is a 14 sided polyhedron with six faces that are squares and eight faces that are hexagons, where like shapes have like dimensions.

The tetrakaidecahedron and rhombic dodecahedron are both volume filling. This property is preferred whenever one sets out to construct assemblages of alveoli to build a microstructural model that is to be solved numerically via a finite element method. The purpose of such an exercise is to homogenize the response of an alveolar assembly up to the macroscopic level, i.e., the level of a continuum mass point, a.k.a., the parenchyma.[36–42] Such a finite element model can serve as a representative volume element (RVE) for parenchyma.

The dodecahedron is an isotropic structure, or very nearly so as we shall show, and is nearly volume filling.[43] A dodecahedron is one of the five perfectly symmetric solids in geometry. It becomes a preferred geometry whenever a single alveolus is to be used as the RVE of homogenization, and from which closed-form solutions have been derived.[25,43–45] Here isotropy of the microstructure ensures an isotropic macro response. Parenchyma, as a tissue, is isotropic[33,46,47]; whereas, lung, as an organ, is a complex, heterogeneous structure.[48,49] This distinction has, from time-to-time, been forgotten.[50]

For the reasons stated above, a dodecahedron, with vertices labeled according to Fig. 6(b), is the geometric structure selected for use in this study. The question of how one assigns a co-ordinate system to a dodecahedron is discussed first. Given

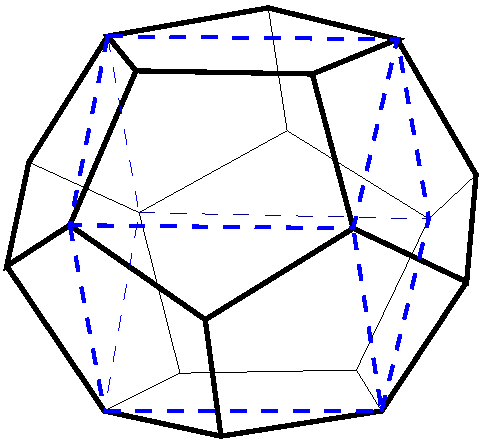

(a) A cube is contained within a dodecahedron, with one of its five possible orientations being displayed. Atop each face of the cube reside four pentagonal sub-areas that form the shape of a hipped roof line.

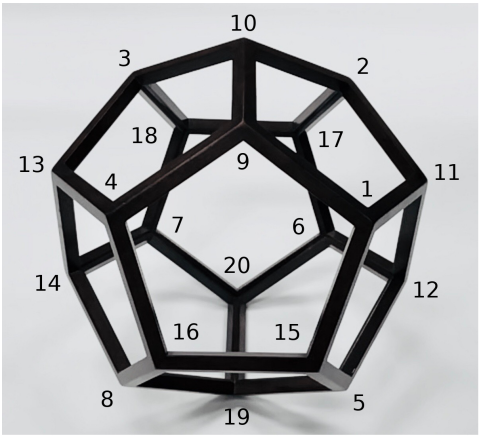

(b) Vertices 1 through 8 are located at the corners of such a cube. The centroid for the cube is also the centroid for the dodecahedron. Vertices 9 through 20 are corners of the hipped roof lines residing above each face of the cube.

Fig. 6 Geometric representations for a dodecahedron

this co-ordinate system, vertices of a dodecahedron are then assigned from which its septal chords and septal membranes are readily established.

2.1 Co-ordinate Indexing

An orthonormal set of base vectors $(\vec{\imath}, \vec{\jmath}, \vec{k})$ is assigned to a dodecahedron whose origin resides at its centroid and whose directions align with a set of far-field base vectors used for reference in one's finite element model of a lung. The question is: How does one orient the indexing scheme of Fig. 6 against this basis? Alternatively: How can one describe a mapping $(\vec{\imath}, \vec{\jmath}, \vec{k}) \overset{?}{\mapsto} (\vec{\mathbf{E}}_1, \vec{\mathbf{E}}_2, \vec{\mathbf{E}}_3)$ wherein an orthonormal set of base vectors $(\vec{\mathbf{E}}_1, \vec{\mathbf{E}}_2, \vec{\mathbf{E}}_3)$ is to serve as the reference basis for our alveolar dodecahedron to which the indexing scheme presented in Fig. 6(b) applies?

Given that a finite element model for lung exists, then a deformation gradient $\mathbf{F}$ can be made available at any mass point therein whereat an alveolus of interest resides. Let the components of this deformation gradient be $F_{ij}, i, j = 1, 2, 3$, when evaluated in the co-ordinate frame $(\vec{\imath}, \vec{\jmath}, \vec{k})$, which is the co-ordinate frame of the finite element analysis. A Gram–Schmidt (or **QR**) decomposition of a non-singular 3×3 matrix results in a tangent vector $\vec{\mathbf{g}}_1$ and normal vector $\vec{\mathbf{g}}_1 \times \vec{\mathbf{g}}_2$ that remain invariant under transformations of the triangular matrix $\mathbf{R}$.[51] These convected base vectors $(\vec{\mathbf{g}}_1, \vec{\mathbf{g}}_2, \vec{\mathbf{g}}_3)$ rotate out of basis $(\vec{\mathbf{E}}_1, \vec{\mathbf{E}}_2, \vec{\mathbf{E}}_3)$ via a Gram rotation.[52] Given this

geometric information, Paul *et al.*[53] were able to provide an answer to the above question of co-ordinate frame selection.

Our approach begins by establishing the extent of transverse shear crossing each of the co-ordinate directions $(\vec{\boldsymbol{\imath}}, \vec{\boldsymbol{\jmath}}, \vec{\boldsymbol{k}})$, as quantified by

$$\mathcal{G}_1 = \frac{\sqrt{F_{21}^2 + F_{31}^2}}{F_{11}}, \quad \mathcal{G}_2 = \frac{\sqrt{F_{12}^2 + F_{32}^2}}{F_{22}}, \quad \mathcal{G}_3 = \frac{\sqrt{F_{13}^2 + F_{23}^2}}{F_{33}}, \tag{1}$$

where $\mathcal{G}_i$ is a measure of the shear deformation cutting across the i^{th} direction. Unit vector $\vec{\mathbf{E}}_1$ is selected as that direction from the set $\{\vec{\boldsymbol{\imath}}, \vec{\boldsymbol{\jmath}}, \vec{\boldsymbol{k}}\}$ which possesses minimal transverse shear. Once selected, there are two possible planes that contain base vector $\vec{\mathbf{E}}_1$, and the one selected whose normal is to be $\vec{\mathbf{E}}_1 \times \vec{\mathbf{E}}_2$ is that plane with the least amount of in-plane shear, which can be determined by taking appropriate dot products between column vectors $\boldsymbol{f}_i = \{F_{1i}\ F_{2i}\ F_{3i}\}^{\mathsf{T}}, i = 1, 2, 3$. Vector $\boldsymbol{f}_i$ has elements taken from the i^{th} column of matrix F_{ji}, which represents the deformation gradient $\mathbf{F}$ evaluated in $(\vec{\boldsymbol{\imath}}, \vec{\boldsymbol{\jmath}}, \vec{\boldsymbol{k}})$. This strategy is summarized in Alg. 1.

Algorithm 1 inputs a deformation gradient $\mathbf{F}$ whose components F_{ij} are evaluated in the co-ordinate system $(\vec{\boldsymbol{\imath}}, \vec{\boldsymbol{\jmath}}, \vec{\boldsymbol{k}})$ associated with, in our case, a finite element model for lung. The algorithm outputs an orthogonal matrix $\mathbf{P}$ that re-indexes the components of deformation gradient F_{ij} into an equivalent form where $\mathbf{F} = \mathcal{F}_{ij}\, \vec{\mathbf{E}}_i \otimes \vec{\mathbf{E}}_j$. It is this re-indexed matrix $\mathcal{F}_{ij}$ that is to be subjected to Gram–Schmidt factorization, which is discussed later in Section 3.

There are six cases that can arise. Their associated orthogonal matrices are

$$[\mathbf{P}_1] = \begin{bmatrix} 1 & 0 & 0 \\ 0 & 1 & 0 \\ 0 & 0 & 1 \end{bmatrix} \qquad [\mathbf{P}_2] = \begin{bmatrix} 1 & 0 & 0 \\ 0 & 0 & 1 \\ 0 & 1 & 0 \end{bmatrix} \qquad [\mathbf{P}_3] = \begin{bmatrix} 0 & 1 & 0 \\ 1 & 0 & 0 \\ 0 & 0 & 1 \end{bmatrix}$$

$$[\mathbf{P}_4] = \begin{bmatrix} 0 & 0 & 1 \\ 1 & 0 & 0 \\ 0 & 1 & 0 \end{bmatrix} \qquad [\mathbf{P}_5] = \begin{bmatrix} 0 & 1 & 0 \\ 0 & 0 & 1 \\ 1 & 0 & 0 \end{bmatrix} \qquad [\mathbf{P}_6] = \begin{bmatrix} 0 & 0 & 1 \\ 0 & 1 & 0 \\ 1 & 0 & 0 \end{bmatrix} \tag{2a}$$

Algorithm 1: Pivoting of the co-ordinate system

Input: Deformation gradient $\mathbf{F}$ with components F_{ij} expressed in $(\vec{\boldsymbol{\imath}}, \vec{\boldsymbol{\jmath}}, \vec{\boldsymbol{k}})$

if $\mathcal{G}_1 \leqslant \mathcal{G}_2$ and $\mathcal{G}_1 \leqslant \mathcal{G}_3$ **then**

  if $\boldsymbol{f}_1 \cdot \boldsymbol{f}_2 \leqslant \boldsymbol{f}_1 \cdot \boldsymbol{f}_3$ **then**

    $[\boldsymbol{\mathcal{F}}_1] = [\mathbf{P}_1]^{\mathsf{T}}[\mathbf{F}][\mathbf{P}_1] : \ [\boldsymbol{\mathcal{F}}] = [\boldsymbol{\mathcal{F}}_1], \ [\mathbf{P}] = [\mathbf{P}_1],$
    $\therefore \ (\vec{\boldsymbol{\imath}}, \vec{\boldsymbol{\jmath}}, \vec{\boldsymbol{k}}) \mapsto (\vec{\mathbf{E}}_1, \vec{\mathbf{E}}_2, \vec{\mathbf{E}}_3)$

  else

    $[\boldsymbol{\mathcal{F}}_2] = [\mathbf{P}_2]^{\mathsf{T}}[\mathbf{F}][\mathbf{P}_2] : \ [\boldsymbol{\mathcal{F}}] = [\boldsymbol{\mathcal{F}}_2], \ [\mathbf{P}] = [\mathbf{P}_2],$
    $\therefore \ (\vec{\boldsymbol{\imath}}, \vec{\boldsymbol{\jmath}}, \vec{\boldsymbol{k}}) \mapsto (\vec{\mathbf{E}}_1, \vec{\mathbf{E}}_3, \vec{\mathbf{E}}_2)$

else if $\mathcal{G}_2 \leqslant \mathcal{G}_1$ and $\mathcal{G}_2 \leqslant \mathcal{G}_3$ **then**

  if $\boldsymbol{f}_1 \cdot \boldsymbol{f}_2 \leqslant \boldsymbol{f}_2 \cdot \boldsymbol{f}_3$ **then**

    $[\boldsymbol{\mathcal{F}}_3] = [\mathbf{P}_3]^{\mathsf{T}}[\mathbf{F}][\mathbf{P}_3] : \ [\boldsymbol{\mathcal{F}}] = [\boldsymbol{\mathcal{F}}_3], \ [\mathbf{P}] = [\mathbf{P}_3],$
    $\therefore \ (\vec{\boldsymbol{\imath}}, \vec{\boldsymbol{\jmath}}, \vec{\boldsymbol{k}}) \mapsto (\vec{\mathbf{E}}_2, \vec{\mathbf{E}}_1, \vec{\mathbf{E}}_3)$

  else

    $[\boldsymbol{\mathcal{F}}_4] = [\mathbf{P}_4]^{\mathsf{T}}[\mathbf{F}][\mathbf{P}_4] : \ [\boldsymbol{\mathcal{F}}] = [\boldsymbol{\mathcal{F}}_4], \ [\mathbf{P}] = [\mathbf{P}_4],$
    $\therefore \ (\vec{\boldsymbol{\imath}}, \vec{\boldsymbol{\jmath}}, \vec{\boldsymbol{k}}) \mapsto (\vec{\mathbf{E}}_2, \vec{\mathbf{E}}_3, \vec{\mathbf{E}}_1)$

else

  if $\boldsymbol{f}_1 \cdot \boldsymbol{f}_3 \leqslant \boldsymbol{f}_2 \cdot \boldsymbol{f}_3$ **then**

    $[\boldsymbol{\mathcal{F}}_5] = [\mathbf{P}_5]^{\mathsf{T}}[\mathbf{F}][\mathbf{P}_5] : \ [\boldsymbol{\mathcal{F}}] = [\boldsymbol{\mathcal{F}}_5], \ [\mathbf{P}] = [\mathbf{P}_5],$
    $\therefore \ (\vec{\boldsymbol{\imath}}, \vec{\boldsymbol{\jmath}}, \vec{\boldsymbol{k}}) \mapsto (\vec{\mathbf{E}}_3, \vec{\mathbf{E}}_1, \vec{\mathbf{E}}_2)$

  else

    $[\boldsymbol{\mathcal{F}}_6] = [\mathbf{P}_6]^{\mathsf{T}}[\mathbf{F}][\mathbf{P}_6] : \ [\boldsymbol{\mathcal{F}}] = [\boldsymbol{\mathcal{F}}_6], \ [\mathbf{P}] = [\mathbf{P}_6],$
    $\therefore \ (\vec{\boldsymbol{\imath}}, \vec{\boldsymbol{\jmath}}, \vec{\boldsymbol{k}}) \mapsto (\vec{\mathbf{E}}_3, \vec{\mathbf{E}}_2, \vec{\mathbf{E}}_1)$

Output: Deformation gradient $\mathbf{F}$ with components $\mathcal{F}_{ij}$ expressed in $(\vec{\mathbf{E}}_1, \vec{\mathbf{E}}_2, \vec{\mathbf{E}}_3)$, as re-indexed by the orthogonal matrix $[\mathbf{P}]$

whose affiliated components for the re-indexed deformation gradient are

$$[\boldsymbol{\mathcal{F}}_1] = \begin{bmatrix} F_{11} & F_{12} & F_{13} \\ F_{21} & F_{22} & F_{23} \\ F_{31} & F_{32} & F_{33} \end{bmatrix} \quad [\boldsymbol{\mathcal{F}}_2] = \begin{bmatrix} F_{11} & F_{13} & F_{12} \\ F_{31} & F_{33} & F_{32} \\ F_{21} & F_{23} & F_{22} \end{bmatrix} \quad [\boldsymbol{\mathcal{F}}_3] = \begin{bmatrix} F_{22} & F_{21} & F_{23} \\ F_{12} & F_{11} & F_{13} \\ F_{32} & F_{31} & F_{33} \end{bmatrix}$$
$$[\boldsymbol{\mathcal{F}}_4] = \begin{bmatrix} F_{22} & F_{23} & F_{21} \\ F_{32} & F_{33} & F_{31} \\ F_{12} & F_{13} & F_{11} \end{bmatrix} \quad [\boldsymbol{\mathcal{F}}_5] = \begin{bmatrix} F_{33} & F_{31} & F_{32} \\ F_{13} & F_{11} & F_{12} \\ F_{23} & F_{21} & F_{22} \end{bmatrix} \quad [\boldsymbol{\mathcal{F}}_6] = \begin{bmatrix} F_{33} & F_{32} & F_{31} \\ F_{23} & F_{22} & F_{21} \\ F_{13} & F_{12} & F_{11} \end{bmatrix} \tag{2b}$$

where case 1 is the default case whose operator $\mathbf{P}_1$ is the identity tensor.

All vectors $\mathbf{V}$ with components $\mathcal{V}_i$ evaluated in $(\vec{\mathbf{E}}_1, \vec{\mathbf{E}}_2, \vec{\mathbf{E}}_3)$ will rotate into $(\vec{\boldsymbol{\imath}}, \vec{\boldsymbol{\jmath}}, \vec{\boldsymbol{k}})$ with components V_i according to the map

$$V_i = P_{ij}\mathcal{V}_j \qquad \text{or inversely} \qquad \mathcal{V}_i = P_{ji}V_j, \tag{3a}$$

while all tensors $\mathbf{T}$ with components $\mathcal{T}_{ij}$ evaluated in $(\vec{\mathbf{E}}_1, \vec{\mathbf{E}}_2, \vec{\mathbf{E}}_3)$ will rotate into $(\vec{\boldsymbol{\imath}}, \vec{\boldsymbol{\jmath}}, \vec{\boldsymbol{k}})$ with components T_{ij} according to the map

$$T_{ij} = P_{ik}\mathcal{T}_{k\ell}P_{j\ell} \qquad \text{or inversely} \qquad \mathcal{T}_{ij} = P_{ki}T_{k\ell}P_{\ell j}, \tag{3b}$$

where the latter appears in Alg. 1 with regards to components of the deformation gradient.

From this point onward, it is assumed that base vectors $(\vec{\mathbf{E}}_1, \vec{\mathbf{E}}_2, \vec{\mathbf{E}}_3)$ are known, and that they serve as the reference basis for our alveolar analysis.

2.2 Geometric Properties of a Regular Pentagon

Figure 7 presents a regular pentagon drawn in its natural co-ordinate system with co-ordinates designated as (ξ, η). Vertices of such a pentagon are placed at

$$\xi = \cos\left(\frac{2(k-1)\pi}{5} + \frac{\pi}{2}\right) \quad \eta = \sin\left(\frac{2(k-1)\pi}{5} + \frac{\pi}{2}\right) \quad k = 1, 2, \ldots, 5 \tag{4}$$

wherein k denotes the vertex number, as assigned in Fig. 7. These vertices inscribe a pentagon within the unit circle.

Lengths of the five chords in a regular pentagon, when measured in its natural co-

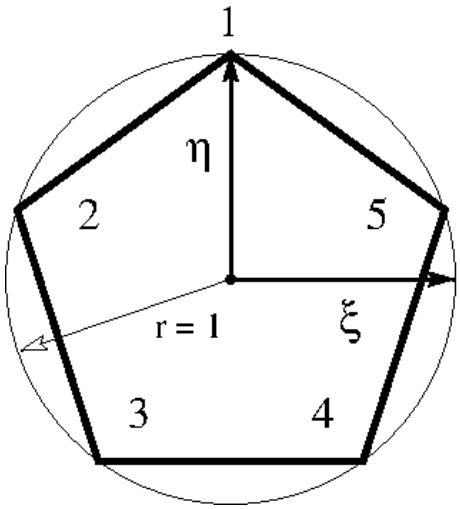

Fig. 7 A regular pentagon inscribed within the unit circle establishes its natural co-ordinate system with co-ordinates (ξ, η) described in Eq. 4, and whose origin is located at its centroid. Vertices are numbered counterclockwise with the uppermost vertex being labeled 1.

ordinate system, are all

$$L^p = 2\cos(\omega) \approx 1.176, \tag{5}$$

while the area of this pentagon is

$$A^p = \tfrac{5}{4}\tan(\omega)\,(L^p)^2 = 5\sin(\omega)\cos(\omega) \approx 2.378, \tag{6}$$

where the area of the unit circle that inscribes this pentagon is $\pi r^2 \approx 3.142$, $r = 1$. The inside angles of a regular pentagon all measure $2\omega = 108^\circ$. All approximations are truncated at four significant figures.

2.3 Geometric Properties of a Regular Dodecahedron

Like the pentagon considered above, which inscribes the unit circle, here we consider a dodecahedron that inscribes the unit sphere. Let this geometry be described in its natural co-ordinate system with co-ordinates (ξ, η, ζ) whose origin is located at its centroid, the center of the sphere. The 20 vertices of this dodecahedron, all of

which touch the unit sphere, are placed at

$$\begin{array}{ccc} \xi & \eta & \zeta \\ \hline \pm 1/\sqrt{3} & \pm 1/\sqrt{3} & \pm 1/\sqrt{3} \\ \pm \phi/\sqrt{3} & \pm 1/\sqrt{3}\phi & 0 \\ 0 & \pm \phi/\sqrt{3} & \pm 1/\sqrt{3}\phi \\ \pm 1/\sqrt{3}\phi & 0 & \pm \phi/\sqrt{3} \end{array} \tag{7}$$

where $\phi = (1 + \sqrt{5})/2 \approx 1.618$, which is also known as the golden ratio.

Lengths of the 30 chords in a regular dodecahedron, when measured in its natural co-ordinate system, are all

$$L^d = \frac{2}{\sqrt{3}\phi} \approx 0.7136, \tag{8}$$

while the volume of such a dodecahedron is

$$V^d = \frac{40}{3\sqrt{3}\phi^3} \tan^2(\omega) \sin(\omega) \approx 2.785, \tag{9}$$

where the volume of the unit sphere that inscribes the dodecahedron is $\frac{4}{3}\pi r^3 \approx 4.189$, $r = 1$.

The scale factor to map between the natural co-ordinates of a pentagon, defined in Eq. 4, with those of a dodecahedron, defined in Eq. 7, is

$$\frac{L^p}{R^p} = \frac{L^d}{R_d^p} \quad \text{or} \quad R_d^p = \frac{R^p L^d}{L^p} = \frac{L^d}{L^p} = \frac{1}{\sqrt{3}\phi \cos(\omega)} \approx 0.6071 \tag{10}$$

because $R^p = 1$, with scale factor R_d^p being the radius that inscribes a pentagon on the surface of a dodecahedron that itself inscribes an unit sphere.

2.4 Dimensions of Human Alveoli

Septal chord length $L(D)$, expressed as a function of alveolar diameter D, can be estimated by considering the areal projection of a dodecahedron onto a plane that contains one of its pentagonal faces, which leads to

$$L = \frac{D}{\tan(\omega)(1 + \cos(\alpha))} \approx \frac{D}{2.685}, \tag{11}$$

where $\alpha = \pi/10 = 18^\circ$. (There are 20, equal, pie-shaped wedges that compose this projected area.) This is an average of the shortest and longest distances across this plane of projection. Alveolar diameter D is a property that can be measured in histological studies of parenchyma.

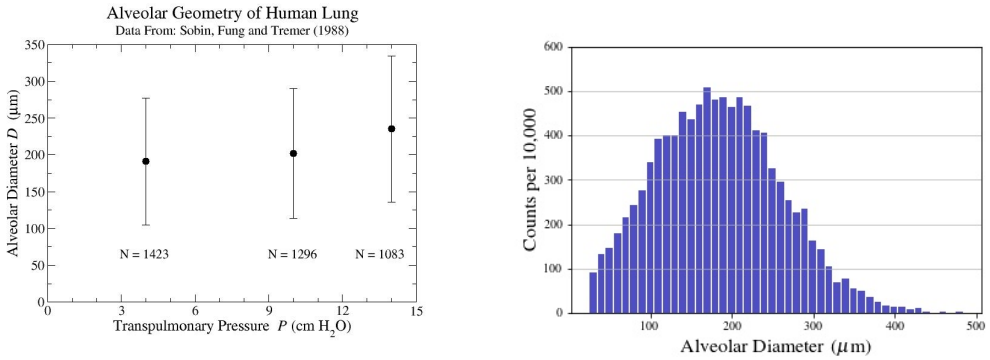

(a) Mean and standard deviations for alveolar diameters in human lung.[54]

(b) A typical histogram for these statistics, truncated at alveolar diameters below 24 μm.

Fig. 8 Alveolar diameters in human lung

To dimension the alveoli of human lung, Sobin *et al*.[54] measured the mean diameter across an individual alveolus, viz., D of Eq. 11, sectioned from human lungs that were fixed at three different pressures. Samples were taken from nine lungs extracted postmortem from individuals between 16 to 89 years of age.* At a transpulmonary pressure of 4 cm H_2O, the mean alveolar diameter was $D = 191 \pm 86$ μm determined from a sampling size of 1423; at a pressure of 10 cm H_2O, $D = 202 \pm 88$ μm determined from a sampling size of 1296; and at a pressure of 14 cm H_2O, $D = 235 \pm 99$ μm determined from a sampling size of 1083. These data are plotted in Fig. 8. All reported and drawn error bounds pertain to plus/minus one standard deviation in error.

*Sobin *et al*.[54] also documented an age effect in these data that has been averaged over here, i.e., ignored.

2.5 Geometric Properties for Irregular Pentagons and Dodecahedra

Formulæ 6 and 9 only apply for regular pentagons and dodecahedra evaluated in their respective natural co-ordinate systems. For irregular dodecahedra, the areas of its irregular pentagons are calculated via*

$$A = \frac{1}{2}\sum_{i=1}^{5}(x_i y_{i+1} - x_{i+1} y_i), \tag{12}$$

where $x_6 \Leftarrow x_1$ and $y_6 \Leftarrow y_1$. In order for the predicted area to be positive when using this formula, it is necessary that the vertices (x_i, y_i) index counterclockwise, as drawn in Fig. 7. The centroid of this pentagon has co-ordinates*

$$c_x = \frac{1}{6A}\sum_{i=1}^{5}(x_i + x_{i+1})(x_i y_{i+1} - x_{i+1} y_i), \tag{13a}$$

$$c_y = \frac{1}{6A}\sum_{i=1}^{5}(y_i + y_{i+1})(x_i y_{i+1} - x_{i+1} y_i), \tag{13b}$$

wherein the vertex co-ordinates x_i and y_i are quantified in a 2D pentagonal frame of reference, e.g., as established later in Fig. 10.

To compute the volume of an irregular dodecahedron, we use the formula†

$$288\, V_{tet}^2 = \begin{vmatrix} 0 & 1 & 1 & 1 & 1 \\ 1 & 0 & \ell_{12}^2 & \ell_{13}^2 & \ell_{14}^2 \\ 1 & \ell_{21}^2 & 0 & \ell_{23}^2 & \ell_{24}^2 \\ 1 & \ell_{31}^2 & \ell_{32}^2 & 0 & \ell_{34}^2 \\ 1 & \ell_{41}^2 & \ell_{42}^2 & \ell_{43}^2 & 0 \end{vmatrix} \tag{14}$$

to calculate each of the 60 individual tetrahedral volumes that collectively fill the volume of an irregular dodecahedron. Here ℓ_{ij} is the length of that tetrahedral edge with vertices i and j; $i, j = 1, 2, 3, 4$; $i \neq j$; with $\ell_{ij} = \ell_{ji}$.

*Bourke, P. "Polygons, meshes." http://paulbourke.net/geometry.

†Colins, KD. "Cayley-Menger Determinant." MathWorld–A Wolfram Web Resource, created by Eric W Weisstein. http://mathworld.wolfram.com/Cayley-MengerDeterminant.html.

Table 1 Natural co-ordinates for the vertices of a regular dodecahedron, as labeled in Fig. 6(b) according to Eq. 7

Vertex	ξ	η	ζ	Vertex	ξ	η	ζ
1	$1/\sqrt{3}$	$1/\sqrt{3}$	$1/\sqrt{3}$	11	$\phi/\sqrt{3}$	$1/\sqrt{3}\phi$	0
2	$1/\sqrt{3}$	$1/\sqrt{3}$	$-1/\sqrt{3}$	12	$\phi/\sqrt{3}$	$-1/\sqrt{3}\phi$	0
3	$-1/\sqrt{3}$	$1/\sqrt{3}$	$-1/\sqrt{3}$	13	$-\phi/\sqrt{3}$	$1/\sqrt{3}\phi$	0
4	$-1/\sqrt{3}$	$1/\sqrt{3}$	$1/\sqrt{3}$	14	$-\phi/\sqrt{3}$	$-1/\sqrt{3}\phi$	0
5	$1/\sqrt{3}$	$-1/\sqrt{3}$	$1/\sqrt{3}$	15	$1/\sqrt{3}\phi$	0	$\phi/\sqrt{3}$
6	$1/\sqrt{3}$	$-1/\sqrt{3}$	$-1/\sqrt{3}$	16	$-1/\sqrt{3}\phi$	0	$\phi/\sqrt{3}$
7	$-1/\sqrt{3}$	$-1/\sqrt{3}$	$-1/\sqrt{3}$	17	$1/\sqrt{3}\phi$	0	$-\phi/\sqrt{3}$
8	$-1/\sqrt{3}$	$-1/\sqrt{3}$	$1/\sqrt{3}$	18	$-1/\sqrt{3}\phi$	0	$-\phi/\sqrt{3}$
9	0	$\phi/\sqrt{3}$	$1/\sqrt{3}\phi$	19	0	$-\phi/\sqrt{3}$	$1/\sqrt{3}\phi$
10	0	$\phi/\sqrt{3}$	$-1/\sqrt{3}\phi$	20	0	$-\phi/\sqrt{3}$	$-1/\sqrt{3}\phi$

2.6 Indexing Scheme for Dodecahedra

In order to implement the dodecahedron as a geometric model for an alveolar sac, as suggested by the images in Fig. 4, it first becomes necessary to introduce a labeling strategy. Such a scheme is arbitrary, but once chosen it enables an analysis to be put forward. The labeling scheme adopted in this work is illustrated in the Fig. 6(b).

The co-ordinates positioning the 20 vertices of a regular dodecahedron in its natural frame of reference are presented in Table 1. According to the labeling scheme of Fig. 6(b), the 30 chords of a dodecahedron are given vertex assignments according to Table 2, while its 12 pentagons are given vertex assignments according to Table 3.

The 60 tetrahedra that fill the volume of the dodecahedron contain vertices according to the following strategy. Beginning with pentagon 1 and sequencing to pentagon 12, two of the four vertices in a tetrahedron come from a side of the pentagon in question with the remaining two vertices being the centroid for the associated pentagon and the centroid for the dodecahedron, i.e., the co-ordinate origin. From Table 3, tetrahedron 1 contains vertices 11 and 2 of pentagon 1, tetrahedron 2 contains vertices 2 and 10, tetrahedron 3 contains vertices 10 and 9, tetrahedron 4 contains vertices 9 and 1, tetrahedron 5 contains vertices 1 and 11, tetrahedron 6 contains vertices 10 and 2 from pentagon 2, etc. The first and fourth vertices of a tetrahedron associate with the centroids of its pentagon and dodecahedron, respectively, with the remaining two being assigned in a right-handed manner such that the first vertex serves as an origin to this tetrahedral triad.

Table 2 Vertices that locate the endpoints of septal chords in a dodecahedron, as labeled in Fig. 6(b)

Chord	Vertices	Chord	Vertices	Chord	Vertices
1	9, 10	11	17, 18	21	7, 18
2	1, 9	12	3, 18	22	7, 14
3	2, 10	13	4, 16	23	13, 14
4	3, 10	14	15, 16	24	8, 14
5	4, 9	15	1, 15	25	8, 16
6	1, 11	16	5, 15	26	5, 19
7	2, 11	17	5, 12	27	6, 20
8	3, 13	18	11, 12	28	7, 20
9	4, 13	19	6, 12	29	8, 19
10	2, 17	20	6, 17	30	19, 20

Table 3 Vertices that locate the corners of regular pentagonal surfaces in a regular dodecahedron, and the chords that connect them. They are indexed counterclockwise when viewed looking from the outside in, and labeled according to Fig. 6(b). The apex for each pentagon resides at the peak of the hipped roof-line for that pentagon. This turns out to be important.

Pentagon	Vertices	Chords
1	11, 2, 10, 9, 1	6, 7, 3, 1, 2
2	10, 2, 17, 18, 3	4, 3, 10, 11, 12
3	13, 4, 9, 10, 3	8, 9, 5, 1, 4
4	9, 4, 16, 15, 1	2, 5, 13, 14, 15
5	15, 5, 12, 11, 1	15, 16, 17, 18, 6
6	17, 2, 11, 12, 6	20, 10, 7, 18, 19
7	18, 7, 14, 13, 3	12, 21, 22, 23, 8
8	16, 4, 13, 14, 8	25, 13, 9, 23, 24
9	12, 5, 19, 20, 6	19, 17, 26, 30, 27
10	14, 7, 20, 19, 8	24, 22, 28, 30, 29
11	20, 7, 18, 17, 6	27, 28, 21, 11, 20
12	19, 5, 15, 16, 8	29, 26, 16, 14, 25

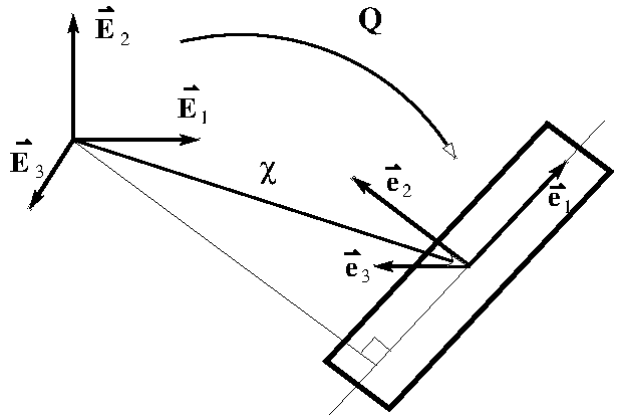

Fig. 9 The co-ordinate system of a chord $(\vec{\mathbf{e}}_1, \vec{\mathbf{e}}_2, \vec{\mathbf{e}}_3)$ relative to the co-ordinate system of its dodecahedron $(\vec{\mathbf{E}}_1, \vec{\mathbf{E}}_2, \vec{\mathbf{E}}_3)$ with origins located at their respective centroids that are offset by a translation χ. These describe a mapping $[\{\vec{\mathbf{e}}_1\}\{\vec{\mathbf{e}}_2\}\{\vec{\mathbf{e}}_3\}] = [\{\vec{\mathbf{E}}_1\}\{\vec{\mathbf{E}}_2\}\{\vec{\mathbf{E}}_3\}][\mathbf{Q}]$ where $\mathbf{Q}$ is an orthogonal rotation. The tangent base vector $\vec{\mathbf{e}}_1$ aligns with the axis of this chord. The normal base vector $\vec{\mathbf{e}}_2$ is coaxial with a line segment drawn from the origin out to the chordal axis such that $\vec{\mathbf{e}}_1 \cdot \vec{\mathbf{e}}_2 = 0$, while the binormal base vector is given by the cross product $\vec{\mathbf{e}}_3 = \vec{\mathbf{e}}_1 \times \vec{\mathbf{e}}_2$.

2.7 Co-Ordinate Systems for Chordal Fibers and Pentagonal Membranes

The dodecahedron used to model an alveolus is considered to be regular in its "natural" configuration, with a capability of being irregular in its reference configuration, and certainly becoming irregular after deformation. The co-ordinate frame of its natural state is taken to have its origin positioned at the centroid of this regular dodecahedron, i.e., at the centroid of its enclosed cube (cf. Fig. 6) or, equivalently, at the origin of that unit sphere for which the dodecahedron inscribes, as presented in Table 1. We denote the base vectors associated with this frame of reference as $(\vec{\mathbf{E}}_1, \vec{\mathbf{E}}_2, \vec{\mathbf{E}}_3)$, assigned according to Section 2. There are three other co-ordinate systems with relevance to our analysis: those for the chordal fibers, those for the pentagonal membranes, and those for the tetrahedral volumes.

The local co-ordinate system of a chordal fiber is presented in Fig. 9. The local co-ordinate system of a pentagonal membrane is presented in Fig. 10. And the local co-ordinate system of a tetrahedral volume is presented in Fig. 11. All three, local, co-ordinate systems are denoted as $(\vec{\mathbf{e}}_1, \vec{\mathbf{e}}_2, \vec{\mathbf{e}}_3)$ and each rotates out of the reference co-ordinate system $(\vec{\mathbf{E}}_1, \vec{\mathbf{E}}_2, \vec{\mathbf{E}}_3)$ of the dodecahedron via its own orthogonal rotation tensor $\mathbf{Q}$.

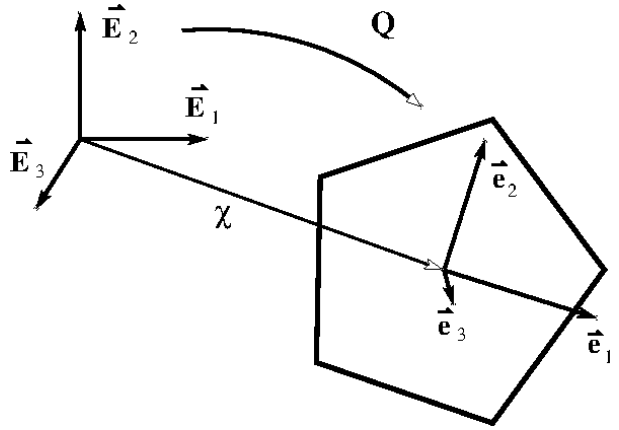

Fig. 10 The co-ordinate system of a pentagon $(\vec{\mathrm{e}}_1, \vec{\mathrm{e}}_2, \vec{\mathrm{e}}_3)$ relative to the co-ordinate system of its dodecahedron $(\vec{\mathbf{E}}_1, \vec{\mathbf{E}}_2, \vec{\mathbf{E}}_3)$ with origins located at their respective centroids that are offset by a translation χ. These describe a mapping $[\{\vec{\mathrm{e}}_1\}\{\vec{\mathrm{e}}_2\}\{\vec{\mathrm{e}}_3\}] = [\{\vec{\mathbf{E}}_1\}\{\vec{\mathbf{E}}_2\}\{\vec{\mathbf{E}}_3\}][\mathsf{Q}]$ where Q is an orthogonal rotation. Base vector $\vec{\mathrm{e}}_1$ is coaxial to a line segment that connects two vertices which locate a pair of shoulders in a pentagon, viz., vertices 2 and 5 in Fig. 7. Base vector $\vec{\mathrm{e}}_2$ is coaxial with a line segment drawn from the head of this pentagon, i.e., vertex 1 in Fig. 7, down to its base such that $\vec{\mathrm{e}}_1 \cdot \vec{\mathrm{e}}_2 = 0$. Base vector $\vec{\mathrm{e}}_3 = \vec{\mathrm{e}}_1 \times \vec{\mathrm{e}}_2$ is the outward normal to this surface.

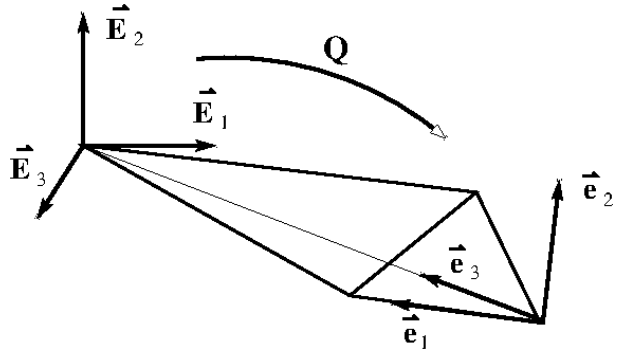

Fig. 11 The co-ordinate system of a tetrahedron $(\vec{\mathrm{e}}_1, \vec{\mathrm{e}}_2, \vec{\mathrm{e}}_3)$ relative to the co-ordinate system of its dodecahedron $(\vec{\mathbf{E}}_1, \vec{\mathbf{E}}_2, \vec{\mathbf{E}}_3)$ with origins located at their respective centroids. These describe a mapping $[\{\vec{\mathrm{e}}_1\}\{\vec{\mathrm{e}}_2\}\{\vec{\mathrm{e}}_3\}] = [\{\vec{\mathbf{E}}_1\}\{\vec{\mathbf{E}}_2\}\{\vec{\mathbf{E}}_3\}][\mathsf{Q}]$ where Q is an orthogonal rotation. Base vector $\vec{\mathrm{e}}_1$ is coaxial to a line segment that connects the centroid of a pentagon with one of the pentagon's vertices. Base vector $\vec{\mathrm{e}}_2$ is normal to $\vec{\mathrm{e}}_1$ and lies in the plane of the pentagon such that $\vec{\mathrm{e}}_1 \cdot \vec{\mathrm{e}}_2 = 0$. Base vector $\vec{\mathrm{e}}_3 = \vec{\mathrm{e}}_1 \times \vec{\mathrm{e}}_2$ points toward the origin of the dodecahedron along the spine that connects the centroid of the dodecahedron with the centroid of a pentagon. Vertex 1 is at the origin of $(\vec{\mathrm{e}}_1, \vec{\mathrm{e}}_2, \vec{\mathrm{e}}_3)$. Vertex 2 is along $\vec{\mathrm{e}}_1$. Vertex 3 lies in the plane of the pentagon. And vertex 4 is at the centroid of the dodecahedron $(\vec{\mathbf{E}}_1, \vec{\mathbf{E}}_2, \vec{\mathbf{E}}_3)$.

3. Kinematics

The irregular dodecahedron used here as a model for alveoli describes a 3D structure comprising 30 1D rods (the septal chords) joined at 20 nodes (the vertices) that collectively circumscribe 12 2D pentagonal membranes (the alveolar septa) that in turn envelop an alveolar sac whose volume is represented using 60 tetrahedra. To be able to describe the overall mechanical response of this 3D dodecahedral structure, it is conjectured to be sufficient to know the individual mechanical responses of its 1D septal chords, its 2D septal membranes, and the 3D void within. Their relevant kinematics are presented here, along with the shape functions used for interpolation and their descriptions of deformation via stretch, using a Lagrangian measure for Laplace stretch[55] as our chosen kinematic field.

3.1 1D Chords

The stretch of a rod under extension is a ratio of its lengths. Specifically, $\lambda := L/L_0$ where L and L_0 are its current and reference lengths, respectively, whose strain and strain rate are taken to be $e = \ln\lambda$ and $\mathrm{d}e = \lambda^{-1}\mathrm{d}\lambda$. This is often referred to as a logarithmic, natural, or true strain. Consequently, the kinematic analysis of a chord is trivial.

3.1.1 Shape Functions for Interpolating a Rod

A two-noded alveolar chord has shape functions N_i, $i = 1, 2$, that, when evaluated in its natural co-ordinate system where $-1 \leqslant \xi \leqslant 1$, describe a matrix with elements

$$\mathbf{N} = \begin{bmatrix} N_1 & N_2 \end{bmatrix} = \begin{bmatrix} \frac{1}{2}(1-\xi) & \frac{1}{2}(1+\xi) \end{bmatrix} \tag{15a}$$

that interpolate vector fields according to

$$\boldsymbol{x}(\xi) = \sum_{i=1}^{2} N_i(\xi)\, x_i, \quad \boldsymbol{u}(\xi) = \sum_{i=1}^{2} N_i(\xi)\, u_i, \tag{15b}$$

etc., and whose spatial gradients are

$$N_{1,\xi} = -\tfrac{1}{2} \quad \text{and} \quad N_{2,\xi} = \tfrac{1}{2}, \tag{15c}$$

wherein ξ is the natural co-ordinate. Components x_i and $u_i := x_i - x_{0i}$, $i = 1, 2$, are their global co-ordinates and displacements, respectively, located at the two nodes of a chord evaluated in the co-ordinate frame $(\vec{\mathbf{e}}_1, \vec{\mathbf{e}}_2, \vec{\mathbf{e}}_3)$ of Fig. 9 with the chordal axis lying in the $\vec{\mathbf{e}}_1$ direction.

3.1.2 Deformation Gradient for a Rod

The deformation gradient in this case is simply

$$\begin{aligned}\mathbf{F}(\xi) = \mathbf{I} + \frac{\partial \boldsymbol{u}}{\partial \xi}\left(\frac{\partial \boldsymbol{x}_0}{\partial \xi}\right)^{-1} &= \mathbf{I} + \sum_{i=1}^{2} N_{i,\xi} u_i \left(\sum_{i=1}^{2} N_{i,\xi} x_{0i}\right)^{-1} \vec{\mathbf{e}}_1 \otimes \vec{\mathbf{e}}_1 \\ &= \mathbf{I} + \frac{u_2 - u_1}{x_{02} - x_{01}} \vec{\mathbf{e}}_1 \otimes \vec{\mathbf{e}}_1 = \frac{x_2 - x_1}{x_{02} - x_{01}} \vec{\mathbf{e}}_1 \otimes \vec{\mathbf{e}}_1, \quad (16)\end{aligned}$$

which is uniform over the length of a chord, i.e., it is independent of ξ.

3.2 2D Triangles

Triangular elements are needed in a support capacity in order to construct our alveolar model; specifically, the four surfaces of a tetrahedron are triangles. What is required of them is a capability to compute the traction acting across such a surface through integration. This requires knowledge of their shape functions and quadrature rules, the latter topic being discussed in Section 5.

3.2.1 Shape Functions for Interpolating a Triangle

The shape functions for a triangle expressed in terms of its natural co-ordinates (ξ, η), where $0 \leqslant \xi \leqslant 1$ and $0 \leqslant \eta \leqslant 1 - \xi$, are given by

$$N_1 = 1 - \xi - \eta \qquad N_2 = \xi \qquad N_3 = \eta \qquad (17a)$$

with gradients of

$$N_{1,\xi} = -1 \qquad N_{2,\xi} = 1 \qquad N_{3,\xi} = 0 \qquad (17b)$$

$$N_{2,\eta} = -1 \qquad N_{2,\eta} = 0 \qquad N_{3,\eta} = 1 \qquad (17c)$$

so that the area of a triangle in its natural co-ordinates is $1/2$.

No further kinematics are required from triangular elements in our analysis.

3.3 2D Irregular Pentagons

The kinematics of an irregular pentagon, on the other hand, are not trivial. Shape functions are required from which deformation gradients can then be constructed. Once a deformation gradient is in hand, the state of stretch occurring within a pentagon at its Gauss points can finally be derived. Several possible decompositions of the deformation gradient are possible, i.e., the notion of stretch is not unique in 2D (nor in 3D). Here we employ the Lagrangian version of Laplace stretch.[56]

3.3.1 Wachspress' Shape Functions for Interpolating an Irregular Pentagon

The idea here is to model each pentagonal face of a dodecahedron with one, pentagonal, finite element. Five constant-strain triangles were originally considered, but their accuracy was found to be wanting when compared with that of a single pentagonal element whenever the deformation becomes non-uniform. There was no difference between them whenever the deformation was just a uniform dilation.

In 1975, Wachspress[57,58] derived a set of shape functions N_i that are capable of interpolating convex polyhedra. His shape functions take on the form of rational polynomials, viz., $N_i = A_i/B$ where A_i and B are polynomials. In contrast, classic isoparametric elements are constructed from polynomial shape functions.[59] For the Wachspress shape functions of a pentagon, the A_i are cubic polynomials, while B is a quadratic polynomial.

Let us consider a convex pentagonal domain Ω defined over $\mathbb{R}^2$ whose vertices have global co-ordinates of

$$(x_1, y_1),\ (x_2, y_2),\ (x_3, y_3),\ (x_4, y_4),\ (x_5, y_5)$$

when evaluated in the pentagonal co-ordinate system $(\vec{\mathbf{e}}_1, \vec{\mathbf{e}}_2)$ of Fig. 10, with $\vec{\mathbf{e}}_3$ being an outward normal to the pentagon. Associated with this set of global co-ordinates is a set of local or natural co-ordinates

$$(\xi_1, \eta_1),\ (\xi_2, \eta_2),\ (\xi_3, \eta_3),\ (\xi_4, \eta_4),\ (\xi_5, \eta_5)$$

that describe a mapping of interpolation where

$$\begin{aligned} x(\xi,\eta) &= \textstyle\sum_{i=1}^{5} N_i(\xi,\eta)\, x_i \\ y(\xi,\eta) &= \textstyle\sum_{i=1}^{5} N_i(\xi,\eta)\, y_i \end{aligned} \qquad \text{or} \qquad \boldsymbol{x}(\boldsymbol{\xi}) = \sum_{i=1}^{5} N_i(\boldsymbol{\xi})\, \boldsymbol{x}_i \tag{18}$$

which relate natural co-ordinates $\boldsymbol{\xi} \equiv (\xi,\eta)$ to global co-ordinates $\boldsymbol{x} \equiv (x,y)$, where $\boldsymbol{x}_i \equiv (x_i, y_i)$ are nodal co-ordinates at the i^{th} vertex, with i indexing counter-clockwise around a pentagon according to Fig. 7. Displacement $\boldsymbol{u}(\boldsymbol{x}) \coloneqq \boldsymbol{x} - \boldsymbol{x}_0$, with reference co-ordinates $\boldsymbol{x}_0 \equiv (x_0, y_0)$, also obeys this mapping

$$\begin{aligned} u(\xi,\eta) &= \textstyle\sum_{i=1}^{5} N_i(\xi,\eta)\, u_i \\ v(\xi,\eta) &= \textstyle\sum_{i=1}^{5} N_i(\xi,\eta)\, v_i \end{aligned} \qquad \text{or} \qquad \boldsymbol{u}(\boldsymbol{\xi}) = \sum_{i=1}^{5} N_i(\boldsymbol{\xi})\, \boldsymbol{u}_i \tag{19}$$

whose components $\boldsymbol{u}_i \equiv (u_i, v_i)$ designate the nodal displacements.

Shape functions $N_i(\boldsymbol{\xi}) \equiv N_i(\xi,\eta)$ are interpolation functions that place any position P with local co-ordinates $\boldsymbol{\xi} \equiv (\xi,\eta) \in \bar{\Omega}$, where $\bar{\Omega} \coloneqq \Omega \cup \partial\Omega$, into their global co-ordinates $\boldsymbol{x} \equiv (x,y)$. The shape functions of Wachspress[57,58] possess the following properties[60]:

1. Partition of unity: $\sum_{i=1}^{5} N_i(\boldsymbol{\xi}) = 1, \quad 0 \leqslant N_i(\boldsymbol{\xi}) \leqslant 1.$
2. Interpolate nodal data: $N_i(\boldsymbol{\xi}_j) = \Xi_{ij}$.
3. Linear completeness: $\sum_{i=1}^{5} N_i(\boldsymbol{\xi})\, \boldsymbol{x}_i = \boldsymbol{x}$.
4. For $\boldsymbol{\xi} \in \Omega$, $N_i(\boldsymbol{\xi})$ is C^∞, but for $\boldsymbol{\xi} \in \partial\Omega$, $N_i(\boldsymbol{\xi})$ is C^0, i.e., interpolation is linear along an edge (or alveolar chord) connecting two neighboring vertices.

Item 4 is often considered a disadvantage of Wachspress shape functions, viz., the linear interpolation along their boundaries. However, this is appropriate for our modeling of alveoli, because the septal boundaries are alveolar chords that are taken to interpolate linearly.

For interpolating a convex, planar, pentagonal shape, the shape functions of Wachspress have polynomials of order three in their numerators, and another polynomial

of order two in their denominators; specifically, we write them here as

$$N_{i+1}(\xi,\eta) = \kappa_i\, A_i(\xi,\eta)/B(\xi,\eta), \qquad i = 1, 2, \ldots, 5 \tag{20a}$$

using a scaling factor of κ_i, where $N_1 \Leftarrow N_6$. The numerators and denominator for interpolating a pentagon take on the general form of

$$\begin{aligned} A_i(\xi,\eta) &= \alpha_{0i} + \alpha_{1i}\xi + \alpha_{2i}\eta + \alpha_{3i}\xi^2 + \alpha_{4i}\xi\eta + \alpha_{5i}\eta^2 \\ &\quad + \alpha_{6i}\xi^3 + \alpha_{7i}\xi^2\eta + \alpha_{8i}\xi\eta^2 + \alpha_{9i}\eta^3, \end{aligned} \tag{20b}$$

$$B(\xi,\eta) = \beta_0 + \beta_1\xi + \beta_2\eta + \beta_3\xi^2 + \beta_4\xi\eta + \beta_5\eta^2, \tag{20c}$$

where coefficients in the numerator, i.e., the A_i, differ with index i, while those in the denominator, viz., the $B \coloneqq \sum_{i=1}^{5} A_i$, are the same for all five shape functions.

We apply the construction technique of Dasgupta[61] to compute the shape functions of Wachspress for an irregular convex pentagon. Consider a chord c_i that connects vertex $\boldsymbol{\xi}_{i-1} = (\xi_{i-1}, \eta_{i-1})$ with vertex $\boldsymbol{\xi}_i = (\xi_i, \eta_i)$ via a straight line segment such that $\ell_i = 0$ with $\ell_i \coloneqq 1 - a_i\xi - b_i\eta$ wherein

$$a_i = \frac{\eta_i - \eta_{i-1}}{\xi_{i-1}\eta_i - \xi_i\eta_{i-1}}, \tag{21a}$$

$$b_i = \frac{\xi_{i-1} - \xi_i}{\xi_{i-1}\eta_i - \xi_i\eta_{i-1}}, \tag{21b}$$

for which Dasgupta derived the following set of constraints

$$\kappa_i = \kappa_{i-1}\left(\frac{a_{i+1}(\xi_{i-1} - \xi_i) + b_{i+1}(\eta_{i-1} - \eta_i)}{a_{i-1}(\xi_i - \xi_{i-1}) + b_{i-1}(\eta_i - \eta_{i-1})}\right) \tag{21c}$$

with recursion starting at $\kappa_1 \coloneqq 1$. Coefficients κ_i enforce property 4 listed above.

With this information in hand, we then derived rational polynomials describing Wachspress' shape functions for a pentagon specified in Eq. 20 in terms of the parameters a_i, b_i, and κ_i. The polynomial coefficients for the A_i in Eq. 20b have

values of

$$\alpha_{0i} = 1 \tag{22a}$$
$$\alpha_{1i} = -(a_{i+1} + a_{i+2} + a_{i+3}) \tag{22b}$$
$$\alpha_{2i} = -(b_{i+1} + b_{i+2} + b_{i+3}) \tag{22c}$$
$$\alpha_{3i} = a_{i+1}a_{i+2} + a_{i+2}a_{i+3} + a_{i+3}a_{i+1} \tag{22d}$$
$$\alpha_{4i} = a_{i+1}(b_{i+2} + b_{i+3}) + a_{i+2}(b_{i+1} + b_{i+3}) + a_{i+3}(b_{i+1} + b_{i+2}) \tag{22e}$$
$$\alpha_{5i} = b_{i+1}b_{i+2} + b_{i+2}b_{i+3} + b_{i+3}b_{i+1} \tag{22f}$$
$$\alpha_{6i} = -a_{i+1}a_{i+2}a_{i+3} \tag{22g}$$
$$\alpha_{7i} = -(a_{i+1}a_{i+2}b_{i+3} + a_{i+1}b_{i+2}a_{i+3} + b_{i+1}a_{i+2}a_{i+3}) \tag{22h}$$
$$\alpha_{8i} = -(a_{i+1}b_{i+2}b_{i+3} + b_{i+1}a_{i+2}b_{i+3} + b_{i+1}b_{i+2}a_{i+3}) \tag{22i}$$
$$\alpha_{9i} = -b_{i+1}b_{i+2}b_{i+3} \tag{22j}$$

which differ for each shape function via index $i = 1, 2, \ldots, 5$, while the polynomial coefficients for B in Eq. 20c have values of

$$\beta_i = \sum_{j=1}^{5} \alpha_{ij}\kappa_j, \qquad i = 0, 1, \ldots, 5 \tag{23}$$

which are the same for all five shape functions. Sums over the four cubic terms in Eq. 22 all vanish—a byproduct of Wachspress' formulation. In the above formulæ, an index count of $i \equiv 0 \implies i = 5$, while index counts of $i \equiv 6 \implies i = 1$, $i \equiv 7 \implies i = 2$, and $i \equiv 8 \implies i = 3$. Shape function N_1 is illustrated in Fig. 12, with like images applying for the other four shape functions.

3.3.2 First Derivatives of the Shape Functions

The first derivatives of Wachspress' shape functions for a pentagon are

$$N_{i+1,\xi}(\xi, \eta) = \kappa_i \mathcal{N}_{i,\xi}(\xi, \eta)/B^2(\xi, \eta), \tag{24a}$$
$$N_{i+1,\eta}(\xi, \eta) = \kappa_i \mathcal{N}_{i,\eta}(\xi, \eta)/B^2(\xi, \eta), \tag{24b}$$

where $N_{i+1,\xi}(\xi, \eta) = \partial N_{i+1}(\xi, \eta)/\partial\xi$ and $N_{i+1,\eta}(\xi, \eta) = \partial N_{i+1}(\xi, \eta)/\partial\eta$ with

$$\mathcal{N}_{i,\xi}(\xi, \eta) = B(\xi, \eta)A_{i,\xi}(\xi, \eta) - B_{,\xi}(\xi, \eta)A_i(\xi, \eta), \tag{24c}$$
$$\mathcal{N}_{i,\eta}(\xi, \eta) = B(\xi, \eta)A_{i,\eta}(\xi, \eta) - B_{,\eta}(\xi, \eta)A_i(\xi, \eta), \tag{24d}$$

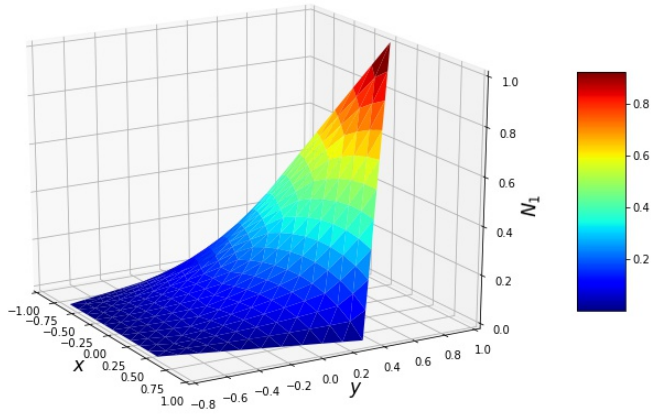

Fig. 12 Wachspress shape functions for a pentagon, in this case, shape function N_1

which contain the polynomials

$$A_{i,\xi}(\xi,\eta) = \alpha_{1i} + 2\alpha_{3i}\xi + \alpha_{4i}\eta + 3\alpha_{6i}\xi^2 + 2\alpha_{7i}\xi\eta + \alpha_{8i}\eta^2, \tag{24e}$$

$$A_{i,\eta}(\xi,\eta) = \alpha_{2i} + \alpha_{4i}\xi + 2\alpha_{5i}\eta + \alpha_{7i}\xi^2 + 2\alpha_{8i}\xi\eta + 3\alpha_{9i}\eta^2, \tag{24f}$$

$$B_{,\xi}(\xi,\eta) = \beta_1 + 2\beta_3\xi + \beta_4\eta, \tag{24g}$$

$$B_{,\eta}(\xi,\eta) = \beta_2 + \beta_4\xi + 2\beta_5\eta, \tag{24h}$$

from which the deformation and displacement gradients are constructed.

3.3.3 Second Derivatives of the Shape Functions

The second derivatives of these shape functions, which we used to test the compatibility conditions of this element, are described by

$$N_{i+1,\xi\xi} = \kappa_i\, \mathfrak{N}_{i,\xi\xi}(\xi,\eta)/B^3(\xi,\eta), \tag{25a}$$

$$N_{i+1,\xi\eta} = \kappa_i\, \mathfrak{N}_{i,\xi\eta}(\xi,\eta)/B^3(\xi,\eta), \tag{25b}$$

$$N_{i+1,\eta\xi} = \kappa_i\, \mathfrak{N}_{i,\eta\xi}(\xi,\eta)/B^3(\xi,\eta), \tag{25c}$$

$$N_{i+1,\eta\eta} = \kappa_i\, \mathfrak{N}_{i,\eta\eta}(\xi,\eta)/B^3(\xi,\eta), \tag{25d}$$

where $N_{i+1,\xi\eta}(\xi,\eta) = \partial^2 N_{i+1}(\xi,\eta)/\partial\xi\partial\eta$, etc., and where

$$\mathfrak{N}_{i,\xi\xi}(\xi,\eta) = B(\xi,\eta)\mathcal{N}_{i,\xi\xi}(\xi,\eta) - 2B_{,\xi}(\xi,\eta)\mathcal{N}_{i,\xi}(\xi,\eta), \tag{25e}$$
$$\mathfrak{N}_{i,\xi\eta}(\xi,\eta) = B(\xi,\eta)\mathcal{N}_{i,\xi\eta}(\xi,\eta) - 2B_{,\xi}(\xi,\eta)\mathcal{N}_{i,\eta}(\xi,\eta), \tag{25f}$$
$$\mathfrak{N}_{i,\eta\xi}(\xi,\eta) = B(\xi,\eta)\mathcal{N}_{i,\eta\xi}(\xi,\eta) - 2B_{,\eta}(\xi,\eta)\mathcal{N}_{i,\xi}(\xi,\eta), \tag{25g}$$
$$\mathfrak{N}_{i,\eta\eta}(\xi,\eta) = B(\xi,\eta)\mathcal{N}_{i,\eta\eta}(\xi,\eta) - 2B_{,\eta}(\xi,\eta)\mathcal{N}_{i,\eta}(\xi,\eta), \tag{25h}$$

wherein

$$\mathcal{N}_{i,\xi\xi}(\xi,\eta) = B(\xi,\eta)A_{i,\xi\xi}(\xi,\eta) - B_{,\xi\xi}(\xi\eta)A_i(\xi\eta), \tag{25i}$$
$$\begin{aligned}\mathcal{N}_{i,\xi\eta}(\xi,\eta) &= B(\xi,\eta)A_{i,\xi\eta}(\xi,\eta) + B_{,\xi}(\xi,\eta)A_{i,\eta}(\xi,\eta)\\ &\quad - B_{,\eta}(\xi,\eta)A_{i,\xi}(\xi,\eta) - B_{,\xi\eta}(\xi,\eta)A_i(\xi,\eta),\end{aligned} \tag{25j}$$
$$\begin{aligned}\mathcal{N}_{i,\eta\xi}(\xi,\eta) &= B(\xi,\eta)A_{i,\eta\xi}(\xi,\eta) + B_{,\eta}(\xi,\eta)A_{i,\xi}(\xi,\eta)\\ &\quad - B_{,\xi}(\xi,\eta)A_{i,\eta}(\xi,\eta) - B_{,\eta\xi}(\xi,\eta)A_i(\xi,\eta),\end{aligned} \tag{25k}$$
$$\mathcal{N}_{i,\eta\eta}(\xi,\eta) = B(\xi,\eta)A_{i,\eta\eta}(\xi,\eta) - B_{,\eta\eta}(\xi,\eta)A_i(\xi,\eta), \tag{25l}$$

which contain polynomials

$$A_{i,\xi\xi}(\xi,\eta) = 2\alpha_{3i} + 6\alpha_{6i}\xi + 2\alpha_{7i}\eta, \tag{25m}$$
$$A_{i,\xi\eta}(\xi,\eta) = \alpha_{4i} + 2\alpha_{7i}\xi + 2\alpha_{8i}\eta, \tag{25n}$$
$$A_{i,\eta\eta}(\xi,\eta) = 2\alpha_{5i} + 2\alpha_{8i}\xi + 6\alpha_{9i}\eta, \tag{25o}$$
$$B_{,\xi\xi}(\xi,\eta) = 2\beta_3, \tag{25p}$$
$$B_{,\xi\eta}(\xi,\eta) = \beta_4, \tag{25q}$$
$$B_{,\eta\eta}(\xi,\eta) = 2\beta_5, \tag{25r}$$

with $A_{i,\xi\eta}(\xi,\eta) = A_{i,\eta\xi}(\xi,\eta)$ and $B_{,\xi\eta}(\xi,\eta) = B_{,\eta\xi}(\xi,\eta)$.

3.3.4 Deformation Gradient for an Irregular Pentagon

Derivatives of displacement (u, v) taken with respect to the local co-ordinates (ξ, η) described in terms of gradients of the shape functions $N_{i,\xi}(\xi,\eta)$ and $N_{i,\eta}(\xi,\eta)$ of a pentagon have components

$$\begin{bmatrix}\partial u/\partial\xi & \partial u/\partial\eta\\ \partial v/\partial\xi & \partial v/\partial\eta\end{bmatrix} = \begin{bmatrix}\sum_{i=1}^{5} N_{i,\xi}(\xi,\eta)\,u_i & \sum_{i=1}^{5} N_{i,\eta}(\xi,\eta)\,u_i\\ \sum_{i=1}^{5} N_{i,\xi}(\xi,\eta)\,v_i & \sum_{i=1}^{5} N_{i,\eta}(\xi,\eta)\,v_i\end{bmatrix}, \tag{26a}$$

where $u \coloneqq x - x_0$ and $v \coloneqq y - y_0$. Gradients of the global co-ordinates (x_0, y_0) evaluated in a reference state taken with respect to the local co-ordinates (ξ, η) have components

$$\begin{bmatrix} \partial x_0/\partial\xi & \partial x_0/\partial\eta \\ \partial y_0/\partial\xi & \partial y_0/\partial\eta \end{bmatrix} = \begin{bmatrix} \sum_{i=1}^{5} N_{i,\xi}(\xi,\eta)\, x_{0i} & \sum_{i=1}^{5} N_{i,\eta}(\xi,\eta)\, x_{0i} \\ \sum_{i=1}^{5} N_{i,\xi}(\xi,\eta)\, y_{0i} & \sum_{i=1}^{5} N_{i,\eta}(\xi,\eta)\, y_{0i} \end{bmatrix}, \tag{26b}$$

wherein (x_{0i}, y_{0i}) are the reference global co-ordinates at the i^{th} vertex, while gradients of the global co-ordinates (x, y) evaluated in the current state taken with respect to the local co-ordinates (ξ, η) have components

$$\begin{bmatrix} \partial x/\partial\xi & \partial x/\partial\eta \\ \partial y/\partial\xi & \partial y/\partial\eta \end{bmatrix} = \begin{bmatrix} \sum_{i=1}^{5} N_{i,\xi}(\xi,\eta)\, x_{i} & \sum_{i=1}^{5} N_{i,\eta}(\xi,\eta)\, x_{i} \\ \sum_{i=1}^{5} N_{i,\xi}(\xi,\eta)\, y_{i} & \sum_{i=1}^{5} N_{i,\eta}(\xi,\eta)\, y_{i} \end{bmatrix}, \tag{26c}$$

whose transpose establishes the Jacobian matrix

$$\mathbf{J} \coloneqq \begin{bmatrix} \partial x/\partial\xi & \partial y/\partial\xi \\ \partial x/\partial\eta & \partial y/\partial\eta \end{bmatrix} = \begin{bmatrix} \sum_{i=1}^{5} N_{i,\xi}(\xi,\eta)\, x_{i} & \sum_{i=1}^{5} N_{i,\xi}(\xi,\eta)\, y_{i} \\ \sum_{i=1}^{5} N_{i,\eta}(\xi,\eta)\, x_{i} & \sum_{i=1}^{5} N_{i,\eta}(\xi,\eta)\, y_{i} \end{bmatrix}, \tag{26d}$$

wherein (x_i, y_i) denote the current global co-ordinates at the i^{th} vertex.

From the above matrices, one can construct the deformation gradient $\mathbf{F} = \partial\boldsymbol{x}/\partial\mathbf{x}_0 = \mathbf{I} + \partial\boldsymbol{u}/\partial\boldsymbol{x}_0$ for an irregular pentagon via

$$\begin{aligned} \mathbf{F}(\xi,\eta) &= \begin{bmatrix} F_{11}(\xi,\eta) & F_{12}(\xi,\eta) \\ F_{21}(\xi,\eta) & F_{22}(\xi,\eta) \end{bmatrix} \\ &= \begin{bmatrix} 1 & 0 \\ 0 & 1 \end{bmatrix} + \begin{bmatrix} \partial u/\partial\xi & \partial u/\partial\eta \\ \partial v/\partial\xi & \partial v/\partial\eta \end{bmatrix} \begin{bmatrix} \partial x_0/\partial\xi & \partial x_0/\partial\eta \\ \partial y_0/\partial\xi & \partial y_0/\partial\eta \end{bmatrix}^{-1}, \end{aligned} \tag{27a}$$

whose inverse is

$$\mathbf{F}^{-1}(\xi,\eta) = \frac{1}{F_{11}(\xi,\eta)F_{22}(\xi,\eta) - F_{21}(\xi,\eta)F_{12}(\xi,\eta)} \begin{bmatrix} F_{22}(\xi,\eta) & -F_{12}(\xi,\eta) \\ -F_{21}(\xi,\eta) & F_{11}(\xi,\eta) \end{bmatrix}, \tag{27b}$$

while its associated displacement gradient $\mathbf{G} = \partial \boldsymbol{u}/\partial \boldsymbol{x}$ is given by

$$\mathbf{G}(\xi,\eta) = \begin{bmatrix} G_{11}(\xi,\eta) & G_{12}(\xi,\eta) \\ G_{21}(\xi,\eta) & G_{22}(\xi,\eta) \end{bmatrix} = \begin{bmatrix} \partial u/\partial \xi & \partial u/\partial \eta \\ \partial v/\partial \xi & \partial v/\partial \eta \end{bmatrix} \begin{bmatrix} \partial x/\partial \xi & \partial x/\partial \eta \\ \partial y/\partial \xi & \partial y/\partial \eta \end{bmatrix}^{-1}, \tag{28}$$

which is not invertible, in general. All are evaluated in the 12 plane belonging to a co-ordinate system $(\vec{\mathbf{e}}_2, \vec{\mathbf{e}}_2, \vec{\mathbf{e}}_3)$ that orients this pentagon, with $\vec{\mathbf{e}}_3$ being normal to its surface, as illustrated in Fig. 10. The deformation and displacement gradients are two, fundamental, kinematic fields commonly used in the construction of constitutive equations.

3.3.5 Compatibility Conditions

To ensure that a deformation is compatible, and therefore integrable, it follows that the curl of its deformation gradient must be zero.[62] This condition is trivially satisfied for the shape functions that we use for 1D chords, 2D triangles, and 3D tetrahedra. However, for the Wachspress shape function used to interpolate pentagons, this needs to be verified. Vanishing of the curl of $\mathbf{F}$ results in two constraint equations for the planar case, they being

$$F_{11,2} = F_{12,1} \qquad \text{and} \qquad F_{22,1} = F_{21,2} \tag{29}$$

whose spatial derivatives associate with the $(\vec{\mathbf{e}}_1, \vec{\mathbf{e}}_2)$ co-ordinate frame.

From Eq. 27, it follows that the spatial derivatives of the deformation gradient are

$$\begin{aligned} \mathbf{F}_{,1}(\xi,\eta) &= \frac{\partial}{\partial x_0} \begin{bmatrix} F_{11}(\xi,\eta) & F_{12}(\xi,\eta) \\ F_{21}(\xi,\eta) & F_{22}(\xi,\eta) \end{bmatrix} \\ &= \frac{\partial \xi}{\partial x_0} \left(\frac{\partial}{\partial \xi} \left(\begin{bmatrix} \partial u/\partial \xi & \partial u/\partial \eta \\ \partial v/\partial \xi & \partial v/\partial \eta \end{bmatrix} \right) \begin{bmatrix} \partial x_0/\partial \xi & \partial x_0/\partial \eta \\ \partial y_0/\partial \xi & \partial y_0/\partial \eta \end{bmatrix}^{-1} - \begin{bmatrix} \partial u/\partial \xi & \partial u/\partial \eta \\ \partial v/\partial \xi & \partial v/\partial \eta \end{bmatrix} \right. \\ &\quad \left. \times \begin{bmatrix} \partial x_0/\partial \xi & \partial x_0/\partial \eta \\ \partial y_0/\partial \xi & \partial y_0/\partial \eta \end{bmatrix}^{-1} \frac{\partial}{\partial \xi} \left(\begin{bmatrix} \partial x_0/\partial \xi & \partial x_0/\partial \eta \\ \partial y_0/\partial \xi & \partial y_0/\partial \eta \end{bmatrix} \right) \begin{bmatrix} \partial x_0/\partial \xi & \partial x_0/\partial \eta \\ \partial y_0/\partial \xi & \partial y_0/\partial \eta \end{bmatrix}^{-1} \right) \end{aligned} \tag{30a}$$

and

$$\mathbf{F}_{,2}(\xi,\eta) = \frac{\partial}{\partial y_0}\begin{bmatrix} F_{11}(\xi,\eta) & F_{12}(\xi,\eta) \\ F_{21}(\xi,\eta) & F_{22}(\xi,\eta) \end{bmatrix}$$
$$= \frac{\partial \eta}{\partial y_0}\left(\frac{\partial}{\partial \eta}\left(\begin{bmatrix} \partial u/\partial\xi & \partial u/\partial\eta \\ \partial v/\partial\xi & \partial v/\partial\eta \end{bmatrix}\right)\begin{bmatrix} \partial x_0/\partial\xi & \partial x_0/\partial\eta \\ \partial y_0/\partial\xi & \partial y_0/\partial\eta \end{bmatrix}^{-1} - \begin{bmatrix} \partial u/\partial\xi & \partial u/\partial\eta \\ \partial v/\partial\xi & \partial v/\partial\eta \end{bmatrix}\right.$$
$$\left.\times \begin{bmatrix} \partial x_0/\partial\xi & \partial x_0/\partial\eta \\ \partial y_0/\partial\xi & \partial y_0/\partial\eta \end{bmatrix}^{-1}\frac{\partial}{\partial \eta}\left(\begin{bmatrix} \partial x_0/\partial\xi & \partial x_0/\partial\eta \\ \partial y_0/\partial\xi & \partial y_0/\partial\eta \end{bmatrix}\right)\begin{bmatrix} \partial x_0/\partial\xi & \partial x_0/\partial\eta \\ \partial y_0/\partial\xi & \partial y_0/\partial\eta \end{bmatrix}^{-1}\right) \tag{30b}$$

wherein

$$\frac{\partial}{\partial\xi}\begin{bmatrix} \partial u/\partial\xi & \partial u/\partial\eta \\ \partial v/\partial\xi & \partial v/\partial\eta \end{bmatrix} = \begin{bmatrix} \sum_{i=1}^5 N_{i,\xi\xi}(\xi,\eta)\,u_i & \sum_{i=1}^5 N_{i,\xi\eta}(\xi,\eta)\,u_i \\ \sum_{i=1}^5 N_{i,\xi\xi}(\xi,\eta)\,v_i & \sum_{i=1}^5 N_{i,\xi\eta}(\xi,\eta)\,v_i \end{bmatrix} \tag{31a}$$
$$\frac{\partial}{\partial\eta}\begin{bmatrix} \partial u/\partial\xi & \partial u/\partial\eta \\ \partial v/\partial\xi & \partial v/\partial\eta \end{bmatrix} = \begin{bmatrix} \sum_{i=1}^5 N_{i,\eta\xi}(\xi,\eta)\,u_i & \sum_{i=1}^5 N_{i,\eta\eta}(\xi,\eta)\,u_i \\ \sum_{i=1}^5 N_{i,\eta\xi}(\xi,\eta)\,v_i & \sum_{i=1}^5 N_{i,\eta\eta}(\xi,\eta)\,v_i \end{bmatrix} \tag{31b}$$

and

$$\frac{\partial}{\partial\xi}\begin{bmatrix} \partial x_0/\partial\xi & \partial x_0/\partial\eta \\ \partial y_0/\partial\xi & \partial y_0/\partial\eta \end{bmatrix} = \begin{bmatrix} \sum_{i=1}^5 N_{i,\xi\xi}(\xi,\eta)\,x_{0i} & \sum_{i=1}^5 N_{i,\xi\eta}(\xi,\eta)\,x_{0i} \\ \sum_{i=1}^5 N_{i,\xi\xi}(\xi,\eta)\,y_{0i} & \sum_{i=1}^5 N_{i,\xi\eta}(\xi,\eta)\,y_{0i} \end{bmatrix} \tag{31c}$$
$$\frac{\partial}{\partial\eta}\begin{bmatrix} \partial x_0/\partial\xi & \partial x_0/\partial\eta \\ \partial y_0/\partial\xi & \partial y_0/\partial\eta \end{bmatrix} = \begin{bmatrix} \sum_{i=1}^5 N_{i,\eta\xi}(\xi,\eta)\,x_{0i} & \sum_{i=1}^5 N_{i,\eta\eta}(\xi,\eta)\,x_{0i} \\ \sum_{i=1}^5 N_{i,\eta\xi}(\xi,\eta)\,y_{0i} & \sum_{i=1}^5 N_{i,\eta\eta}(\xi,\eta)\,y_{0i} \end{bmatrix} \tag{31d}$$

with $\partial\xi/\partial x_0$ and $\partial\eta/\partial y_0$ effectively being scaling factors that we take to be described as a ratio of septal chord lengths; specifically, let

$$\frac{\partial\xi}{\partial x_0} \simeq \frac{\partial\eta}{\partial y_0} \approx \frac{L(\xi,\eta)}{L_0(x,y)} = \frac{\cos(\omega)}{\sqrt{A_0/5\tan(\omega)}}, \tag{32}$$

where $L(\xi,\eta)$ is the septal length of a pentagonal edge in its natural configuration, as drawn in Fig. 7, while $L_0(x,y)$ is the actual, alveolar, septal length with $A_0(x,y)$ being the area of an alveolar septum in its reference state. This formula follows from Eqs. 5 and 6.

Note: We study compatibility only for the purpose of assessing applicability in our choice of selecting Wachspress shape functions. Otherwise, it is not required in our

modeling of an alveolus via a dodecahedron.

3.3.6 Gram–Schmidt Decomposition of the Deformation Gradient

To describe kinematics of a planar membrane, an upper-triangular Gram–Schmidt decomposition of the deformation gradient $\mathbf{F}$ is used in lieu of the symmetric polar decomposition that is commonly adopted.[56,63–66] McLellan[51,67] was the first to propose a triangular decomposition of $\mathbf{F}$, to prove its uniqueness and existence, and to establish many of its physical properties. This idea has been rediscovered several times since then.[63,68,69] A thorough history of the **QR** (Gram–Schmidt) decomposition has been written by Leon *et al.*,[70] with a brief history regarding its application to kinematics being given in Freed *et al.*[56] Compatibility conditions have been analyzed in the context of **QR** kinematics for mechanics problems in two[71] and three[72] spatial dimensions.

A Lagrangian Gram–Schmidt factorization of the deformation gradient $\mathbf{F}$ is written here as $\mathbf{F} = \boldsymbol{\mathcal{R}}\boldsymbol{\mathcal{U}}$, where the rotation $\boldsymbol{\mathcal{R}}$ is orthogonal and the Laplace stretch $\boldsymbol{\mathcal{U}}$ is upper-triangular.[56*] (An Eulerian Gram–Schmidt factorization has just been derived,[55] but it came along too late to adopt in this study. Its application is a topic for future study.) This triangular measure of stretch possesses an inherent property in two space: the direction aligned with the rotated 1-axis, denoted as $\vec{\boldsymbol{g}}_1$, remains invariant under transformation $\boldsymbol{\mathcal{U}}$,[51] i.e., it is a material vector in a neighborhood surrounding that particle whereat $\mathbf{F}$ is evaluated.[52] This property has some interesting ramifications addressed in Section 3.3.6.2.

3.3.6.1 **QR** Factorization of $\mathbf{F}$

The 2×2 deformation gradient associated with a planar membrane has a Gram–Schmidt decomposition expressed in terms of four physical attributes. Three of these attributes describe deformation. They are defined as[65]

$$a = \sqrt{F_{11}^2 + F_{21}^2}, \quad b = \frac{F_{11}F_{22} - F_{12}F_{21}}{\sqrt{F_{11}^2 + F_{21}^2}}, \quad g = \frac{F_{11}F_{12} + F_{22}F_{21}}{F_{11}^2 + F_{21}^2}, \tag{33}$$

*The **QR** rotation $\boldsymbol{\mathcal{R}}$ and stretch $\boldsymbol{\mathcal{U}}$ tensors are distinct from those that arise from a polar decomposition of a deformation gradient, typically denoted as $\mathbf{R}$ and $\mathbf{U}$, as found in any, modern, continuum mechanics text. McLellan[51,67] introduced the Laplace stretch in 1976, which he denoted as $\mathbf{H}$, while Srinivasa[63] denoted it as $\tilde{\mathbf{F}}$ in his 2012 paper.

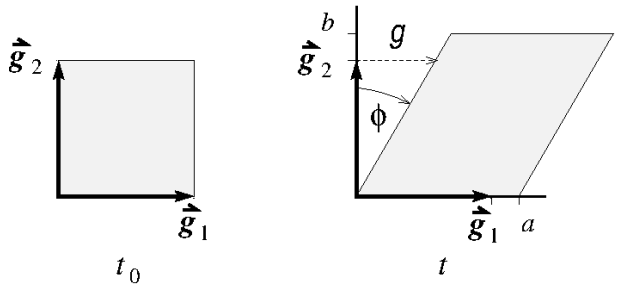

Fig. 13 Physical attributes of a planar deformation: a and b represent elongations, while $g = \tan\phi$ denotes the magnitude of shear. They are measured in a physical frame of reference with unit base vectors $(\vec{\mathbf{g}}_1, \vec{\mathbf{g}}_2)$ where $\vec{\mathbf{g}}_1$ embeds in the material.

thereby populating Laplace stretch $\boldsymbol{\mathcal{U}}$ and its inverse $\boldsymbol{\mathcal{U}}^{-1}$ with components

$$\boldsymbol{\mathcal{U}} = \begin{bmatrix} a & ag \\ 0 & b \end{bmatrix} \qquad \text{and} \qquad \boldsymbol{\mathcal{U}}^{-1} = \begin{bmatrix} 1/a & -g/b \\ 0 & 1/b \end{bmatrix}, \tag{34}$$

where a and b are the principal elongations (ratios of current lengths to reference lengths) and g is the extent of in-plane shear, as measured in a co-ordinate frame $(\vec{\mathbf{g}}_1, \vec{\mathbf{g}}_2)$ illustrated in Fig. 13. It is worth pointing out that the components of Laplace stretch, viz., $\mathcal{U}_{ij}$, are evaluated in the reference co-ordinate system $(\vec{\mathbf{e}}_1, \vec{\mathbf{e}}_2)$ of the pentagon, as $\mathbf{F} = F_{ij}\, \vec{\mathbf{e}}_i \otimes \vec{\mathbf{e}}_j$, but their physical interpretations arise in the Gram rotated co-ordinate system $(\vec{\mathbf{g}}_1, \vec{\mathbf{g}}_2)$.

Orthogonal tensor $\boldsymbol{\mathcal{R}} = \left[\vec{\mathbf{g}}_1 \;\middle|\; \vec{\mathbf{g}}_2\right] = \delta_{ij}\, \vec{\mathbf{g}}_i \otimes \vec{\mathbf{e}}_j = \mathcal{R}_{ij}\, \vec{\mathbf{e}}_i \otimes \vec{\mathbf{e}}_j$ rotates the reference co-ordinate axes $(\vec{\mathbf{e}}_1, \vec{\mathbf{e}}_2)$ into a physical co-ordinate system $(\vec{\mathbf{g}}_1, \vec{\mathbf{g}}_2)$ through an angle θ, which is the fourth physical attribute arising from a **QR** factorization of $\mathbf{F}$. This angle of rotation describes a proper orthogonal matrix, specifically

$$\boldsymbol{\mathcal{R}} = \begin{bmatrix} \cos\theta & -\sin\theta \\ \sin\theta & \cos\theta \end{bmatrix}, \tag{35}$$

with

$$\sin\theta = \frac{F_{21}}{\sqrt{F_{11}^2 + F_{21}^2}}, \quad \cos\theta = \frac{F_{11}}{\sqrt{F_{11}^2 + F_{21}^2}} \quad \therefore \quad \theta = \tan^{-1}\left(\frac{F_{21}}{F_{11}}\right) \tag{36}$$

where a positive angle θ corresponds with a counterclockwise rotation of physical axes $(\vec{\mathbf{g}}_1, \vec{\mathbf{g}}_2)$ about reference axes $(\vec{\mathbf{e}}_1, \vec{\mathbf{e}}_2)$.

From the four independent components of a planar deformation gradient F_{ij} come three deformation attributes, i.e., a, b, and g, and one rotational attribute, i.e., θ.

3.3.6.2 Dilemma

Until recently,[53] there has been a tacit assumption in prior applications of Gram–Schmidt factorizations of $\mathbf{F}$. Specifically, the physical base vectors $(\vec{\mathbf{g}}_1, \vec{\mathbf{g}}_2)$ satisfy a geometric condition whereby the physical 1-direction $\vec{\mathbf{g}}_1$ rotates out of the reference 1-direction $\vec{\mathbf{e}}_1$, but this need not always be the case. Physical vector $\vec{\mathbf{g}}_1$ could equally likely rotate out of the 2-direction $\vec{\mathbf{e}}_2$ of the reference frame. At issue is not: How the physical base vectors orient in space? That is managed by Gram's procedure. Rather, at issue is: How do the physical base vectors index with respect to the reference base vectors? This topic is addressed in Section 2 for the 3D case; below, we address this topic for the 2D case.

To illustrate the concern, consider two deformation histories, as drawn in Fig. 14, each of which describes a simple shear taking place in the plane of a membrane. In one case shear occurs in the 1-direction, while in the other case shear occurs in the 2-direction. There are no elongations in either deformation considered. These motions lead to different Gram–Schmidt factorizations of the deformation gradient. When following the protocol of Eqs. 33–36, these factorizations are found to be

$$\mathbf{F} = \begin{bmatrix} 1 & \gamma \\ 0 & 1 \end{bmatrix} \implies \boldsymbol{\mathcal{R}} = \begin{bmatrix} 1 & 0 \\ 0 & 1 \end{bmatrix}, \quad \boldsymbol{\mathcal{U}} = \begin{bmatrix} 1 & \gamma \\ 0 & 1 \end{bmatrix} \tag{37a}$$

and

$$\mathbf{F} = \begin{bmatrix} 1 & 0 \\ \gamma & 1 \end{bmatrix} \implies \begin{cases} \boldsymbol{\mathcal{R}} = \dfrac{1}{\sqrt{1+\gamma^2}} \begin{bmatrix} 1 & -\gamma \\ \gamma & 1 \end{bmatrix} \\ \boldsymbol{\mathcal{U}} = \begin{bmatrix} \sqrt{1+\gamma^2} & \gamma \\ 0 & 1 \,/\, \sqrt{1+\gamma^2} \end{bmatrix} \end{cases} \tag{37b}$$

respectively, where we see that shear $\mathcal{U}_{12}$ has the same physical interpretation in both cases, viz., γ, but elongations $\mathcal{U}_{11}$ and $\mathcal{U}_{22}$ do not, viz., $\mathcal{U}_{11} = 1$ and $\mathcal{U}_{22} = 1$ in Eq. 37a, whereas $\mathcal{U}_{11} = \sqrt{1+\gamma^2}$ and $\mathcal{U}_{22} = 1/\sqrt{1+\gamma^2}$ for the motion described in Eq. 37b. Consequently, two geometric interpretations are produced for just one physical mode of deformation. This cannot be!

The only difference between the motions that lead to the two deformation gradients

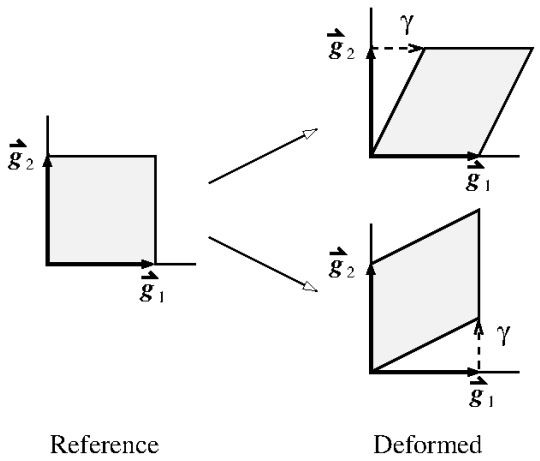

Fig. 14 The left graphic designates a reference configuration while the right two graphics designate deformed configurations, both in basis $(\vec{\mathbf{g}}_1, \vec{\mathbf{g}}_2)$. The top graphic associates with the motion of Eq. 37a, while the bottom graphic associates with the motion of Eq. 37b.

presented in Eq. 37 is one's choice for labeling the co-ordinate directions. Matrix operations of row and column pivoting, taken from linear algebra, allow one to transform the lower-triangular form of Eq. 37b into an upper-triangular form like Eq. 37a; hence, producing an unified physical interpretation for both shearing motions, and thereby providing a means for establishing a remedy to this dilemma.

3.3.6.3 Remedy

For 2D membranes, there are only two co-ordinate re-indexings that are possible (for 3D solids there are six, cf. Section 2). The default is no re-indexing at all, in which case

$$[\mathbf{P}] = [\mathbf{P}_0] := \begin{bmatrix} 1 & 0 \\ 0 & 1 \end{bmatrix} \qquad \Longrightarrow \qquad \begin{bmatrix} \mathcal{F}_{11} & \mathcal{F}_{12} \\ \mathcal{F}_{21} & \mathcal{F}_{22} \end{bmatrix} := \begin{bmatrix} F_{11} & F_{12} \\ F_{21} & F_{22} \end{bmatrix} \tag{38a}$$

while in the second case there is a re-indexing specified by

$$[\mathbf{P}] = [\mathbf{P}_1] := \begin{bmatrix} 0 & 1 \\ 1 & 0 \end{bmatrix} \qquad \Longrightarrow \qquad \begin{bmatrix} \mathcal{F}_{11} & \mathcal{F}_{12} \\ \mathcal{F}_{21} & \mathcal{F}_{22} \end{bmatrix} := \begin{bmatrix} F_{22} & F_{21} \\ F_{12} & F_{11} \end{bmatrix} \tag{38b}$$

where components $\mathcal{F}_{ij} = P_{ki} F_{k\ell} P_{\ell j}$ are the components to be used in the Gram–Schmidt factorization presented in Section 3.3.6.1, see also Section 2, and where $\mathbf{P} \in \{\mathbf{P}_0, \mathbf{P}_1\}$ is orthogonal, i.e., $\mathbf{P}\mathbf{P}^{\mathsf{T}} = \mathbf{P}^{\mathsf{T}}\mathbf{P} = \mathbf{I}$ with $\det \mathbf{P} = \pm 1$; specifically, $\det \mathbf{P}_0 = +1$ while $\det \mathbf{P}_1 = -1$.

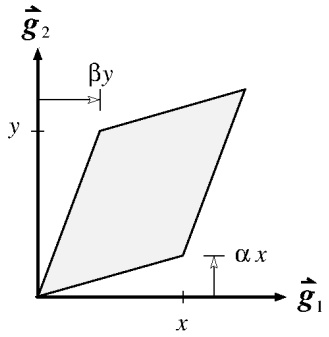

Fig. 15 A general description for homogeneous planar deformation, where $x, y \in \mathbb{R}_+$ and $\alpha, \beta \in \mathbb{R}$. Shears α and β are drawn in their positive sense.

The challenge in implementing such a strategy is to determine when to switch from $\mathbf{P}_0$ (case 1) to $\mathbf{P}_1$ (case 2), or back again, viz., from $\mathbf{P}_1$ to $\mathbf{P}_0$. Continuity in the physical fields of deformation (a, b, g) must be satisfied in order for such a change in co-ordinate frame to be physically meaningful. To this end, it is useful to represent the components of a planar deformation gradient as

$$\begin{bmatrix} \mathcal{F}_{11} & \mathcal{F}_{12} \\ \mathcal{F}_{21} & \mathcal{F}_{22} \end{bmatrix} = \begin{cases} \text{case 1}: & \begin{bmatrix} F_{11} & F_{12} \\ F_{21} & F_{22} \end{bmatrix} = \begin{bmatrix} x & \beta y \\ \alpha x & y \end{bmatrix} \\ \text{case 2}: & \begin{bmatrix} F_{22} & F_{21} \\ F_{12} & F_{11} \end{bmatrix} = \begin{bmatrix} y & \alpha x \\ \beta y & x \end{bmatrix} \end{cases} \tag{39}$$

where $x = F_{11}$ and $y = F_{22}$ are elongations, while ratios $\alpha = F_{21}/F_{11}$ and $\beta = F_{12}/F_{22}$ are magnitudes of shear, as illustrated in Fig. 15.

The physical attributes for Laplace stretch, as they pertain to the two cases in Eq. 38, written in terms of components F_{ij} from $\mathbf{F} = F_{ij}\, \vec{\mathbf{e}}_i \otimes \vec{\mathbf{e}}_j$ as defined in Eq. 39, are respectively given by

$$\tilde{a} = x\sqrt{1+\alpha^2} \qquad \hat{a} = y\sqrt{1+\beta^2} \tag{40a}$$

$$\tilde{b} = y(1-\alpha\beta) \,/\, \sqrt{1+\alpha^2} \qquad \hat{b} = x(1-\alpha\beta) \,/\, \sqrt{1+\beta^2} \tag{40b}$$

$$\tilde{g} = y(\alpha+\beta) \,/\, x(1+\alpha^2) \qquad \hat{g} = x(\alpha+\beta) \,/\, y(1+\beta^2) \tag{40c}$$

$$\tilde{\theta} = \tan^{-1}(-\alpha) \qquad \hat{\theta} = \tan^{-1}(-\beta) \tag{40d}$$

where attributes in the left column apply to case 1 (i.e., Eq. 38a) while those in the right column apply to case 2 (viz., Eq. 38b). The actual set of physical attributes

$\{a, b, g, \theta\}$ that are to be used when quantifying Laplace stretch and its inverse, according to Eq. 34, are then selected via the strategy

$$\text{if } |\tilde{g}| \geqslant |\hat{g}| : \qquad \{\tilde{a}, \tilde{b}, \tilde{g}, \tilde{\theta}\} \mapsto \{a, b, g, \theta\} \tag{41a}$$

$$\text{else } |\tilde{g}| \leqslant |\hat{g}| : \qquad \{\hat{a}, \hat{b}, \hat{g}, \hat{\theta}\} \mapsto \{a, b, g, \theta\}, \tag{41b}$$

where it is easily verified that $\tilde{a} = \hat{a}$ and $\tilde{b} = \hat{b}$ whenever $\tilde{g} = \hat{g}$; consequently, the physical attributes of deformation a, b, g remain continuous across a co-ordinate switch, however, the angle of co-ordinate rotation θ will not be continuous across such a switch between co-ordinate frames, as they represent rotations out of different co-ordinate directions. A like statement applies in the 3D case whenever one uses the re-indexing scheme presented in Section 2, i.e., the physical attributes of Laplace stretch remain continuous across a re-indexing of one's co-ordinate frame.[53]

The above strategy returns matrices for the rotation and Laplace stretch described in Eq. 37a for both deformation gradients presented in Eq. 37. The dilemma is remedied. Laplace stretch, as remedied, therefore has an unique physical interpretation. Co-ordinate re-indexing ensures that the invariant properties of Laplace stretch[51] are adhered to.

The above protocol is the 2D version of the 3D version[53] presented in Section 2. It is easier to understand what is happening in the 2D case, which is why more detail is presented here. It may certainly happen that even when the 3D co-ordinates for the dodecahedron are re-indexed, there may be one or more of the 12 pentagons whose 2D co-ordinates need to be re-indexed, too.

There are three kinematic variables that describe deformation in a planar membrane: elongation ratios a and b and simple shear g. These variables will vary both temporally and spatially throughout a pentagon whenever Wachspress' shape functions are used.

3.3.7 Thermodynamic Strains and Strain Rates

In terms of the above physical attributes for stretch, i.e., a, b, and g, and their reference values, viz., a_0, b_0, and g_0, one can define a set of strain attributes derived

from thermodynamics, specifically[73]

$$\xi \coloneqq \ln\left(\sqrt{\frac{a}{a_0}\frac{b}{b_0}}\right) \qquad \mathrm{d}\xi = \frac{1}{2}\left(\frac{\mathrm{d}a}{a} + \frac{\mathrm{d}b}{b}\right) \tag{42a}$$

$$\varepsilon \coloneqq \ln\left(\sqrt{\frac{a}{a_0}\frac{b_0}{b}}\right) \qquad \mathrm{d}\varepsilon = \frac{1}{2}\left(\frac{\mathrm{d}a}{a} - \frac{\mathrm{d}b}{b}\right) \tag{42b}$$

$$\gamma \coloneqq g - g_0 \qquad \mathrm{d}\gamma = \mathrm{d}g \tag{42c}$$

whose rates are exact differentials, i.e., they are independent of path—a tacit requirement from thermodynamics.[74] Here ξ denotes a dilation (uniform areal stretch), ε denotes a squeeze (pure shear), and γ denotes a (simple) shear.

3.3.7.1 Stretch Rates

The following approximations for stretch rates were derived by Freed and Zamani.[52] From these, the various strain rates listed in Eq. 42 can be established.

A forward difference formula is used to approximate rates in the reference configuration for the various stretch attributes, as obtained from $\mathrm{d}\boldsymbol{\mathcal{U}}_0 = (\boldsymbol{\mathcal{U}}_1 - \boldsymbol{\mathcal{U}}_0)/\mathrm{d}t + \mathcal{O}(\mathrm{d}t)$ that, neglecting higher-order terms, produces

$$\mathrm{d}a_0 = \frac{a_1 - a_0}{\mathrm{d}t}, \quad \mathrm{d}b_0 = \frac{b_1 - b_0}{\mathrm{d}t}, \quad \mathrm{d}g_0 = \frac{a_1}{a_0}\left(\frac{g_1 - g_0}{\mathrm{d}t}\right), \tag{43}$$

where $\mathrm{d}t = t_1 - t_0$ is the applied time step. A backward difference formula $\mathrm{d}\boldsymbol{\mathcal{U}}_1 = (\boldsymbol{\mathcal{U}}_1 - \boldsymbol{\mathcal{U}}_0)/\mathrm{d}t + \mathcal{O}(\mathrm{d}t)$ is used to estimate rates for the various stretch attributes at the end of its first integration step that, neglecting higher-order terms, give

$$\mathrm{d}a_1 = \frac{a_1 - a_0}{\mathrm{d}t}, \quad \mathrm{d}b_1 = \frac{b_1 - b_0}{\mathrm{d}t}, \quad \mathrm{d}g_1 = \frac{a_0}{a_1}\left(\frac{g_1 - g_0}{\mathrm{d}t}\right). \tag{44}$$

Curiously, there is a distinction in how the shear rates are approximated at the two nodes for this first interval of integration.

Equations 43 and 44 are first-order approximations for these derivatives. Second-order approximations can be established whenever $i > 0$ provided the stepsize for step $[i, i+1]$ equals the stepsize for step $[i-1, i]$, where state $i = 0$ associates with an initial condition. The backward difference formula $\mathrm{d}\boldsymbol{\mathcal{U}}_{i+1} = (3\boldsymbol{\mathcal{U}}_{i+1} - 4\boldsymbol{\mathcal{U}}_i +$

$\boldsymbol{\mathcal{U}}_{i-1})/2\mathrm{d}t + \mathcal{O}\big((\mathrm{d}t)^2\big)$ then produces rates for the stretch attributes of

$$\begin{aligned}
\mathrm{d}a_{i+1} &= \frac{3a_{i+1} - 4a_i + a_{i-1}}{2\mathrm{d}t} \\
\mathrm{d}b_{i+1} &= \frac{3b_{i+1} - 4b_i + b_{i-1}}{2\mathrm{d}t} \\
\mathrm{d}g_{i+1} &= \frac{2a_i}{a_{i+1}}\left(\frac{g_{i+1} - g_i}{\mathrm{d}t}\right) - \frac{a_{i-1}}{a_{i+1}}\left(\frac{g_{i+1} - g_{i-1}}{2\mathrm{d}t}\right),
\end{aligned} \tag{45}$$

which require stretch attributes a_{i-1}, b_{i-1}, and g_{i-1} to be stored in a finite element setting.

3.4 3D Irregular Dodecahedra

The primary kinematic variables needed to describe the deformation of an irregular dodecahedron used as a model for an alveolar sac are its volume V (see Section 2) and the differential change in volume $\mathrm{d}V$, with the former following from Eq. 14 and the latter coming from a suitable finite difference formula. Whenever the material filling an alveolar sac is air (its normal healthy condition), no further breakdown of these kinematics is required.

However, whenever an alveolar sac is filled with fluid (blood, interstitial fluids, pflem, etc.), this fluid can be expected to behave solid-like in the face of a passing shock wave. In this situation, the non-uniform measures for strain (i.e., shears) can be expected to produce non-uniform responses in stress.

3.4.1 Shape Functions for Interpolating an Irregular Tetrahedron

The shape functions associated with the four vertices of a tetrahedron N_i, $i = 1, 2, 3, 4$, are defined as

$$N_1 = 1 - \xi - \eta - \zeta, \quad N_2 = \xi, \quad N_3 = \eta, \quad N_4 = \zeta, \tag{46a}$$

where ξ, η and ζ represent natural co-ordinates with $0 \leqslant \xi \leqslant 1$, $0 \leqslant \eta \leqslant 1 - \xi$ and $0 \leqslant \zeta \leqslant 1 - \xi - \eta$. Gradients of these shape functions are

$$\begin{aligned}
&N_{1,\xi} = -1, \quad N_{1,\eta} = -1, \quad N_{1,\zeta} = -1 \\
&N_{2,\xi} = 1, \quad N_{2,\eta} = 0, \quad N_{2,\zeta} = 0 \\
&N_{3,\xi} = 0, \quad N_{3,\eta} = 1, \quad N_{3,\zeta} = 0 \\
&N_{4,\xi} = 0, \quad N_{4,\eta} = 0, \quad N_{4,\zeta} = 1
\end{aligned} \tag{46b}$$

and consequently the deformation gradient will be constant throughout its volume, like the deformation gradients used for chords and triangles.

3.4.1.1 Deformation Gradient for an Irregular Tetrahedron

The deformation gradient for a volume element is constructed from

$$\mathbf{F}(\xi,\eta,\zeta) = \begin{bmatrix} 1 & 0 & 0 \\ 0 & 1 & 0 \\ 0 & 0 & 1 \end{bmatrix} + \begin{bmatrix} \partial u/\partial\xi & \partial u/\partial\eta & \partial u/\partial\zeta \\ \partial v/\partial\xi & \partial v/\partial\eta & \partial v/\partial\zeta \\ \partial w/\partial\xi & \partial w/\partial\eta & \partial w/\partial\zeta \end{bmatrix} \begin{bmatrix} \partial x_0/\partial\xi & \partial x_0/\partial\eta & \partial x_0/\partial\zeta \\ \partial y_0/\partial\xi & \partial y_0/\partial\eta & \partial y_0/\partial\zeta \\ \partial z_0/\partial\xi & \partial z_0/\partial\eta & \partial z_0/\partial\zeta \end{bmatrix}^{-1} \tag{47}$$

such that, for the four-node tetrahedron considered here, one has

$$\begin{aligned} \begin{bmatrix} \partial u/\partial\xi & \partial u/\partial\eta & \partial u/\partial\zeta \\ \partial v/\partial\xi & \partial v/\partial\eta & \partial v/\partial\zeta \\ \partial w/\partial\xi & \partial w/\partial\eta & \partial w/\partial\zeta \end{bmatrix} &= \begin{bmatrix} \sum_{i=1}^4 N_{i,\xi} u_i & \sum_{i=1}^4 N_{i,\eta} u_i & \sum_{i=1}^4 N_{i,\zeta} u_i \\ \sum_{i=1}^4 N_{i,\xi} v_i & \sum_{i=1}^4 N_{i,\eta} v_i & \sum_{i=1}^4 N_{i,\zeta} v_i \\ \sum_{i=1}^4 N_{i,\xi} w_i & \sum_{i=1}^4 N_{i,\eta} w_i & \sum_{i=1}^4 N_{i,\zeta} w_i \end{bmatrix} \\ &= \begin{bmatrix} u_2 - u_1 & u_3 - u_1 & u_4 - u_1 \\ v_2 - v_1 & v_3 - v_1 & v_4 - v_1 \\ w_2 - w_1 & w_3 - w_1 & w_4 - w_1 \end{bmatrix} \end{aligned} \tag{48a}$$

whose nodal displacements $\boldsymbol{u}_i := \boldsymbol{x}_i - \boldsymbol{x}_{0i}$, $i = 1,2,3,4$, have components of $\boldsymbol{u}_i = u_i\,\vec{\mathbf{E}}_1 + v_i\,\vec{\mathbf{E}}_2 + w_i\,\vec{\mathbf{E}}_3$ with $u_i := x_i - x_{0i}$, $v_i := y_i - y_{0i}$, and $w_i := z_i - z_{0i}$, evaluated in the reference co-ordinate frame $(\vec{\mathbf{E}}_1, \vec{\mathbf{E}}_2, \vec{\mathbf{E}}_3)$ of the dodecahedron, and

$$\begin{aligned} \begin{bmatrix} \partial x_0/\partial\xi & \partial x_0/\partial\eta & \partial x_0/\partial\zeta \\ \partial y_0/\partial\xi & \partial y_0/\partial\eta & \partial y_0/\partial\zeta \\ \partial z_0/\partial\xi & \partial z_0/\partial\eta & \partial z_0/\partial\zeta \end{bmatrix} &= \begin{bmatrix} \sum_{i=1}^4 N_{i,\xi} x_{0i} & \sum_{i=1}^4 N_{i,\eta} x_{0i} & \sum_{i=1}^4 N_{i,\zeta} x_{0i} \\ \sum_{i=1}^4 N_{i,\xi} y_{0i} & \sum_{i=1}^4 N_{i,\eta} y_{0i} & \sum_{i=1}^4 N_{i,\zeta} y_{0i} \\ \sum_{i=1}^4 N_{i,\xi} z_{0i} & \sum_{i=1}^4 N_{i,\eta} z_{0i} & \sum_{i=1}^4 N_{i,\zeta} z_{0i} \end{bmatrix} \\ &= \begin{bmatrix} x_{02} - x_{01} & x_{03} - x_{01} & x_{04} - x_{01} \\ y_{02} - y_{01} & y_{03} - y_{01} & y_{04} - y_{01} \\ z_{02} - z_{01} & z_{03} - z_{01} & z_{04} - z_{01} \end{bmatrix} \end{aligned} \tag{48b}$$

whose initial nodal positions are $\boldsymbol{x}_{0i} = x_{0i}\,\vec{\mathbf{E}}_1 + y_{0i}\,\vec{\mathbf{E}}_2 + z_{0i}\,\vec{\mathbf{E}}_3$ at vertex i. This matrix is invertible, because the four vertices of a tetrahedron are distinct. The Jacobian matrix is therefore given by

$$\mathbf{J} := \begin{bmatrix} \partial x/\partial\xi & \partial y/\partial\xi & \partial z/\partial\xi \\ \partial x/\partial\eta & \partial y/\partial\eta & \partial z/\partial\eta \\ \partial x/\partial\zeta & \partial y/\partial\zeta & \partial z/\partial\zeta \end{bmatrix} = \begin{bmatrix} \sum_{i=1}^4 N_{i,\xi} x_i & \sum_{i=1}^4 N_{i,\xi} y_i & \sum_{i=1}^4 N_{i,\xi} z_i \\ \sum_{i=1}^4 N_{i,\eta} x_i & \sum_{i=1}^4 N_{i,\eta} y_i & \sum_{i=1}^4 N_{i,\eta} z_i \\ \sum_{i=1}^4 N_{i,\zeta} x_i & \sum_{i=1}^4 N_{i,\zeta} y_i & \sum_{i=1}^4 N_{i,\zeta} z_i \end{bmatrix}$$
$$= \begin{bmatrix} x_2 - x_1 & y_2 - y_1 & z_2 - z_1 \\ x_3 - x_1 & y_3 - y_1 & z_3 - z_1 \\ x_4 - x_1 & y_4 - y_1 & z_4 - z_1 \end{bmatrix} \tag{48c}$$

whose determinant is used in integrations. The current nodal positions have components $\boldsymbol{x}_i = x_i\,\vec{\mathbf{E}}_1 + y_i\,\vec{\mathbf{E}}_2 + z_i\,\vec{\mathbf{E}}_3$, $i = 1, 2, 3, 4$, in the dodecahedral frame $(\vec{\mathbf{E}}_1, \vec{\mathbf{E}}_2, \vec{\mathbf{E}}_3)$. The Jacobian matrix remains invertible provided that the four vertices of a tetrahedron remain distinct.

3.4.2 QR Factorization of F

The re-indexed deformation gradient presented in Section 2 has a Gram–Schmidt decomposition that we denote as $\mathbf{F} = \boldsymbol{\mathcal{R}}\boldsymbol{\mathcal{U}}$ whose components are an orthogonal rotation matrix $\boldsymbol{\mathcal{R}} = \left[\vec{\mathbf{g}}_1 \;\middle|\; \vec{\mathbf{g}}_2 \;\middle|\; \vec{\mathbf{g}}_3\right] = \delta_{ij}\,\vec{\mathbf{g}}_i \otimes \vec{\mathbf{E}}_j = \mathcal{R}_{ij}\,\vec{\mathbf{E}}_i \otimes \vec{\mathbf{E}}_j$ and an upper-triangular matrix $\boldsymbol{\mathcal{U}} = \mathcal{U}_{ij}\,\vec{\mathbf{E}}_i \otimes \vec{\mathbf{E}}_j$ called Laplace stretch,[56] both evaluated in the reference co-ordinate frame $(\vec{\mathbf{E}}_1, \vec{\mathbf{E}}_2, \vec{\mathbf{E}}_3)$, so that $\mathbf{F} = \mathcal{F}_{ij}\,\vec{\mathbf{E}}_i \otimes \vec{\mathbf{E}}_j = \mathcal{R}_{ik}\mathcal{U}_{kj}\,\vec{\mathbf{E}}_i \otimes \vec{\mathbf{E}}_j$, and therefore $\mathcal{F}_{ij} = \mathcal{R}_{ik}\mathcal{U}_{kj}$.

The components of Laplace stretch $\mathcal{U}_{ij}$ are readily gotten through a Cholesky factorization of the right Cauchy–Green deformation tensor $\mathbf{C} = \mathcal{C}_{ij}\,\vec{\mathbf{E}}_i \otimes \vec{\mathbf{E}}_j$ with tensor components $\mathcal{C}_{ij} = \mathcal{F}_{ki}\,\mathcal{F}_{kj}$ that relate to their physical attributes via[73]

$$\boldsymbol{\mathcal{U}} = \begin{bmatrix} a & a\gamma & a\beta \\ 0 & b & b\alpha \\ 0 & 0 & c \end{bmatrix} \quad \text{with inverse} \quad \boldsymbol{\mathcal{U}}^{-1} = \begin{bmatrix} 1/a & -\gamma/b & -(\beta - \alpha\gamma)/c \\ 0 & 1/b & -\alpha/c \\ 0 & 0 & 1/c \end{bmatrix} \tag{49}$$

with tensor components $\mathcal{U}_{ij}$ being evaluated according to formulæ[63]

$$\begin{aligned}
&\mathcal{U}_{11} = \sqrt{\mathcal{C}_{11}} \quad \mathcal{U}_{12} = \mathcal{C}_{12}/\mathcal{U}_{11} \qquad \mathcal{U}_{13} = \mathcal{C}_{13}/\mathcal{U}_{11} \\
&\mathcal{U}_{21} = 0 \qquad \mathcal{U}_{22} = \sqrt{\mathcal{C}_{22} - \mathcal{U}_{12}^2} \quad \mathcal{U}_{23} = \big(\mathcal{C}_{23} - \mathcal{U}_{12}\mathcal{U}_{13}\big)/\mathcal{U}_{22} \\
&\mathcal{U}_{31} = 0 \qquad \mathcal{U}_{32} = 0 \qquad \mathcal{U}_{33} = \sqrt{\mathcal{C}_{33} - \mathcal{U}_{13}^2 - \mathcal{U}_{23}^2}
\end{aligned} \tag{50}$$

implying that the physical attributes for Laplace stretch can be evaluated via

$$a := \mathcal{U}_{11}, \quad b := \mathcal{U}_{22}, \quad c := \mathcal{U}_{33}, \quad \alpha := \frac{\mathcal{U}_{23}}{\mathcal{U}_{22}}, \quad \beta := \frac{\mathcal{U}_{13}}{\mathcal{U}_{11}}, \quad \gamma := \frac{\mathcal{U}_{12}}{\mathcal{U}_{11}}, \tag{51}$$

where a, b, and c are three, orthogonal, elongation ratios, and where α, β, and γ are three, orthogonal, simple shears, with a_0, b_0, c_0, α_0, β_0, and γ_0 denoting their values in some reference state. The elongations must be positive, whereas the shears may be of either sign. Collectively, they constitute a complete set of physical attributes for describing stretch from which constitutive equations can then be constructed.

No eigenvalue/eigenvector analysis is required to acquire either the stretch components or their attributes when using this technique.[63] The eigenvalues and eigenvectors of the triangular Laplace stretch equate with the eigenvalues and eigenvectors of the symmetric polar stretch *only* in an absence of shear.[68] Laplace stretch associates with the geometric description of a cube deforming into a parallelepiped; whereas, polar stretch associates with the geometric description of a sphere deforming into an ellipsoid. They are distinct geometric measures for stretch.

3.4.3 Thermodynamic Strains and Strain Rates

In terms of the above physical attributes for stretch, one can define an useful set of strain attributes derived from thermodynamics, specifically[73]

$$\Xi := \ln\left(\sqrt[3]{\frac{a}{a_0}\frac{b}{b_0}\frac{c}{c_0}}\right) \qquad \mathrm{d}\Xi = \frac{1}{3}\left(\frac{\mathrm{d}a}{a} + \frac{\mathrm{d}b}{b} + \frac{\mathrm{d}c}{c}\right) \tag{52a}$$

$$\varepsilon_1 := \ln\left(\sqrt[3]{\frac{a}{a_0}\frac{b_0}{b}}\right) \qquad \mathrm{d}\varepsilon_1 = \frac{1}{3}\left(\frac{\mathrm{d}a}{a} - \frac{\mathrm{d}b}{b}\right) \tag{52b}$$

$$\varepsilon_2 := \ln\left(\sqrt[3]{\frac{b}{b_0}\frac{c_0}{c}}\right) \qquad \mathrm{d}\varepsilon_2 = \frac{1}{3}\left(\frac{\mathrm{d}b}{b} - \frac{\mathrm{d}c}{c}\right) \tag{52c}$$

$$\gamma_1 := \alpha - \alpha_0 \qquad \mathrm{d}\gamma_1 = \mathrm{d}\alpha \tag{52d}$$

$$\gamma_2 := \beta - \beta_0 \qquad \mathrm{d}\gamma_2 = \mathrm{d}\beta \tag{52e}$$

$$\gamma_3 := \gamma - \gamma_0 \qquad \mathrm{d}\gamma_3 = \mathrm{d}\gamma \tag{52f}$$

whose rates are exact differentials, i.e., they are independent of path—a tacit requirement from thermodynamics.[74] Here Ξ represents dilatation, ε_1 is a squeeze in the 12 plane, and ε_2 is a squeeze in the 23 plane, while γ_1 is a shear in the 23 plane, γ_2 is a shear in the 13 plane, and γ_3 is a shear in the 12 plane, which are three, orthogonal, simple shearing motions. There is a third squeeze, too, viz., $\varepsilon_3 = -\varepsilon_1 - \varepsilon_2$, but it is not an independent descriptor of strain.

3.4.3.1 Stretch Rates

The following approximations for stretch rates were derived by Freed and Zamani.[52] From these, the various strain rates listed in Eq. 52 can be established.

A forward difference formula is used to approximate rates in the reference configuration for the various stretch attributes, as obtained from $\mathrm{d}\boldsymbol{\mathcal{U}}_0 = (\boldsymbol{\mathcal{U}}_1 - \boldsymbol{\mathcal{U}}_0)/\mathrm{d}t + \mathcal{O}(\mathrm{d}t)$. Neglecting higher-order terms, this produces

$$\begin{aligned} \mathrm{d}a_0 &= \frac{a_1 - a_0}{\mathrm{d}t} & \mathrm{d}\alpha_0 &= \frac{b_1}{b_0}\left(\frac{\alpha_1 - \alpha_0}{\mathrm{d}t}\right) \\ \mathrm{d}b_0 &= \frac{b_1 - b_0}{\mathrm{d}t} & \mathrm{d}\beta_0 &= \frac{a_1}{a_0}\left(\frac{\beta_1 - \beta_0}{\mathrm{d}t}\right) \\ \mathrm{d}c_0 &= \frac{c_1 - c_0}{\mathrm{d}t} & \mathrm{d}\gamma_0 &= \frac{a_1}{a_0}\left(\frac{\gamma_1 - \gamma_0}{\mathrm{d}t}\right). \end{aligned} \tag{53}$$

A backward difference formula $\mathrm{d}\boldsymbol{\mathcal{U}}_1 = (\boldsymbol{\mathcal{U}}_1 - \boldsymbol{\mathcal{U}}_0)/\mathrm{d}t + \mathcal{O}(\mathrm{d}t)$ is used to estimate

rates for the various stretch attributes at the end of its first integration step, from which it follows that

$$\begin{aligned} \mathrm{d}a_1 &= \frac{a_1 - a_0}{\mathrm{d}t} \qquad \mathrm{d}\alpha_1 = \frac{b_0}{b_1}\left(\frac{\alpha_1 - \alpha_0}{\mathrm{d}t}\right) \\ \mathrm{d}b_1 &= \frac{b_1 - b_0}{\mathrm{d}t} \qquad \mathrm{d}\beta_1 = \frac{a_0}{a_1}\left(\frac{\beta_1 - \beta_0}{\mathrm{d}t}\right) \\ \mathrm{d}c_1 &= \frac{c_1 - c_0}{\mathrm{d}t} \qquad \mathrm{d}\gamma_1 = \frac{a_0}{a_1}\left(\frac{\gamma_1 - \gamma_0}{\mathrm{d}t}\right). \end{aligned} \tag{54}$$

Curiously, there is a distinction in how the shear rates are approximated at the two nodes belonging to this first interval of integration.

Equations 53 and 54 are first-order approximations for these derivatives. Second-order approximations can be established whenever $i > 0$ provided the stepsize for step $[i, i+1]$ equals the stepsize for step $[i-1, i]$, where state $i = 0$ associates with an initial condition. The backward difference formula $\mathrm{d}\boldsymbol{\mathcal{U}}_{i+1} = (3\boldsymbol{\mathcal{U}}_{i+1} - 4\boldsymbol{\mathcal{U}}_i + \boldsymbol{\mathcal{U}}_{i-1})/2\mathrm{d}t + \mathcal{O}\big((\mathrm{d}t)^2\big)$ produces differential stretch rates of

$$\begin{aligned} \mathrm{d}a_{i+1} &= \frac{3a_{i+1} - 4a_i + a_{i-1}}{2\mathrm{d}t} \\ \mathrm{d}b_{i+1} &= \frac{3b_{i+1} - 4b_i + b_{i-1}}{2\mathrm{d}t} \\ \mathrm{d}c_{i+1} &= \frac{3c_{i+1} - 4c_i + c_{i-1}}{2\mathrm{d}t} \\ \mathrm{d}\alpha_{i+1} &= 2\frac{b_i}{b_{i+1}}\left(\frac{\alpha_{i+1} - \alpha_i}{\mathrm{d}t}\right) - \frac{b_{i-1}}{b_{i+1}}\left(\frac{\alpha_{i+1} - \alpha_{i-1}}{2\mathrm{d}t}\right) \\ \mathrm{d}\beta_{i+1} &= 2\frac{a_i}{a_{i+1}}\left(\frac{\beta_{i+1} - \beta_i}{\mathrm{d}t}\right) - \frac{a_{i-1}}{a_{i+1}}\left(\frac{\beta_{i+1} - \beta_{i-1}}{2\mathrm{d}t}\right) \\ \mathrm{d}\gamma_{i+1} &= 2\frac{a_i}{a_{i+1}}\left(\frac{\gamma_{i+1} - \gamma_i}{\mathrm{d}t}\right) - \frac{a_{i-1}}{a_{i+1}}\left(\frac{\gamma_{i+1} - \gamma_{i-1}}{2\mathrm{d}t}\right), \end{aligned} \tag{55}$$

which require data to be stored for the previous state associated with step $i - 1$.

3.5 Code Verification: Kinematics

The thermodynamic conjugate pairs of Freed *et al.*[55,65,66,73] result in the following geometric/thermodynamic strain measures for our dodecahedral model. For 1D rods: an axial strain $e = \ln(L/L_0)$. For 2D membranes: a dilation $\xi = \ln\sqrt{ab/a_0b_0}$ $= \ln\sqrt{A/A_0}$, a squeeze (or pure shear) $\varepsilon = \ln\sqrt{ab_0/a_0b} = \ln\sqrt{\Gamma/\Gamma_0}$, and a (simple) shear $\gamma = g - g_0$. And for 3D dodecahedra: a dilatation $\Xi = \ln\sqrt[3]{V/V_0}$ and,

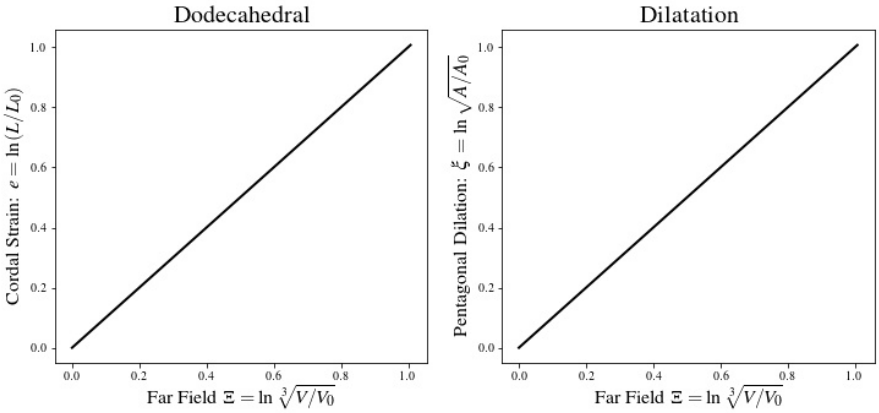

Fig. 16 Response of a dodecahedron exposed to an isotropic motion of dilatation. The abscissa is the control variable and the ordinates are response variables. The right graphic plots the areal response of the pentagons $\xi = \ln\sqrt{A/A_0}$, while the left graphic plots the axial response of the chords $e = \ln(L/L_0)$. Both are plotted against the volumetric response of the dodecahedron $\Xi = \ln\sqrt[3]{V/V_0}$. Here V denotes dodecahedral volume, A denotes pentagonal area, and L denotes chordal length, all being evaluated in the current state, whose reference values are V_0, A_0 and L_0.

for those cases where the medium within an alveolar sac can support non-uniform stresses, two squeezes $\varepsilon_1 = \ln\sqrt[3]{ab_0/a_0b}$ and $\varepsilon_2 = \ln\sqrt[3]{bc_0/b_0c}$ plus three shears $\gamma_1 = \alpha - \alpha_0$, $\gamma_2 = \beta - \beta_0$, and $\gamma_3 = \gamma - \gamma_0$.

3.5.1 Isotropic Motions

Imposing an uniform far-field motion of a volumetric expansion onto our dodecahedral model results in a dodecahedral dilatation ($\Xi := \ln\sqrt[3]{V/V_0}$) that equals its pentagonal dilation ($\xi := \ln\sqrt{A/A_0}$) that equals its chordal strain ($e := \ln(L/L_0)$). These three strain measures follow from the 3-mode thermodynamic theory of Freed *et al.*,[55,65,66] as presented above. Other choices for strain measures do not result in one-to-one relationships when exposed to an isotropic motion like those observed here. This is a particularly useful result in that it establishes a meaningful scaling in terms of strains between the three dimensions, cf. Fig. 16. It also provides for a verification of the numerical implementation of our dodecahedral model.

3.5.1.1 Geometric vs. Thermodynamic Strains

There are two types of strain measures that one can use to quantify deformation within a pentagon of a dodecahedron: geometric and thermodynamic. For the uniform far-field motion of volumetric expansion, only a thermodynamic strain known as dilation, i.e., $\xi = \ln\sqrt{ab/a_0b_0}$, varies with the motion, and its response equals

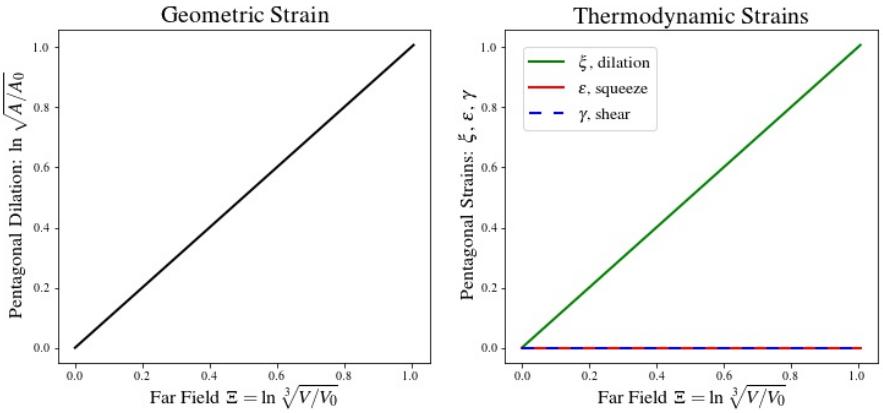

Fig. 17 Response of a dodecahedron exposed to a far-field isotropic motion of dilatation. The abscissa is the control variable and the ordinates are response variables. The right graphic plots the three thermodynamic strains, as they apply to a pentagon, while the left graphic plots the geometric strain of a pentagon.

that of the geometric strain $\ln \sqrt{A/A_0}$, see Fig. 17. Also present in this graph is an observation that the thermodynamic strains for squeeze ε and shear γ do not contribute under motions of pure dilatation, as expected. This further verifies the numerical implementation of our dodecahedral model.

To put this into perspective, we compare with studies done by multiple investigators where ratios of alveolar surface area, viz., A/A_0, have been measured in rat, rabbit, guinea pig, and cat, cf. Roan and Waters[30] (Table 1). These experiments considered ranges that went as low as 25% and as high as 100% of total lung capacity. Taking statistics of their tabulation produced results of $A/A_0 = 1.47 \pm 0.44$ during inflation and $A/A_0 = 1.18 \pm 0.14$ during deflation, which correspond to a $\xi = \ln \sqrt{A/A_0} = 0.19 \pm 0.18$ for inflation and a $\xi = \ln \sqrt{A/A_0} = 0.08 \pm 0.07$ for deflation. These areal strain values coincide with chordal strains of $e = \ln(L/L_0) = 0.13$ measured *in vivo* around the periphery of an alveolus in rat lung, as reported by Perlman and Bhattachary.[75] Our kinematics have been verified well past these physiologic ranges, viz., for dilatations up to 100% logarithmic strain.

3.5.2 Isochoric Motions

The motions of pure and simple shears are volume preserving. Imposing these shears as far-field motions onto our dodecahedral model produced the results displayed in Fig. 18. For a simple shear, the numerical model is in error by about machine precision, i.e., $\epsilon_m \approx 2.2 \times 10^{-16}$, for strains up to 100%, while for pure

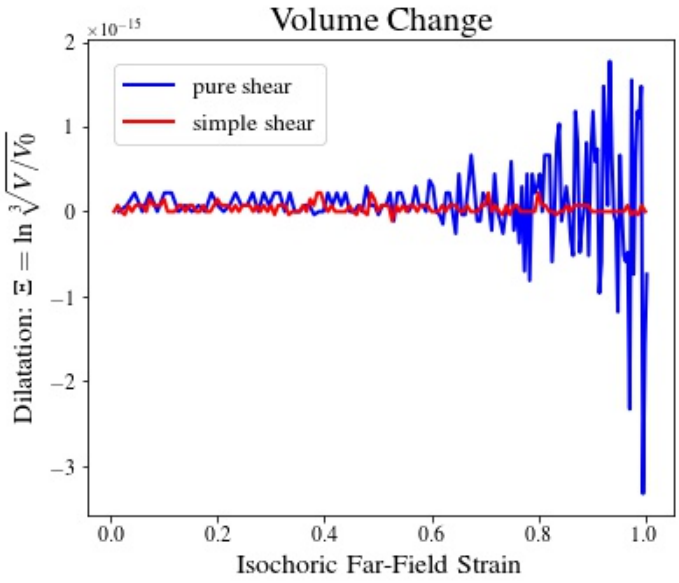

Fig. 18 Response of a dodecahedron exposed to far-field motions of pure and simple shears. Note that the ordinate is $\times 10^{-15}$ and machine precision is $\sim 2.2 \times 10^{-16}$.

shear (a special case of squeeze in 3D) the model is in error by about machine precision for strains up to of about 60%, after which the error increases up to about $10\epsilon_m$ at strains around 100%. This further verifies the numerical implementation of our dodecahedral model.

3.5.2.1 Geometric Strains

How the 30 chords and 12 irregular pentagons deform under far-field motions of pure shear is displayed in Fig. 19. Figure 18 demonstrates that the overall response of a dodecahedron is isochoric during pure shear. Regardless, Fig. 19 demonstrates that individual chordal and pentagonal constituents deform in a non-homogeneous manner, where the strains have been calculated as geometric changes in dodecahedral shape. This result agrees with *in vivo* observations made by Perlman and Bhattacharya[75] where confocal microscopy was used to image a breathing rat lung.

For the chords, there are six independent responses for dodecahedral motions of pure shear: two chords each for three of these lines, and eight chords each for the remaining three curves present in the left images of Fig. 19. For pentagons, there are three independent responses with four pentagons responding according to each curve shown in the right images. Although different chords and pentagons deform

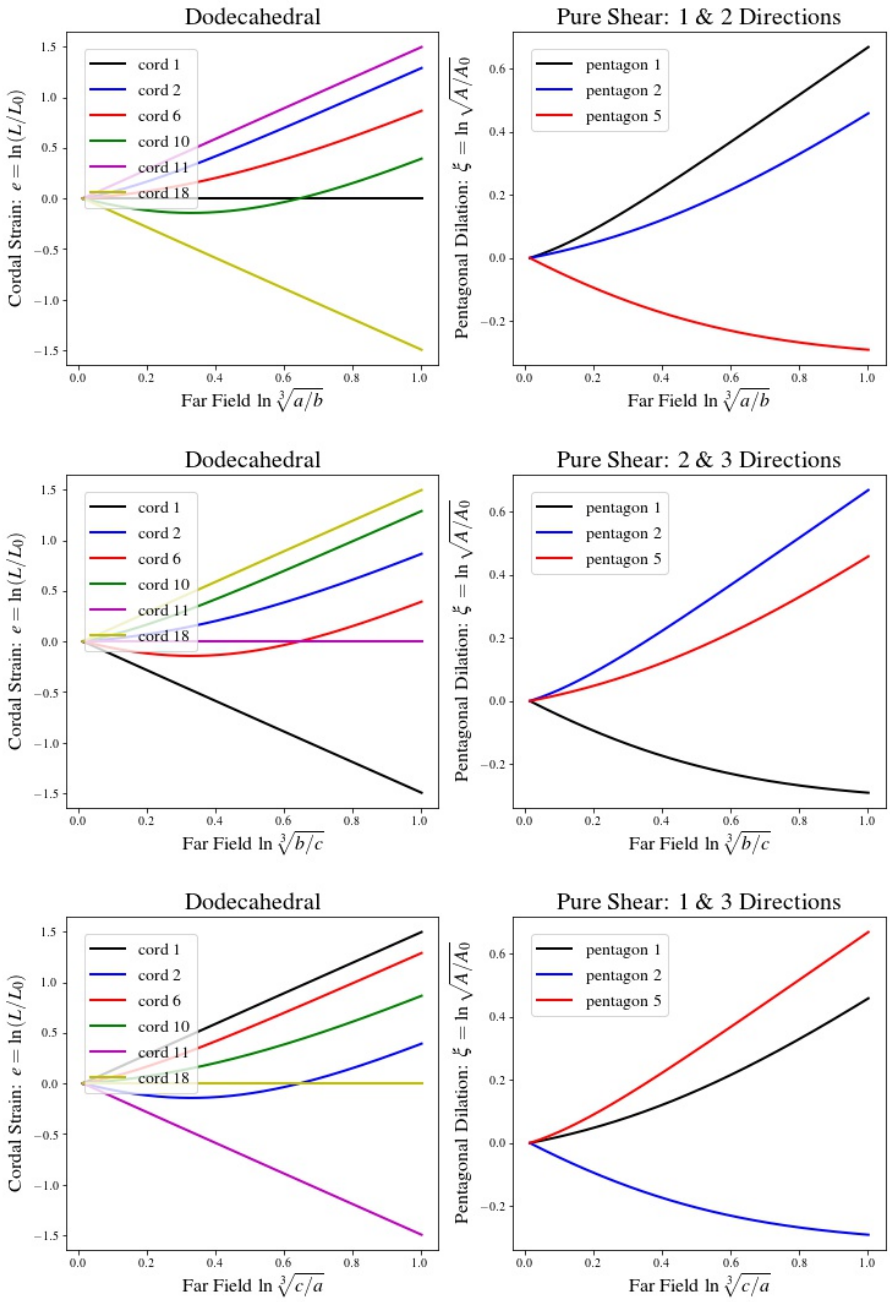

Fig. 19 Response of a dodecahedron exposed to far-field pure-shear motions in the sense of Treloar[76]: $a = \ell$, $b = 1/\ell$ and $c = 1$ in the top images; $a = 1$, $b = \ell$ and $c = 1/\ell$ in the middle images; and $a = 1/\ell$, $b = 1$ and $c = \ell$ in the bottom images, with ℓ denoting an elongation of extrusion. In all six graphic images, the relevant (controlled) motion of the far-field pure shear is plotted along the abscissa. In each image pair, the right graphic presents pentagonal dilations, while the left graphic presents chordal elongations. Only unique responses are plotted; repetitions are not.

differently when sheared in different directions, their collective responses are the same regardless of the far-field direction being sheared. Consequently, the local geometric response of a dodecahedron is isotropic under the far-field motions of pure shear.

How the 30 chords and 12 irregular pentagons deform under far-field motions of simple shear is displayed in Fig. 20. Figure 18 demonstrates that the overall response of a dodecahedron is isochoric during a far-field simple shear. Figure 20 demonstrates that the individual chordal and pentagonal constituents deform in a non-homogeneous manner during simple shears, like they do for pure shears. However, unlike pure shears whose collective chordal and pentagonal responses remain isotropic, here they diverge slightly from isotropy under motions of simple shear. Simple shears in the 12 and 23 planes have the same collective response; whereas, simple shear in the 13 plane has a slightly different response with respect to changes in the shearing direction.

Figures 16–20 show that a dodecahedron is (nearly, but not completely) isotropic in its kinematic response, as measured by the geometric strains $e = \ln(L/L_0)$, $\xi = \ln\sqrt{A/A_0}$, and $\Xi = \ln\sqrt[3]{V/V_0}$. Furthermore, even though a far-field deformation is homogeneous, in accordance with our Conjecture on pg. 7, the local deformations within the individual constituents of an alveolus will typically be heterogeneous, which agrees with imaging data.[75]

3.5.2.2 Thermodynamic Strains

Addressing the septal response, modeled here as a set of 12 irregular pentagons per alveolus, we desire to come to a determination regarding how to best model the deformation occurring within these alveolar septa. In the section above we investigated the geometric response of alveolar septa via the strain measure $\ln\sqrt{A/A_0}$, which quantifies dilation.

The thermodynamic strains arising from a Gram–Schmidt factorization of the deformation gradient put forward in Section 3.3.6 specify three strain measures pertinent to a membrane: dilation $\xi = \ln\sqrt{ab/a_0b_0}$, squeeze $\varepsilon = \ln\sqrt{ab_0/a_0b}$, and shear $\gamma = g - g_0$, where elongations a and b and magnitude of shear g are illustrated in Fig. 13. Of these, dilation is an uniform response, while squeeze and shear describe isochoric non-uniform responses. To acquire them requires knowing the deformation gradient.

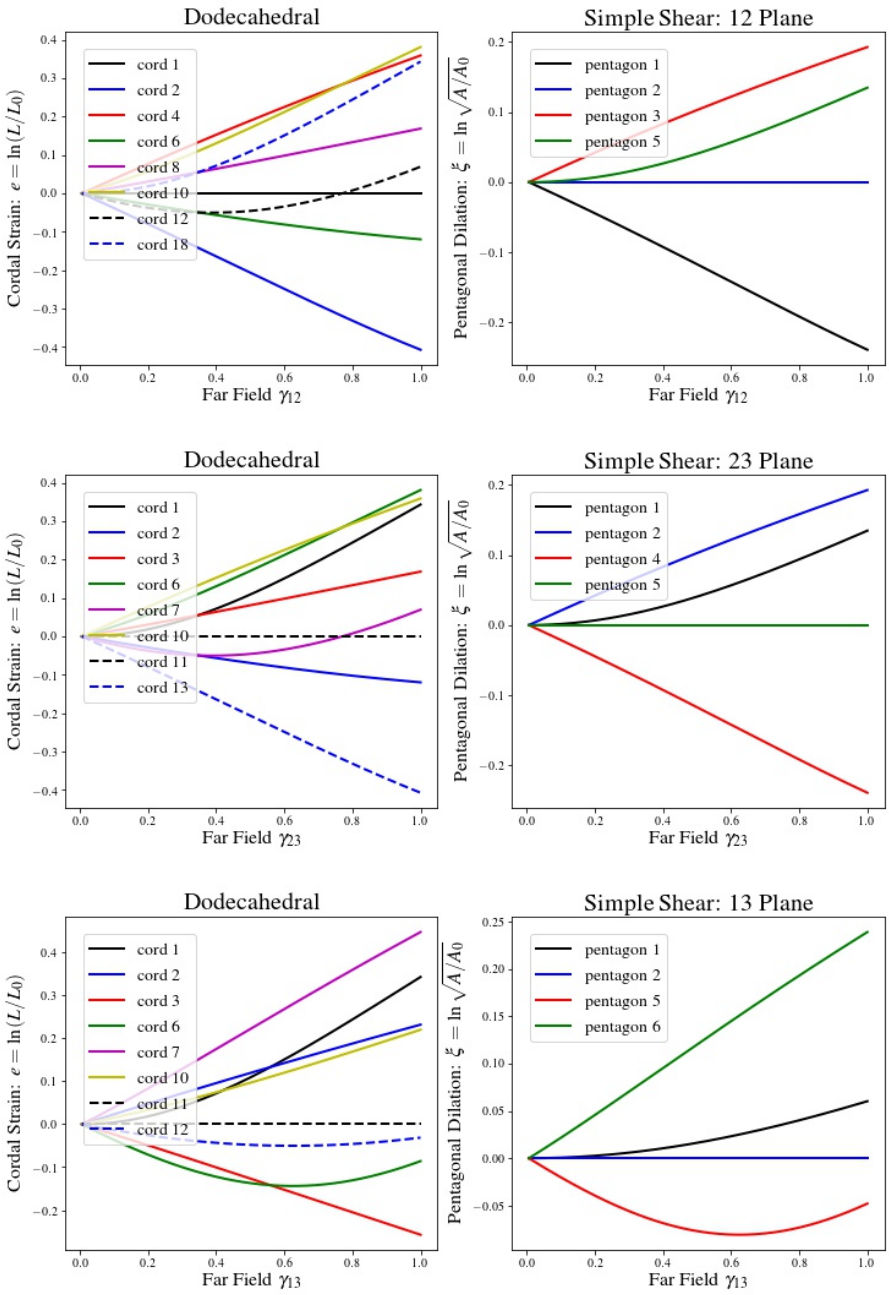

Fig. 20 Response of a dodecahedron exposed to far-field simple-shear motions. In all six graphic images, the relevant (controlled) motion of simple shear is plotted along the abscissa. In each image pair, the right graphic presents pentagonal dilations, while the left graphic presents chordal elongations. Only unique responses are plotted; repetitions are not. Responses in the 13 plane differ slightly from those of the 12 and 23 planes.

The curves in Figs. 19 and 20 were obtained from geometric measures for chordal strain $\ln(L/L_0)$ and areal dilation $\ln\sqrt{A/A_0}$. They were computed under separate far-field conditions of pure and simple shears. The curves in Figs. 21 and 22 were obtained from thermodynamic measures for membrane strain under the same far-field deformations. The strains of dilation ξ, squeeze ε, and shear γ were computed in accordance with Section 3.3.6 using deformation gradients gotten from the pentagonal shape functions of Wachspress[57] discussed in Section 3.3.1.*

Figures 19–22 allow us to conclude that if septal dilation were the only mode of planar deformation thought to cause a mechanical response, then knowledge of the geometric strain $\xi = \ln\sqrt{A/A_0}$ would be adequate; there would be no need to introduce a separate finite element discretization of the septal planes for acquiring their deformation gradients. However, if the non-uniform responses of squeeze ε and shear γ are thought to contribute to the overall mechanical response of these membranes, then the shape functions of Wachspress[57,58] ought to be used for acquiring the deformation gradient within a septal plane. We found, but do not present figures to support this observation, that constant-strain triangles are not accurate enough for our application whenever non-uniform deformations are considered. Strains derived from Wachspress shape functions are inhomogeneous; consequently, the deformation gradient will need to be evaluated at each Gauss point of integration within a pentagon, cf. Section 5.2.1.3.

3.5.3 Co-ordinate Pivoting

The pivoting strategy of Section 3.3.6.3 used to address the physical dilemma of Section 3.3.6.2 did not engage often during our assessment of the code, but it did arise at least twice with effects illustrated in Figs. 23 and 24. Here one can see that there is a clear effect on the shear response within four pentagonal planes; however, no change is observed to have occurred in either the dilation or squeeze responses, as expected. It is not always possible to know when or where a co-ordinate relabeling ought to occur; consequently, the algorithm put forward in Section 3.3.6.3 is deemed necessary.

*Five constant-strain triangles were also used to quantify the deformation gradient for each pentagonal surface at its centroid—the common vertex to all five triangles. This approach provided accurate descriptions for uniform strain, i.e., dilation ξ, but not for the two non-uniform strains, viz., squeeze ε and shear γ; hence, our preference to use Wachspress shape functions for alveolar planes.

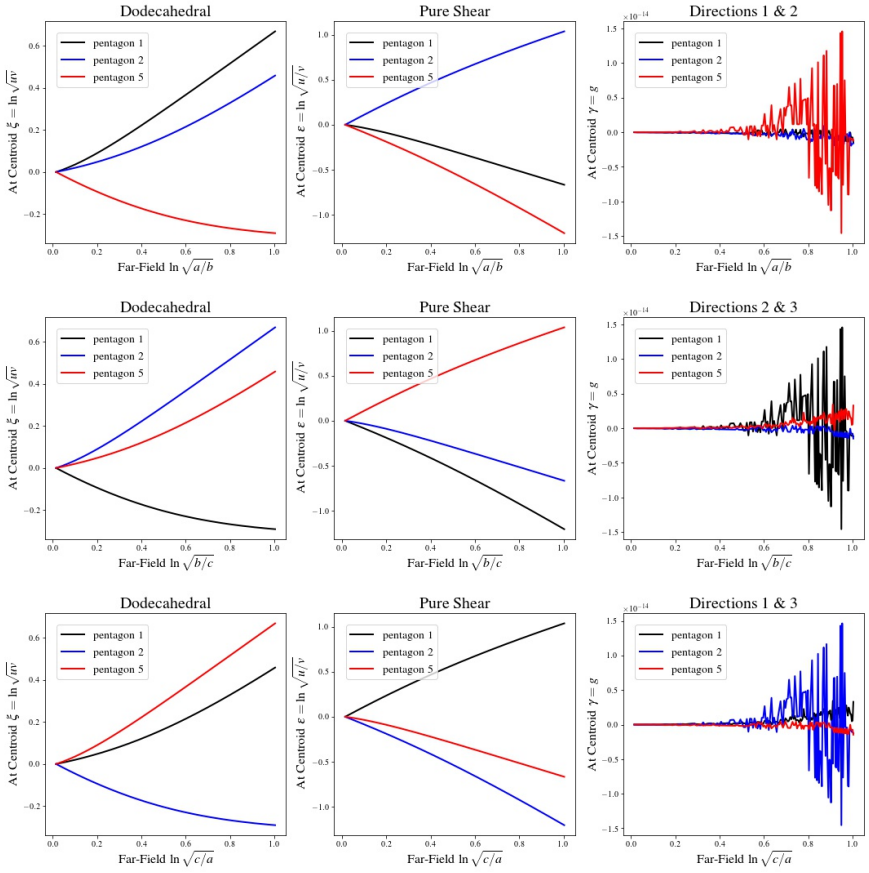

Fig. 21 Same boundary conditions as in Fig. 19. Pentagonal areas were used to compute dilation in Fig. 19. The shape functions of Wachspress were used to compute dilation here. The uniform response in the right column of Fig. 19 and in the left column above are the same, providing additional assurance that the code has been correctly implemented. The squeeze response shown in the center column is the same for all three orientations of far-field pure shear, i.e., this response is isotropic. The right column has ordinates scaled by 10^{-14} implicating that there is no effective simple shear response occurring within any pentagonal surface of the dodecahedron whenever it is subjected to a far-field motion of pure shear.

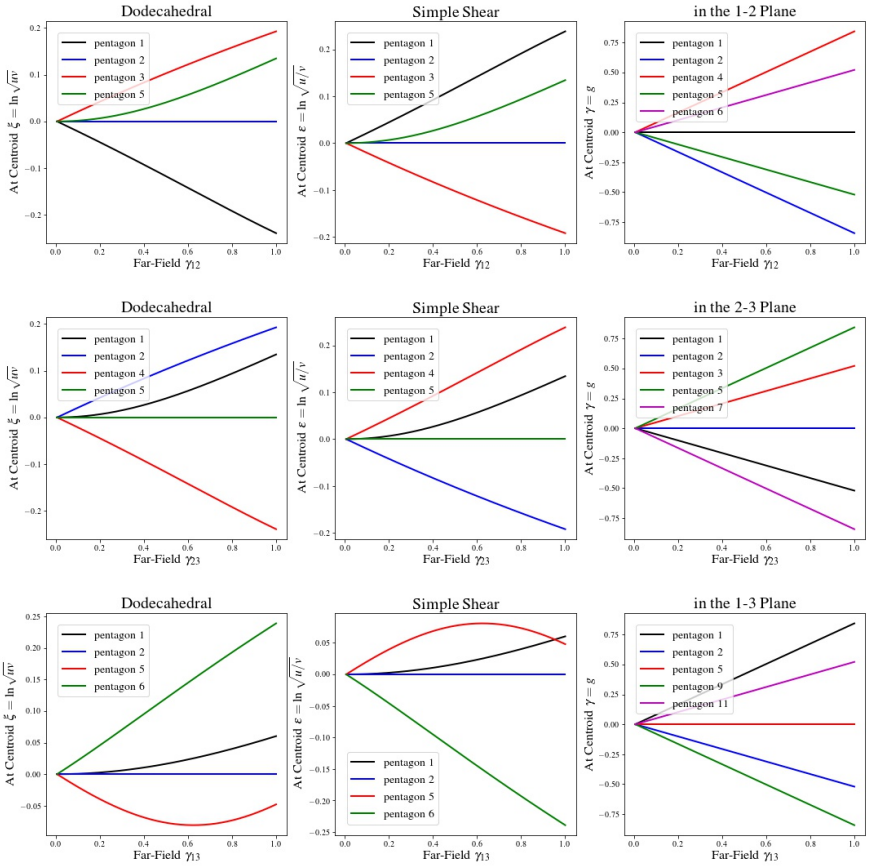

Fig. 22 Same boundary conditions as in Fig. 20. Pentagonal areas were used to compute dilation in Fig. 20. The shape functions of Wachspress were used to compute dilation here. The uniform response in the right column of Fig. 20 and in the left column above are the same, providing additional assurance that the code has been correctly implemented. Like the dilational responses of the left column, the squeeze responses of the center column are the same in the 12 and 23 planes, but differ in the 13 plane. In all cases, the simple shear response of any pentagonal plane is proportional to that of the far-field shear imposed, further substantiating the code's implementation. The shear response of the septal membranes is isotropic.

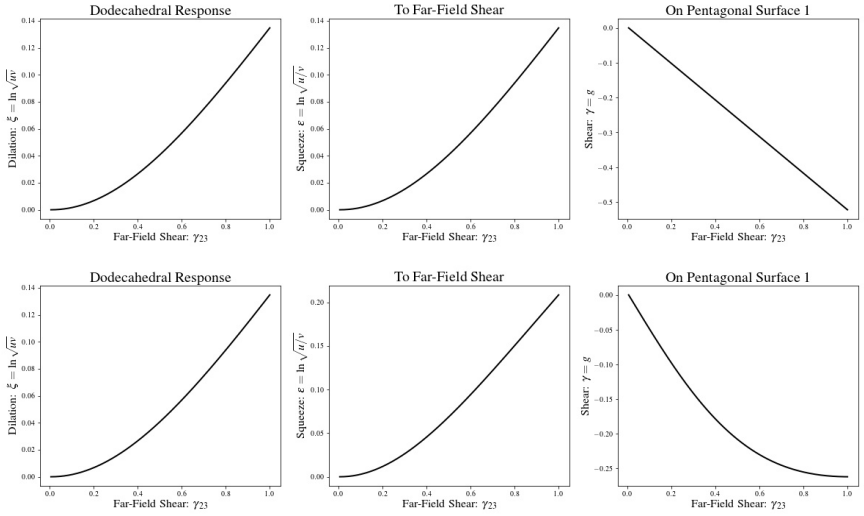

Fig. 23 A far-field shear of γ_{23} is imposed on the dodecahedron. Pentagons 1 and 8 exhibit the plotted response. The top set of figures result whenever the pivoting strategy of Section 3.3.6.3 is used, while the bottom set of figures result whenever no pivoting strategy is employed. The dilation (left graphs) and squeeze (center graphs) responses are not effected by pivoting, only shear (right graphs) is effected. Pivoting maintains a linear shear response under a far-field shearing of the dodecahedron, as desired.

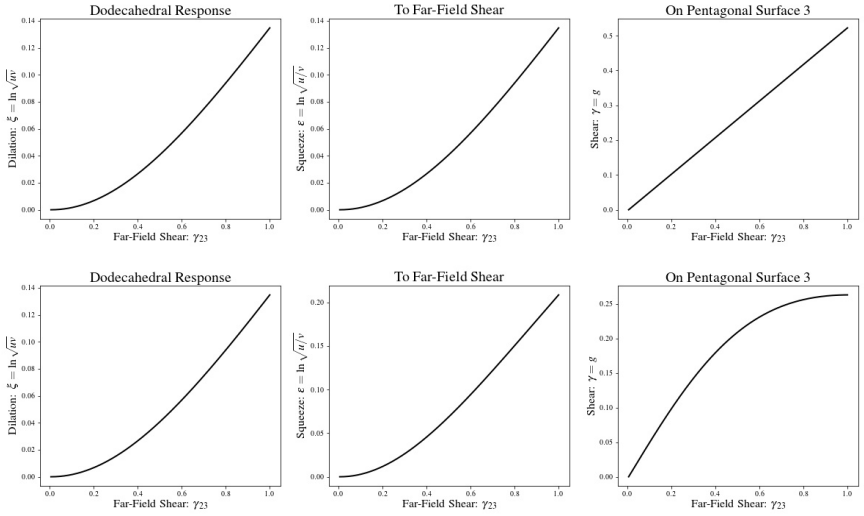

Fig. 24 A far-field shear of γ_{23} is imposed on the dodecahedron. Pentagons 3 and 10 exhibit the plotted response. The top set of figures result whenever the pivoting strategy of Section 3.3.6.3 is used, while the bottom set of figures result whenever no pivoting strategy is employed. The dilation (left graphs) and squeeze (center graphs) responses are not effected by pivoting, only shear (right graphs) is effected. Pivoting maintains a linear shear response under a far-field shearing of the dodecahedron, as desired.

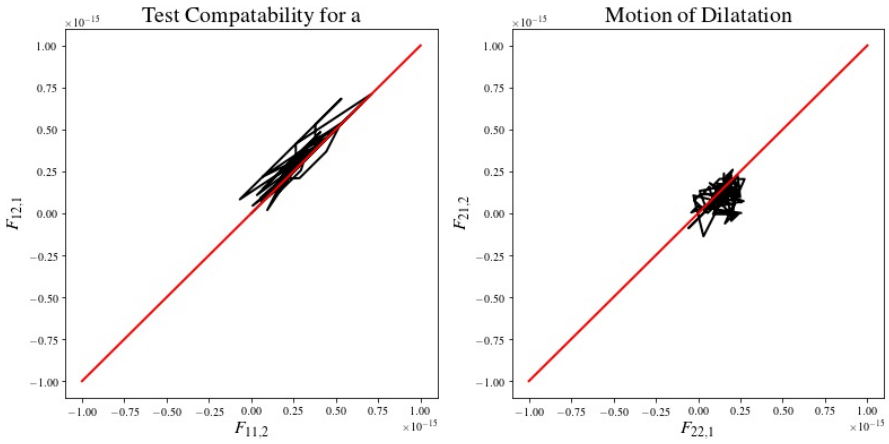

Fig. 25 Planar compatibility requires $F_{11,2} = F_{12,1}$ and $F_{22,1} = F_{21,2}$ where the left-hand sides of these formulæ are plotted as the abscissæ and the right-hand sides are plotted as the ordinates. For compatibility, the response ought to lie along the 45° diagonal, which is drawn in red over the range of $\pm 10^{-15}$ where machine precision is about 2.2×10^{-16}. Here the motion is one of uniform dilatation out to 100% strain.

3.5.4 Compatible Membrane Deformations

For a deformation to be compatible, and therefore integrable, the curl of its deformation gradient must vanish, viz., $\text{curl}(\mathbf{F}) = \mathbf{0}$.[62] Equation 29 provides constraint equations for the compatibility of planar motions, e.g., septal planes of an alveolus. Here we test to make sure that these conditions are satisfied within the pentagonal planes of our alveolar dodecahedron, assuming that the shape functions of Wachspress apply.

Figure 25 presents the compatibility response at the centroid of a typical pentagonal plane during the uniform expansion of a regular dodecahedron out to 100% strain. Theoretically, all four derivatives should be zero for this motion. Actually, their values are on the order of machine precision. Most importantly, whenever they are not zero, they lie along the 45° diagonal, thereby verifying compatibility in the case of a dilatation.

Similarly, Figs. 26 and 27 present typical responses for testing compatibility during far-field pure shear (Fig. 26) and simple shear (Fig. 27) deformations. In both cases, one of the four pentagons around the girth of the dodecahedron (viz., #5) has been selected, as both modes of deformation are activated in this pentagon. In both cases, errors are typically less than 10 times machine precision, thereby verifying

compatibility in the cases of squeeze and shear.

This collective set of graphs, Figs. 25–27, investigate the constraint of compatibility in terms of the three fundamental modes of deformation: dilatation, squeeze, and shear. These figures verify that the constraint of compatibility is satisfied when using the pentagonal shape functions of Wachspress[57,58] in our dodecahedral model, as errors are typically less than 10 times machine precision. This has been verified out to deformations that are at least 3 times those of their normal physiologic range.

Our kinematic analysis of a dodecahedron has been verified, both theoretically and numerically.

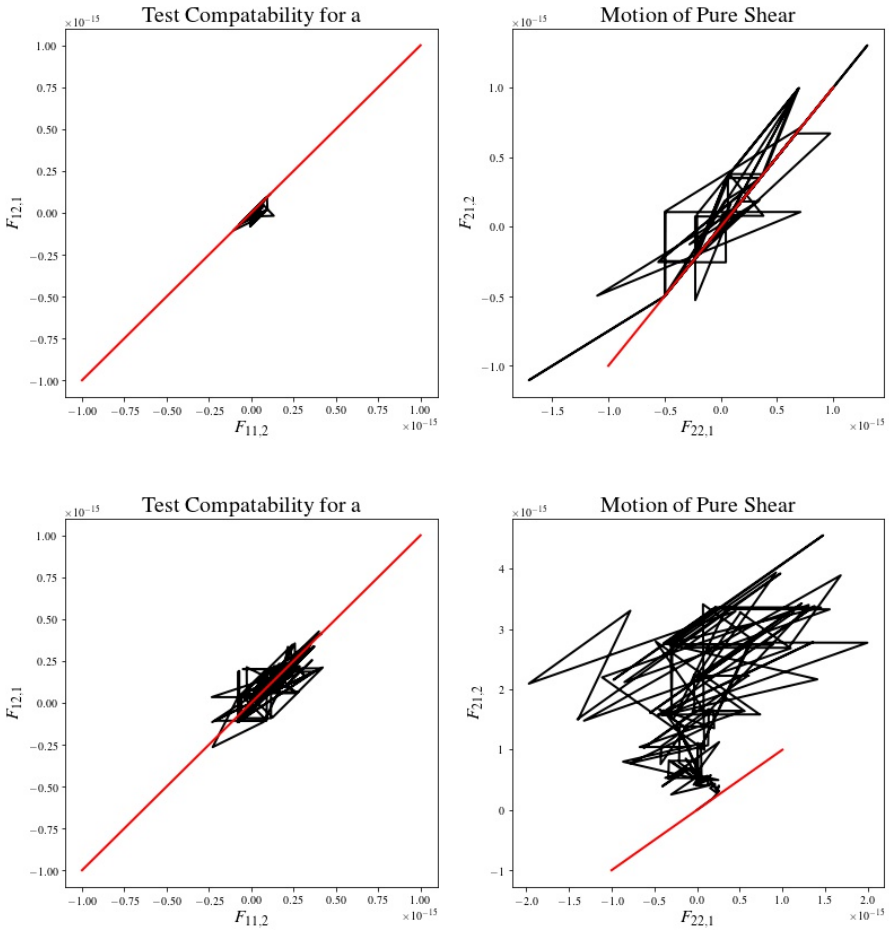

Fig. 26 Planar compatibility requires $F_{11,2} = F_{12,1}$ and $F_{22,1} = F_{21,2}$ where the left-hand sides of these formulæ are plotted as the abscissæ and the right-hand sides are plotted as the ordinates. For compatibility, the response ought to lie along the 45° diagonal, which is drawn in red over the range of $\pm 10^{-15}$ where machine precision is about 2.2×10^{-16}. Here the motion is one of pure shear out to 100% strain with elongation occurring in the 1-direction, contraction occurring in the 2-direction, while the 3-direction is held fixed. These results pertain to pentagon 5: nodes 15, 5, 12, 11, 1, cf. Fig. 6 and Table 3. The top row of figures is the best response among the Gauss points, while the bottom row of figures is the worst response.

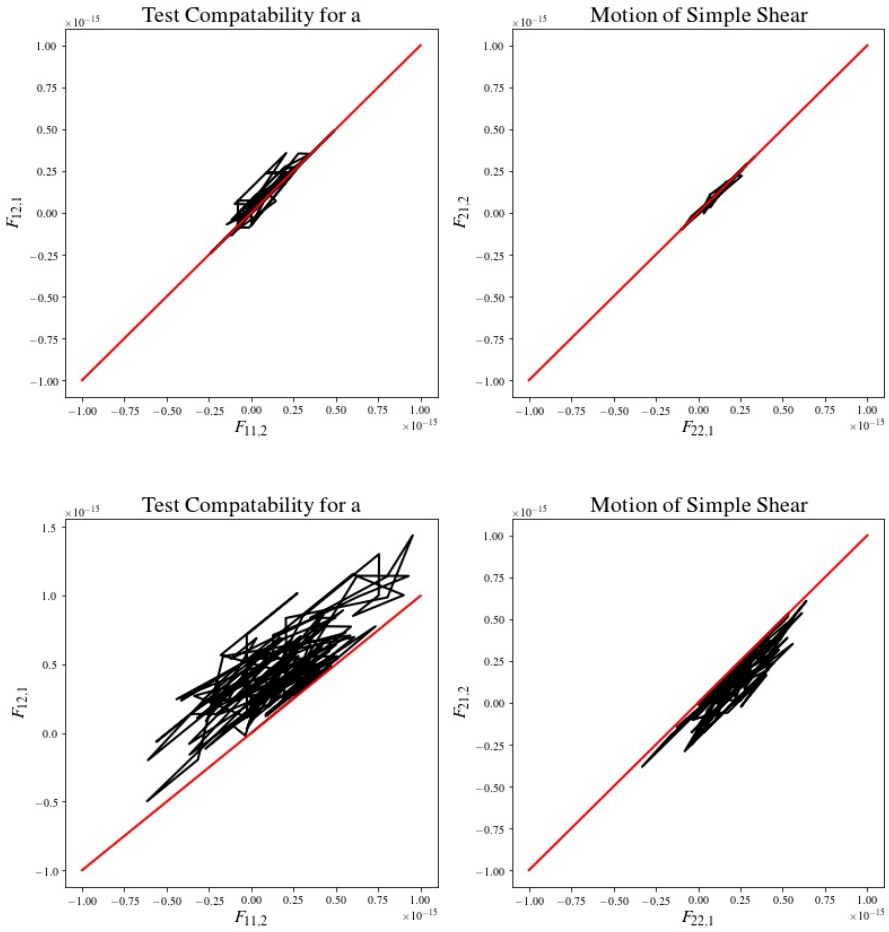

Fig. 27 Planar compatibility requires $F_{11,2} = F_{12,1}$ and $F_{22,1} = F_{21,2}$ where the left-hand sides of these formulæ are plotted as the abscissæ and the right-hand sides are plotted as the ordinates. For compatibility, the response ought to lie along the 45° diagonal, which is drawn in red over the range of $\pm 10^{-15}$ where machine precision is about 2.2×10^{-16}. Here the motion is one of simple shear out to 100% strain, shearing along 1-2 planes in the 1-direction. These results pertain to pentagon 5: nodes 15, 5, 12, 11, 1, cf. Fig. 6 and Table 3. The top row of figures is the best response among the Gauss points, while the bottom row of figures is the worst response.

4. Constitutive Theory

Roan and Waters[30] and Suki *et al*.[77,78] have both written extensive review articles on the mechanics of parenchyma. They have provided detailed information about the structural constituents of alveoli. And they have discussed their influence on the overall mechanical response of parenchyma. Of particular relevance, from a mechanics perspective, are the constituent building blocks of alveolar tissue: collagen (types I and III, predominantly), elastin, proteoglycans and other structural proteins, surfactant, and cells (epithelial and endothelial, predominantly). These constituents are assembled in such a manner so as to produce a variety of alveolar sub-structures that are essentially 1D (alveolar chords), 2D (alveolar septa), and 3D (alveolar sacs) in their geometric construction.

A dodecahedron is used here as a geometric model for an alveolus,[35] cf. Figs. 4 and 6. This model comprises 30 1D rods that represent alveolar chords, 12 2D membranes that represent alveolar septa, considered here to be pentagonal in shape, and 1 3D cavity filled with air (or fluid in the case of a contusion caused by injury, or of an edema caused by disease) whose geometry is considered to be dodecahedral in shape. The thermoelastic constitutive equations presented here for spatial chords and membranes are derived in the Appendix. Elastic behavior is sufficient for our intended application of studying alveoli subjected to traveling stress waves.

We recall from our kinematic study of a dodecahedron that the geometric strains (i.e., $e := \ln(L/L_0)$ for the elongation of septal chords, $\xi := \ln\sqrt{A/A_0}$ for the dilation of septal membranes, and $\Xi := \ln\sqrt[3]{V/V_0}$ for the dilatation of alveolar volume) are equivalent to one another under motions of uniform expansion/compression. These three, geometric, strain measures also exist as thermodynamic strains, each associating with a distinct and unique conjugate stress.[66,73]

Constitutive equations are a derived consequence from physical laws governing thermodynamic processes. Here we derive constitutive equations applicable for modeling 1D thermoelastic fibers (alveolar chords), 2D thermoelastic membranes (alveolar septa), and 3D thermoelastic volumes (alveolar sacs). In Section 4, we assume that the motions are uniform in their spatial dimension. Later, in Sections 4.1.3 and 4.2.3.1, the non-uniform motions of squeeze and shear are included into our thermodynamic framework for membranes and volumes. Section 4.3.3.1 pulls these results together, sufficient for the intended purpose of modeling the three structural

facets that compose an alveolus. Specifically, all geometric entities (alveolar chords, alveolar septa, and alveolar sacs) are now described in terms of stresses (dyne/cm^2) instead of their intensive thermodynamic forces (force, surface tension, or stress). This is done to facilitate implementation of these models into code, and to facilitate interpretations of their results by engineers and scientists. This section closes with a discussion of their implementation into finite elements in Section 4.4.4.2 along with a set of examples created to verify our code, also in Section 4.4.4.2. The biologic constitutive equations presented in this part are derived in the Appendix from an implicit theory of elasticity.

4.1 Green Thermoelastic Solids: Uniform Motions in 1D, 2D, and 3D

Combining the First and Second Laws of Thermodynamics governing uniform, reversible, adiabatic processes results in the following three formulæ, one per dimension; they are

$$\text{In 1D:} \qquad \mathrm{d}U = \theta\,\mathrm{d}\eta + \tfrac{1}{\rho_{1D}}\,F\,\mathrm{d}L/L \tag{56a}$$

$$\text{In 2D:} \qquad \mathrm{d}U = \theta\,\mathrm{d}\eta + \tfrac{1}{\rho_{2D}}\,T\,\mathrm{d}A/A \tag{56b}$$

$$\text{In 3D:} \qquad \mathrm{d}U = \theta\,\mathrm{d}\eta - \tfrac{1}{\rho_{3D}}\,P\,\mathrm{d}V/V \tag{56c}$$

wherein U is an internal energy density (erg/g = dyne.cm/g), which is a function of state, θ is a temperature in Kelvin ($273 + {}^\circ$C), η is an entropy density (erg/g.K), L is a length of line (cm), A is an area of surface (cm^2), V is a volume of space (cm^3), F is a force (dyne), T is a surface tension (dyne/cm), and P is a pressure (dyne/cm^2 = barye), whereas the mass densities ρ_{1D} (g/cm), ρ_{2D} (g/cm^2), or ρ_{3D} (g/cm^3) associate with a reference state of per unit length, per unit area, or per unit volume, as appropriate. Pressure P is assigned to be positive whenever a body undergoes hydrostatic compression, as classically assigned. However, per accepted practice in continuum mechanics, the sign of pressure may flip back and forth depending upon what pressure we are talking about in lung mechanics, e.g., it is common to refer to transpulmonary pressures as being positive (not negative). Typically, the trace of stress is positive for this measure of pressure.

4.1.1 Constitutive Equations

Because the internal energy density U is a state function, its differential rate of change describes a Pfaffian form[74] out of which the following constitutive formulæ

are readily obtained:

$$\text{In 1D:} \quad \theta = \partial_\eta U(\eta, \ln(L/L_0)) \qquad F = \rho_{1D}\, \partial_{\ln(L/L_0)} U(\eta, \ln(L/L_0)) \tag{57a}$$

$$\text{In 2D:} \quad \theta = \partial_\eta U(\eta, \ln(A/A_0)) \qquad T = \rho_{2D}\, \partial_{\ln(A/A_0)} U(\eta, \ln(A/A_0)) \tag{57b}$$

$$\text{In 3D:} \quad \theta = \partial_\eta U(\eta, \ln(V/V_0)) \qquad -P = \rho_{3D}\, \partial_{\ln(V/V_0)} U(\eta, \ln(V/V_0)) \tag{57c}$$

where strains are logarithms of dimension-appropriate stretches. As a matter of convenience, we adopt the notation $\partial_\eta U := \partial U/\partial\eta$, etc. Employing the geometric strains of Section 3, viz., $e := \ln(L/L_0)$, $\xi := \ln\sqrt{A/A_0}$, and $\Xi := \ln\sqrt[3]{V/V_0}$ with differential rates of $\mathrm{d}e = L^{-1}\,\mathrm{d}L$, $\mathrm{d}\xi = \frac{1}{2}A^{-1}\,\mathrm{d}A$, and $\mathrm{d}\Xi = \frac{1}{3}V^{-1}\,\mathrm{d}V$, these constitutive equations take on the simpler form of

$$\text{In 1D:} \qquad \theta = \partial_\eta U(\eta, e) \qquad F = \rho_{1D}\, \partial_e U(\eta, e) \tag{58a}$$

$$\text{In 2D:} \qquad \theta = \partial_\eta U(\eta, \xi) \qquad \pi = \rho_{2D}\, \partial_\xi U(\eta, \xi) \tag{58b}$$

$$\text{In 3D:} \qquad \theta = \partial_\eta U(\eta, \Xi) \qquad \Pi = \rho_{3D}\, \partial_\Xi U(\eta, \Xi) \tag{58c}$$

wherein $\pi := 2T$ and $\Pi := -3P$ are the measures for surface tension and pressure that we use in this work. We find it useful to use this negative measure for pressure because the transpulmonary pressure in lung, under normal physiologic conditions, is typically negative; hence, Π would be positive in its specification of transpulmonary pressure. The above constitutive equations describe Green thermoelastic solids of specified dimension undergoing uniform motions in adiabatic enclosures.

We consider response variables for temperature and force/surface-tension/pressure to be C^1 functions of state; therefore, the internal energy U is a C^2 function of state in a Green thermoelastic solid undergoing uniform adiabatic motions (cf. Weinhold[79] and Gilmore[80]). Under these conditions of smoothness, one can differentiate Eq. 58, thereby producing the following collection of coupled, partial, differential

equations

$$\text{In 1D:} \qquad \begin{Bmatrix} \mathrm{d}\theta \\ \mathrm{d}F \end{Bmatrix} = \begin{bmatrix} \partial_{\eta\eta} U & \partial_{\eta e} U \\ \rho_{1D}\, \partial_{e\eta} U & \rho_{1D}\, \partial_{ee} U \end{bmatrix} \begin{Bmatrix} \mathrm{d}\eta \\ \mathrm{d}e \end{Bmatrix} \tag{59a}$$

$$\text{In 2D:} \qquad \begin{Bmatrix} \mathrm{d}\theta \\ \mathrm{d}\pi \end{Bmatrix} = \begin{bmatrix} \partial_{\eta\eta} U & \partial_{\eta\xi} U \\ \rho_{2D}\, \partial_{\xi\eta} U & \rho_{2D}\, \partial_{\xi\xi} U \end{bmatrix} \begin{Bmatrix} \mathrm{d}\eta \\ \mathrm{d}\xi \end{Bmatrix} \tag{59b}$$

$$\text{In 3D:} \qquad \begin{Bmatrix} \mathrm{d}\theta \\ \mathrm{d}\Pi \end{Bmatrix} = \begin{bmatrix} \partial_{\eta\eta} U & \partial_{\eta\Xi} U \\ \rho_{3D}\, \partial_{\Xi\eta} U & \rho_{3D}\, \partial_{\Xi\Xi} U \end{bmatrix} \begin{Bmatrix} \mathrm{d}\eta \\ \mathrm{d}\Xi \end{Bmatrix} \tag{59c}$$

where mixed partial derivatives obey $\partial_{e\eta} U = \partial^2 U / \partial e \partial \eta = \partial^2 U / \partial \eta \partial e = \partial_{\eta e} U$, etc., that in the thermodynamics literature are referred to as Maxwell's relations; they are also known as Silvester's criteria for the integrability of a Pfaffian form.

Exchanging cause and effect between entropy and temperature in Eq. 59 gives rise to the following:
In 1D:

$$\begin{Bmatrix} \mathrm{d}\eta \\ \mathrm{d}F \end{Bmatrix} = \begin{bmatrix} \theta / \partial_{\eta\eta} U & -\partial_{\eta e} U / \partial_{\eta\eta} U \\ \rho_{1D} \theta\, \partial_{e\eta} U / \partial_{\eta\eta} U & \rho_{1D} (\partial_{ee} U - \partial_{e\eta} U \cdot \partial_{\eta e} U / \partial_{\eta\eta} U) \end{bmatrix} \begin{Bmatrix} \theta^{-1}\, \mathrm{d}\theta \\ \mathrm{d}e \end{Bmatrix} \tag{60a}$$

In 2D:

$$\begin{Bmatrix} \mathrm{d}\eta \\ \mathrm{d}\pi \end{Bmatrix} = \begin{bmatrix} \theta / \partial_{\eta\eta} U & -\partial_{\eta\xi} U / \partial_{\eta\eta} U \\ \rho_{2D} \theta\, \partial_{\xi\eta} U / \partial_{\eta\eta} U & \rho_{2D} (\partial_{\xi\xi} U - \partial_{\xi\eta} U \cdot \partial_{\eta\xi} U / \partial_{\eta\eta} U) \end{bmatrix} \begin{Bmatrix} \theta^{-1}\, \mathrm{d}\theta \\ \mathrm{d}\xi \end{Bmatrix} \tag{60b}$$

In 3D:

$$\begin{Bmatrix} \mathrm{d}\eta \\ \mathrm{d}\Pi \end{Bmatrix} = \begin{bmatrix} \theta / \partial_{\eta\eta} U & -\partial_{\eta\Xi} U / \partial_{\eta\eta} U \\ \rho_{3D} \theta\, \partial_{\Xi\eta} U / \partial_{\eta\eta} U & \rho_{3D} (\partial_{\Xi\Xi} U - \partial_{\Xi\eta} U \cdot \partial_{\eta\Xi} U / \partial_{\eta\eta} U) \end{bmatrix} \begin{Bmatrix} \theta^{-1}\, \mathrm{d}\theta \\ \mathrm{d}\Xi \end{Bmatrix} \tag{60c}$$

where we recall that $\mathrm{d}e = L^{-1}\, \mathrm{d}L$, $\mathrm{d}\xi = \frac{1}{2} A^{-1}\, \mathrm{d}A$, and $\mathrm{d}\Xi = \frac{1}{3} V^{-1}\, \mathrm{d}V$, so that we have logarithmic rates describing both components in each of the right-hand vectors above. Here we adopt the independent variables of a Helmholtz free energy, namely temperature and strain, but we do not employ his potential, preferring to retain the internal energy potential so as to ensure a proper incorporation of Maxwell's constraint.

Constitutive equations (Eqs. 59 and 60) take on the form of a hypo-elastic material model,[81] which is ideal for numerical implementation whenever one uses solution techniques like those presented in Section 5.

4.1.2 Material Response Functions

Experiments are performed for the purpose of characterizing material behavior. In mechanics, we relate measured material properties to gradients and curvatures of thermodynamic potentials, out of which material models are constructed. Experiments are typically done to quantify the following material properties, defined here as tangents to response curves, and selected per a material's physical dimension.
In 1D:

$$C_F := \left.\frac{\mathrm{d}\eta}{\theta^{-1}\,\mathrm{d}\theta}\right|_{\mathrm{d}F=0} \quad \alpha_F := \left.\frac{L^{-1}\,\mathrm{d}L}{\theta^{-1}\,\mathrm{d}\theta}\right|_{\mathrm{d}F=0} \qquad E_\theta := \left.\frac{\mathrm{d}F}{L^{-1}\,\mathrm{d}L}\right|_{\mathrm{d}\theta=0} \tag{61a}$$

In 2D:

$$C_T := \left.\frac{\mathrm{d}\eta}{\theta^{-1}\,\mathrm{d}\theta}\right|_{\mathrm{d}T=0} \quad \alpha_T := \left.\frac{A^{-1}\,\mathrm{d}A}{\theta^{-1}\,\mathrm{d}\theta}\right|_{\mathrm{d}T=0} = 2\alpha_F \quad M_\theta := \left.\frac{\mathrm{d}T}{A^{-1}\,\mathrm{d}A}\right|_{\mathrm{d}\theta=0} \tag{61b}$$

In 3D:

$$C_P := \left.\frac{\mathrm{d}\eta}{\theta^{-1}\,\mathrm{d}\theta}\right|_{\mathrm{d}P=0} \quad \alpha_P := \left.\frac{V^{-1}\,\mathrm{d}V}{\theta^{-1}\,\mathrm{d}\theta}\right|_{\mathrm{d}P=0} = 3\alpha_F \quad K_\theta := \left.\frac{-\mathrm{d}P}{V^{-1}\,\mathrm{d}V}\right|_{\mathrm{d}\theta=0} \tag{61c}$$

whose analogs, as secant functions, are defined in the Appendix.

The various thermal strain coefficients α_F, α_T, α_P are, however, distinct from one another. Even though each is dimensionless, each is defined with respect to its own physical dimension. Nevertheless, because $\ln(L/L_0) = \frac{1}{2}\ln(A/A_0) = \frac{1}{3}\ln(V/V_0)$, it follows that $\alpha_T = 2\alpha_F$ and $\alpha_P = 3\alpha_F$, so there is really just one thermal strain coefficient, i.e., α_F, that, hereafter, is denoted as α_t where the subscript t denotes *tangent*.* It is noteworthy to point out that what one typically refers to as the coefficient of thermal expansion, i.e., α (1/K), is distinct from the thermal strain coefficient, viz., α_t (dimensionless); specifically, $\alpha_t = \alpha\theta_0$ for small temperature excursions, cf. the Appendix.

The various specific heats C_F, C_T, C_P (erg/g.K) are distinct, yet essentially, they are equivalent as each is defined per unit mass, insensitive to dimension. They are evaluated at a fixed thermodynamic force, which does depend upon dimension. Hereafter,

*In the Appendix, sub/super script t is used to denote *tangent*; whereas, sub/super script s is used to denote *secant*, e.g., $\mathrm{d}F = E_t\,\mathrm{d}e$ whereas $F = E_s\,e$. Here, the defined material properties are tangent properties. Secant properties, and their definitions, can be found in the Appendix. Both secant and tangent moduli are used in the variational formulation put forward in Section 6.

we will denote the tangent response to specific heat as C_t that, in the Appendix, is shown to relate to the secant version of specific heat C_s via

$$\text{1D:} \qquad C_t = C_s - \alpha_s \frac{F - F_0}{\rho_{1D}\theta} \tag{62a}$$

$$\text{2D:} \qquad C_t = C_s - \alpha_s \frac{\pi - \pi_0}{\rho_{2D}\theta} \tag{62b}$$

$$\text{3D:} \qquad C_t = C_s - \alpha_s \frac{\Pi - \Pi_0}{\rho_{3D}\theta} \tag{62c}$$

where C_s is the density of specific heat at constant pressure that one typically finds tabulated in the literature. Usually, the secant and tangent versions for the thermal strain coefficient are equivalent, i.e., $\alpha_s \equiv \alpha_t$. Here F_0, π_0, and Π_0 are the force, surface tension, and pressure associated with some specified reference state, i.e., it is in this state where their conjugate strains are assigned to zero, viz., $e_0 = 0$, $\xi_0 = 0$, and $\Xi_0 = 0$ even though $F_0 \neq 0$, $\pi_0 \neq 0$, and $\Pi_0 \neq 0$, in general.

The various tangent moduli E_θ, M_θ, and K_θ are also distinct. They have different dimensions. Material property E_θ is a modulus of extension (dyne); material property M_θ is a modulus of dilation (dyne/cm); and material property K_θ is a modulus of dilatation (dyne/cm^2), a.k.a. the bulk modulus, with each modulus being measured at a fixed temperature. Shear moduli are discussed later in Sections 4.1.3 and 4.2.3.1. The above material properties are gradients. They constitute tangents to their associated physical response curves, and as such, are denoted hereafter as E_t, M_t, and K_t. Consequently, they need not be of constant value throughout state space, like a Hookean material would suppose them to be. In other words, the secant and tangent moduli need not be the same at any given state. This is an important characteristic for the hypo-elastic constructions of Eqs. 59 and 60, as they pertain to our application.

In terms of the thermoelastic material properties given in Eq. 61, of which there are three per dimension, the internal energy density has three curvatures that associate with it.

For 1D materials:

$$\partial_{\eta\eta}U = \frac{\rho_{1D}\theta^2}{\rho_{1D}C_t\theta - \alpha_t^2 E_t} \tag{63a}$$

$$\partial_{ee}U = \frac{C_t E_t \theta}{\rho_{1D}C_t\theta - \alpha_t^2 E_t} \tag{63b}$$

$$\partial_{\eta e}U \equiv \partial_{e\eta}U = \frac{-\alpha_t E_t \theta}{\rho_{1D}C_t\theta - \alpha_t^2 E_t} \tag{63c}$$

For 2D materials:

$$\partial_{\eta\eta}U = \frac{\rho_{2D}\theta^2}{\rho_{2D}C_t\theta - 4\alpha_t^2 M_t} \tag{63d}$$

$$\partial_{\xi\xi}U = \frac{4C_t M_t \theta}{\rho_{2D}C_t\theta - 4\alpha_t^2 M_t} \tag{63e}$$

$$\partial_{\eta\xi}U \equiv \partial_{\xi\eta}U = \frac{-4\alpha_t M_t \theta}{\rho_{2D}C_t\theta - 4\alpha_t^2 M_t} \tag{63f}$$

For 3D materials (cf. Weinhold[79] and Gilmore[80]):

$$\partial_{\eta\eta}U = \frac{\rho_{3D}\theta^2}{\rho_{3D}C_t\theta - 9\alpha_t^2 K_t} \tag{63g}$$

$$\partial_{\Xi\Xi}U = \frac{9C_t K_t \theta}{\rho_{3D}C_t\theta - 9\alpha_t^2 K_t} \tag{63h}$$

$$\partial_{\eta\Xi}U \equiv \partial_{\Xi\eta}U = \frac{-9\alpha_t K_t \theta}{\rho_{3D}C_t\theta - 9\alpha_t^2 K_t} \tag{63i}$$

These materials constants are constrained by thermodynamics in that

$$0 < E_t < \frac{\rho_{1D}C_t\theta}{\alpha_t^2}, \quad 0 < M_t < \frac{\rho_{2D}C_t\theta}{4\alpha_t^2}, \quad 0 < K_t < \frac{\rho_{3D}C_t\theta}{9\alpha_t^2} \tag{64}$$

which ensure that their respective thermodynamic Jacobians cannot become singular. Singularities can and do occur, e.g., during a phase change in a crystal,[67,80] but such processes are not expected to arise in our application.

4.1.3 Thermoelastic Models for Modeling Alveoli: Uniform Motions

We now write down our constitutive formulæ for quantifying uniform responses in thermoelastic solids of 1, 2, and 3 dimensions. They are thermoelastic constitutive equations (Eq. 60) with Helmholtz variables expressed in terms of the material properties defined in Eq. 61 assigned to the internal energy density U according to

Eq. 63, with outcomes of

$$\text{For 1D:} \qquad \begin{Bmatrix} \mathrm{d}\eta \\ \mathrm{d}F \end{Bmatrix} = \begin{bmatrix} C_t - \alpha_t^2 E_t/\rho\theta & \alpha_t E_t/\rho\theta \\ -\alpha_t E_t & E_t \end{bmatrix} \begin{Bmatrix} \theta^{-1}\,\mathrm{d}\theta \\ \mathrm{d}e \end{Bmatrix} \tag{65a}$$

$$\text{For 2D:} \qquad \begin{Bmatrix} \mathrm{d}\eta \\ \mathrm{d}\pi \end{Bmatrix} = \begin{bmatrix} C_t - 4\alpha_t^2 M_t/\rho\theta & 4\alpha_t M_t/\rho\theta \\ -4\alpha_t M_t & 4M_t \end{bmatrix} \begin{Bmatrix} \theta^{-1}\,\mathrm{d}\theta \\ \mathrm{d}\xi \end{Bmatrix} \tag{65b}$$

$$\text{For 3D:} \qquad \begin{Bmatrix} \mathrm{d}\eta \\ \mathrm{d}\Pi \end{Bmatrix} = \begin{bmatrix} C_t - 9\alpha_t^2 K_t/\rho\theta & 9\alpha_t K_t/\rho\theta \\ -9\alpha_t K_t & 9K_t \end{bmatrix} \begin{Bmatrix} \theta^{-1}\,\mathrm{d}\theta \\ \mathrm{d}\Xi \end{Bmatrix} \tag{65c}$$

where we simplify our expressions by suppressing the dimension for which mass density applies. This is considered to be understood. There are four material properties for each dimension (e.g., for 1D materials they are ρ, C_t, α_t, and E_t) with the latter three being tangent properties defined according to Eq. 61.

The upper-left element in each matrix of Eq. 65 represents a heat capacity evaluated at constant strain—a material property not easily measured. Whereas, the specific heat evaluated at constant pressure (viz., the C_s found in the 11 matrix component of these tangent moduli, as established in Eq. 62) is more amenable to experiments, and is the property that one typically finds in published data tables.

Constitutive equations, Eqs. 65a–65c, derived here from the First and Second Laws of Thermodynamics, describe thermoelastic materials undergoing uniform motions through adiabatic processes. They present themselves as hypo-elastic material models,[81] which are often preferred for incorporating constitutive equations into finite element packages.

Equation 65 has cause and effect variables that are appropriate for our multi-scale application. In this process, a localization procedure pulls the temperature θ and deformation gradient $\mathbf{F}$ taken from the parenchyma scale (e.g., Gauss points in a finite element grid of lung) down to the level of an alveolar scale (in our modeling, a dodecahedron). Differential strain rates $\mathrm{d}\boldsymbol{\mathcal{U}}\cdot\boldsymbol{\mathcal{U}}^{-1}$ are then constructed through appropriate finite difference formulæ, where $\boldsymbol{\mathcal{U}}$ denotes the Laplace stretch.[56] These continuum rates are then mapped into our local thermodynamic rates, with alveolar entropy and stress following from a numerical integration of the above constitutive equations. These constitutive equations apply to the various facets of our dodecahedral model for an alveolar sac through a finite element discretization. Afterword, an homogenization procedure takes the updated alveolar entropy and nodal tractions,

and pushes them up to the continuum level as averaged parenchymal entropy and parenchymal stresses.

4.2 Green Thermoelastic Membranes: Non-Uniform Motions

The First and Second Laws of Thermodynamics governing a reversible adiabatic process are described by the formula $\mathrm{d}U = \theta\,\mathrm{d}\eta + \frac{1}{\rho}\,\mathrm{d}W$, where $\mathrm{d}W$ is the mechanical power expended by stressing a material element of mass density ρ. For the case of a 2D planar membrane, a mass density of $\rho \Leftarrow \rho_{2D}$ applies, with its change in mechanical work being expressed as[55,65,66]

$$\mathrm{d}W = \mathrm{tr}\left(\begin{bmatrix}\mathcal{S}_{11} & \mathcal{S}_{12}\\ \mathcal{S}_{21} & \mathcal{S}_{22}\end{bmatrix}\begin{bmatrix}a^{-1}\,\mathrm{d}a & (a/b)\,\mathrm{d}g\\ 0 & b^{-1}\,\mathrm{d}b\end{bmatrix}\right) = \pi\,\mathrm{d}\xi + \sigma\,\mathrm{d}\varepsilon + \tau\,\mathrm{d}\gamma, \tag{66a}$$

wherein $\mathcal{S}_{ij}$ are the components of a surface tension evaluated in the co-ordinate frame of a membrane.

Equation 66a conjectures that the First and Second Laws of Thermodynamics can be expressed as a differential equation known as a Pfaffian form that, in this case, looks like

$$\mathrm{d}U = \theta\,\mathrm{d}\eta + \tfrac{1}{\rho}\big(\pi\,\mathrm{d}\xi + \sigma\,\mathrm{d}\varepsilon + \tau\,\mathrm{d}\gamma\big), \tag{66b}$$

where $\{\pi, \sigma, \tau\}$ describes a set of intensive scalar-valued stresses whose thermodynamic conjugates $\{\xi, \varepsilon, \gamma\}$ describe a set of extensive scalar-valued strains. This contrasts with the classic approach, where the work done is decomposed into a scalar-valued isotropic part and a tensor-valued deviatoric part. The above thermodynamic strains are defined in Section 3.3.6.1, while their conjugate stresses, and how they relate to the tensor components of stress, are discussed below.

Conjugate pair (ξ, π) describes a dilation $2\,\mathrm{d}\xi \Leftarrow A^{-1}\,\mathrm{d}A$ caused by a surface tension $\pi \Leftarrow 2T$ where $\xi := \ln\sqrt{A/A_0}$ and $\pi := \mathcal{S}_{11} + \mathcal{S}_{22}$. This pair describes the uniform contribution to stress power discussed in Section 4. Pair (ε, σ) describes a squeeze ε (or pure shear) caused by a normal-stress difference $\sigma := \mathcal{S}_{11} - \mathcal{S}_{22}$. And pair (γ, τ) describes an in-plane shear γ caused by a shear stress τ. Collectively, pairs (ε, σ) and (γ, τ) account for any non-uniform contributions to stress power, i.e., contributions from other than uniform dilation. These pairs are quantified in Section 4.4.3.

4.2.1 General Constitutive Equations

Because a change in the internal energy $\mathrm{d}U$ governing a reversible adiabatic process is described by an exact differential,[74] with $U(\eta, \xi, \varepsilon, \gamma)$ in the case of a planar membrane, it follows that a constitutive response for a Green thermoelastic membrane is described by

$$\begin{aligned} \theta &= \partial_\eta U(\eta, \xi, \varepsilon, \gamma) \qquad & \pi &= \rho\, \partial_\xi U(\eta, \xi, \varepsilon, \gamma) \\ \sigma &= \rho\, \partial_\varepsilon U(\eta, \xi, \varepsilon, \gamma) \qquad & \tau &= \rho\, \partial_\gamma U(\eta, \xi, \varepsilon, \gamma). \end{aligned} \tag{67}$$

Considering each intensive variable, viz., θ, π, σ, and τ, to be at least a C^1 function of the set of extensive variables $(\eta, \xi, \varepsilon, \gamma)$, thereby implies that the internal energy U is at least a C^2 function of state. Therefore, the constitutive expressions in Eq. 67 can be recast into the following system of differential equations:

$$\begin{Bmatrix} \mathrm{d}\theta \\ \mathrm{d}\pi \\ \mathrm{d}\sigma \\ \mathrm{d}\tau \end{Bmatrix} = \begin{bmatrix} \partial_{\eta\eta} U & \partial_{\eta\xi} U & \partial_{\eta\varepsilon} U & \partial_{\eta\gamma} U \\ \rho\, \partial_{\xi\eta} U & \rho\, \partial_{\xi\xi} U & \rho\, \partial_{\xi\varepsilon} U & \rho\, \partial_{\xi\gamma} U \\ \rho\, \partial_{\varepsilon\eta} U & \rho\, \partial_{\varepsilon\xi} U & \rho\, \partial_{\varepsilon\varepsilon} U & \rho\, \partial_{\varepsilon\gamma} U \\ \rho\, \partial_{\gamma\eta} U & \rho\, \partial_{\gamma\xi} U & \rho\, \partial_{\gamma\varepsilon} U & \rho\, \partial_{\gamma\gamma} U \end{bmatrix} \begin{Bmatrix} \mathrm{d}\eta \\ \mathrm{d}\xi \\ \mathrm{d}\varepsilon \\ \mathrm{d}\gamma \end{Bmatrix} \tag{68}$$

whose upper-left 2×2 sub-matrix also appears in Eq. 59b, which governs the uniform contribution of a response. The above 4×4 matrix describes the full non-uniform response permissible by a Green thermoelastic membrane undergoing an adiabatic process.

For our application, it is reasonable to assume that the presence of a non-uniform planar motion will not cause an uniform planar response. Said differently, it is reasonable to assume that pure ε and simple γ shears will not affect a change in either temperature θ or surface tension π. As such, $\partial_{\eta\varepsilon} U = \partial_{\eta\gamma} U = \partial_{\xi\varepsilon} U = \partial_{\xi\gamma} U = 0$, and Eq. 68 simplifies to

$$\begin{Bmatrix} \mathrm{d}\theta \\ \mathrm{d}\pi \\ \mathrm{d}\sigma \\ \mathrm{d}\tau \end{Bmatrix} = \begin{bmatrix} \partial_{\eta\eta} U & \partial_{\eta\xi} U & 0 & 0 \\ \rho\, \partial_{\xi\eta} U & \rho\, \partial_{\xi\xi} U & 0 & 0 \\ 0 & 0 & \rho\, \partial_{\varepsilon\varepsilon} U & \rho\, \partial_{\varepsilon\gamma} U \\ 0 & 0 & \rho\, \partial_{\gamma\varepsilon} U & \rho\, \partial_{\gamma\gamma} U \end{bmatrix} \begin{Bmatrix} \mathrm{d}\eta \\ \mathrm{d}\xi \\ \mathrm{d}\varepsilon \\ \mathrm{d}\gamma \end{Bmatrix}$$

with $\partial_{\varepsilon\eta} U = \partial_{\gamma\eta} U = \partial_{\varepsilon\xi} U = \partial_{\gamma\xi} U = 0$ following because of Maxwell's relationships. Furthermore, it is considered that the pure and simple shear responses

act independently, too, so that $\partial_{\gamma\varepsilon}U = \partial_{\varepsilon\gamma}U = 0$.* Converting the above internal energy formulation into its Helmholtz equivalent produces two uncoupled matrix equations; they are

$$\begin{Bmatrix} \mathrm{d}\eta \\ \mathrm{d}\pi \end{Bmatrix} = \begin{bmatrix} \theta/\partial_{\eta\eta}U & -\partial_{\eta\xi}U/\partial_{\eta\eta}U \\ \rho\theta\,\partial_{\xi\eta}U/\partial_{\eta\eta}U & \rho\big(\partial_{\xi\xi}U - \partial_{\xi\eta}U\cdot\partial_{\eta\xi}U/\partial_{\eta\eta}U\big) \end{bmatrix} \begin{Bmatrix} \theta^{-1}\,\mathrm{d}\theta \\ \mathrm{d}\xi \end{Bmatrix} \tag{69a}$$

where both $\theta^{-1}\,\mathrm{d}\theta$ and $\mathrm{d}\xi = \frac{1}{2}A^{-1}\,\mathrm{d}A$ are logarithmic rates, and

$$\begin{Bmatrix} \mathrm{d}\sigma \\ \mathrm{d}\tau \end{Bmatrix} = \rho \begin{bmatrix} \partial_{\varepsilon\varepsilon}U & 0 \\ 0 & \partial_{\gamma\gamma}U \end{bmatrix} \begin{Bmatrix} \mathrm{d}\varepsilon \\ \mathrm{d}\gamma \end{Bmatrix} \tag{69b}$$

where $\mathrm{d}\varepsilon = \Gamma^{-1}\,\mathrm{d}\Gamma$ is also logarithmic in structure, while $\mathrm{d}\gamma = \mathrm{d}g$ is linear in its deformation field. All diagonal based strains are logarithmic, while all off-diagonal based strains are linear in our conjugate pair approach. Equation 69 is the general form for a Green thermoelastic membrane appropriate for our application.

Note: The uniform response Eq. 69a and the non-uniform response Eq. 69b are, by supposition, decoupled in this constitutive construction. There is experimental evidence that the bulk and shear moduli of parenchyma both depend upon transpulmonary pressure.[7,9,82,83] It is conjectured that this is a structural effect of alveolar geometry; it is not a characteristic of the constituents that compose an alveolus. As such, we do not couple the uniform and non-uniform responses in the constitutive framework of Eq. 69 at this time in order that we may test this conjecture.

4.2.2 Material Response Functions

The material model put forward here for a thermoelastic membrane has a mass density per unit area of ρ and five material properties that appear as tangent functions: a specific heat C_t at constant tension, a lineal thermal strain coefficient α_t at constant tension, an areal modulus M_t at constant temperature, a squeeze modulus N_t at constant shear, and a shear modulus G_t at constant squeeze. The density of specific heat C_t is defined as

$$C_t := \left.\frac{\mathrm{d}\eta}{\theta^{-1}\,\mathrm{d}\theta}\right|_T = \left.\frac{\mathrm{d}\eta}{\theta^{-1}\,\mathrm{d}\theta}\right|_\pi, \tag{70a}$$

*There is a second-order coupling that can exist between the modes of squeeze and shear in a 3D solid. It is the Poynting effect,[66] but this effect is thought not to arise to a level of significance in a 2D biologic membrane.

where θ is temperature, η is entropy density, and $\pi = \mathcal{S}_{11} + \mathcal{S}_{22} = 2T$ is the surface tension in a membrane. C_t is commonly referred to in the literature as the specific heat at constant pressure. The lineal thermal strain coefficient α_t is defined as

$$\alpha_t \coloneqq \left.\frac{L^{-1}\,\mathrm{d}L}{\theta^{-1}\,\mathrm{d}\theta}\right|_T = \frac{1}{2}\left.\frac{A^{-1}\,\mathrm{d}A}{\theta^{-1}\,\mathrm{d}\theta}\right|_T = \left.\frac{\mathrm{d}\xi}{\theta^{-1}\,\mathrm{d}\theta}\right|_\pi , \tag{70b}$$

which, here, is a dimensionless material property. $A = ab$ denotes a relative area with $\xi = \ln\sqrt{A/A_0}$ being the areal strain, a.k.a. dilation. This property is not the thermal expansion coefficient commonly used in the literature, which has dimensions of reciprocal temperature, cf. the Appendix. The associated, uniform, areal modulus M_t is defined as

$$M_t \coloneqq \left.\frac{\mathrm{d}T}{A^{-1}\,\mathrm{d}A}\right|_\theta = \left.\frac{\mathrm{d}\frac{1}{2}(\mathcal{S}_{11}+\mathcal{S}_{22})}{A^{-1}\,\mathrm{d}A}\right|_\theta = \frac{1}{4}\left.\frac{\mathrm{d}\pi}{\mathrm{d}\xi}\right|_\theta , \tag{70c}$$

which is the 2D version of a 3D bulk modulus. A new modulus introduced by Freed *et al.*,[65] which they call the in-plane squeeze modulus N_t, is defined as

$$N_t \coloneqq \left.\frac{\mathrm{d}N_1}{\Gamma^{-1}\,\mathrm{d}\Gamma}\right|_g = \left.\frac{\mathrm{d}(\mathcal{S}_{11}-\mathcal{S}_{22})}{\Gamma^{-1}\,\mathrm{d}\Gamma}\right|_g = \frac{1}{2}\left.\frac{\mathrm{d}\sigma}{\mathrm{d}\varepsilon}\right|_\gamma , \tag{70d}$$

where $\sigma = \mathcal{S}_{11} - \mathcal{S}_{22}$ is a normal-stress difference, often denoted as N_1 in the polymers literature, and where $\Gamma = a/b$ is the stretch of squeeze with $\varepsilon = \ln\sqrt{\Gamma/\Gamma_0}$ being the strain of squeeze, while $\gamma = g - g_0$ determines the shear strain. Finally, an in-plane shear modulus G_t is defined as

$$G_t \coloneqq \frac{1}{\Gamma}\left.\frac{\mathrm{d}\mathcal{S}_{21}}{\mathrm{d}g}\right|_\Gamma = \left.\frac{\mathrm{d}\tau}{\mathrm{d}\gamma}\right|_\varepsilon , \tag{70e}$$

where $\tau \coloneqq \Gamma\mathcal{S}_{21}$ establishes the shear stress.

4.2.3 Constitutive Equations Governing a Thermoelastic Membrane

It is the Gibbs free-energy potential (viz., $\mathcal{G}(\theta,\pi,\sigma,\tau) = U - \theta\eta - \pi\xi - \sigma\varepsilon - \tau\gamma$, which exchanges cause and effect with that of the internal energy $U(\eta,\xi,\varepsilon,\gamma)$), that is most easily expressed in terms of the above material properties, cf. the Appendix;

specifically, considering that

$$\begin{Bmatrix} \mathrm{d}\eta \\ \mathrm{d}\xi \\ \mathrm{d}\varepsilon \\ \mathrm{d}\gamma \end{Bmatrix} = - \begin{bmatrix} \partial_{\theta\theta}\mathcal{G} & \partial_{\theta\pi}\mathcal{G} & 0 & 0 \\ \rho\,\partial_{\pi\theta}\mathcal{G} & \rho\,\partial_{\pi\pi}\mathcal{G} & 0 & 0 \\ 0 & 0 & \rho\,\partial_{\sigma\sigma}\mathcal{G} & 0 \\ 0 & 0 & 0 & \rho\,\partial_{\tau\tau}\mathcal{G} \end{bmatrix} \begin{Bmatrix} \mathrm{d}\theta \\ \mathrm{d}\pi \\ \mathrm{d}\sigma \\ \mathrm{d}\tau \end{Bmatrix}$$

where $\partial_{\theta\pi}\mathcal{G} = \partial_{\pi\theta}\mathcal{G}$ from Maxwell's constraint, then incorporating material property definitions put forward in Eq. 70 into the above differential equation gives

$$\begin{Bmatrix} \mathrm{d}\eta \\ \mathrm{d}\xi \\ \mathrm{d}\varepsilon \\ \mathrm{d}\gamma \end{Bmatrix} = \begin{bmatrix} C_t & \alpha_t/\rho\theta & 0 & 0 \\ \alpha_t & 1/4M_t & 0 & 0 \\ 0 & 0 & 1/2N_t & 0 \\ 0 & 0 & 0 & 1/G_t \end{bmatrix} \begin{Bmatrix} \theta^{-1}\,\mathrm{d}\theta \\ \mathrm{d}\pi \\ \mathrm{d}\sigma \\ \mathrm{d}\tau \end{Bmatrix}$$

where gradients $\partial\eta/\partial\theta$, $\partial\xi/\partial\theta$, and $\partial\pi/\partial\xi$ relate to the material properties through $\partial_{\theta\theta}\mathcal{G} = \partial\eta/\partial\theta$, $\rho\,\partial_{\pi\theta}\mathcal{G} = \partial\xi/\partial\theta = \rho\,\partial_{\theta\pi}\mathcal{G}$, and $\rho\,\partial_{\pi\pi}\mathcal{G} = \partial\xi/\partial\pi = (\partial\pi/\partial\xi)^{-1}$. The upper-left 2×2 sub-matrix, which describes the uniform contribution to a response, can be rearranged to read as

$$\begin{Bmatrix} \mathrm{d}\eta \\ \mathrm{d}\pi \end{Bmatrix} = \begin{bmatrix} C_t - 4\alpha_t^2 M/\rho\theta & 4\alpha_t M/\rho\theta \\ -4\alpha_t M & 4M \end{bmatrix} \begin{Bmatrix} \theta^{-1}\,\mathrm{d}\theta \\ \mathrm{d}\xi \end{Bmatrix} \tag{71a}$$

where $M = M_t(\theta, \xi, \pi)$, while the non-uniform or shear response of Eq. 69b is given quite simply by

$$\begin{Bmatrix} \mathrm{d}\sigma \\ \mathrm{d}\tau \end{Bmatrix} = \begin{bmatrix} 2N & 0 \\ 0 & G \end{bmatrix} \begin{Bmatrix} \mathrm{d}\varepsilon \\ \mathrm{d}\gamma \end{Bmatrix} \tag{71b}$$

where $N = N_t(\varepsilon, \sigma)$ and $G = G_t(\gamma, \tau)$. Collectively, moduli M_t, N_t, and G_t describe the tangent mechanical response of a thermoelastic membrane. These moduli can depend upon both stress and strain, in accordance with the implicit theory of elasticity presented in the Appendix.

4.2.3.1 The Poisson Effect

The areal modulus M_t is ideally determined from an equibiaxial experiment. Assuming knowledge of its value, then given the following definition for an areal

Poisson's ratio

$$\nu := -\frac{\mathrm{d}b/b}{\mathrm{d}a/a},$$

it immediately follows that the squeeze modulus N_t can be determined from an uniaxial experiment where traction is applied along that axis from which elongation a is measured; specifically,

$$N_t = 2M_t\,\frac{1-\nu}{1+\nu} \quad \text{given that} \quad \mathcal{S}_{11} \neq 0 \quad \text{and} \quad \mathcal{S}_{21} = \mathcal{S}_{22} = 0,$$

provided that the temperature θ is held constant. Consequently, $\frac{2}{3}M_t \leqslant N_t \leqslant 2M_t$ follows whenever $0 \leqslant \nu \leqslant 1/2$, so the squeeze modulus N_t is observed to play an analogous role as the shear modulus μ does in the classical theory of elasticity.

If one were to consider such a membrane as having an uniform thickness h varying with deformation to preserve volume, then $\nu = 1/2$ and Eq. 71b becomes

$$\begin{Bmatrix} \mathrm{d}\sigma \\ \mathrm{d}\tau \end{Bmatrix} = \begin{bmatrix} 4M_t/3 & 0 \\ 0 & G_t \end{bmatrix} \begin{Bmatrix} \mathrm{d}\varepsilon \\ \mathrm{d}\gamma \end{Bmatrix} \tag{71c}$$

which is a useful result, as now there are just two moduli needed to establish through experiments, viz., M_t and G_t. This result is independent of any assumed functional form for these material parameters.

Note: The conjugate pair approach presented here allows for a distinct shear modulus G that can take on any positive value. This is important because shear experiments done on soft tissues, which, unfortunately, are few in number, tend to produce shear moduli that are many orders in magnitude smaller than their bulk moduli, e.g., in parenchyma their ratio is $K/G \approx 10^4$ (150 MPa vs. 10–54 kPa).[84] Classically, such a result has been used to argue that a material can be modeled, to a reasonable approximation, as being ideally incompressible, with the consequence being that $G \ll K$. In the conjugate pair approach, incompressibility of a planar membrane response implicates that Eq. 71c describes their non-uniform response. The idea of modeling parenchyma as an incompressible material is in complete opposition with its true physiologic nature; however, it is an appropriate assumption when modeling the alveolar membranes that make up parenchyma at the microscopic level. In classical theory, incompressibility constrains its shear modulus G. In the conjugate pair theory, incompressibility constrains its squeeze modulus N.[8,9,55,56,65,66,73] The shear

modulus in the conjugate pair theory has no counterpart in the classical theory.

4.3 Green Thermoelastic Solids: Non-Uniform Motions

The First and Second Laws of Thermodynamics governing a reversible adiabatic process done on a 3D body result in the formula $\mathrm{d}U = \theta\,\mathrm{d}\eta + \frac{1}{\rho}\,\mathrm{d}W$, where $\mathrm{d}W$ is the mechanical power expended by stressing a body with a mass density of ρ; specifically,[55,65,66]

$$\begin{aligned}\mathrm{d}W &= \mathrm{tr}\left(\begin{bmatrix}\mathcal{S}_{11} & \mathcal{S}_{12} & \mathcal{S}_{13}\\ \mathcal{S}_{21} & \mathcal{S}_{22} & \mathcal{S}_{23}\\ \mathcal{S}_{31} & \mathcal{S}_{32} & \mathcal{S}_{33}\end{bmatrix}\begin{bmatrix}a^{-1}\,\mathrm{d}a & (a/b)\,\mathrm{d}\gamma & (a/c)(\mathrm{d}\beta-\alpha\,\mathrm{d}\gamma)\\ 0 & b^{-1}\,\mathrm{d}b & (b/c)\,\mathrm{d}\alpha\\ 0 & 0 & c^{-1}\,\mathrm{d}c\end{bmatrix}\right)\\ &= \Pi\,\mathrm{d}\Xi + \sum_{i=1}^{3}\left(\sigma_i\,\mathrm{d}\varepsilon_i + \tau_i\,\mathrm{d}\gamma_i\right),\end{aligned} \tag{72a}$$

which is subject to constraints $\sigma_3 = -(\sigma_1+\sigma_2)$ and $\mathrm{d}\varepsilon_3 = -(\mathrm{d}\varepsilon_1+\mathrm{d}\varepsilon_2)$. Consequently, six of the seven conjugate pairs in this formulation are independent, as one ought to expect. Stress components $\mathcal{S}_{ij}$ can be either rotated into the Kirchhoff stress of an Eulerian frame, or they can be pulled back into the second Piola–Kirchhoff stress of a Lagrangian frame.

The above expression conjectures that the thermodynamics of a 3D elastic solid contained within the confines of an adiabatic enclosure can be described by the Pfaffian equation

$$\mathrm{d}U = \theta\,\mathrm{d}\eta + \frac{1}{\rho}\left(\Pi\,\mathrm{d}\Xi + \sum_{i=1}^{2}\sigma_i\,\mathrm{d}\varepsilon_i + (\sigma_1+\sigma_2)(\mathrm{d}\varepsilon_1+\mathrm{d}\varepsilon_2) + \sum_{i=1}^{3}\tau_i\,\mathrm{d}\gamma_i\right), \tag{72b}$$

where stresses $\{\Pi, \sigma_1, \sigma_2, \tau_1, \tau_2, \tau_3\}$ describe a set of independent, scalar-valued, intensive variables, and where strains $\{\Xi, \varepsilon_1, \varepsilon_2, \gamma_1, \gamma_2, \gamma_3\}$ describe a set of independent, scalar-valued, extensive variables. This contrasts with the classic approach where the work done decomposes into a scalar-valued isotropic part and a tensor-valued deviatoric part. A direct consequence of adopting a triangular construction for strain rate is that the pure- and simple-shear contributions of a deviatoric response can be further separated into independent scalar contributions that are nearly orthogonal to one another; whereas, they remain coupled into one tensor field whenever a symmetric construction for strain rate is adopted, which is standard practice

today. The above thermodynamic strains are defined in Section 3.4.2, while their conjugate stresses and how they relate to commonly used stress tensors is discussed later.

4.3.1 Constitutive Equations

Because a change in the internal energy $\mathrm{d}U$ governing a reversible adiabatic process is described by an exact differential,[74] with $U(\eta, \Xi, \varepsilon_1, \varepsilon_2, \gamma_1, \gamma_2, \gamma_3)$ in three space, it necessarily follows that a constitutive response for a Green thermoelastic solid is governed by a constitutive equation for temperature[73]

$$\theta = \partial_\eta U(\eta, \Xi, \varepsilon_1, \varepsilon_2, \gamma_1, \gamma_2, \gamma_3), \tag{73a}$$

a constitutive equation for pressure

$$\Pi = \rho\, \partial_\Xi U(\eta, \Xi, \varepsilon_1, \varepsilon_2, \gamma_1, \gamma_2, \gamma_3), \tag{73b}$$

two constitutive equations for the normal-stress differences

$$\begin{Bmatrix} \sigma_1 \\ \sigma_2 \end{Bmatrix} = \frac{1}{3} \begin{bmatrix} 2 & -1 \\ -1 & 2 \end{bmatrix} \begin{Bmatrix} \rho\, \partial_{\varepsilon_1} U(\eta, \Xi, \varepsilon_1, \varepsilon_2, \gamma_1, \gamma_2, \gamma_3) \\ \rho\, \partial_{\varepsilon_2} U(\eta, \Xi, \varepsilon_1, \varepsilon_2, \gamma_1, \gamma_2, \gamma_3) \end{Bmatrix}, \tag{73c}$$

and three constitutive equations for the shear stresses

$$\tau_1 = \rho\, \partial_{\gamma_1} U(\eta, \Xi, \varepsilon_1, \varepsilon_2, \gamma_1, \gamma_2, \gamma_3), \tag{73d}$$

$$\tau_2 = \rho\, \partial_{\gamma_2} U(\eta, \Xi, \varepsilon_1, \varepsilon_2, \gamma_1, \gamma_2, \gamma_3), \tag{73e}$$

$$\tau_3 = \rho\, \partial_{\gamma_3} U(\eta, \Xi, \varepsilon_1, \varepsilon_2, \gamma_1, \gamma_2, \gamma_3), \tag{73f}$$

where the coupled expressions for the two squeeze stresses in Eq. 73c arise from the energetic contribution

$$\partial_{\varepsilon_1} U\, \mathrm{d}\varepsilon_1 + \partial_{\varepsilon_2} U\, \mathrm{d}\varepsilon_2 = \sigma_1\, \mathrm{d}\varepsilon_1 + \sigma_2\, \mathrm{d}\varepsilon_2 + (\sigma_1 + \sigma_2)(\mathrm{d}\varepsilon_1 + \mathrm{d}\varepsilon_2)$$

that incorporates constraints $\sigma_3 = -(\sigma_1 + \sigma_2)$ and $\mathrm{d}\varepsilon_3 = -(\mathrm{d}\varepsilon_1 + \mathrm{d}\varepsilon_2)$ into the work done, viz., $\sigma_3\, \mathrm{d}\varepsilon_3$ does work, and as such, conjugate pair $(\sigma_3, \varepsilon_3)$ has an influence on constitutive response, even though they are not independent variables.

Considering each, independent, intensive variable, i.e., θ, Π, σ_1, σ_2, τ_1, τ_2, τ_3, to be at least a C^1 function of each, independent, extensive variable, viz., η, Ξ, ε_1,

ε_2, γ_1, γ_2, γ_3, then the internal energy U will be at least a C^2 function of state, and therefore the constitutive expressions of Eq. 73 can be recast into the following system of differential equations:

$$\begin{Bmatrix} \mathrm{d}\theta \\ \mathrm{d}\Pi \\ \mathrm{d}\sigma_1 \\ \mathrm{d}\sigma_2 \\ \mathrm{d}\tau_1 \\ \mathrm{d}\tau_2 \\ \mathrm{d}\tau_3 \end{Bmatrix} = \begin{bmatrix} \partial_{\eta\eta}U & \partial_{\eta\Xi}U & \partial_{\eta\varepsilon_1}U & \partial_{\eta\varepsilon_2}U & \partial_{\eta\gamma_1}U & \partial_{\eta\gamma_2}U & \partial_{\eta\gamma_3}U \\ \rho\,\partial_{\Xi\eta}U & \rho\,\partial_{\Xi\Xi}U & \rho\,\partial_{\Xi\varepsilon 1}U & \rho\,\partial_{\Xi\varepsilon 2}U & \rho\,\partial_{\Xi\gamma_1}U & \rho\,\partial_{\Xi\gamma_2}U & \rho\,\partial_{\Xi\gamma_3}U \\ \rho\,M_{1\eta} & \rho\,M_{1\Xi} & \rho\,M_{1\varepsilon_1} & \rho\,M_{1\varepsilon_2} & \rho\,M_{1\gamma_1} & \rho\,M_{1\gamma_2} & \rho\,M_{1\gamma_3} \\ \rho\,M_{2\eta} & \rho\,M_{2\Xi} & \rho\,M_{2\varepsilon_1} & \rho\,M_{2\varepsilon_2} & \rho\,M_{2\gamma_1} & \rho\,M_{2\gamma_2} & \rho\,M_{2\gamma_3} \\ \rho\,\partial_{\gamma_1\eta}U & \rho\,\partial_{\gamma_1\Xi}U & \rho\,\partial_{\gamma_1\varepsilon_1}U & \rho\,\partial_{\gamma_1\varepsilon_2}U & \rho\,\partial_{\gamma_1\gamma_1}U & \rho\,\partial_{\gamma_1\gamma_2}U & \rho\,\partial_{\gamma_1\gamma_3}U \\ \rho\,\partial_{\gamma_2\eta}U & \rho\,\partial_{\gamma_2\Xi}U & \rho\,\partial_{\gamma_2\varepsilon_1}U & \rho\,\partial_{\gamma_2\varepsilon_2}U & \rho\,\partial_{\gamma_2\gamma_1}U & \rho\,\partial_{\gamma_2\gamma_2}U & \rho\,\partial_{\gamma_2\gamma_3}U \\ \rho\,\partial_{\gamma_3\eta}U & \rho\,\partial_{\gamma_3\Xi}U & \rho\,\partial_{\gamma_3\varepsilon_1}U & \rho\,\partial_{\gamma_3\varepsilon_2}U & \rho\,\partial_{\gamma_3\gamma_1}U & \rho\,\partial_{\gamma_3\gamma_2}U & \rho\,\partial_{\gamma_3\gamma_3}U \end{bmatrix} \begin{Bmatrix} \mathrm{d}\eta \\ \mathrm{d}\Xi \\ \mathrm{d}\varepsilon_1 \\ \mathrm{d}\varepsilon_2 \\ \mathrm{d}\gamma_1 \\ \mathrm{d}\gamma_2 \\ \mathrm{d}\gamma_3 \end{Bmatrix} \tag{74}$$

whose upper-left 2×2 sub-matrix also appears in Eq. 59c, which governs the uniform contribution of a response. The squeeze response of Eq. 73c associates with tangent moduli that are defined accordingly

$$M_{1\eta} = \tfrac{1}{3}\big(2\partial_{\varepsilon_1\eta}U - \partial_{\varepsilon_2\eta}U\big) \qquad M_{2\eta} = \tfrac{1}{3}\big(2\partial_{\varepsilon_2\eta}U - \partial_{\varepsilon_1\eta}U\big) \tag{75a}$$

$$M_{1\Xi} = \tfrac{1}{3}\big(2\partial_{\varepsilon_1\Xi}U - \partial_{\varepsilon_2\Xi}U\big) \qquad M_{2\Xi} = \tfrac{1}{3}\big(2\partial_{\varepsilon_2\Xi}U - \partial_{\varepsilon_1\Xi}U\big) \tag{75b}$$

$$M_{1\varepsilon_1} = \tfrac{1}{3}\big(2\partial_{\varepsilon_1\varepsilon_1}U - \partial_{\varepsilon_2\varepsilon_1}U\big) \qquad M_{2\varepsilon_1} = \tfrac{1}{3}\big(2\partial_{\varepsilon_2\varepsilon_1}U - \partial_{\varepsilon_1\varepsilon_1}U\big) \tag{75c}$$

$$M_{1\varepsilon_2} = \tfrac{1}{3}\big(2\partial_{\varepsilon_1\varepsilon_2}U - \partial_{\varepsilon_2\varepsilon_2}U\big) \qquad M_{2\varepsilon_2} = \tfrac{1}{3}\big(2\partial_{\varepsilon_2\varepsilon_2}U - \partial_{\varepsilon_1\varepsilon_2}U\big) \tag{75d}$$

$$M_{1\gamma_1} = \tfrac{1}{3}\big(2\partial_{\varepsilon_1\gamma_1}U - \partial_{\varepsilon_2\gamma_1}U\big) \qquad M_{2\gamma_1} = \tfrac{1}{3}\big(2\partial_{\varepsilon_2\gamma_1}U - \partial_{\varepsilon_1\gamma_1}U\big) \tag{75e}$$

$$M_{1\gamma_2} = \tfrac{1}{3}\big(2\partial_{\varepsilon_1\gamma_2}U - \partial_{\varepsilon_2\gamma_2}U\big) \qquad M_{2\gamma_2} = \tfrac{1}{3}\big(2\partial_{\varepsilon_2\gamma_2}U - \partial_{\varepsilon_1\gamma_2}U\big) \tag{75f}$$

$$M_{1\gamma_3} = \tfrac{1}{3}\big(2\partial_{\varepsilon_1\gamma_3}U - \partial_{\varepsilon_2\gamma_3}U\big) \qquad M_{2\gamma_3} = \tfrac{1}{3}\big(2\partial_{\varepsilon_2\gamma_3}U - \partial_{\varepsilon_1\gamma_3}U\big) \tag{75g}$$

so that, collectively, Eqs. 74 and 75 describe the full non-uniform response permissible by a Green thermoelastic solid expressed as a hypo-elastic material undergoing an adiabatic process.

As in the case of membranes, it is reasonable to assume that the presence of a non-uniform motion will not cause an uniform response. For our application, it is also reasonable to assume that there is no coupling between the modes of squeeze and shear.* Furthermore, it is assumed that there is no coupling betwixt the two independent squeeze modes, nor between the three independent shear modes. Consequently, all mixed partial derivatives that associate with a non-uniform response

*The Poynting effect is a second-order effect that couples squeeze and shear.[66] It is assumed that such a coupling does not play a contributing role in the current application, and can therefore be neglected.

are taken to be zero, and therefore Eqs. 74 and 75 simplify to

$$
\begin{aligned}
&\begin{Bmatrix} \mathrm{d}\theta & \mathrm{d}\Pi & \mathrm{d}\sigma_1 & \mathrm{d}\sigma_2 & \mathrm{d}\tau_1 & \mathrm{d}\tau_2 & \mathrm{d}\tau_3 \end{Bmatrix}^{\mathsf{T}} \\
&= \begin{bmatrix}
\partial_{\eta\eta}U & \partial_{\eta\Xi}U & 0 & 0 & 0 & 0 & 0 \\
\rho\,\partial_{\Xi\eta}U & \rho\,\partial_{\Xi\Xi}U & 0 & 0 & 0 & 0 & 0 \\
0 & 0 & \rho\frac{2}{3}\partial_{\varepsilon_1\varepsilon_1}U & -\rho\frac{1}{3}\partial_{\varepsilon_2\varepsilon_2}U & 0 & 0 & 0 \\
0 & 0 & -\rho\frac{1}{3}\partial_{\varepsilon_1\varepsilon_1}U & \rho\frac{2}{3}\partial_{\varepsilon_2\varepsilon_2}U & 0 & 0 & 0 \\
0 & 0 & 0 & 0 & \rho\,\partial_{\gamma_1\gamma_1}U & 0 & 0 \\
0 & 0 & 0 & 0 & 0 & \rho\,\partial_{\gamma_2\gamma_2}U & 0 \\
0 & 0 & 0 & 0 & 0 & 0 & \rho\,\partial_{\gamma_3\gamma_3}U
\end{bmatrix}
\begin{Bmatrix} \mathrm{d}\eta \\ \mathrm{d}\Xi \\ \mathrm{d}\varepsilon_1 \\ \mathrm{d}\varepsilon_2 \\ \mathrm{d}\gamma_1 \\ \mathrm{d}\gamma_2 \\ \mathrm{d}\gamma_3 \end{Bmatrix}
\end{aligned}
$$

where what may appear as being a coupling between $\mathrm{d}\sigma_1$ and $\mathrm{d}\sigma_2$ is actually a consequence arising from the two constraint equations $\mathrm{d}\sigma_3 = -(\mathrm{d}\sigma_1 + \mathrm{d}\sigma_2)$ and $\mathrm{d}\varepsilon_3 = -(\mathrm{d}\varepsilon_1 + \mathrm{d}\varepsilon_2)$.

The above system of equations can be rewritten as three independent systems of differential equations; specifically, the first differential matrix equation is

$$
\begin{Bmatrix} \mathrm{d}\theta \\ \mathrm{d}\Pi \end{Bmatrix} = \begin{bmatrix} \partial_{\eta\eta}U & \partial_{\eta\Xi}U \\ \rho\,\partial_{\Xi\eta}U & \rho\,\partial_{\Xi\Xi}U \end{bmatrix} \begin{Bmatrix} \mathrm{d}\eta \\ \mathrm{d}\Xi \end{Bmatrix}
$$

that when rewritten in terms of Helmholz state variables becomes

$$
\begin{Bmatrix} \mathrm{d}\eta \\ \mathrm{d}\Pi \end{Bmatrix} = \begin{bmatrix} \theta/\partial_{\eta\eta}U & -\partial_{\eta\Xi}U/\partial_{\eta\eta}U \\ \rho\theta\,\partial_{\Xi\eta}U/\partial_{\eta\eta}U & \rho\big(\partial_{\Xi\Xi}U - \partial_{\Xi\eta}U\cdot\partial_{\eta\Xi}U/\partial_{\eta\eta}U\big) \end{bmatrix} \begin{Bmatrix} \theta^{-1}\,\mathrm{d}\theta \\ \mathrm{d}\Xi \end{Bmatrix} \tag{76a}
$$

recalling that $\mathrm{d}\Xi = \frac{1}{3}V^{-1}\,\mathrm{d}V$, plus a full matrix equation that governs the squeeze response

$$
\begin{Bmatrix} \mathrm{d}\sigma_1 \\ \mathrm{d}\sigma_2 \end{Bmatrix} = \frac{\rho}{3}\begin{bmatrix} 2\,\partial_{\varepsilon_1\varepsilon_1}U & -\partial_{\varepsilon_2\varepsilon_2}U \\ -\partial_{\varepsilon_1\varepsilon_1}U & 2\,\partial_{\varepsilon_2\varepsilon_2}U \end{bmatrix} \begin{Bmatrix} \mathrm{d}\varepsilon_1 \\ \mathrm{d}\varepsilon_2 \end{Bmatrix} \tag{76b}
$$

and a diagonal matrix equation that governs the shear response

$$
\begin{Bmatrix} \mathrm{d}\tau_1 \\ \mathrm{d}\tau_2 \\ \mathrm{d}\tau_3 \end{Bmatrix} = \rho\begin{bmatrix} \partial_{\gamma_1\gamma_1}U & 0 & 0 \\ 0 & \partial_{\gamma_2\gamma_2}U & 0 \\ 0 & 0 & \partial_{\gamma_3\gamma_3}U \end{bmatrix} \begin{Bmatrix} \mathrm{d}\gamma_1 \\ \mathrm{d}\gamma_2 \\ \mathrm{d}\gamma_3 \end{Bmatrix} \tag{76c}
$$

to which we now seek an interpretation when expressed in terms of a set of specified material properties.

4.3.2 Material Properties

The material model put forward here is for a general thermoelastic solid with mass density ρ that has, at most, 8 material properties/functions: a specific heat C_t and a lineal thermal strain coefficient α_t, both evaluated at constant pressure, a bulk modulus K_t evaluated at constant temperature, two squeeze moduli N_1 and N_2 evaluated at constant shear, and three shear moduli G_1, G_2, and G_3 evaluated at constant squeeze. The specific heat C_t density is defined as

$$C_t := \left.\frac{\mathrm{d}\eta}{\theta^{-1}\,\mathrm{d}\theta}\right|_P = \left.\frac{\mathrm{d}\eta}{\theta^{-1}\,\mathrm{d}\theta}\right|_\Pi , \tag{77a}$$

where θ is temperature, η is entropy density, and $\Pi := \mathcal{S}_{11} + \mathcal{S}_{22} + \mathcal{S}_{33} =: -3P$ is a negative pressure. The lineal thermal strain coefficient α_t is defined as

$$\alpha_t := \left.\frac{L^{-1}\,\mathrm{d}L}{\theta^{-1}\,\mathrm{d}\theta}\right|_P = \frac{1}{3}\left.\frac{V^{-1}\,\mathrm{d}V}{\theta^{-1}\,\mathrm{d}\theta}\right|_P = \left.\frac{\mathrm{d}\Xi}{\theta^{-1}\,\mathrm{d}\theta}\right|_\Pi , \tag{77b}$$

where $V = abc$ denotes a relative volume with $\Xi = \ln\sqrt[3]{V/V_0}$ being volumetric strain, a.k.a. dilatation. **Note**: The above definition for thermal strain, which is dimensionless, is *not* equivalent to the coefficient for thermal expansion commonly used in mechanics, which has units of reciprocal temperature, cf. the Appendix. The associated bulk modulus K_t is defined as

$$K_t := -\left.\frac{\mathrm{d}P}{V^{-1}\,\mathrm{d}V}\right|_\theta = \frac{1}{9}\left.\frac{\mathrm{d}\Pi}{\mathrm{d}\Xi}\right|_\theta , \tag{77c}$$

that together with C_t and α_t describe the uniform response. Considering transpulmonary pressure $P < 0$ under normal physiologic conditions; so $\Pi > 0$, not $P < 0$, is the more intuitive measure for working with the trace of stress when describing transpulmonary pressure.

The non-uniform response is described in terms of two in-plane squeeze moduli N_1 and N_2 that are defined as

$$N_1 := \left.\frac{\mathrm{d}(\mathcal{S}_{11} - \mathcal{S}_{22})}{\Gamma_1^{-1}\,\mathrm{d}\Gamma_1}\right|_{\Gamma_2} = \frac{1}{3}\left.\frac{\mathrm{d}\sigma_1}{\mathrm{d}\varepsilon_1}\right|_{\varepsilon_2} , \tag{77d}$$

$$N_2 := \left.\frac{\mathrm{d}(\mathcal{S}_{22} - \mathcal{S}_{33})}{\Gamma_2^{-1}\,\mathrm{d}\Gamma_2}\right|_{\Gamma_1} = \frac{1}{3}\left.\frac{\mathrm{d}\sigma_2}{\mathrm{d}\varepsilon_2}\right|_{\varepsilon_1} , \tag{77e}$$

where $\sigma_1 \coloneqq \mathcal{S}_{11} - \mathcal{S}_{22}$ and $\sigma_2 \coloneqq \mathcal{S}_{22} - \mathcal{S}_{33}$ are commonly referred to as the first and second normal-stress differences, respectively, in the polymers literature, with $\Gamma_1 \coloneqq a/b$ and $\Gamma_2 \coloneqq b/c$ being their conjugate squeeze stretches, and with $\varepsilon_1 = \ln \sqrt[3]{\Gamma_1/\Gamma_{0\,1}}$ and $\varepsilon_2 = \ln \sqrt[3]{\Gamma_2/\Gamma_{0\,2}}$ being their conjugate squeeze strains. Finally, there are three in-plane shear moduli G_1, G_2, and G_3 that are defined as

$$G_1 \coloneqq \Gamma_2 \left.\frac{\mathrm{d}\mathcal{S}_{32}}{\mathrm{d}\gamma_1}\right|_{\Gamma_2}, \tag{77f}$$

$$G_2 \coloneqq \Gamma_1\Gamma_2 \left.\frac{\mathrm{d}\mathcal{S}_{31}}{\mathrm{d}\gamma_2}\right|_{\Gamma_1\Gamma_2}, \tag{77g}$$

$$G_3 \coloneqq \Gamma_1 \left.\frac{\mathrm{d}\mathcal{S}_{21}}{\mathrm{d}\gamma_3}\right|_{\Gamma_1,\gamma_1,\tau_2}, \tag{77h}$$

where $\tau_1 \coloneqq \Gamma_2\mathcal{S}_{32}$, $\tau_2 \coloneqq \Gamma_1\Gamma_2\mathcal{S}_{31}$, and $\tau_3 \coloneqq \Gamma_1\mathcal{S}_{21} - \alpha\tau_2$ quantify the three shear stresses, with $\gamma_1 \coloneqq \alpha - \alpha_0$, $\gamma_2 \coloneqq \beta - \beta_0$, and $\gamma_3 \coloneqq \gamma - \gamma_0$ being their respective shear strains.

A material is said to be "isotropic" in our constitutive framework if its squeeze moduli can be described via a single material function, i.e., $N_1 = N_t(\sigma_1, \varepsilon_1)$ and $N_2 = N_t(\sigma_2, \varepsilon_2)$, and if its shear moduli can be described via a single material function, viz., $G_1 = G_t(\tau_1, \gamma_1)$, $G_2 = G_t(\tau_2, \gamma_2)$, and $G_3 = G_t(\tau_3, \gamma_3)$. In other words, the two squeeze response curves may have different tangents at any given moment, but these tangents are evaluated from the same material function for squeeze. A like statement applies to shear. In this regard, parenchyma is isotropic. An isotropic thermoelastic solid, in our approach, is characterized by its mass density ρ along with five, tangent, material properties: C_t, α_t, K_t, N_t, and G_t where subscript t denotes that these are tangent properties (vs. secant properties, which are discussed in the Appendix). This notion of isotropy is different from that of classical theory, where only four material properties apply: a specific heat, a coefficient for thermal expansion, a bulk modulus, and a shear modulus.

4.3.3 Constitutive Equations Governing a Thermoelastic Solid

In terms of the material properties put forward in Eq. 77, the uniform response of the thermoelastic solid given in Eq. 76a takes on the form of

$$\begin{Bmatrix} \mathrm{d}\eta \\ \mathrm{d}\Pi \end{Bmatrix} = \begin{bmatrix} C_t - 9\alpha^2 K/\rho\theta & 9\alpha K/\rho\theta \\ -9\alpha K & 9K \end{bmatrix} \begin{Bmatrix} \theta^{-1}\mathrm{d}\theta \\ \mathrm{d}\Xi \end{Bmatrix}, \quad \begin{matrix} \alpha = \alpha_t \\ K = K_t(\theta, \Pi, \Xi) \end{matrix} \tag{78a}$$

while the non-uniform squeeze response is described by

$$\begin{Bmatrix} \mathrm{d}\sigma_1 \\ \mathrm{d}\sigma_2 \end{Bmatrix} = \frac{3}{2} \begin{bmatrix} 2N_1 & -N_2 \\ -N_1 & 2N_2 \end{bmatrix} \begin{Bmatrix} \mathrm{d}\varepsilon_1 \\ \mathrm{d}\varepsilon_2 \end{Bmatrix}, \qquad \begin{aligned} N_1 &= N_t(\sigma_1, \varepsilon_1) \\ N_2 &= N_t(\sigma_2, \varepsilon_2) \end{aligned} \tag{78b}$$

and the non-uniform shear response is described by

$$\begin{Bmatrix} \mathrm{d}\tau_1 \\ \mathrm{d}\tau_2 \\ \mathrm{d}\tau_3 \end{Bmatrix} = \begin{bmatrix} G_1 & 0 & 0 \\ 0 & G_2 & 0 \\ 0 & 0 & G_3 \end{bmatrix} \begin{Bmatrix} \mathrm{d}\gamma_1 \\ \mathrm{d}\gamma_2 \\ \mathrm{d}\gamma_3 \end{Bmatrix}, \qquad \begin{aligned} G_1 &= G_t(\tau_1, \gamma_1) \\ G_2 &= G_t(\tau_2, \gamma_2) \\ G_3 &= G_t(\tau_3, \gamma_3) \end{aligned} \tag{78c}$$

which is the general form for a thermoelastic solid that we shall use going forward. These moduli are expressed as depending upon both stress and strain, in accordance with the implicit theory of elasticity presented in the Appendix.

4.3.3.1 The Poisson Effect

Assuming that the bulk modulus K_t is known, then the squeeze modulus N_t for an isotropic material can be determined from a single uniaxial experiment by measuring its Poisson response via

$$\nu := -\frac{\mathrm{d}b/b}{\mathrm{d}a/a} = -\frac{\mathrm{d}c/c}{\mathrm{d}a/a},$$

from which it follows that

$$N_t = 3K_t \frac{1-2\nu}{1+\nu} \quad \text{provided that} \quad \mathcal{S}_{11} \neq 0 \quad \text{and} \quad \mathcal{S}_{22} = \mathcal{S}_{33} = 0,$$

where temperature θ has been held constant. Consequently, $N_t = 2\mu$ where μ is the shear modulus from the classical theory of elasticity. On the other hand, our shear modulus G_t is distinct from the shear modulus μ employed by the classical theory of elasticity where strains and rotations are infinitesimal in extent—an assumption not imposed by our approach.

4.4 Modeling an Alveolus

To facilitate the numerical implementation of our models and interpretations of their results by engineers and scientists who will use our framework, this section converts all fields defined in 1D and 2D into their 3D analogs; specifically, forces and surface tensions are converted into stresses, all moduli will now have units of

stress, all thermal strain coefficients associate with linear expansions, and all mass densities relate mass to volume.

Only one-third of the cross-sectional area of an alveolar chord, and only one-half of the wall thickness of an alveolar septum associate with any given dodecahedron.[43] Specifically, a third of the total force carried by a septal fiber belongs with the given alveolus, with the remaining two-thirds of the transmitted force belonging to its two adjoining alveoli. Likewise, only half of the surface traction carried along a septal membrane belongs with the given alveolus, with the other half of its surface traction belonging to its adjacent alveoli. Like statements apply for their entropies.

About 75% of the acting transpulmonary pressure (the difference between pleural and alveolar pressures) is carried by the alveolar structure, with the remaining 25% being carried by the pleural membrane encasing the lung.[85]

4.4.1 Constraints/Assumptions for Alveoli Subjected to Shock Waves

Because the primary purpose for the alveolar model being constructed here is to better understand alveolar behavior as a shock wave passes over it, there are certain assumptions that we impose upon our model that under normal or different physiologic conditions might otherwise not apply.

First: An alveolus is considered to be an adiabatic pressure vessel in which air and heat cannot move into or out of as a shock wave passes over it, simply because the wave speed is too fast. There is insufficient time for these transport phenomena to occur. This relates to the "closed-cell" approximation used by Clayton *et al.*[7,9,11] in the dynamic loading of their continuum model for parenchyma.

Second: Tissues that compose lung are viscoelastic[34,86] mixtures of collagen, elastin, cells, and the ground substance.[30,78] Whenever a lung is subjected to a shock wave, there is insufficient time for the viscous characteristics in a viscoelastic response to manifest themselves; hence, the overall response is modeled as glassy elastic.[7,9,11]

Third: Even though one could construct a mixture theory for the modeling of alveolar membranes, like we do for alveolar chords, it would be challenging to establish their boundary conditions, nor would we be able to construct the necessary experiments to parameterize them. Consequently, an isotropic, elastic, homogeneous continuum is assumed for modeling the planar septa.

Fourth: Temperature remains continuous in a jump across the kinematic discontinuity caused by a shock wave traveling through a compressible gas.[87] As such, temperature is expected to be continuous across the spatial discontinuity of a shock wave traveling through parenchyma, too. Nevertheless, temperature is expected to change both in front of and behind a traveling wave, where the alveolar sac first compresses and then expands. Throughout this excursion, the overall process is considered to be adiabatic, in accordance with the first assumption. Furthermore, because temperature changes are expected to be small, and wave speeds are fast, the finite element models being developed here assume temperature remains constant. Continuum modeling[7,9,11] suggests that the constant temperature assumption for dynamic lung compression is not severe.

Fifth: The air/membrane interface of an alveolus is lined with a surfactant, which is a thin bi-lipid film that has a significant role to play during normal lung function. This film reduces alveolar surface tension to help advert total lung collapse at maximum exhale.[88] Even so, some alveoli still collapse, getting re-recruited during a later breath. Models have been proposed for both surfactant[89] and alveolar recruitment,[90] but these effects are not included here as they are not thought to play a significant role in lung mechanics when a lung becomes subjected to a shock wave. Instead, surface tension is assigned a prestress to effectively account for this physiologic condition.

Sixth: Matsuda *et al*.[91] found the diameters of collagen and elastin fibers that circumscribe an alveolar mouth to be about 5–7 times larger than those of their septal chords. The alveolar mouth, with its thicker fibers and open face that attach an alveolus to an alveolar duct, is modeled here as a phantom face, viz., with fibers sized like any of the other 11 pentagonal elements composing a dodecahedron, and a twelfth phantom face placed where an alveolar mouth would otherwise reside.[25] Kimmel and Budiansky supported this conjecture via a private communication they had with Prof TA Wilson, after which Kimmel and Budiansky wrote:[45]

> "Professor TA Wilson notes that the present model does not take explicit account of either alveolar openings or their fibrous boundaries. Wilson suggests that the elastic resistance of the ring boundaries tends to make up for the missing surface tension in the holes, so that neglect of both effects may be self-compensating."

Table 4 Mean and standard deviations in variance for the square root of septal chord diameters $\sqrt{D}$ reported by Sobin *et al*.[54] These septal chords comprise collagen and elastin fibers that act independent of one another, and therefore, they are considered to be loaded in parallel with one another.

transpulmonary pressure	$4\,\mathrm{cm\,H_2O}$		
age	15–35	36–45	> 65
collagen: $\sqrt{D},\ (\mu\mathrm{m})^{1/2}$	0.952 ± 0.242	0.958 ± 0.255	1.045 ± 0.270
elastin: $\sqrt{D},\ (\mu\mathrm{m})^{1/2}$	0.957 ± 0.239	0.970 ± 0.213	1.093 ± 0.274
transpulmonary pressure	$14\,\mathrm{cm\,H_2O}$		
age	15–35	36–45	> 65
collagen: $\sqrt{D},\ (\mu\mathrm{m})^{1/2}$	0.955 ± 0.246	0.994 ± 0.237	1.054 ± 0.279
elastin: $\sqrt{D},\ (\mu\mathrm{m})^{1/2}$	0.956 ± 0.237	0.988 ± 0.263	1.079 ± 0.281

This conjecture of Kimmel and Budiansky,[45] along with the experimental findings of Matsuda *et al*.,[91] provide a pathway by which one can scale the surface traction carried by a single alveolar membrane with that of the chords that envelope it. In other words, this provides an avenue for parameterizing the membrane model in an otherwise void of relevant experimental data needed to estimate its parameters.

Seventh: Alveolar surfaces are modeled as membranes, not plates, and therefore are assumed to have no out-of-plane bending stiffness. This is in concert with our assumption that the septal chords are modeled as rods, not beams, because of their slenderness ratio. Furthermore, these septa tend to be flat because there are roughly equal pressures acting on both sides of these membranes, thereby eliminating any curvature, which is the driving force behind out-of-plane bending[34] and, we surmise, also helps to suppress wrinkling.

4.4.2 Modeling Septal Chords Subjected to Shock Waves

Alveoli are biologic structures constructed of septal chords that circumscribe alveolar membranes that envelope an alveolar sac whereat gas exchange occurs. These chords comprise individual collagen and elastin fibers loaded in parallel.[54,91] The extent of elastic energy stored within a chord will depend upon the diameters D^c and D^e and length L of these individual fibers.* Let superscript c denote collagen,

*Sobin *et al*.[54] considered that the stored energy of chords also depends upon their curvature, which they measured and quantified, i.e., they considered these chords to be beams. However, with a slenderness ratio of $\bar{L}/\bar{D} = 102 \pm 12$, which we obtained from analyzing their data, it is reasonable to model them as rods, not beams. Consequently, the dodecahedral space truss used as an alveolar model is considered to be a pinned truss, not a rigid truss, thereby greatly simplifying the boundary value problem.

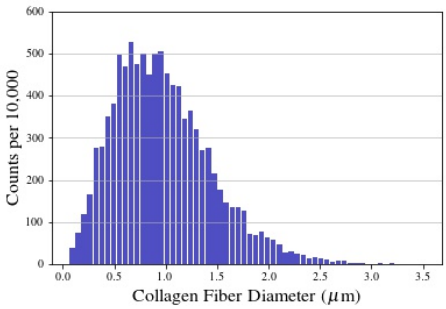

(a) Histogram for collagen chord diameters.

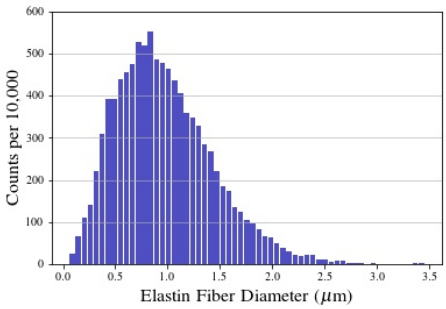

(b) Histogram for elastin chord diameters.

Fig. 28 Typical histograms for alveolar chord diameters constructed using the statistics reported in Table 4. Their tails weigh heavy at the larger diameters, because their distributions are normal in the square root of their diameters. These two histograms are virtually identical.

and superscript e denote elastin. Sobin *et al.*[54] determined that the square root of their diameters $\sqrt{D}$ distribute normally, with a mean $\bar{D}^{1/2}$ and standard deviation $\sigma_{\sqrt{D}}$ that also depend upon age and transpulmonary pressure, as presented in Table 4 and illustrated in Fig. 28.

The collagen and elastin fibers that make up a septal chord have the same length L, they experience the same strain e, and they exist at the same temperature θ; therefore, we employ Eq. 65a as the governing constitutive equation to describe their mechanical behaviors; specifically, for the collagen fiber in an alveolar chord:

$$\begin{Bmatrix} \mathrm{d}\eta^c \\ \mathrm{d}s^c \end{Bmatrix} = \begin{bmatrix} C_t^c - (\alpha_t^c)^2 E^c/\rho^c\theta & \alpha_t^c E^c/\rho^c\theta \\ -\alpha_t^c E^c & E^c \end{bmatrix} \begin{Bmatrix} \theta^{-1}\,\mathrm{d}\theta \\ L^{-1}\,\mathrm{d}L \end{Bmatrix}, \tag{79a}$$

where $E^c = E_t^c(\theta, e, s^c)$, and for the elastin fiber in an alveolar chord:

$$\begin{Bmatrix} \mathrm{d}\eta^e \\ \mathrm{d}s^e \end{Bmatrix} = \begin{bmatrix} C_t^e - (\alpha_t^e)^2 E^e/\rho^e\theta & \alpha_t^e E^e/\rho^e\theta \\ -\alpha_t^e E^e & E^e \end{bmatrix} \begin{Bmatrix} \theta^{-1}\,\mathrm{d}\theta \\ L^{-1}\,\mathrm{d}L \end{Bmatrix}, \tag{79b}$$

where $E^e = E_t^e(\theta, e, s^e)$, and where η^c and η^e are the entropy densities (erg/g.K) for collagen and elastin; $s^c := \lambda F^c/A_0^c$ and $s^e := \lambda F^e/A_0^e$ are the chordal stresses (barye = dyne/cm^2) carried by the collagen and elastin fibers, wherein $\lambda = L/L_0$ is the fiber stretch, A_0^c and A_0^e are their traction-free cross-sectional areas (cm^2), and F^c and F^e are the forces (dyne) they transmit. Parameters C_t^c and C_t^e are their specific heats at constant pressure (erg/g.K), α_t^c and α_t^e are their lineal thermal strain

coefficients, E^e and E^e are their elastic moduli (dyne/cm^2 = erg/cm^3), and ρ^c and ρ^e are their mass densities (g/cm^3). These differential equations are subject to initial conditions considered to be $s_0^c = s^c|_{L=L_0}$, $s_0^e = s^e|_{L=L_0}$, $\eta^c = \eta_0^c$, and $\eta^e = \eta_0^e$, where η_0^c and η_0^e are their respective entropy densities at rest. *In vivo*, s_0^c and s_0^e are positive valued, cf. the Appendix; whereas, *ex vivo*, s_0^c and s_0^e would be zero valued.

The actual force and entropy of an individual septal chord in our alveolar model is taken to be one third of a fiber's calculated values, as determined by Eq. 79, because each alveolar chord is typically shared between three adjoining alveoli; consequently,

$$F^f = (A_0^c s^c + A_0^e s^e)/3\lambda \quad \text{and} \quad S^f = (\rho^c V_0^c \eta^c + \rho^e V_0^e \eta^e)/3, \tag{80}$$

where F^f (dyne) is a third of the fiber's force carried by a septal chord, and S^f (erg/K) is a third of the fiber's entropy.

Collagen is a fiber comprising numerous, long, slender, wavy filaments whose waviness, known as crimp, straightens under sufficient deformation.[92,93] Elastin is a linked fiber network, much like an elastomer, whose filaments between crosslinks rotate to align with an axis of loading under sufficient deformation.[94,95] Consequently, collagen and elastin both recruit constituent filaments with increasing deformation into an overall, load-bearing, fiber response. The internal energies of collagen and elastin may therefore be thought of as comprising a molecular configuration energy and a mechanical strain energy. As such, both collagen and elastin are modeled as Freed–Rajagopal[96] biologic fibers, which are described in terms of two such internal energies. Their model is derived from the theory of implicit elasticity, cf. the Appendix. According to their model, Eq. A-7, tangent compliances for collagen and elastin, pertinent to the hypo-elastic constitutive formulation of Eq. 79, are described by

$$\frac{1}{E_t^c(\theta, s^c, e)} = \frac{e_{1_{\max}}^c - e_1^c}{E_1^c e_{1_{\max}}^c + 2(s^c - s_0^c)} + \frac{1}{E_2^c}, \tag{81a}$$

$$\frac{1}{E_t^e(\theta, s^e, e)} = \frac{e_t^e - e_1^e}{E_1^e e_t^e + 2(s^e - s_0^e)} + \frac{1}{E_2^e}, \tag{81b}$$

whose internal strains are established from

$$e_1^c = e - \alpha_t^c \ln\left(\frac{\theta}{\theta_0}\right) - \frac{s^c - s_0^c}{E_2^c}, \tag{81c}$$

$$e_1^e = e - \alpha_t^e \ln\left(\frac{\theta}{\theta_0}\right) - \frac{s^e - s_0^e}{E_2^e}, \tag{81d}$$

with θ_0 being body temperature, i.e., 310 K. Material constants E_1^c and E_2^c are the two asymptotic moduli for collagen that bound its response, i.e., $E_1^c \leqslant E_t^c \leqslant E_2^c$, while E_1^e and E_2^e are the two asymptotic moduli for elastin that bound its response, viz., $E_1^e \leqslant E_t^e \leqslant E_2^e$, both having units of stress (barye = dyne/cm^2), with $e_{1_{\max}}^c$ and $e_{2_{\max}}^e$ being their respective transition strains (see their derivation in the Appendix), i.e., they are the limiting/maximum states of internal conformation strain. Collagen fibers are considered to fracture whenever the strain of stretching molecular bonds exceeds $e_f^c := s_f^c/E_2^c$, where s_f^c is the fracture stress. In contrast, elastin fibers are assumed to remain intact. (Elastin ruptures at strains in excess of 250%, which vastly exceeds the strain range that alveoli are exposed to.)

Moduli $E_t^c = E_1^c E_2^c/(E_1^c + E_2^c)$ and $E_t^e = E_1^e E_2^e/(E_1^e + E_2^e)$ are considered to apply for stresses less than their respective reference stress, viz., for $s^c < s_0^c$ or $s^e < s_0^e$, to which we assign values of $s_0^c = \frac{1}{2}E_1^c e_{1_{\max}}^c$ and $s_0^e = \frac{1}{2}E_1^e e_{1_{\max}}^e$. At these reference stresses, L is set to L_0 and therefore strain $e = 0$. This is done to help ensure a stable numerical implementation, as long slender rods readily buckle under compressive loads—a phenomenon not modeled here. Prestressing fibers is also nature's way of ensuring their structural integrity.

Material properties needed to model septal chords are listed in Tables 4 and 5. From Eq. 64, these elastic moduli are bound from above by Eq. 64 implying that $E_{\max}^c = 2.25 \times 10^{12}$ barye (dyne/cm^2) and $E_{\max}^e = 1.7 \times 10^{12}$ barye. We therefore observe that E_2^c and E_2^e are about 10^5 times smaller than $E_{\max}^c$ and $E_{\max}^e$, which seems reasonable for *in vivo* fibers. This theoretical upper bound for a collagen molecule is about 100 times greater than what have been measured by testing collagen fibrils under ideal laboratory conditions.[105] Like results have been found for metals.

4.4.3 Modeling Alveolar Septa Subjected to Shock Waves

The thermoelastic response of a planar membrane used to model alveolar septa, as described in Eq. 71, is governed by the following pair of differential equations. The first set of ODEs establishes the uniform response of a membrane, as described in

Table 5 Physical properties for hydrated collagen and elastin fibers. Collagen denatures at around 60°C,[97] i.e., above this temperature collagen will shrink rapidly—an effect not modeled here.

Collagen		
Parameter	**Value**	**Reference**
ρ^c [g/cm^3]	1.34	Fels[98]
η_0^c [erg/g.K]	3.7×10^7	
C_p^c [erg/g.K]	1.7×10^7	Kanagy[99]
$\alpha_s^c = \alpha_t^c$	0.056	Weir[100]
$e^c_{1_{\max}}$	0.09 ± 0.018	estimated from TLC $\approx 30\%$
e_f^c	0.25 ± 0.025	
E_1^c [barye]	$5.0 \pm 1.0 \times 10^5$	
E_2^c [barye]	$5.0 \pm 0.5 \times 10^7$	
s_0^e [barye]	$E_1^c e^c_{1_{\max}}/2$	
Elastin		
ρ^e [g/cm^3]	1.31	Lillie and Gosline[101]
η_0^e [erg/g.K]	3.4×10^7	Shadwick and Gosline[102]
C_p^e [erg/g.K]	4.2×10^7	Kakivaya and Hoeve[103]
$\alpha_s^e = \alpha_t^e$	0.1	Lillie and Gosline[101]
$e^e_{1_{\max}}$	0.4 ± 0.08	Shadwick and Gosline[102]
E_1^e [barye]	$2.3 \pm 0.3 \times 10^6$	Urry[95] [Fig. 18]
E_2^e [barye]	$1.0 \pm 0.1 \times 10^7$	Lillie and Gosline[104] [Fig. 5]
s_0^e [barye]	$E_1^e e^e_{1_{\max}}/2$	

Eq. 71a, viz.,

$$\begin{Bmatrix} \mathrm{d}\eta \\ \mathrm{d}s^\pi \end{Bmatrix} = \begin{bmatrix} C_t - 4\alpha_t^2 M/\rho\theta & 4\alpha_t M/\rho\theta \\ -4\alpha_t M & 4M \end{bmatrix} \begin{Bmatrix} \theta^{-1}\,\mathrm{d}\theta \\ \mathrm{d}\xi \end{Bmatrix}, \quad M = M_t(\theta, s^\pi, \xi),$$

where $s^\pi := \pi/h$ has units of stress (dyne/cm^2) with h denoting height or thickness of the setpal membrane. Assuming the volume of a septal membrane remains constant, thickness would obey $h = h_0 \exp(-2\xi)$ with h_0 being its reference thickness. Tangent modulus M is an areal equivalent of the bulk modulus. The second set of ODEs establishes the non-uniform response of a membrane, as described in Eq. 71b, such that upon assuming incompressibility per Eq. 71c, results in

$$\begin{Bmatrix} \mathrm{d}s^\sigma \\ \mathrm{d}s^\tau \end{Bmatrix} = \begin{bmatrix} 4M/3 & 0 \\ 0 & G \end{bmatrix} \begin{Bmatrix} \mathrm{d}\varepsilon \\ \mathrm{d}\gamma \end{Bmatrix}, \quad G = G_t(s^\tau, \gamma),$$

where $s^\sigma := \sigma/h$ and $s^\tau := \tau/h$ also have units of stress (dyne/cm^2), with G being the tangent modulus for in-plane (simple) shear.

From a mechanics perspective, we know a great deal more about alveolar chords

Table 6 The elastic properties reported here are for visceral pleura taken from Freed *et al.*[65] and parenchyma taken from Saraf et al.,[84] divided by 10 to adjust for septal thickness vs. basement membrane thickness. The thermophysical properties lie between that of water and collagen, weighted toward that of water, and evaluated at body temperature.

Property	Value
ρ [g/cm^3]	1.1
η_0 [erg/g.K]	5.0×10^6
C_p [erg/g.K]	2.1×10^7
α_t	0.037
$\xi_{1_{\max}}$	0.24 ± 0.24
ξ_f	0.2
M_1 [barye]	$1.0 \pm 0.1 \times 10^4$
M_2 [barye]	$3.0 \pm 0.1 \times 10^6$
s_0^π [barye]	$M_1 \xi_{1_{\max}}/2$
$\gamma_{1_{\max}}$	$3\xi_{1_{\max}}/2$
G_1 [barye]	$M_1/25$
G_2 [barye]	$M_2/25$

than we know about alveolar septa. More judgment will therefore be required in our construction and parameterization of a material model for alveolar membranes.

A typical alveolar septum is 4–5 μm thick[78] with an outside layer of epithelial cells that encase capillaries built from endothelial cells along with a basement membrane that comprises unorganized collagen and elastin filaments, plus proteoglycans and other extracellular proteins. This basement membrane, roughly at mid-plane in an alveolar septum, has a width of about $0.5\,\mu$m.[30] Inertial forces generated by these membranes are to be based upon a membrane thickness of $\sim 5\ \mu$m with an approximate density of water, while the structural forces that they carry are to be based upon a basement membrane thickness of $\sim 0.5\ \mu$m.

It is not known how much of the mechanical load is actually carried by the cells in an alveolar septum vs. the extracellular basement membrane they encase, but it is generally thought that this basement membrane carries the majority of the load.[78] Therefore, by diminishing the moduli that are appropriate for describing a basement membrane with thickness $\sim 0.5\ \mu$m by a factor of 10, one gets an estimate for the effective septal moduli—an estimate applicable when modeling a whole septal membrane with thickness $\sim 5\ \mu$m. We employ the model parameters specified in Table 6, which are based upon this assumption.

Collagen and elastin appear as thin filaments randomly oriented and somewhat uniformly dispersed throughout a basement membrane, unlike the strongly aligned

fibers that appear in septal chords. Furthermore, there are large numbers of proteins dispersed throughout these septa. Consequently, for our purposes, we model this collective ensemble of tissue and structure types as a homogeneous isotropic membrane modeled after the Freed–Rajagopal biologic fiber[96] that we have extended to membranes[65] in the Appendix, specifically

$$\frac{1}{M_t(\theta,\xi,s^\pi)} = \frac{\xi_{1_{\max}} - \xi_1}{M_1\xi_{1_{\max}} + \frac{1}{2}(s^\pi - s_0^\pi)} + \frac{1}{M_2} \qquad \xi_1 = \xi - \alpha_t \ln\left(\frac{\theta}{\theta_0}\right) - \frac{s^\pi - s_0^\pi}{4M_2} \tag{82a}$$

and

$$\frac{1}{G_t(\gamma,s^\tau)} = \frac{\operatorname{sgn}(\gamma_1)\,\gamma_{1_{\max}} - \gamma_1}{G_1\operatorname{sgn}(\gamma_1)\,\gamma_{1_{\max}} + 2s^\tau} + \frac{1}{G_2} \qquad \gamma_1 = \gamma - \frac{s^\tau}{G_2}, \tag{82b}$$

where compliant, initial, tangent moduli M_1 and G_1 and stiff, terminal, tangent moduli M_2 and G_2 bound their respective responses so that $M_1 \leqslant M_t \leqslant M_2$ and $G_1 \leqslant G_t \leqslant G_2$, with a gradual transition between their asymptotic bounds occurring around strains of $\xi_{1_{\max}}$ and $\gamma_{1_{\max}}$, and with membrane failure or rupture being considered to only occur in the dilation mode whenever $\xi > \xi_f$.

Whenever $s^\pi < s_0^\pi$, modulus M_t is assigned a value of $M_t = M_1M_2/(M_1 + M_2)$ that is the tangent modulus at reference stress s_0^π, which we take to be $\frac{1}{2}M_1\xi_{1_{\max}}$. Negative surface tensions cause wrinkling of a membrane surface, which is not addressed here. In contrast, the shear modulus G_t maintains applicability whenever its arguments become negative valued, which is handled via the sign function introduced in Eq. 82b.

Finite element technology is used to interpolate entropy and stress, integrated at the Gauss points, to entropy and force at the vertices of a pentagon, which are vertices of the dodecahedron, cf. Section 6. The actual entropies and forces interpolated to these nodes are halved, because each septal plane belongs to two adjoining alveoli.

4.4.4 Modeling an Alveolar Volume Subjected to Shock Waves

Alveoli are connected to bronchial trees via alveolar ducts. Under normal conditions, air moves in and out of the alveoli via these ducts. However, when subjected to a stress wave passing over an alveolus, there is no time for the transport of air to take place.[7,9,11,12] Hence, we can consider the air (and heat) within an alveolus to become "trapped", and the pressure to be uniform therein. The governing thermo-

dynamic process is therefore adiabatic. It is under this condition that we model the volumetric response of an alveolar sac.

4.4.4.1 Alveoli Filled with Air

Considering the water saturated air within an alveolus to be an ideal gas, then[106]

$$PV = nR\theta \quad \text{or} \quad \frac{PV}{\theta} = \frac{P_0 V_0}{\theta_0} = nR = \text{constant} \tag{83}$$

where, in our case, P_0 is taken to be the atmospheric pressure at sea level (1 bar or 10^5 Pa or 10^6 barye), with V_0 being that alveolar volume whereat alveolar pressure and plural pressure are both atmospheric, while $\theta_0 = 37^\circ$C = 310 K is assigned as body temperature. Parameter n is the molar content of gas within an alveolus, and R is the universal gas constant.

The material properties associated with an ideal gas contained within an adiabatic enclosure are

$$\alpha_t := \frac{\theta}{L}\left.\frac{\partial L}{\partial \theta}\right|_P = \frac{\theta}{3V}\left.\frac{\partial V}{\partial \theta}\right|_P = \frac{1}{3\theta_0}\frac{P_0}{P}\frac{V_0}{V} \tag{84a}$$

and

$$K_t := -V\left.\frac{\partial P}{\partial V}\right|_\theta = P_0\frac{\theta}{\theta_0}\frac{V_0}{V} \tag{84b}$$

with the other two material properties pertaining to moist air at body temperature* being its mass density ρ of 1.125×10^{-3} g/cm^3 and its specific heat C_t of 1.007×10^7 erg/g.K at constant pressure, constrained by $K_t < K_{\max} = \rho C_t \theta/\alpha_t^2 \approx \rho C_t \theta_0/9 = 3.9 \times 10^5$ barye. An alveolar sac, when modeled as an adiabatic pressure vessel filled with an ideal gas, is described by

$$\begin{Bmatrix} \mathrm{d}\eta \\ -3\,\mathrm{d}P \end{Bmatrix} = \begin{bmatrix} C_t - 9\alpha_t^2 K_t/\rho\theta & 9\alpha_t K_t/\rho\theta \\ -9\alpha_t K_t & 9K_t \end{bmatrix} \begin{Bmatrix} \theta^{-1}\,\mathrm{d}\theta \\ \mathrm{d}\Xi \end{Bmatrix}, \tag{65c}$$

where the entropy within an alveolar sac is given by $S^a = \rho V \eta$ whose initial condition is $S_0^a = \rho V_0 \eta_0$ with $\rho\eta_0$ being the entropy per unit volume of humid air at body temperature and atmospheric pressure, viz., $\rho\eta_0 = 7.770 \times 10^4$ erg/cm^3.K.

*Physical properties for air were taken from the website `www.peacesoftware.de` hosted by Berndt Wischnewski.

Equation 65c, in conjunction with the physical properties describing an ideal gas given in Eq. 84, results in the following differential equation governing pressure:

$$\frac{\mathrm{d}P}{P} = \frac{P_0}{P}\frac{V_0}{V}\frac{\theta}{\theta_0}\left(\frac{P_0}{P}\frac{V_0}{V}\frac{\theta}{\theta_0}\,\frac{\mathrm{d}\theta}{\theta} - \frac{\mathrm{d}V}{V}\right),$$

wherein pressure, volume, and temperature all appear as logarithmic rates.

Pressure P is mapped to nodal forces at the vertices of a dodecahedron in our alveolar model. This requires finite element technology, which is discussed in Section 6.

4.4.4.2 Alveoli Filled with Fluid

In lung tissues that are not healthy, fluids may fill alveolar volumes at various regions throughout a lung, e.g., as could have been caused by injury, pneumonia, etc. In such localities the mechanical response of the local parenchyma will be vastly stiffer than that of healthy tissue, and as such, it will respond very differently to an imposed traveling shock wave. For example, the speed of a wave moving over alveoli filled with fluid will be several orders in magnitude faster than the speed of the same wave moving over healthy alveoli filled with air.

In the presence of a passing shock wave, we suppose that an unhealthy alveolar sac, like a healthy one, can be modeled as an adiabatic enclosure, but now the fluid within such an alveolus is considered to behave, momentarily, like an elastic solid, viz., as the glassy, elastic, upper-bound response of a viscoelastic liquid, which blood is, for example.

The thermoelastic response of an alveolar volume, as described in Eq. 78, is governed by three sets of uncoupled differential equations. The first set of ODEs establishes the uniform response of Eq. 78a described by

$$\begin{Bmatrix} \mathrm{d}\eta \\ \mathrm{d}\Pi \end{Bmatrix} = \begin{bmatrix} C_t - 9\alpha_t^2 K/\rho\theta & 9\alpha_t K/\rho\theta \\ -9\alpha_t K & 9K \end{bmatrix} \begin{Bmatrix} \theta^{-1}\,\mathrm{d}\theta \\ \mathrm{d}\Xi \end{Bmatrix}, \quad K = K_t(\theta, \Pi, \Xi),$$

with the second set of ODEs in Eq. 78b governing the squeeze response

$$\begin{Bmatrix} \mathrm{d}\sigma_1 \\ \mathrm{d}\sigma_2 \end{Bmatrix} = \frac{3}{2}\begin{bmatrix} 2N_1 & -N_2 \\ -N_1 & 2N_2 \end{bmatrix} \begin{Bmatrix} \mathrm{d}\varepsilon_1 \\ \mathrm{d}\varepsilon_2 \end{Bmatrix}, \quad \begin{aligned} N_1 &= N_t(\sigma_1, \varepsilon_1) \\ N_2 &= N_t(\sigma_2, \varepsilon_2) \end{aligned}$$

while the third set of ODEs in Eq. 78c governs the shear response

$$\begin{Bmatrix} \mathrm{d}\tau_1 \\ \mathrm{d}\tau_2 \\ \mathrm{d}\tau_3 \end{Bmatrix} = \begin{bmatrix} G_1 & 0 & 0 \\ 0 & G_2 & 0 \\ 0 & 0 & G_3 \end{bmatrix} \begin{Bmatrix} \mathrm{d}\gamma_1 \\ \mathrm{d}\gamma_2 \\ \mathrm{d}\gamma_3 \end{Bmatrix}, \quad \begin{aligned} G_1 &= G_t(\tau_1, \gamma_1) \\ G_2 &= G_t(\tau_2, \gamma_2) \\ G_3 &= G_t(\tau_3, \gamma_3) \end{aligned}$$

that, collectively, can be used to describe the thermoelastic response of a volume of material.

How these are to be parameterized will be addressed in future research.

4.5 Code Verification and Capabilities of the Constitutive Equations

Figure 29 illustrates what a typical thermomechanical response for a collagen fiber would be expected to look like *in vivo* (top row) and *ex vivo* (bottom row) for 30 typical fibers, as predicted by the Freed–Rajagopal[96] model derived in Section A.2.1 of the Appendix. The *in vivo* response typifies how fibers are prestressed in the various alveolar structures of parenchyma. The material properties for collagen used to create this figure came from Table 5. Stress/strain curves are shown in the left column, while entropy/strain curves are shown in the right column. The top row provides their absolute responses, while the bottom row provides their relative responses. *In vivo*, biologic fibers do not associate with reference states that are void of stress. This is apparent in the upper-left graph (s vs. e), whose response is normalized in the lower-left graph ($s - s_0$ vs. e), and likewise for entropy. The graphs that follow plot relative values.

Figure 29 presents stress/strain and entropy/strain response curves out to 5% strain. Figure 30 extends the deformation out to 10%, 20%, 30%, and 40% strains. In all of these figures we observe that any additional contribution to the entropy caused by deformation can be neglected (it being less than 1 part out of 10^4). In addition to possessing a capability of having stressed fibers in their reference state, established via $s_0 := \frac{1}{2} E_1 e_{1_{\max}}$ and as seen in Fig. 29, our fiber model also accounts for fiber rupture, which is considered to be triggered at a maximum stress of $s_f := E_2 e_f$. Ruptures start at around 30% strain for the specified material parameters. In these figures, material properties E_1, E_2, and $e_{1_{\max}}$ for collagen were all assigned random values according to their respective probabilistic distributions taken from Table 5. Employing 75 steps to integrate each response (sufficient for drawing nice curves)

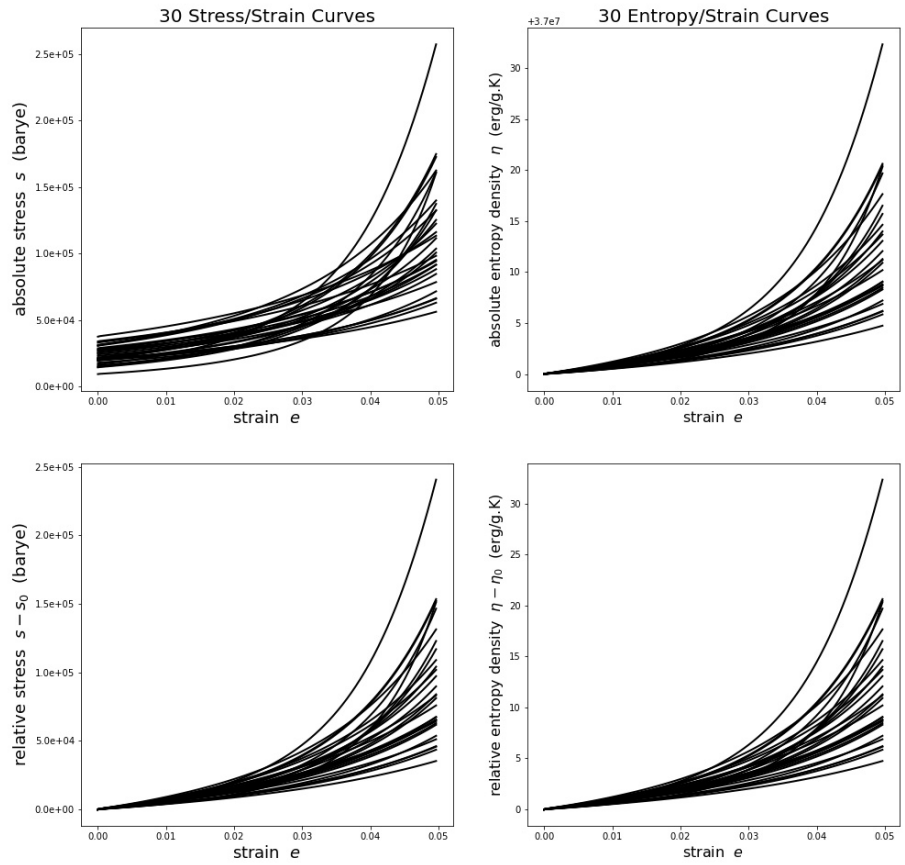

Fig. 29 Typical stress/strain (left column) and entropy/strain (right column) response curves for collagen fibers loaded *in vivo* to 5% strain. The top row presents their absolute responses, while the bottom row presents their relative responses. A reference fiber length, whereat strain is arbitrarily set to zero, has been selected to associate with half the available stretch that can be attributed to molecular reconfiguration.

results in numerical errors of integration (right column in Fig. 30), specifically, in local truncation errors that were found to be on the order of the square root of machine precision, which is considered to be very good.

Like Figs. 29 and 30, material properties E_1, E_2, and $e_{1_{\max}}$ were each assigned random values for both elastin and collagen using parameters taken from Table 5 for the purpose of constructing the 30 curves presented in each plot of Fig. 31 for septal chords. Plus, their fiber lengths and diameters were likewise assigned random values according to their respective probabilistic distributions taken from Fig. 8, using formula 11, and the data from Table 4. Figure 31 presents realistic variability with what one should expect for chordal responses in the alveoli of lung. Both the chordal force and entropy (actual entropy, not entropy density) were calculated using the rule of mixtures based upon volume fractions of collagen vs. elastin. The change in chordal entropy was so small that variability caused by variation in volume fraction dominates this response; hence, relative changes in entropy ($S - S_0$) had to be plotted to visualize the effect. In the septal chords that failed during this analysis, it was collagen fibers that ruptured with elastin fibers continuing to carry load.

The three conjugate pairs that describe a membrane's response are presented as rows in Fig. 32—one row per experiment, with there being 30 curves per plot. These conjugate pairs describe: uniform dilation (s^π, ξ), non-uniform squeeze (s^σ, ε), and non-uniform (simple) shear (s^τ, γ). The three motions that we consider include dilation

$$a = \lambda \qquad b = \lambda \qquad g - g_0 = 0 \tag{85a}$$

pure shear[64]

$$a = \frac{\sqrt{\lambda^2 + \lambda^{-2}}}{\sqrt{2}} \qquad b = \frac{\sqrt{2}}{\sqrt{\lambda^2 + \lambda^{-2}}} \qquad g - g_0 = \frac{\lambda^2 - \lambda^{-2}}{\lambda^2 + \lambda^{-2}} \tag{85b}$$

and simple shear

$$a = 1 \qquad b = 1 \qquad g - g_0 \neq 0 \tag{85c}$$

where λ denotes a stretch with $\lambda_0 = 1$. For dilation: $\xi = \ln \lambda$, $\varepsilon = 0$, and $\gamma = 0$; for pure shear: $\xi = 0$, $\varepsilon = \ln\left(\frac{1}{2}(\lambda^2 + \lambda^{-2})\right)$, and $\gamma = (\lambda^2 - \lambda^{-2})/(\lambda^2 + \lambda^{-2})$; and for

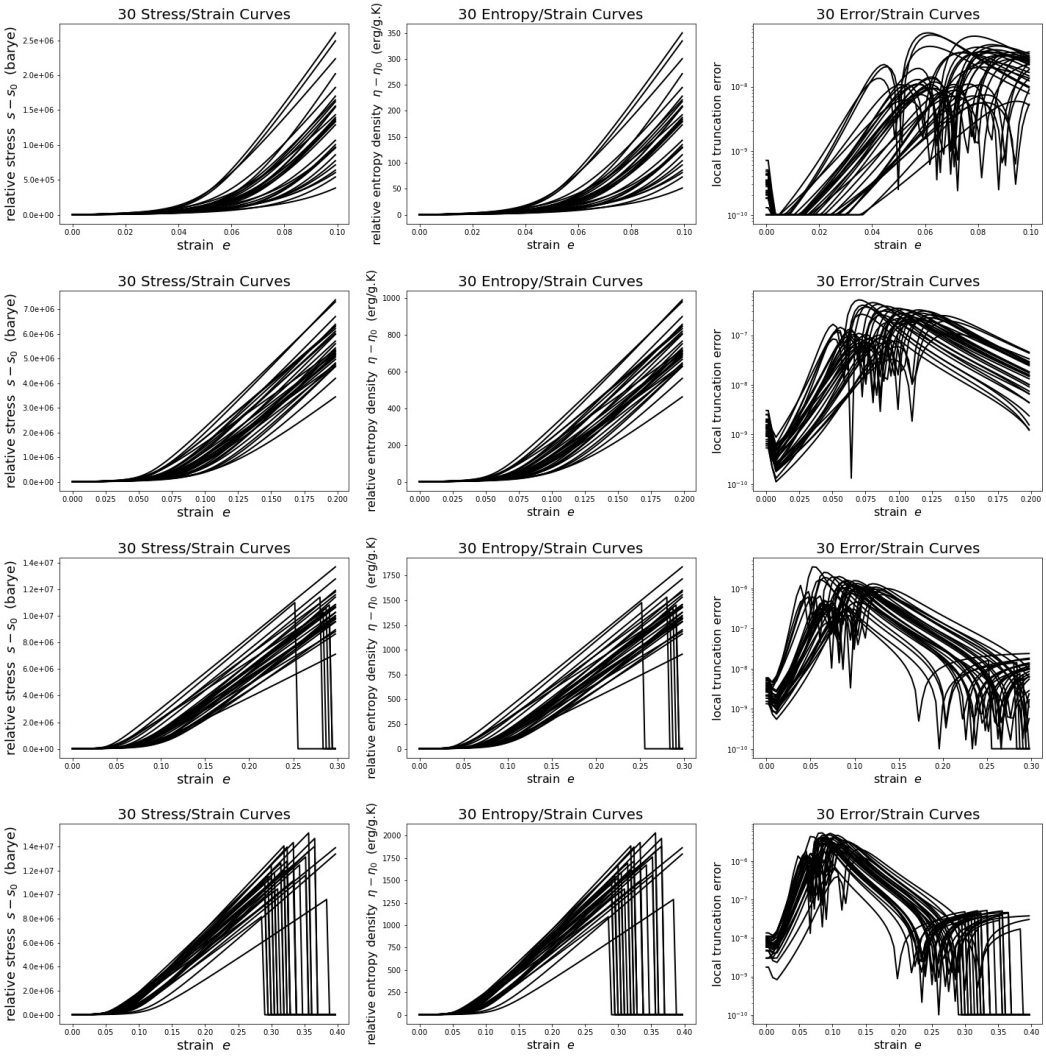

Fig. 30 Stress/strain (left column), entropy density/strain (center column), and local truncation error/strain (right column) curves for collagen using the material parameters listed in Table 5, which are described in terms of probability distributions. The top row is for strains out to 10%, the second row is for strains out to 20%, the third row is for strains out to 30%, and the fourth row is for strains out to 40%. There were no fiber failures in those that were stretched out to 10% and 20% strain. Six of the 30 fibers failed in those stretched out to 30% strain, while 28 of the 30 fibers failed for those stretched out to 40% strain. The local truncation errors plotted here associate with the PECE integrator presented in Eq. 87 of Section 5 using 75 steps of integration, with errors less than 10^{-10} set at 10^{-10}. The reported truncation errors never exceeded 0.001%.

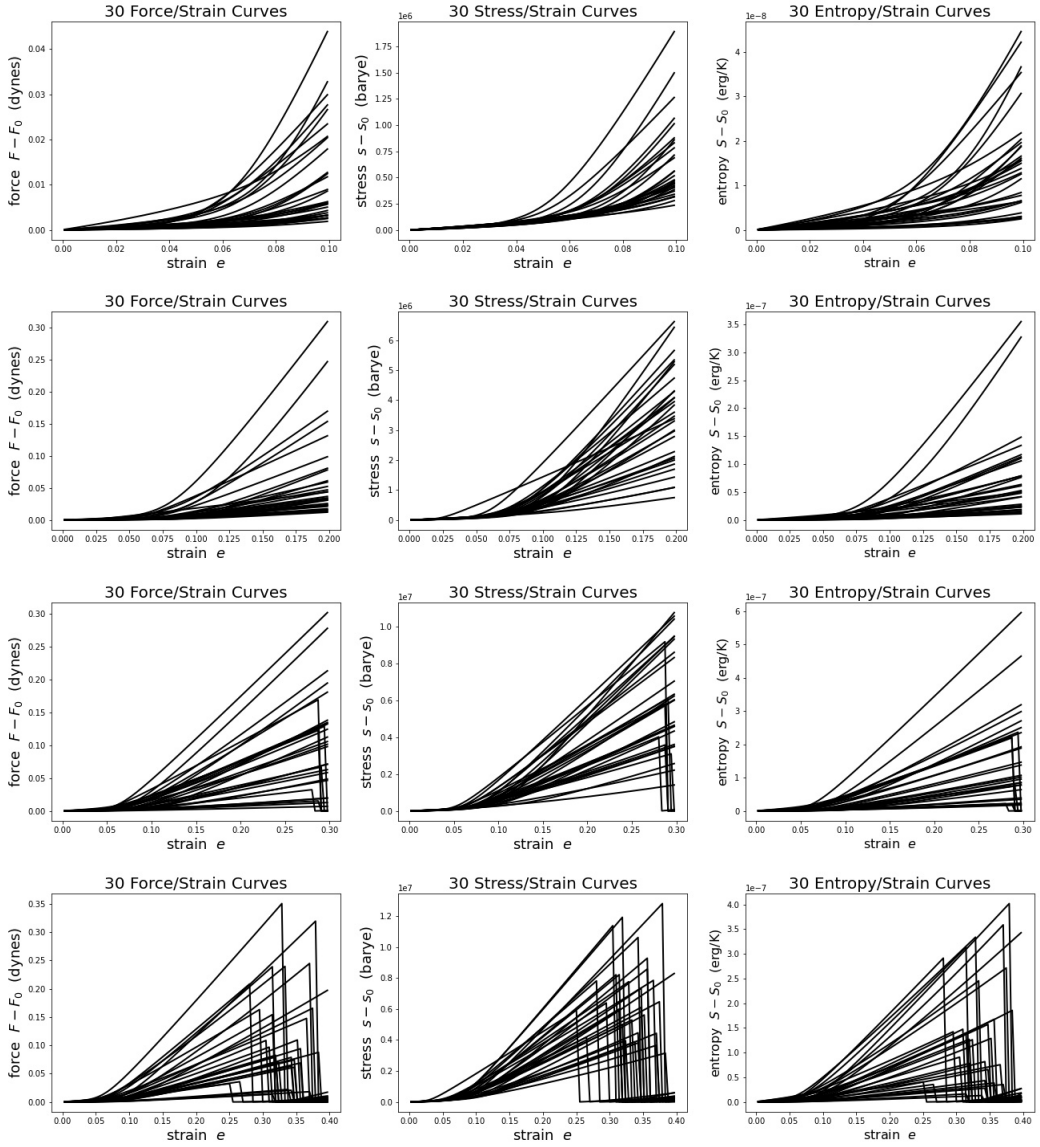

Fig. 31 Relative force/strain (left column), relative nominal stress/strain (center column), and relative entropy/strain (right column) curves for septal chords comprised of individual collagen and elastin fibers whose material parameters are listed in Table 5, which are described in terms of probability distributions. The top row is for strains out to 10%, the second row is for strains out to 20%, the third row is for strains out to 30%, and the fourth row is for strains out to 40%. There were no fiber failures in those that were stretched out to 10% and 20% strain. Six of the 30 collagen fibers failed in those stretched out to 30% strain with none of the elastin fibers failing, while 29 of the 30 collagen fibers failed for those stretched out to 40% strain, again, with none of the elastin fibers failing.

simple shear: $\xi = 0$, $\varepsilon = 0$, and $\gamma = g - g_0$. The constitutive model is that of Eqs. 71 and 82, applying material parameters (and their variability) given in Table 6. In the dilation experiment (top row) there is only uniform (s^π, ξ) response. There are no non-uniform responses, neither (s^σ, ε) nor (s^τ, γ) in an uniform dilation, either theoretical or numerical. The conjugate pairs are uncoupled here. Likewise, in the simple shear experiment (bottom row) there is only a non-uniform (s^τ, γ) response. Theoretically, there is neither uniform (s^π, ξ) nor non-uniform (s^σ, ε) responses in a non-uniform simple shear. However, we observe some numerical error arising in the uniform response—on the order of 1 part in 10^{12} and, therefore, negligible. The pure shear experiment (middle row) is dominated by both a squeeze (s^σ, ε) and a shear (s^τ, γ) response, with there being a small, systematic, dilational coupling through pair (s^π, ξ) that is on the order of 1 part in 10^6. This is the greatest numerical error in our implementation, but still it is sufficiently small so that it can be neglected without concern. Eight of the 30 dilation experiments presented here resulted in membrane rupture. As currently modeled, rupture only associates with the dilational response in septal membranes.

Recently, Birzle *et al.*[107] performed experiments on thin slices of rat parenchyma loaded in tension where they removed the collagen and/or elastin fiber content through collagenase and elastase treatment baths to study their individual behaviors and their interactions under load.

Observation: The change in entropy caused by deformation has been shown to be negligible when compared with the entropy present in its reference state. As such, entropy and its conjugate, i.e., temperature, will not be modeled in our finite element representations of alveoli being exposed to traveling shock waves.

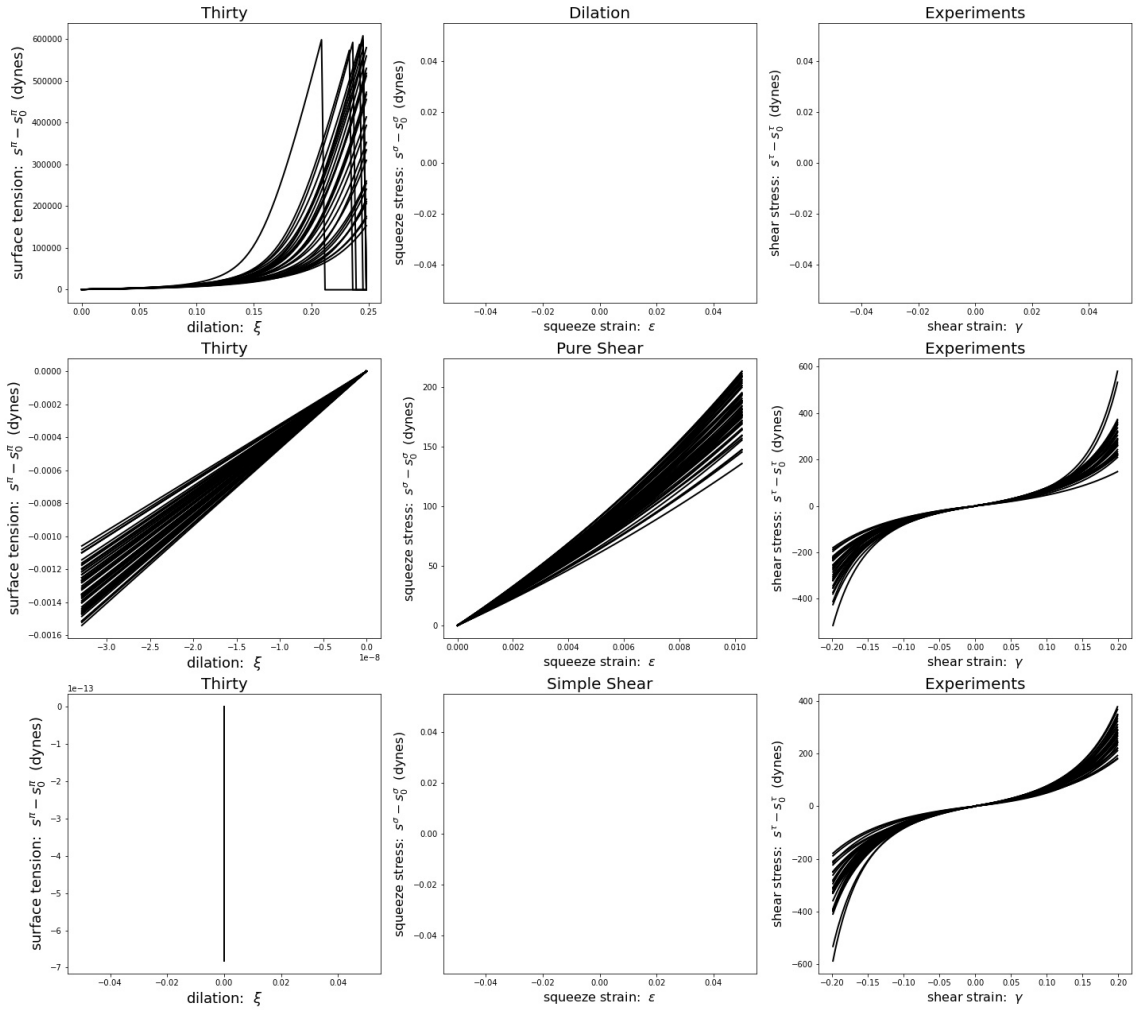

Fig. 32 Membrane response from 30 numerical experiments whose constitutive behavior is described by Eqs. 71 and 82 using the parameters listed in Table 6. The first column gives the $(s^\pi - s_0^\pi, \xi)$ conjugate pair response, the second column gives the $(s^\sigma - s_0^\sigma, \varepsilon)$ conjugate pair response, while the third column gives the $(s^\tau - s_0^\tau, \gamma)$ conjugate pair response. The first row represents a dilation experiment described by Eq. 85a) the second row represents a pure shear experiment described by Eq. 85b, while the third row represents a simple shear experiment described by Eq. 85c. During these numerical experiments, eight membranes ruptured under dilation, while none ruptured during these pure and simple shear experiments.

5. Numerical Integrators

This analysis tool, which models alveolar geometry as a dodecahedron, requires numerical methods for the temporal integration of its constitutive equations (systems of first-order ODEs) and their governing equations of motion (systems of second-order ODEs), and for the spatial integrations of length of line, area of surface, and volume of space that pertain to the various finite-element geometries used. Some results obtained at the Gauss points may need to be mapped out to their nodal locations, so extrapolation procedures that are consistent with the shape (interpolation) functions are also derived for the various elements and quadrature rules selected.

5.1 ODE Solvers

The constitutive equations used to describe our alveolar model present themselves as ODEs that need to be integrated, cf. Section 4.3.3.1. To this end, we employ the PECE (Predict, Evaluate, Correct, re-Evaluate) algorithms of Freed[108] suitable for solving stiff systems of first- and second-order differential equations. These methods are based upon Gear's well-known, second-order, backward, difference formula (BDF2) that appears in Eqs. 87c and 91e.

Time t is considered to be the independent variable, discretized over an interval in time $[t_0, t_I]$ for which I solutions are to be extracted at nodes $i = 1, 2, \ldots, I$ spaced at uniform intervals in time with a common step size of $\mathrm{d}t = (t_I - t_0)/I$ separating them, where time t_0 associates with the initial condition.

5.1.1 PECE Solver for First-Order ODEs

Let $\mathbf{x}(t)$ be a vector of independent control variables described in terms of time t, and let $\mathbf{y}(\mathbf{x})$ be a vector of dependent response variables obeying a differential equation of evolution $\dot{\mathbf{y}} = \mathbf{f}(\mathbf{x}, \mathbf{y})\,\dot{\mathbf{x}}$, or equivalently $\mathrm{d}\mathbf{y} = \mathbf{f}(\mathbf{x}, \mathbf{y})\,\dot{\mathbf{x}}\,\mathrm{d}t = \mathbf{f}(\mathbf{x}, \mathbf{y})\,\mathrm{d}\mathbf{x}$, subject to an initial condition $\mathbf{y}_0 = \mathbf{y}(\mathbf{x}_0)$ where $\mathbf{x}_0 = \mathbf{x}(t_0)$, with matrix $\mathbf{f}(\mathbf{x}, \mathbf{y})$ establishing the constitutive response for the system.

The two-step method put forward here incrementally solves such an ODE, returning solutions associated with the next moment in time t_{i+1}, i.e., it acquires $\mathbf{y}_{i+1}$, given knowledge of the previous $\mathbf{y}_{i-1}$ and current $\mathbf{y}_i$ solutions plus their rates $\dot{\mathbf{y}}_{i-1}$ and $\dot{\mathbf{y}}_i$, with the corrector also depending upon $\dot{\mathbf{y}}_{i+1}$; consequently, the corrector is an implicit method, which is the source of the method's stability properties.

5.1.1.1 Start-Up Algorithm

Multi-step methods are not self-starting. As such, Heun's method (a forward-Euler predictor with a trapezoidal corrector) is used to start this integrator; specifically,

$$\begin{aligned}
&\text{Predict} && \mathbf{y}_1^p = \mathbf{y}_0 + \dot{\mathbf{y}}_0\,\mathrm{d}t + \mathcal{O}\big((\mathrm{d}t)^2\big) && \text{(86a)}\\
&\text{Evaluate} && \dot{\mathbf{y}}_1^p = \mathbf{f}(\mathbf{x}_1, \mathbf{y}_1^p)\,\dot{\mathbf{x}}_1 && \text{(86b)}\\
&\text{Correct} && \mathbf{y}_1 = \mathbf{y}_0 + \tfrac{1}{2}\big(\dot{\mathbf{y}}_1^p + \dot{\mathbf{y}}_0\big)\mathrm{d}t + \mathcal{O}\big((\mathrm{d}t)^3\big) && \text{(86c)}\\
&\text{Re-Evaluate} && \dot{\mathbf{y}}_1 = \mathbf{f}(\mathbf{x}_1, \mathbf{y}_1)\,\dot{\mathbf{x}}_1 && \text{(86d)}
\end{aligned}$$

wherein $\dot{\mathbf{y}}_0 = \mathbf{f}(\mathbf{x}_0, \mathbf{y}_0)\,\dot{\mathbf{x}}_0$. Its predictor is the forward Euler method, while its corrector is the trapezoidal rule. The order of accuracy for a method (the exponent on $\mathrm{d}t$ in $\mathcal{O}$), as they appear in the above big oh operators, $\mathcal{O}$, pertains to a single step of integration. The overall order of the integrator, when integrated over a sequence of steps, is one less than the exponent inside the $\mathcal{O}$ operator. Therefore, Euler's method is first-order accurate, and the trapezoidal method is second-order accurate.

5.1.1.2 Two-Step ODE Solver

The two-step method of Freed[108] for solving first-order ODEs is

$$\begin{aligned}
&\text{Predict} && \mathbf{y}_{i+1}^p = \tfrac{1}{3}\big(4\mathbf{y}_i - \mathbf{y}_{i-1}\big) + \tfrac{2}{3}\big(2\dot{\mathbf{y}}_i - \dot{\mathbf{y}}_{i-1}\big)\mathrm{d}t + \mathcal{O}\big((\mathrm{d}t)^3\big) && \text{(87a)}\\
&\text{Evaluate} && \dot{\mathbf{y}}_{i+1}^p = \mathbf{f}(\mathbf{x}_{i+1}, \mathbf{y}_{i+1}^p)\,\dot{\mathbf{x}}_{i+1} && \text{(87b)}\\
&\text{Correct} && \mathbf{y}_{i+1} = \tfrac{1}{3}\big(4\mathbf{y}_i - \mathbf{y}_{i-1}\big) + \tfrac{2}{3}\dot{\mathbf{y}}_{i+1}^p\mathrm{d}t + \mathcal{O}\big((\mathrm{d}t)^3\big) && \text{(87c)}\\
&\text{Re-Evaluate} && \dot{\mathbf{y}}_{i+1} = \mathbf{f}(\mathbf{x}_{i+1}, \mathbf{y}_{i+1})\,\dot{\mathbf{x}}_{i+1} && \text{(87d)}
\end{aligned}$$

whose corrector is the well-known BDF2 formula made popular by Gear, for which Freed has provided a predictor. This method is second-order accurate in both its predictor and corrector.

Both the predictor and corrector of this PECE scheme have a solution $\mathbf{y}$ with a weight of 1, and a rate $\dot{\mathbf{y}}$ with a weight of $\frac{2}{3}\mathrm{d}t$; hence, this predictor/corrector pair is internally consistent, i.e., the predictor and corrector will produce the same result whenever they integrate over a constant $\dot{\mathbf{y}}$ field.

The evaluate/correct (EC) steps of a PECE method are often iterated over until a convergence criterion is satisfied. Such methods are typically denoted as PE$(\mathrm{CE})^m$, where m specifies the number of iterations imposed.

5.1.2 A Relevant Example

In our finite element implementation, a hypo-elastic material model[81] is introduced to describe the constitutive response of an alveolus whereby

$$\dot{\boldsymbol{\sigma}} = \mathbf{M}(\boldsymbol{\epsilon}, \boldsymbol{\sigma})\, \dot{\boldsymbol{\epsilon}} \quad \text{or equivalently}^{109} \quad \mathrm{d}\boldsymbol{\sigma} = \mathbf{M}(\boldsymbol{\epsilon}, \boldsymbol{\sigma})\, \mathrm{d}\boldsymbol{\epsilon},$$

where $\boldsymbol{\epsilon}$ is a vector of thermodynamic strains, $\boldsymbol{\sigma}$ is a vector of thermodynamic stresses, and $\mathbf{M}$ is a square matrix comprising their tangent moduli, which can depend upon both stress and strain in our application; specifically, the response is

$$\boldsymbol{\sigma}_{1D} = \{\eta, s\}^{\mathsf{T}}, \quad \boldsymbol{\sigma}_{2D} = \{\eta, s^{\pi}, s^{\sigma}, s^{\tau}\}^{\mathsf{T}}, \quad \boldsymbol{\sigma}_{3D} = \{\eta, \Pi, \sigma_1, \sigma_2, \tau_1, \tau_2, \tau_3\}^{\mathsf{T}},$$

where η is entropy and the rest of its constituents are stress attributes. Their thermodynamic conjugates are the control variables

$$\boldsymbol{\epsilon}_{1D} = \{\theta, e\}^{\mathsf{T}}, \quad \boldsymbol{\epsilon}_{2D} = \{\theta, \xi, \varepsilon, \gamma\}^{\mathsf{T}}, \quad \boldsymbol{\epsilon}_{3D} = \{\theta, \Xi, \varepsilon_1, \varepsilon_2, \gamma_1, \gamma_2, \gamma_3\}^{\mathsf{T}},$$

where θ is temperature and the rest of its constituents are strain attributes. In the 2D and 3D cases, these stress/strain attributes arise from Gram–Schmidt decompositions of their respective deformation gradients (cf. Sections 3.3.6.1 and 4.4.3). Constructing tangent moduli $\mathbf{M}(\boldsymbol{\epsilon}, \boldsymbol{\sigma})$ is the topic of Section 4. Both strain $\boldsymbol{\epsilon}$ and stress $\boldsymbol{\sigma}$ appear as arguments in our tangent moduli, i.e., the model is implicit.

Equation 86 is used to take the first step of integration; specifically,

Predict	$\boldsymbol{\sigma}_1^p = \boldsymbol{\sigma}_0 + \dot{\boldsymbol{\sigma}}_0\, \mathrm{d}t$
Evaluate	$\dot{\boldsymbol{\sigma}}_1^p = \mathbf{M}(\boldsymbol{\epsilon}, \boldsymbol{\sigma}_1^p)\, \dot{\boldsymbol{\epsilon}}_1$
Correct	$\boldsymbol{\sigma}_1 = \boldsymbol{\sigma}_0 + \frac{1}{2}\big(\dot{\boldsymbol{\sigma}}_1^p + \dot{\boldsymbol{\sigma}}_0\big)\mathrm{d}t$
Re-Evaluate	$\dot{\boldsymbol{\sigma}}_1 = \mathbf{M}(\boldsymbol{\epsilon}_1, \boldsymbol{\sigma}_1)\, \dot{\boldsymbol{\epsilon}}_1$

where $\dot{\boldsymbol{\sigma}}_0 = \mathbf{M}(\boldsymbol{\epsilon}_0, \boldsymbol{\sigma}_0)\, \dot{\boldsymbol{\epsilon}}_0$. The remaining steps of integration follow according to

Eq. 87; specifically,

$$
\begin{aligned}
&\text{Predict} && \boldsymbol{\sigma}^{p}_{i+1} = \tfrac{1}{3}\big(4\boldsymbol{\sigma}_i - \boldsymbol{\sigma}_{i-1}\big) + \tfrac{2}{3}\big(2\,\dot{\boldsymbol{\sigma}}_i - \dot{\boldsymbol{\sigma}}_{i-1}\big)\mathrm{d}t \\
&\text{Evaluate} && \dot{\boldsymbol{\sigma}}^{p}_{i+1} = \mathbf{M}(\boldsymbol{\epsilon}_{i+1}, \boldsymbol{\sigma}^{p}_{i+1})\,\dot{\boldsymbol{\epsilon}}_{i+1} \\
&\text{Correct} && \boldsymbol{\sigma}_{i+1} = \tfrac{1}{3}\big(4\boldsymbol{\sigma}_i - \boldsymbol{\sigma}_{i-1}\big) + \tfrac{2}{3}\,\dot{\boldsymbol{\sigma}}^{p}_{i+1}\,\mathrm{d}t \\
&\text{Re-Evaluate} && \dot{\boldsymbol{\sigma}}_{i+1} = \mathbf{M}(\boldsymbol{\epsilon}_{i+1}, \boldsymbol{\sigma}_{i+1})\,\dot{\boldsymbol{\epsilon}}_{i+1}
\end{aligned}
$$

whose strain rates $\dot{\boldsymbol{\epsilon}}$ are computed according to Section 3.4.3.

5.1.3 PECE Solver for Second-Order ODEs

Now let $\mathbf{u}$ denote a vector of dependent variables obeying a differential equation of evolution $\mathrm{d}^2\mathbf{u}(t)/\mathrm{d}t^2 = \ddot{\mathbf{u}} = \mathbf{f}(t, \mathbf{u}, \dot{\mathbf{u}})$ subjected to the pair of initial conditions $\mathbf{u}_0 = \mathbf{u}(t_0)$ and $\dot{\mathbf{u}}_0 = \dot{\mathbf{u}}(t_0)$. One may think of $\mathbf{u}$ as being displacements whose rates $\dot{\mathbf{u}}$ are their velocities $\mathbf{v}$, with $\ddot{\mathbf{u}} = \dot{\mathbf{v}}$ representing their accelerations $\mathbf{a}$.

The two-step method put forward here incrementally solves such an ODE, returning solutions associated with the next moment in time t_{i+1} for both displacement $\mathbf{u}_{i+1}$ and velocity $\dot{\mathbf{u}}_{i+1}$. To update displacement to $\mathbf{u}_{i+1}$, the predictor requires knowledge of the previous fields $\mathbf{u}_{i-1}$, $\dot{\mathbf{u}}_{i-1}$, and $\ddot{\mathbf{u}}_{i-1}$ plus the current fields $\mathbf{u}_i$, $\dot{\mathbf{u}}_i$, and $\ddot{\mathbf{u}}_i$, with the corrector also requiring knowledge of $\dot{\mathbf{u}}_{i+1}$ and $\ddot{\mathbf{u}}_{i+1}$. Likewise, to update the velocity to $\dot{\mathbf{u}}_{i+1}$, the predictor requires knowledge of the previous fields $\dot{\mathbf{u}}_{i-1}$ and $\ddot{\mathbf{u}}_{i-1}$ plus the current fields $\dot{\mathbf{u}}_i$ and $\ddot{\mathbf{u}}_i$, with the corrector also requiring knowledge of $\ddot{\mathbf{u}}_{i+1}$. Both predictors are explicit, and both correctors are implicit. It is this implicit quality that provides numeric stability for the integrator.

5.1.3.1 Start-Up Algorithm

Again, multi-step methods are not self-starting, so a one-step method is needed to take the first step of integration; specifically, we employ

$$
\begin{aligned}
&\text{Predict} && \mathbf{u}^{p}_1 = \mathbf{u}_0 + \dot{\mathbf{u}}_0\,\mathrm{d}t + \tfrac{1}{2}\ddot{\mathbf{u}}_0(\mathrm{d}t)^2 + \mathcal{O}\big((\mathrm{d}t)^3\big) && \text{(90a)} \\
& && \dot{\mathbf{u}}^{p}_1 = \dot{\mathbf{u}}_0 + \ddot{\mathbf{u}}_0\,\mathrm{d}t + \mathcal{O}\big((\mathrm{d}t)^2\big) && \text{(90b)} \\
&\text{Evaluate} && \ddot{\mathbf{u}}^{p}_1 = \mathbf{f}(t_1, \mathbf{u}^{p}_1, \dot{\mathbf{u}}^{p}_1) && \text{(90c)} \\
&\text{Correct} && \mathbf{u}_1 = \mathbf{u}_0 + \tfrac{1}{2}(\dot{\mathbf{u}}^{p}_1 + \dot{\mathbf{u}}_0)\mathrm{d}t - \tfrac{1}{12}(\ddot{\mathbf{u}}^{p}_1 - \ddot{\mathbf{u}}_0)(\mathrm{d}t)^2 + \mathcal{O}\big((\mathrm{d}t)^4\big) && \text{(90d)} \\
& && \dot{\mathbf{u}}_1 = \dot{\mathbf{u}}_0 + \tfrac{1}{2}(\ddot{\mathbf{u}}^{p}_1 + \ddot{\mathbf{u}}_0)\mathrm{d}t + \mathcal{O}\big((\mathrm{d}t)^3\big) && \text{(90e)} \\
&\text{Re-Evaluate} && \ddot{\mathbf{u}}_1 = \mathbf{f}(t_1, \mathbf{u}_1, \dot{\mathbf{u}}_1) && \text{(90f)}
\end{aligned}
$$

wherein $\ddot{\mathbf{u}}_0 = \mathbf{f}(t_0, \mathbf{u}_0, \dot{\mathbf{u}}_0)$ and $t_1 = t_0 + \mathrm{d}t$.

5.1.3.2 Two-Step ODE Solver

The two-step method of Freed[108] for solving second-order ODEs is

$$\begin{aligned}
&\text{Predict} && \mathbf{u}^p_{i+1} = \tfrac{1}{3}(4\mathbf{u}_i - \mathbf{u}_{i-1}) + \tfrac{1}{6}(3\dot{\mathbf{u}}_i + \dot{\mathbf{u}}_{i-1})\mathrm{d}t \\
&&& \qquad + \tfrac{1}{36}(31\ddot{\mathbf{u}}_i - \ddot{\mathbf{u}}_{i-1})(\mathrm{d}t)^2 + \mathcal{O}\big((\mathrm{d}t)^4\big) && \text{(91a)} \\
&&& \dot{\mathbf{u}}^p_{i+1} = \tfrac{1}{3}(4\dot{\mathbf{u}}_i - \dot{\mathbf{u}}_{i-1}) + \tfrac{2}{3}(2\ddot{\mathbf{u}}_i - \ddot{\mathbf{u}}_{i-1})\mathrm{d}t + \mathcal{O}\big((\mathrm{d}t)^3\big) && \text{(91b)} \\
&\text{Evaluate} && \ddot{\mathbf{u}}^p_{i+1} = \mathbf{f}(t_{i+1}, \mathbf{u}^p_{i+1}, \dot{\mathbf{u}}^p_{i+1}) && \text{(91c)} \\
&\text{Correct} && \mathbf{u}_{n+1} = \tfrac{1}{3}(4\mathbf{u}_i - \mathbf{u}_{i-1}) + \tfrac{1}{24}(\dot{\mathbf{u}}^p_{i+1} + 14\dot{\mathbf{u}}_i + \dot{\mathbf{u}}_{i-1})\mathrm{d}t \\
&&& \qquad + \tfrac{1}{72}(10\ddot{\mathbf{u}}^p_{i+1} + 51\ddot{\mathbf{u}}_i - \ddot{\mathbf{u}}_{i-1})(\mathrm{d}t)^2 + \mathcal{O}\big((\mathrm{d}t)^4\big) && \text{(91d)} \\
&&& \dot{\mathbf{u}}_{i+1} = \tfrac{1}{3}(4\dot{\mathbf{u}}_i - \dot{\mathbf{u}}_{i-1}) + \tfrac{2}{3}\ddot{\mathbf{u}}^p_{i+1}\,\mathrm{d}t + \mathcal{O}\big((\mathrm{d}t)^3\big) && \text{(91e)} \\
&\text{Re-Evaluate} && \ddot{\mathbf{u}}_{i+1} = \mathbf{f}(t_{i+1}, \mathbf{u}_{i+1}, \dot{\mathbf{u}}_{i+1}) && \text{(91f)}
\end{aligned}$$

which is a second-order method for integrating velocities $\dot{\mathbf{u}}$, and a third-order method for integrating displacements $\mathbf{u}$.

This PECE solver for velocity $\dot{\mathbf{u}}$ has a predictor and a corrector, i.e., Eqs. 91b and 91e, that are the same as those of method (i.e., 87a and 87c), and as such, this predictor/corrector pair for integrating velocity is consistent. Likewise, in both the predictor and corrector for integrating displacement $\mathbf{u}$, contributions from the solution $\mathbf{u}$ have a weight of 1, contributions from the velocities $\dot{\mathbf{u}}$ have a weight of $\frac{2}{3}\mathrm{d}t$, and contributions from the accelerations $\ddot{\mathbf{u}}$ have a weight of $\frac{5}{6}(\mathrm{d}t)^2$; hence, this predictor/corrector pair is internally consistent, too.

5.1.4 A Relevant Example

The finite element problem that we consider here requires solutions for the second-order ODE

$$\mathbf{M}\ddot{\mathbf{u}} + \mathbf{C}\dot{\mathbf{u}} + \mathbf{K}\mathbf{u} = \mathbf{f}(t, \mathbf{u}, \dot{\mathbf{u}})$$

where $\mathbf{u}$, $\dot{\mathbf{u}}$, and $\ddot{\mathbf{u}}$ are the displacement, velocity, and acceleration vectors, $\mathbf{M}$ is a mass matrix, $\mathbf{C}$ and $\mathbf{K}$ are tangent and secant stiffness matrices, while $\mathbf{f}(t, \mathbf{u}, \dot{\mathbf{u}})$ is a forcing function. In our application, matrices $\mathbf{M}$, $\mathbf{C}$, and $\mathbf{K}$ vary with deformation.

Given initial conditions $\mathbf{u}_0$ and $\dot{\mathbf{u}}_0$, establish initial matrices $\mathbf{M}_0 = \mathbf{M}(\mathbf{u}_0)$ and $\mathbf{C}_0 = \mathbf{C}(\mathbf{u}_0)$, noting that $\mathbf{K}_0\mathbf{u}_0 = \mathbf{0}$ because $\mathbf{u}_0 = \mathbf{0}$. For this system of ODEs, the

first step to be taken follows algorithm (Eq. 90) and is implemented as

$$
\begin{aligned}
&\text{Predict} && \mathbf{u}_1^p = \mathbf{u}_0 + \dot{\mathbf{u}}_0\,\mathrm{d}t + \tfrac{1}{2}\ddot{\mathbf{u}}_0(\mathrm{d}t)^2 \\
& && \dot{\mathbf{u}}_1^p = \dot{\mathbf{u}}_0 + \ddot{\mathbf{u}}_0\,\mathrm{d}t \\
&\text{Evaluate} && \ddot{\mathbf{u}}_1^p = \mathbf{M}_0^{-1}\big(\mathbf{f}(t_1, \mathbf{u}_1^p, \dot{\mathbf{u}}_1^p) - \mathbf{C}_0\dot{\mathbf{u}}_0\big) \\
&\text{Correct} && \mathbf{u}_1 = \mathbf{u}_0 + \tfrac{1}{2}(\dot{\mathbf{u}}_1^p + \dot{\mathbf{u}}_0)\mathrm{d}t - \tfrac{1}{12}(\ddot{\mathbf{u}}_1^p - \ddot{\mathbf{u}}_0)(\mathrm{d}t)^2 \\
& && \dot{\mathbf{u}}_1 = \dot{\mathbf{u}}_0 + \tfrac{1}{2}(\ddot{\mathbf{u}}_1^p + \ddot{\mathbf{u}}_0)\mathrm{d}t \\
&\text{Re-Evaluate} && \ddot{\mathbf{u}}_1 = \mathbf{M}_0^{-1}\big(\mathbf{f}(t_1, \mathbf{u}_1, \dot{\mathbf{u}}_1) - \mathbf{C}_0\dot{\mathbf{u}}_0\big) \\
&\text{Update Matrices} && \mathbf{M}_1 = \mathbf{M}(\mathbf{u}_1), \quad \mathbf{C}_1 = \mathbf{C}(\mathbf{u}_1), \quad \mathbf{K}_1 = \mathbf{K}(\mathbf{u}_1)
\end{aligned}
$$

with continued steps being governed by algorithm (Eq. 91), which takes on the form of

$$
\begin{aligned}
&\text{Predict} && \mathbf{u}_{i+1}^p = \tfrac{1}{3}(4\mathbf{u}_i - \mathbf{u}_{i-1}) + \tfrac{1}{6}(3\dot{\mathbf{u}}_i + \dot{\mathbf{u}}_{i-1})\mathrm{d}t \\
& && \qquad + \tfrac{1}{36}(31\ddot{\mathbf{u}}_i - \ddot{\mathbf{u}}_{i-1})(\mathrm{d}t)^2 \\
& && \dot{\mathbf{u}}_{i+1}^p = \tfrac{1}{3}(4\dot{\mathbf{u}}_i - \dot{\mathbf{u}}_{i-1}) + \tfrac{2}{3}(2\ddot{\mathbf{u}}_i - \ddot{\mathbf{u}}_{i-1})\mathrm{d}t \\
&\text{Evaluate} && \ddot{\mathbf{u}}_{i+1}^p = \mathbf{M}_i^{-1}\big(\mathbf{f}(t_{i+1}, \mathbf{u}_{i+1}^p, \dot{\mathbf{u}}_{i+1}^p) - \mathbf{C}_i\dot{\mathbf{u}}_i - \mathbf{K}_i\mathbf{u}_i\big) \\
&\text{Correct} && \mathbf{u}_{i+1} = \tfrac{1}{3}(4\mathbf{u}_i - \mathbf{u}_{i-1}) + \tfrac{1}{24}(\dot{\mathbf{u}}_{i+1}^p + 14\dot{\mathbf{u}}_i + \dot{\mathbf{u}}_{i-1})\mathrm{d}t \\
& && \qquad + \tfrac{1}{72}(10\ddot{\mathbf{u}}_{i+1}^p + 51\ddot{\mathbf{u}}_i - \ddot{\mathbf{u}}_{i-1})(\mathrm{d}t)^2 \\
& && \dot{\mathbf{u}}_{i+1} = \tfrac{1}{3}(4\dot{\mathbf{u}}_i - \dot{\mathbf{u}}_{i-1}) + \tfrac{2}{3}\ddot{\mathbf{u}}_{i+1}^p\,\mathrm{d}t \\
&\text{Re-Evaluate} && \ddot{\mathbf{u}}_{i+1} = \mathbf{M}_i^{-1}\big(\mathbf{f}(t_{i+1}, \mathbf{u}_{i+1}, \dot{\mathbf{u}}_{i+1}) - \mathbf{C}_i\dot{\mathbf{u}}_i - \mathbf{K}_i\mathbf{u}_i\big) \\
&\text{Update Matrices} && \mathbf{M}_{i+1} = \mathbf{M}(\mathbf{u}_{i+1}),\ \mathbf{C}_{i+1} = \mathbf{C}(\mathbf{u}_{i+1}),\ \mathbf{K}_{i+1} = \mathbf{K}(\mathbf{u}_{i+1})
\end{aligned}
$$

where $\mathbf{K}_i\mathbf{u}_i$ returns an internal force due to stress that has accumulated from initial time t_0 to current time t_i, while $\mathbf{C}_i\dot{\mathbf{u}}_i$ returns an incremental addition to this internal force that has accumulated between current time t_i and future time $t_{i+1} = t_i + \mathrm{d}t$.

We observe that the mass matrix must not be ill conditioned in order for this algorithm to work as intended. In those cases where the mass matrix does not change with time, it will only need to be evaluated and inverted once. This is an advantage over using the popular Newmark[110] integrator, where matrix evaluation and inversion are required at every step along a solution path.

5.2 Quadrature Rules for Spatial Integration

In a general finite element setting, information comes into an element via its nodes. Once there, it gets interpolated into its interior Gauss points, where the constitutive equations are solved and spatial integrations occur. In some applications, and in particular, in ours, one also needs to be able to take fields (e.g., a damage parameter) whose constitutive equations have been integrated at the Gauss points of an element, and extrapolate this information back out to the exterior nodes of the element.

Particular to our application, a suite of nodes is common betwixt three, separate, finite-element models that share 20 common vertices. These vertices establish the geometry of a dodecahedron used as the model for a microscopic alveolus. The resultant microscopic force at each vertex arises from *i*) a finite element model of 30 1D rods representing the alveolar chords, *ii*) a finite element model of 12 2D pentagons representing the alveolar membranes, and *iii*) a finite element model of 60 3D tetrahedra representing the alveolar sac. The microscopic forces coming from these three geometric models are summed at their 20 common vertices. These resultant microscopic forces are then collectively homogenized to yield an averaged macroscopic state of stress at a chosen location in the parenchyma.

Feasibility of this solution strategy hinges upon one's ability to extrapolate information at the Gauss points out to their nodal positions. This requires an intermingling between an element's shape functions used for interpolation with its quadrature rule used for integration.

5.2.1 Interpolations: Nodal Points $\mapsto$ Gauss Points
Extrapolations: Gauss Points $\mapsto$ Nodal Points

Shape functions are introduced for interpolating within an element; specifically, consider an arbitrary field, say f, whose values are known at the nodes, then

$$f(\boldsymbol{\xi}_k) = \sum_{i=1}^{n} N_i(\boldsymbol{\xi}_k) f(\boldsymbol{x}_i) \qquad\qquad k = 1, 2, \ldots, m \tag{94a}$$

where the $\boldsymbol{x}_i$ are co-ordinates that locate one of the n nodes in an element of interest, and where the $\boldsymbol{\xi}_i$ are co-ordinates that locate one of its m Gauss points, both being evaluated in the natural co-ordinate system of the element. The transformation in Eq. 94a maps a point $\boldsymbol{x}$ in an element of a mesh to a point $\boldsymbol{\xi}$ in its natural element. Functions N_i are the so-called shape functions. They obey $\sum_{i=1}^{n} N_i(\boldsymbol{\xi}) = 1 \; \forall \; \boldsymbol{\xi}$.

A corresponding extrapolation scheme can therefore be written down as

$$f(\boldsymbol{x}_k) = \sum_{i=1}^{m} M_i(\boldsymbol{x}_k) f(\boldsymbol{\xi}_i) \qquad\qquad k = 1, 2, \ldots, n \tag{94b}$$

where the M_i denote extrapolation functions, i.e., they take values of function f, now assumed to be known at all Gauss points $\boldsymbol{\xi}_i$, $i = 1, 2, \ldots, m$, and extrapolate them out to their individual nodal points $\boldsymbol{x}_k$, $k \in \{1, 2, \ldots, n\}$. They obey $\sum_{i=1}^{m} M_i(\boldsymbol{x}) = 1 \; \forall \; \boldsymbol{x}$.

The interpolation/extrapolation functions of interest here also obey the following constraints: either

$$1 = \sum_{i=1}^{n} N_i(\boldsymbol{\xi}_j) M_j(\boldsymbol{x}_i) \qquad\qquad j = 1, 2, \ldots, m \tag{94c}$$

$$0 = \sum_{i=1}^{n} N_i(\boldsymbol{\xi}_j) M_k(\boldsymbol{x}_i) \qquad\qquad j, k = 1, 2, \ldots, m, \quad j \neq k \tag{94d}$$

or

$$1 = \sum_{i=1}^{m} M_i(\boldsymbol{x}_j) N_j(\boldsymbol{\xi}_i) \qquad\qquad j = 1, 2, \ldots, n \tag{94e}$$

$$0 = \sum_{i=1}^{m} M_i(\boldsymbol{x}_j) N_k(\boldsymbol{\xi}_i) \qquad\qquad j, k = 1, 2, \ldots, n, \quad j \neq k \tag{94f}$$

which follow from substituting Eq. 94b into Eq. 94a, or vice versa. In this regard, such a pair of interpolation/extrapolation functions are said to be self-consistent. In other words, if a field whose values are known at the nodal points is interpolated down to the Gauss points, and then extrapolated back out to the nodal points, then the outgoing values located at the nodes will equal their incoming values at these nodes. The overall process is therefore self-consistent. As straightforward as this procedure is, we found no satisfactory explanation of it in a finite element text.

Whenever $m = n$, the matrices that come about from the interpolation and extrapolation coefficients are reciprocal to one another, with the 0's and 1's of Eqs. 94c and 94d or 94e and 94f associating with the individual components of an identity matrix. Consequently, our need to extrapolate information, as well as interpolate it, strongly suggests that the number of Gauss points selected ought to equal the number of nodal points associated with a given element geometry, albeit this is not a strict requirement for self-consistency.

As an example, a self-consistent strategy for a tetrahedron interpolates via

$$\begin{Bmatrix} f(\boldsymbol{\xi}_1) \\ f(\boldsymbol{\xi}_2) \\ f(\boldsymbol{\xi}_3) \\ f(\boldsymbol{\xi}_4) \end{Bmatrix} = \begin{bmatrix} N_1(\boldsymbol{\xi}_1) & N_2(\boldsymbol{\xi}_1) & N_3(\boldsymbol{\xi}_1) & N_4(\boldsymbol{\xi}_1) \\ N_1(\boldsymbol{\xi}_2) & N_2(\boldsymbol{\xi}_2) & N_3(\boldsymbol{\xi}_2) & N_4(\boldsymbol{\xi}_2) \\ N_1(\boldsymbol{\xi}_3) & N_2(\boldsymbol{\xi}_3) & N_3(\boldsymbol{\xi}_3) & N_4(\boldsymbol{\xi}_3) \\ N_1(\boldsymbol{\xi}_4) & N_2(\boldsymbol{\xi}_4) & N_3(\boldsymbol{\xi}_4) & N_4(\boldsymbol{\xi}_4) \end{bmatrix} \begin{Bmatrix} f(\boldsymbol{x}_1) \\ f(\boldsymbol{x}_2) \\ f(\boldsymbol{x}_3) \\ f(\boldsymbol{x}_4) \end{Bmatrix}$$

and extrapolates via

$$\begin{Bmatrix} f(\boldsymbol{x}_1) \\ f(\boldsymbol{x}_2) \\ f(\boldsymbol{x}_3) \\ f(\boldsymbol{x}_4) \end{Bmatrix} = \begin{bmatrix} M_1(\boldsymbol{x}_1) & M_2(\boldsymbol{x}_1) & M_3(\boldsymbol{x}_1) & M_4(\boldsymbol{x}_1) \\ M_1(\boldsymbol{x}_2) & M_2(\boldsymbol{x}_2) & M_3(\boldsymbol{x}_2) & M_4(\boldsymbol{x}_2) \\ M_1(\boldsymbol{x}_3) & M_2(\boldsymbol{x}_3) & M_3(\boldsymbol{x}_3) & M_4(\boldsymbol{x}_3) \\ M_1(\boldsymbol{x}_4) & M_2(\boldsymbol{x}_4) & M_3(\boldsymbol{x}_4) & M_4(\boldsymbol{x}_4) \end{bmatrix} \begin{Bmatrix} f(\boldsymbol{\xi}_1) \\ f(\boldsymbol{\xi}_2) \\ f(\boldsymbol{\xi}_3) \\ f(\boldsymbol{\xi}_4) \end{Bmatrix}$$

where vectors $\boldsymbol{x}_1$, $\boldsymbol{x}_2$, $\boldsymbol{x}_3$, and $\boldsymbol{x}_4$ hold the co-ordinates for its four nodal points, and where vectors $\boldsymbol{\xi}_1$, $\boldsymbol{\xi}_2$, $\boldsymbol{\xi}_3$, and $\boldsymbol{\xi}_4$ hold the co-ordinates of their Gauss points, all evaluated in the natural co-ordinate system of the element. The matrices in the above mappings will be inverses of one another in a self-consistent construction.

Our three-model, finite-element modeling of an alveolus requires the use of rods with two nodes, triangles with three nodes, tetrahedra with four nodes, and pentagons with five nodes. We now provide consistent interpolation/extrapolation procedures for these four geometries. This requires the selection of a two-point quadrature rule for rods, a three-point quadrature rule for triangles, a four-point quadrature rule for tetrahedra, and a five-point quadrature rule for pentagons. Our selections for quadrature, and their associated interpolation/extrapolation maps, are presented in the following subsections.

5.2.1.1 Self-Consistent Interpolation/Extrapolation Procedures for Rods

Considering a rod with two Gauss points, the interpolation of an arbitrary field (say f, whose values are known at nodal points x_i, $i = 1, 2$) into approximated values located at Gauss points ξ_i, assigned according to Table 7, while selecting shape (interpolation) functions $N_1 = \frac{1}{2}(1 - \xi)$ and $N_2 = \frac{1}{2}(1 + \xi)$, where $-1 \leqslant \xi \leqslant 1$, results in an interpolation map that sends values for a field known at the element nodes down to its Gauss points via

$$\begin{Bmatrix} f(-\sqrt{3}/3) \\ f(\sqrt{3}/3) \end{Bmatrix} = \frac{1}{6} \begin{bmatrix} 3 + \sqrt{3} & 3 - \sqrt{3} \\ 3 - \sqrt{3} & 3 + \sqrt{3} \end{bmatrix} \begin{Bmatrix} f(-1) \\ f(1) \end{Bmatrix} \tag{95a}$$

that, upon applying the methodology put forward in Eq. 94, leads to a straightforward extrapolation formula that maps values for a field of interest from the element Gauss points out to its nodes via

$$\begin{Bmatrix} f(-1) \\ f(1) \end{Bmatrix} = \frac{1}{2\sqrt{3}} \begin{bmatrix} \sqrt{3} + 3 & \sqrt{3} - 3 \\ \sqrt{3} - 3 & \sqrt{3} + 3 \end{bmatrix} \begin{Bmatrix} f(-\sqrt{3}/3) \\ f(\sqrt{3}/3) \end{Bmatrix}. \tag{95b}$$

This extrapolation matrix can be found in Oñate[111] (p. 332). As a check, each row in this matrix sums to 1. Furthermore, the matrices in Eqs. 95a and 95b are reciprocals to one another, as they must be.

Table 7 A quadrature rule for integrating functions over a length of line. This quadrature rule approximates $\int_{-1}^{1} f(\xi)\,\mathrm{d}\xi$ using two Gauss points, i.e., $\int_{-1}^{1} f(\xi)\,\mathrm{d}\xi \approx \sum_{i=1}^{2} w_i f(\xi_i)$. The weights of quadrature w_i sum to its length, because $L = \int_{-1}^{1} \mathrm{d}\xi = 2$. This quadrature rule is due to Christoffel. It integrates polynomials along a line exactly up through second order.

node	ξ co-ordinate	weight
1	$-\sqrt{3}/3$	1
2	$\sqrt{3}/3$	1

5.2.1.2 Self-Consistent Interpolation/Extrapolation Procedures for Triangles

Now, considering a triangle with three Gauss points, the interpolation of an arbitrary field f whose values are known at nodal points $\boldsymbol{x}_i$, $i = 1, 2, 3$, into approximated values located at Gauss points $\boldsymbol{\xi}$, assigned according to Table 8, while selecting shape (interpolation) functions $N_1 = 1 - \xi - \eta$, $N_2 = \xi$, and $N_3 = \eta$, where

Table 8 A simple quadrature rule for integrating functions over the area of a triangle. This quadrature rule approximates $\int_0^1 \int_0^{1-\xi} f(\xi,\eta)\,\mathrm{d}\eta\,\mathrm{d}\xi$ using three Gauss points, i.e., $\int_0^1 \int_0^{1-\xi} f(\xi,\eta)\,\mathrm{d}\eta\,\mathrm{d}\xi \approx \sum_{i=1}^{3} w_i f(\xi_i,\eta_i)$. The weights of quadrature w_i sum to its area, because $A = \int_0^1 \int_0^{1-\xi} \mathrm{d}\eta\,\mathrm{d}\xi = 1/2$. This quadrature rule is due to Strang. It integrates polynomials over a triangular region exactly up through second order. As a point of reference, its centroid has co-ordinates ($1/3$, $1/3$).

node	ξ co-ordinate	η co-ordinate	weight
1	1/6	1/6	1/6
2	2/3	1/6	1/6
3	1/6	2/3	1/6

$0 \leqslant \xi \leqslant 1$ and $0 \leqslant \eta \leqslant 1 - \xi$, results in an interpolation that maps according to

$$\begin{Bmatrix} f(1/6,\,1/6) \\ f(2/3,\,1/6) \\ f(1/6,\,2/3) \end{Bmatrix} = \frac{1}{6} \begin{bmatrix} 4 & 1 & 1 \\ 1 & 4 & 1 \\ 1 & 1 & 4 \end{bmatrix} \begin{Bmatrix} f(0,0) \\ f(1,0) \\ f(0,1) \end{Bmatrix} \tag{96a}$$

that, upon applying the methodology put forward in Eq. 94, which requires some algebra, leads to a simple extrapolation formula applicable for triangles when evaluated in their natural co-ordinate system, viz.,

$$\begin{Bmatrix} f(0,0) \\ f(1,0) \\ f(0,1) \end{Bmatrix} = \frac{1}{3} \begin{bmatrix} 5 & -1 & -1 \\ -1 & 5 & -1 \\ -1 & -1 & 5 \end{bmatrix} \begin{Bmatrix} f(1/6,\,1/6) \\ f(2/3,\,1/6) \\ f(1/6,\,2/3) \end{Bmatrix}. \tag{96b}$$

As a check, each row in both matrices sums to 1 and, as expected, these matrices are reciprocals to one another.

5.2.1.3 Self-Consistent Interpolation/Extrapolation Procedures for Pentagons

We only know of two papers where quadrature formulæ have been derived for integrating over the area of a pentagon.[112,113] Neither presents tables for their nodes and weights of quadrature. Only mathematical methodologies are provided, from which one can numerically construct such tables. More importantly, for our application, neither of their strategies exploits the symmetry properties of a pentagon. Their formulæ, which can be highly accurate, unfortunately do not meet our needs.

Because we seek a quadrature rule for regular pentagons that employs five Gauss points, and pentagons possess five radial lines of symmetry, it is reasonable to con-

sider that the five nodes of quadrature that we seek lie along these five radial lines. Specifically, we seek a quadrature rule for a pentagon whose nodes are located at $\boldsymbol{x}_i$, $i = 1, 2, \ldots, 5$, and whose Gauss points are located at $\boldsymbol{\xi}_i$, $i = 1, 2, \ldots, 5$, with

$$\boldsymbol{x}_1 = \big(\cos(\pi/2), \sin(\pi/2)\big) \qquad \boldsymbol{\xi}_1 = \ell \boldsymbol{x}_1 \tag{97a}$$

$$\boldsymbol{x}_2 = \big(\cos(9\pi/10), \sin(9\pi/10)\big) \qquad \boldsymbol{\xi}_2 = \ell \boldsymbol{x}_2 \tag{97b}$$

$$\boldsymbol{x}_3 = \big(\cos(13\pi/10), \sin(13\pi/10)\big) \qquad \boldsymbol{\xi}_3 = \ell \boldsymbol{x}_3 \tag{97c}$$

$$\boldsymbol{x}_4 = \big(\cos(17\pi/10), \sin(17\pi/10)\big) \qquad \boldsymbol{\xi}_4 = \ell \boldsymbol{x}_4 \tag{97d}$$

$$\boldsymbol{x}_5 = \big(\cos(\pi/10), \sin(\pi/10)\big) \qquad \boldsymbol{\xi}_5 = \ell \boldsymbol{x}_5 \tag{97e}$$

where lines radiating from the origin out to each vertex $\boldsymbol{x}_i$ have unit length, while the lines that radiate out to the Gauss points $\boldsymbol{\xi}_i$ each have a shorter length of ℓ.

Implementing the strategies that underlie Gauss quadrature, length ℓ represents a distance from the pentagon's centroid out to the centroid of a quadrilateral. In our case, this area (one of five equivalent areas) is a four-sided polygon whose apex has an inside angle of 108°, whose two shoulders have right angles, while the inside angle is 72° at the origin. A little bit of algebra and geometry leads to the result

$$\ell = \frac{1 + \sin(3\pi/10)}{3 \sin(3\pi/10)} \approx 0.7454, \tag{98a}$$

whose area becomes the associated weight of quadrature, it being

$$w = \sin(3\pi/10) \cos(3\pi/10) \approx 0.4755, \tag{98b}$$

which is one-fifth the area of a regular pentagon, cf. Eq. 6. To the best of our knowledge, the quadrature rule put forward in Eqs. 97 and 98 for pentagons is new to the literature.

Interpolation is described through shape functions. Adopting the shape functions of Wachspress, which are constructed in Section 3.3.1 for a pentagon, while using the

quadrature rule of Eqs. 97 and 98, results in a symmetric interpolation map of

$$\begin{Bmatrix} f(\boldsymbol{\xi}_1) \\ f(\boldsymbol{\xi}_2) \\ f(\boldsymbol{\xi}_3) \\ f(\boldsymbol{\xi}_4) \\ f(\boldsymbol{\xi}_5) \end{Bmatrix} = \begin{bmatrix} a & b & c & c & b \\ b & a & b & c & c \\ c & b & a & b & c \\ c & c & b & a & b \\ b & c & c & b & a \end{bmatrix} \begin{Bmatrix} f(\boldsymbol{x}_1) \\ f(\boldsymbol{x}_2) \\ f(\boldsymbol{x}_3) \\ f(\boldsymbol{x}_4) \\ f(\boldsymbol{x}_5) \end{Bmatrix} \tag{99a}$$

whose matrix elements are $a = 0.6901471673508344$, $b = 0.1367959452017669$, and $c = 0.0181304711228159$, and whose paired extrapolation map is

$$\begin{Bmatrix} f(\boldsymbol{x}_1) \\ f(\boldsymbol{x}_2) \\ f(\boldsymbol{x}_3) \\ f(\boldsymbol{x}_4) \\ f(\boldsymbol{x}_5) \end{Bmatrix} = \frac{1}{\Delta} \begin{bmatrix} x & y & z & z & y \\ y & x & y & z & z \\ z & y & x & y & z \\ z & z & y & x & y \\ y & z & z & y & x \end{bmatrix} \begin{Bmatrix} f(\boldsymbol{\xi}_1) \\ f(\boldsymbol{\xi}_2) \\ f(\boldsymbol{\xi}_3) \\ f(\boldsymbol{\xi}_4) \\ f(\boldsymbol{\xi}_5) \end{Bmatrix} \tag{99b}$$

wherein

$$x = a^2 + (a-b)(b+c) - c^2, \tag{99c}$$

$$y = (b+c)c - (a+b)b, \tag{99d}$$

$$z = b^2 - (a-b)c - c^2, \tag{99e}$$

$$\Delta = a^2 - (a+b)b - (a-3b)c - c^2, \tag{99f}$$

where, as a check, $\sum_{i=1}^{5} N_i(\boldsymbol{\xi}_j) = 1$ and $\sum_{i=1}^{5} M_i(\boldsymbol{x}_j) = 1$ for $j = 1, 2, \ldots, 5$, and therefore, $a + 2(b+c) = 1$ and $x + 2(y+z) = \Delta$. Furthermore, these coefficient matrices for interpolation and extrapolation are inverses to one another.

5.2.1.4 Self-Consistent Interpolation/Extrapolation Procedures for Tetrahedra

We now consider a tetrahedron with four Gauss points. Here the interpolation of an arbitrary field f whose values are known at nodal points $\boldsymbol{x}_i$, $i = 1, 2, 3, 4$, into approximated values located at Gauss points $\boldsymbol{\xi}_i$, assigned according to Table 9, while selecting shape functions $N_1 = 1 - \xi - \eta - \zeta$, $N_2 = \xi$, $N_3 = \eta$, and $N_4 = \zeta$, bounded by $0 \leqslant \xi \leqslant 1$, $0 \leqslant \eta \leqslant 1 - \xi$, and $0 \leqslant \zeta \leqslant 1 - \xi - \eta$, leads to the

Table 9 A simple quadrature rule for integrating functions over the volume of a tetrahedron. This quadrature rule approximates $\int_0^1 \int_0^{1-\xi} \int_0^{1-\xi-\eta} f(\xi,\eta,\zeta)\,\mathrm{d}\zeta\,\mathrm{d}\eta\,\mathrm{d}\xi$ using four Gauss points, i.e., $\int_0^1 \int_0^{1-\xi} \int_0^{1-\xi-\eta} f(\xi,\eta,\zeta)\,\mathrm{d}\zeta\,\mathrm{d}\eta\,\mathrm{d}\xi \approx \sum_{i=1}^4 w_i f(\xi_i,\eta_i,\zeta_i)$. The weights of quadrature w_i sum to its volume, because $V = \int_0^1 \int_0^{1-\xi} \int_0^{1-\xi-\eta} \mathrm{d}\zeta\,\mathrm{d}\eta\,\mathrm{d}\xi = 1/6$. This quadrature rule is due to Keast. It integrates polynomials over a tetrahedral region exactly up through second order. As a point of reference, its centroid has co-ordinates ($1/4$, $1/4$, $1/4$).

node	ξ co-ordinate	η co-ordinate	ζ co-ordinate	weight
1	0.1381966011250105	0.1381966011250105	0.1381966011250105	1/24
2	0.5854101966249685	0.1381966011250105	0.1381966011250105	1/24
3	0.1381966011250105	0.5854101966249685	0.1381966011250105	1/24
4	0.1381966011250105	0.1381966011250105	0.5854101966249685	1/24

following interpolation formula

$$\begin{Bmatrix} f(a,a,a) \\ f(b,a,a) \\ f(a,b,a) \\ f(a,a,b) \end{Bmatrix} = \begin{bmatrix} 1-3a & a & a & a \\ 1-2a-b & b & a & a \\ 1-2a-b & a & b & a \\ 1-2a-b & a & a & b \end{bmatrix} \begin{Bmatrix} f(0,0,0) \\ f(1,0,0) \\ f(0,1,0) \\ f(0,0,1) \end{Bmatrix} \tag{100a}$$

that, upon applying the methodology put forward in Eq. 94, which now requires a good deal of algebra, results in the following extrapolation formula for tetrahedra

$$\begin{Bmatrix} f(0,0,0) \\ f(1,0,0) \\ f(0,1,0) \\ f(0,0,1) \end{Bmatrix} = \frac{1}{b-a} \begin{bmatrix} 2a+b & -a & -a & -a \\ 2a+b-1 & 1-a & -a & -a \\ 2a+b-1 & -a & 1-a & -a \\ 2a+b-1 & -a & -a & 1-a \end{bmatrix} \begin{Bmatrix} f(a,a,a) \\ f(b,a,a) \\ f(a,b,a) \\ f(a,a,b) \end{Bmatrix} \tag{100b}$$

where $a = 0.1381966011250105$ and $b = 0.5854101966249685$ from Table 9. As a check, each row in the above matrices sums to 1. Unlike the interpolation/ extrapolation formulæ for rods, triangles, and pentagons, whose matrices of transformation are symmetric, the interpolation/extrapolation matrices for a tetrahedron are not symmetric. Lack of symmetry in a quadrature rule is not uncommon, but in our application, such symmetries are advantageous. Nevertheless, for a tetrahedron, quadrature symmetry is not necessary.

6. Variational Formulation

The problem that we have set up to solve is cast in a Lagrangian setting and takes on the general form of a second-order ODE; specifically,

$$\boldsymbol{F} = \mathbf{K}\,\boldsymbol{\Delta} + \mathbf{C}\,\dot{\boldsymbol{\Delta}} + \mathbf{M}\,\ddot{\boldsymbol{\Delta}}, \tag{101a}$$

that under conditions of equilibrium (i.e., whenever $\ddot{\boldsymbol{\Delta}} = \dot{\boldsymbol{\Delta}} = \mathbf{0}$) reduces to

$$\boldsymbol{F} = \mathbf{K}\,\boldsymbol{\Delta}, \tag{101b}$$

where $\mathbf{K}$ is a secant stiffness matrix, $\mathbf{C}$ is a tangent stiffness matrix*, $\mathbf{M}$ is a mass matrix, and $\boldsymbol{F}$ is a force vector, while vector $\boldsymbol{\Delta}$ contains the assembled nodal displacements with $\dot{\boldsymbol{\Delta}}$ and $\ddot{\boldsymbol{\Delta}}$ denoting their velocities and accelerations.

Our problem of interest is the dynamic mechanical response of an alveolus, whose geometry is modeled as a dodecahedron. The shape of an irregular dodecahedron is described by a set of 20 vertices, each experiencing displacements of

$$\mathbf{u}_i^{(v)} = \left\{ u_i^{(v)} \quad v_i^{(v)} \quad w_i^{(v)} \right\}^{\mathsf{T}}, \tag{102a}$$

where at the beginning of a solution step $u_i^{(v)} := x_i^{(v)} - x_0^{(v)}$, $v_i^{(v)} := y_i^{(v)} - y_0^{(v)}$, and $w_i^{(v)} := z_i^{(v)} - z_0^{(v)}$, while at the end of that solution step $u_{i+1}^{(v)} = x_{i+1}^{(v)} - x_0^{(v)}$, $v_{i+1}^{(v)} = y_{i+1}^{(v)} - y_0^{(v)}$, and $w_{i+1}^{(v)} = z_{i+1}^{(v)} - z_0^{(v)}$, with $(x^{(v)}, y^{(v)}, z^{(v)})$ denoting co-ordinates for vertex v in the co-ordinate frame $(\vec{\mathbf{E}}_1, \vec{\mathbf{E}}_2, \vec{\mathbf{E}}_3)$ of a dodecahedron, as established in Section 2. The velocities at these vertices are

$$\dot{\mathbf{u}}_i^{(v)} = \left\{ \dot{u}_i^{(v)} \quad \dot{v}_i^{(v)} \quad \dot{w}_i^{(v)} \right\}^{\mathsf{T}}, \tag{102b}$$

*In the literature, matrix $\mathbf{C}$ is typically utilized as a damping matrix; however, there are presently no damping mechanisms in our alveolar model. For example, viscoelastic effects are often important when modeling biologic tissues. Nevertheless, they can be neglected here, because the event of a shock wave passing over an alveolus happens so fast that viscoelastic effects do not have a chance to manifest themselves. Tissue response will be glassy elastic during such an event. Here $\mathbf{C}$ provides for an elastic *tangent* response, while $\mathbf{K}$ provides for an elastic *secant* response.

where at the beginning of a solution step $\dot{\delta}_i = \frac{1}{2\mathrm{d}t}(\delta_{i+1} - \delta_{i-1})$, while at the end of that solution step $\dot{\delta}_{i+1} = \frac{1}{2\mathrm{d}t}(3\delta_{i+1} - 4\delta_i + \delta_{i-1})$, with $\delta \in \{u^{(v)}, v^{(v)}, w^{(v)}\}$. Likewise, their accelerations are

$$\ddot{\mathbf{u}}_i^{(v)} = \left\{ \ddot{u}_i^{(v)} \quad \ddot{v}_i^{(v)} \quad \ddot{w}_i^{(v)} \right\}^{\mathsf{T}}, \tag{102c}$$

where at the beginning of a solution step $\ddot{\delta}_i = \frac{1}{(\mathrm{d}t)^2}(\delta_{i+1} - 2\delta_i + \delta_{i-1})$, while at the end of that solution step $\ddot{\delta}_{i+1} = \frac{1}{(\mathrm{d}t)^2}(2\delta_{i+1} - 5\delta_i + 4\delta_{i-1} - \delta_{i-2})$. An evaluation of these nodal fields requires knowledge of the co-ordinates for each vertex at states $i+1$, i, $i-1$, and $i-2$. All finite difference equations listed above are second-order formulæ.

Symbol $\boldsymbol{\Delta}$ is used to denote an assemblage of all nodal displacements, while symbol $\mathbf{u}^{(v)}$ is used to denote the nodal displacement of an individual vertex (node) v located within this model, of which there are 20 in our dodecahedral model. These 20 vertices uniquely establish 30 alveolar chords, 12 alveolar membranes, and the alveolar sac enveloped by them, cf. Section 2.

Our problem is not cast as a typical finite element solution, in the sense that we know the nodal displacements $\boldsymbol{\Delta}$, velocities $\dot{\boldsymbol{\Delta}}$, and accelerations $\ddot{\boldsymbol{\Delta}}$ *a priori*, for which nodal forces $\boldsymbol{F}$ are to be found. Furthermore, the constitutive responses of the local structural members composing the alveolus are also interrogated by our model construction (e.g., local stress-strain histories, damage/rupture, etc.), given an imposed far-field deformation history. Typically, boundary conditions are known for which displacements are determined in a weak sense, which is the opposite of our situation. Inputs for our model are considered to come from a finite element model of a torso subjected to an impact caused by either a ballistic projectile or a blast wave. Say, for example, that a location of interest in the lung has been selected. What will serve as input to our dodecahedral model will be a history of the deformation gradient sequenced in time and taken from that element containing this location of interest. For example, if 8-noded brick elements are used, then the deformation gradient will be constant over its volume.

An element of size 1 mm^3 (which is at the resolution capability of current lung imaging technologies) would then have 100 to 200 alveoli in it. Consequently, taking a statistical average over many dodecahedral model runs ought to provide a reasonable representation for the parenchymal response at that lung location. Pre-

dictions coming from our dodecahedral model can be compared with predictions coming from a continuum model used to represent the parenchyma of lung in a torso model. This information from our microscopic alveolar model will allow for refinement and parameterization of a macroscopic continuum model for parenchyma. This is particularly relevant because the spongy nature of lung tissue makes it extremely difficult to perform dynamic experiments that are suitable for parameterizing such continuum models.[114,115]

The assembled nodal forces $\boldsymbol{F}(\boldsymbol{T})$, discussed in Section 6.4.3.4, depend on stresses $\boldsymbol{T}$ evaluated at the Gauss points, as do the tangent and secant stiffness matrices, i.e., $\mathbf{C}(\boldsymbol{T})$ and $\mathbf{K}(\boldsymbol{T})$, which thereby couples the system of equations that are to be solved. As such, an iterative solver is proposed. The mass matrix $\mathbf{M}$ will vary between solution steps, too, but not because the mass matrix of a particular element changes, but rather, because rotations of the local co-ordinate systems for the elements about the global reference frame for the dodecahedron can become large, and as such, effect change in the assembled mass matrix.

The stress that arises from $\mathbf{K}\boldsymbol{\Delta}$ is due to an elastic deformation that begins in some reference state (at an initial time t_0) and ends at the current state (at present time t_i). The stress that arises from $\mathbf{C}\dot{\boldsymbol{\Delta}}$ is due to an additional elastic deformation that begins in this current state (at time t_i) and ends at some nearby state (at a future time $t_{i+1} = t_i + \mathrm{d}t$). An inertial contribution to stress results from $\mathbf{M}\ddot{\boldsymbol{\Delta}}$.

The solution strategy adopted here mimics that of a predictor/corrector method used for solving ODEs. At the beginning of a current solution step, the solution at the end of its previous step takes on the form of

$$\boldsymbol{F}_i = \mathbf{K}_i\boldsymbol{\Delta}_i + \mathrm{M}_i\ddot{\boldsymbol{\Delta}}_i, \tag{103a}$$

where $\boldsymbol{F}_i = \boldsymbol{F}(\boldsymbol{T}_i)$ and $\mathbf{K}_i = \mathbf{K}(\boldsymbol{T}_i)$. Recall that there is no damping in our model, so there is no $\dot{\boldsymbol{\Delta}}_i$ contribution entering here. At the beginning of a step the stiffness response arises singularly from a secant modulus. Meanwhile, the response at the end of the time step is considered to be described by a predictor of the form

$$\boldsymbol{F}^p_{i+1} = \mathbf{K}_i\boldsymbol{\Delta}_i + \mathbf{C}_i\dot{\boldsymbol{\Delta}}_i + \mathrm{M}_i\ddot{\boldsymbol{\Delta}}_i,$$

where $\boldsymbol{F}_{i+1}^{p} = \boldsymbol{F}(\boldsymbol{T}_{i+1}^{p})$. Subtracting Eq. 103a from the above equation produces

$$\boldsymbol{F}_{i+1}^{p} = \boldsymbol{F}_{i} + \mathbf{C}_{i}\dot{\boldsymbol{\Delta}}_{i}, \tag{103b}$$

where we observe that the tangent stiffness matrix $\mathbf{C}_i = \mathbf{C}(\boldsymbol{T}_i)$ is used to extrapolate the known value for $\boldsymbol{F}_i$ into an estimate (prediction) for its next value, viz., $\boldsymbol{F}_{i+1}^{p}$. This step is similar in concept to an arbitrary Lagrangian–Eulerian (ALE) finite element formulation.[116] At this point in the solution process, one evaluates the mass and secant stiffness matrices according to $\mathbf{M}_{i+1}$ and $\mathbf{K}_{i+1} = \mathbf{K}(\boldsymbol{T}_{i+1}^{p})$ and then corrects the solution via

$$\boldsymbol{F}_{i+1} = \mathbf{K}_{i+1}\boldsymbol{\Delta}_{i+1} + \mathbf{M}_{i+1}\ddot{\boldsymbol{\Delta}}_{i+1}, \tag{103c}$$

where $\boldsymbol{F}_{i+1} = \boldsymbol{F}(\boldsymbol{T}_{i+1})$, while $\dot{\boldsymbol{\Delta}}_{i+1}$ and $\ddot{\boldsymbol{\Delta}}_{i+1}$ are approximated using backward difference formulæ, as they are positioned at the end of the solution step. A reevaluation of $\mathbf{K}_{i+1} = \mathbf{K}(\boldsymbol{T}_{i+1})$ now takes place, and Eq. 103c is iterated on until convergence. In preparation for advancing to the next solution step, one evaluates the tangent stiffness matrix $\mathbf{C}_{i+1} = \mathbf{C}(\boldsymbol{T}_{i+1})$.

Equation 103 is not self-starting. To start, because $\ddot{\boldsymbol{\Delta}}_0 = \boldsymbol{\Delta}_0 = \mathbf{0}$, it follows that

$$\boldsymbol{F}_{1}^{p} = \boldsymbol{F}_{0} + \mathbf{C}_{0}\dot{\boldsymbol{\Delta}}_{0}, \tag{104a}$$

where $\boldsymbol{F}_0 = \boldsymbol{F}(\boldsymbol{T}_0)$ denotes a residual force or prestress that must exist in biologic tissues, while $\mathbf{C}_0 = \mathbf{C}(\boldsymbol{T}_0)$ and $\boldsymbol{F}_1^p = \boldsymbol{F}(\boldsymbol{T}_1^p)$. Here $\dot{\boldsymbol{\Delta}}_0$ is to be approximated using an Euler forward step. After evaluating $\mathbf{K}_1 = \mathbf{K}(\boldsymbol{T}_1^p)$, a correction is computed

$$\boldsymbol{F}_{1} = \mathbf{K}_{1}\boldsymbol{\Delta}_{1}, \tag{104b}$$

where $\boldsymbol{F}_1 = \boldsymbol{F}(\boldsymbol{T}_1)$. This allows for an improvement $\mathbf{K}_1 = \mathbf{K}(\boldsymbol{T}_1)$ that can be inserted back into the above equation, iterating until convergence. Upon convergence, one determines the mass matrix $\mathbf{M}_1$ and the tangent stiffness matrix $\mathbf{C}_1 = \mathbf{C}(\boldsymbol{T}_1)$ in preparation for advancing to solution step 2.

It is during the second solution interval whereat nodal accelerations can first be computed, so that with Eq. 104b applying at the start of this interval, and with the following predictor considered to apply at the end of the interval

$$\boldsymbol{F}_2^p = \mathbf{K}_1\boldsymbol{\Delta}_1 + \mathbf{C}_1\dot{\boldsymbol{\Delta}}_1 + \mathbf{M}_1\ddot{\boldsymbol{\Delta}}_1$$

then subtracting Eq. 104b from this equation finds the solution advances via

$$\boldsymbol{F}_2^p = \boldsymbol{F}_1 + \mathbf{C}_1\dot{\boldsymbol{\Delta}}_1 + \mathbf{M}_1\ddot{\boldsymbol{\Delta}}_1 \tag{104c}$$

where $\boldsymbol{F}_2^p = \boldsymbol{F}(\boldsymbol{T}_2^p)$. At this point there is enough information to estimate the nodal accelerations $\ddot{\boldsymbol{\Delta}}_1$, as displacement data are available for $i + 1 = 2$. Both $\dot{\boldsymbol{\Delta}}_1$ and $\ddot{\boldsymbol{\Delta}}_1$ are approximated using central difference formulæ. Upon evaluating the mass matrix $\mathbf{M}_2$ and the secant stiffness matrix $\mathbf{K}_2 = \mathbf{K}(\boldsymbol{T}_2^p)$, a corrected solution at the end of the step is computed via

$$\boldsymbol{F}_2 = \mathbf{K}_2\boldsymbol{\Delta}_2 + \mathbf{M}_2\ddot{\boldsymbol{\Delta}}_2, \tag{104d}$$

where $\ddot{\boldsymbol{\Delta}}_2 \leftarrow \ddot{\boldsymbol{\Delta}}_1$, because at this juncture there is not enough nodal displacement information to estimate acceleration at the end of this step, while $\dot{\boldsymbol{\Delta}}_2$ is approximated using a backward difference formula. Equation 104d allows for an improvement for $\mathbf{K}_2 = \mathbf{K}(\boldsymbol{T}_2)$ that can be inserted back into itself, iterating until convergence. Upon convergence, one determines the tangent stiffness matrix $\mathbf{C}_2 = \mathbf{C}(\boldsymbol{T}_1)$ in preparation for advancing to solution step 3.

Equation 103 is used to advance all solution steps from the third step onward.

As a modeling simplification, the alveolar chords, the alveolar membranes, and the alveolar sac are each considered to be described by their own finite element model. It is assumed that there is no coupling occurring between these three structural groups. This is an important simplification, because the mass and compliance of these three geometric structures are vastly different, and as such, if not decoupled, these differences in mass and compliance would become problematic sources out

of which numerical difficulties would likely arise.

From physics, we know that forces add, and therefore, the nodal forces coming from these three finite-element models can be summed. From these three sources for microscopic alveolar force, one can construct a homogenized (averaged) state of macroscopic stress descriptive of the parenchymal response.

Consequently, we construct three, individual, finite-element models governed by the following three systems of differential equations

$$\boldsymbol{F}_{1\mathrm{D}} = \mathbf{K}_{1\mathrm{D}}\,\boldsymbol{\Delta} + \mathbf{C}_{1\mathrm{D}}\,\dot{\boldsymbol{\Delta}} + \mathbf{M}_{1\mathrm{D}}\,\ddot{\boldsymbol{\Delta}}, \tag{105a}$$

$$\boldsymbol{F}_{2\mathrm{D}} = \mathbf{K}_{2\mathrm{D}}\,\boldsymbol{\Delta} + \mathbf{C}_{2\mathrm{D}}\,\dot{\boldsymbol{\Delta}} + \mathbf{M}_{2\mathrm{D}}\,\ddot{\boldsymbol{\Delta}}, \tag{105b}$$

$$\boldsymbol{F}_{3\mathrm{D}} = \mathbf{K}_{3\mathrm{D}}\,\boldsymbol{\Delta} + \mathbf{C}_{3\mathrm{D}}\,\dot{\boldsymbol{\Delta}} + \mathbf{M}_{3\mathrm{D}}\,\ddot{\boldsymbol{\Delta}}. \tag{105c}$$

The assembled nodal displacements $\boldsymbol{\Delta}$, velocities $\dot{\boldsymbol{\Delta}}$, and accelerations $\ddot{\boldsymbol{\Delta}}$ are common fields betwixt them, i.e., each problem is cast as a 3D analysis. Subscript 1D associates with alveolar chords that assemble into a 3D space truss, subscript 2D associates with alveolar membranes that assemble into a 3D tiled balloon-like structure, and subscript 3D associates with an alveolar sac. Again, it is thought to be beneficial to split the overall problem space into these three sub-problems due to the vast differences in their structural mass and compliance.

When assembled, vectors $\boldsymbol{F}$, $\boldsymbol{\Delta}$, $\dot{\boldsymbol{\Delta}}$, and $\ddot{\boldsymbol{\Delta}}$ have lengths of 60 for the alveolar chord and alveolar membrane models, and a length of 63 for the alveolar sac model, while matrices $\mathbf{K}$, $\mathbf{C}$, and $\mathbf{M}$ have dimensions of $60{\times}60$ for the alveolar chord and alveolar membrane models, and dimensions of $63{\times}63$ for the alveolar sac model. The model for alveolar volume has an extra node located at the centroid of the dodecahedron, i.e., the co-ordinate origin, which is a node in common betwixt all 60 tetrahedra used to fill the volume of a dodecahedron in this alveolar model.

The objective of this section is to derive the elemental mass matrix, the two stiffness matrices (secant and tangent), plus the forcing functions and necessary boundary conditions, and to then assemble them for analysis.

6.1 Mass Matrices

The consistent mass matrix of an element,[117] when quantified in the element's coordinate frame $(\vec{\mathbf{e}}_1, \vec{\mathbf{e}}_2, \vec{\mathbf{e}}_3)$, is defined as follows: For 1D elements,

$$\mathbf{M}_{\mathrm{C1D}} = \int_L \rho\, \mathbf{N}^{\mathsf{T}}\mathbf{N}\, A\, \mathrm{d}L \qquad M_{ij}^{\mathrm{C1D}} = \int_L \rho\, N_{1i} N_{1j}\, A\, \mathrm{d}L \tag{106a}$$

with $i, j = 1, 2, \ldots, n$ where n is the number of nodal points. For 2D elements,

$$\mathbf{M}_{\mathrm{C2D}} = \int_A \rho\, \mathbf{N}^{\mathsf{T}}\mathbf{N}\, H\, \mathrm{d}A \qquad M_{ij}^{\mathrm{C2D}} = \int_A \rho \sum_{k=1}^{2} N_{ki} N_{kj}\, H\, \mathrm{d}A \tag{106b}$$

with $i, j = 1, 2, \ldots, 2n$ where n is the number of nodal points. And for 3D elements,

$$\mathbf{M}_{\mathrm{C3D}} = \int_V \rho\, \mathbf{N}^{\mathsf{T}}\mathbf{N}\, \mathrm{d}V \qquad M_{ij}^{\mathrm{C3D}} = \int_V \rho \sum_{k=1}^{3} N_{ki} N_{kj}\, \mathrm{d}V \tag{106c}$$

with $i, j = 1, 2, \ldots, 3n$ where n is the number of nodal points. For a rod, $\mathbf{M}_{\mathrm{C1D}}$ is a 2×2 matrix; for a pentagon, $\mathbf{M}_{\mathrm{C2D}}$ is a 10×10 matrix; and for a tetrahedron, $\mathbf{M}_{\mathrm{C3D}}$ is a 12×12 matrix. In each expression, ρ is mass per unit volume, $\mathbf{N}$ is a matrix of shape functions for the element of interest, L is length, H is height, A is area, and V is volume.

These mass matrices are said to be consistent in that they are calculated with the same shape functions that are used to create their stiffness matrices. Consistent mass matrices are symmetric because $\mathbf{N}^{\mathsf{T}}\mathbf{N}$ is symmetric. Unfortunately, for all of the elements that we employ, matrices $\mathbf{N}^{\mathsf{T}}\mathbf{N}$ are singular, which is not a desirable feature.

One form of a lumped mass matrix is where the entries from each row of a consistent mass matrix are summed and placed in their respective diagonal entries.[118] Specifically, for 1D elements,

$$M_{ii}^{\mathrm{L1D}} = \sum_{j=1}^{n} M_{ij}^{\mathrm{C1D}} = \int_L \rho N_{1i} \sum_{j=1}^{n} N_{1j}\, A\, \mathrm{d}L, \qquad M_{ij}^{\mathrm{L1D}} = 0 \quad i \neq j \tag{107a}$$

with $i = 1, 2, \ldots, n$ where n is the number of nodal points. For 2D elements,

$$M_{ii}^{\mathrm{L2D}} = \sum_{j=1}^{2n} M_{ij}^{\mathrm{C2D}} = \int_A \rho \sum_{k=1}^{2} N_{ki} \sum_{j=1}^{2n} N_{kj}\, H \,\mathrm{d}A, \quad M_{ij}^{\mathrm{L2D}} = 0 \quad i \neq j \tag{107b}$$

with $i = 1, 2, \ldots, 2n$ where n is the number of nodal points. And for 3D elements,

$$M_{ii}^{\mathrm{L3D}} = \sum_{j=1}^{3n} M_{ij}^{\mathrm{C3D}} = \int_V \rho \sum_{k=1}^{3} N_{ki} \sum_{j=1}^{3n} N_{kj}\, \mathrm{d}V, \qquad M_{ij}^{\mathrm{L3D}} = 0 \quad i \neq j \tag{107c}$$

with $i = 1, 2, \ldots, 3n$ where n is the number of nodal points.

A lumped-consistent (or weighted) mass matrix $\mathbf{M}_{\mathrm{W}}$ can then be created as follows

$$\mathbf{M}_{\mathrm{W}} = (1 - \mu)\, \mathbf{M}_{\mathrm{C}} + \mu\, \mathbf{M}_{\mathrm{L}},$$

wherein μ is a free scalar parameter for weighting between the consistent and lumped mass matrices. The reason for mixing $\mathbf{M}_{\mathrm{C}}$ and $\mathbf{M}_{\mathrm{L}}$ is to achieve a non-singular mass matrix by making the resulting matrix diagonally dominant. In this work, μ is taken to be a half, i.e., an averaged mass matrix is adopted, which has a nice property of minimizing low frequency dispersion. Specifically, we select

$$\mathbf{M}_{\mathrm{1D}} \coloneqq \tfrac{1}{2}(\mathbf{M}_{\mathrm{C1D}} + \mathbf{M}_{\mathrm{L1D}}), \tag{108a}$$

$$\mathbf{M}_{\mathrm{2D}} \coloneqq \tfrac{1}{2}(\mathbf{M}_{\mathrm{C2D}} + \mathbf{M}_{\mathrm{L2D}}), \tag{108b}$$

$$\mathbf{M}_{\mathrm{3D}} \coloneqq \tfrac{1}{2}(\mathbf{M}_{\mathrm{C3D}} + \mathbf{M}_{\mathrm{L3D}}) \tag{108c}$$

as our means for constructing mass matrices. Each of these mass matrices is invertible that, for example, is a requirement of the numerical solution strategy presented in Section 5.1.4.

6.1.1 Mass Matrix for a Chord

A two-noded alveolar chord (a pinned beam in finite element terminology) has shape functions N_i that aggregate into a 1×2 matrix of shape functions when evaluated in their natural co-ordinate system wherein $-1 \leqslant \xi \leqslant 1$, viz.,

$$\mathbf{N}(\xi) = \begin{bmatrix} N_1 & N_2 \end{bmatrix} = \begin{bmatrix} \frac{1}{2}(1 - \xi) & \frac{1}{2}(1 + \xi) \end{bmatrix} \tag{109a}$$

whose constituents have gradients

$$N_{1,\xi} = -1/2 \quad \text{and} \quad N_{2,\xi} = 1/2 \tag{109b}$$

from which a symmetric matrix arises to become the backbone for this mass matrix (which happens to be singular), its components being

$$\mathbf{N}^{\mathsf{T}}\mathbf{N}(\xi_i) = \frac{1}{4}\begin{bmatrix} 1 - 2\xi_i + \xi_i^2 & 1 - \xi_i^2 \\ 1 - \xi_i^2 & 1 + 2\xi_i + \xi_i^2 \end{bmatrix} \tag{109c}$$

where ξ_i designates a co-ordinate for the i^{th} Gauss point associated with a specific Gauss quadrature rule for integration, which in our case comes from Table 7.

The determinant $|\mathbf{J}|$ of Jacobian matrix $\mathbf{J}$ is used to transform the integrals in Eqs. 106 and 107 from natural co-ordinates into the co-ordinate system $(\vec{\mathbf{e}}_1, \vec{\mathbf{e}}_2, \vec{\mathbf{e}}_3)$ of a chord, cf. Fig. 9. Its value is

$$\mathbf{J} \equiv |\mathbf{J}| = \sum\nolimits_{i=1}^{2} N_{i,\xi}(\xi)\, x_i = -\tfrac{1}{2} \cdot -\tfrac{1}{2}L + \tfrac{1}{2} \cdot \tfrac{1}{2}L = \tfrac{1}{2}L \tag{110}$$

given nodal co-ordinates of $x_1 = -\frac{1}{2}L$ and $x_2 = \frac{1}{2}L$, where L is the length of our alveolar chord. The Jacobian matrix $\mathbf{J}$ and its determinant $|\mathbf{J}|$ are equivalent in the case of a rod, because this geometric space is one dimensional.

The consistent mass matrix for a 1D alveolar chord modeled as a two-noded rod, when evaluated in the co-ordinate system of the chord, becomes

$$\begin{aligned} \mathbf{M}_{\text{C1D}} &= \int_0^L \rho\, \mathbf{N}^{\mathsf{T}}\mathbf{N}\, A \,\mathrm{d}x = \int_{-1}^{1} \rho\, \mathbf{N}^{\mathsf{T}}\mathbf{N}\, A\, |\mathbf{J}| \,\mathrm{d}\xi \\ &= |\mathbf{J}| \sum_{i=1}^{m} \rho_i A_i\, \mathbf{N}^{\mathsf{T}}\mathbf{N}(\xi_i)\, w_i \\ &= \frac{L}{2} \sum_{i=1}^{m} \frac{\rho_i A_i w_i}{4} \begin{bmatrix} 1 - 2\xi_i + \xi_i^2 & 1 - \xi_i^2 \\ 1 - \xi_i^2 & 1 + 2\xi_i + \xi_i^2 \end{bmatrix} \end{aligned} \tag{111}$$

where $\mathbf{N}(\xi_i)$ is a matrix of shape functions evaluated at a node of quadrature ξ_i whose associated weight of quadrature is w_i, both evaluated at Gauss point i for a selected Gauss integration rule comprising m Gauss points. Table 7 presents values for the co-ordinates ξ_i and weights w_i of quadrature where two Gauss points of integration ($m = 2$) are employed for integrating over a length of chord.

A lumped mass matrix for a 1D alveolar chord, when evaluated in the co-ordinate system of a chord is

$$\begin{aligned}\mathbf{M}_{\text{L1D}} &= \sum_{\text{rows}} \frac{L}{2} \sum_{i=1}^{m} \frac{\rho_i A_i w_i}{4} \begin{bmatrix} 1-2\xi_i+\xi_i^2 & 1-\xi_i^2 \\ 1-\xi_i^2 & 1+2\xi_i+\xi_i^2 \end{bmatrix} \\ &= \frac{L}{2} \sum_{i=1}^{m} \frac{\rho_i A_i w_i}{2} \begin{bmatrix} 1-\xi_i & 0 \\ 0 & 1+\xi_i \end{bmatrix}.\end{aligned} \tag{112}$$

It is seen that the mass matrix in Eq. 111 is singular at any given Gauss point, whereas the mass matrix in Eq. 112 has a reciprocal, except whenever $\xi = \pm 1$, which are points not realized in Gaussian quadrature rules.

A chordal mass matrix that is appropriate for biologic fibers, and that associates with the Gauss quadrature rule listed in Table 7, has a consistent mass matrix of

$$\mathbf{M}_{\text{C1D}} = \frac{\rho_1 A_1 L}{12} \begin{bmatrix} 2+\sqrt{3} & 1 \\ 1 & 2-\sqrt{3} \end{bmatrix} + \frac{\rho_2 A_2 L}{12} \begin{bmatrix} 2-\sqrt{3} & 1 \\ 1 & 2+\sqrt{3} \end{bmatrix} \tag{113a}$$

and a lumped mass matrix of

$$\mathbf{M}_{\text{L1D}} = \frac{\rho_1 A_1 L}{12} \begin{bmatrix} 3+\sqrt{3} & 0 \\ 0 & 3-\sqrt{3} \end{bmatrix} + \frac{\rho_2 A_2 L}{12} \begin{bmatrix} 3-\sqrt{3} & 0 \\ 0 & 3+\sqrt{3} \end{bmatrix} \tag{113b}$$

that when averaged become

$$\mathbf{M}_{\text{1D}} = \frac{\rho_1 A_1 L}{24} \begin{bmatrix} 5+2\sqrt{3} & 1 \\ 1 & 5-2\sqrt{3} \end{bmatrix} + \frac{\rho_2 A_2 L}{24} \begin{bmatrix} 5-2\sqrt{3} & 1 \\ 1 & 5+2\sqrt{3} \end{bmatrix} \tag{113c}$$

with $\mathbf{M}_{\text{1D}}$ being the 1D mass matrix that we implement. Because the mass of an alveolar chord does not change when exposed to a traveling shock wave, it follows that $\rho AL = \rho_0 A_0 L_0$, and as such, this mass matrix only needs to be evaluated once.

In contrast with engineered structures, like steel trusses, where bars have uniform mass density over their lengths, and typically have uniform cross-sectional areas, too, biologic fibers, like alveolar chords, have mass densities ρ_i and cross-sectional areas A_i that vary along their lengths, and hence, they remain properties of the Gauss points and cannot be pulled out in front of the summation, as is usually done.

The finer details of constructing a mass matrix have been presented above, because

the level of complexity is relatively small in the case of a chord. Much of this finer detail is omitted in the following presentations, since the complexity in these cases is more substantial.

6.1.1.1 Assembly of Chordal Mass Matrices

In our alveolar model comprising septal chords, there are 20 nodes (vertices) whose numbering scheme and natural co-ordinates (those of a regular dodecahedron) are specified in Table 1. Connecting these 20 nodes are 30 line segments (septal chords) whose numbering scheme and associated nodal numbers are specified in Table 2.

In 3D analyses, the components M_{ij}^{1D} of mass matrix $\mathbf{M}_{\mathrm{1D}}$ from Eq. 113 populate a mass matrix $\boldsymbol{M}_{\mathrm{1D}}^{(e)}$ for element e, $e \in \{1, 2, \ldots, 30\}$, accordingly

$$\boldsymbol{M}_{\mathrm{1D}}^{(e)} = \left[\begin{array}{ccc|ccc} M_{11}^{\mathrm{1D}} & 0 & 0 & M_{12}^{\mathrm{1D}} & 0 & 0 \\ 0 & 0 & 0 & 0 & 0 & 0 \\ 0 & 0 & 0 & 0 & 0 & 0 \\ \hline M_{21}^{\mathrm{1D}} & 0 & 0 & M_{22}^{\mathrm{1D}} & 0 & 0 \\ 0 & 0 & 0 & 0 & 0 & 0 \\ 0 & 0 & 0 & 0 & 0 & 0 \end{array}\right] \tag{114}$$

so that, e.g., given the formula $\boldsymbol{f} = \mathbf{M}\ddot{\boldsymbol{u}}$, one would have

$$\left\{\begin{array}{c} f_1^{(i)} \\ f_2^{(i)} \\ f_3^{(i)} \\ \hline f_1^{(j)} \\ f_2^{(j)} \\ f_3^{(j)} \end{array}\right\} = \left[\begin{array}{ccc|ccc} M_{11}^{\mathrm{1D}} & 0 & 0 & M_{12}^{\mathrm{1D}} & 0 & 0 \\ 0 & 0 & 0 & 0 & 0 & 0 \\ 0 & 0 & 0 & 0 & 0 & 0 \\ \hline M_{21}^{\mathrm{1D}} & 0 & 0 & M_{22}^{\mathrm{1D}} & 0 & 0 \\ 0 & 0 & 0 & 0 & 0 & 0 \\ 0 & 0 & 0 & 0 & 0 & 0 \end{array}\right] \left\{\begin{array}{c} \ddot{u}_1^{(i)} \\ \ddot{u}_2^{(i)} \\ \ddot{u}_3^{(i)} \\ \hline \ddot{u}_1^{(j)} \\ \ddot{u}_2^{(j)} \\ \ddot{u}_3^{(j)} \end{array}\right\}$$

where element e has nodes i and j, with all components being evaluated in the co-ordinate system $(\vec{\mathbf{e}}_1, \vec{\mathbf{e}}_2, \vec{\mathbf{e}}_3)^{(e)}$. Only an axial force is carried by the chord. No transverse forces are present. Also, no moments of inertia have been introduced. Like mass matrix $\mathbf{M}_{\mathrm{1D}}$, Mass matrix $\boldsymbol{M}_{\mathrm{1D}}^{(e)}$ is constant, and therefore only needs to be evaluated once.

To rotate this mass matrix for an element from its co-ordinate system for a chord $(\vec{\mathbf{e}}_1, \vec{\mathbf{e}}_2, \vec{\mathbf{e}}_3)^{(e)}$ into the fixed co-ordinate system for a dodecahedron $(\vec{\mathbf{E}}_1, \vec{\mathbf{E}}_2, \vec{\mathbf{E}}_3)$, where it can be assembled with the mass matrices from the other 29 chordal ele-

ments, one must first apply the orthogonal transformation

$$\mathbf{R}_{1\mathrm{D}}^{(e)} = \left[\begin{array}{ccc|ccc} Q_{11}^{(e)} & Q_{12}^{(e)} & Q_{13}^{(e)} & 0 & 0 & 0 \\ Q_{21}^{(e)} & Q_{22}^{(e)} & Q_{23}^{(e)} & 0 & 0 & 0 \\ Q_{31}^{(e)} & Q_{32}^{(e)} & Q_{33}^{(e)} & 0 & 0 & 0 \\ \hline 0 & 0 & 0 & Q_{11}^{(e)} & Q_{12}^{(e)} & Q_{13}^{(e)} \\ 0 & 0 & 0 & Q_{21}^{(e)} & Q_{22}^{(e)} & Q_{23}^{(e)} \\ 0 & 0 & 0 & Q_{31}^{(e)} & Q_{32}^{(e)} & Q_{33}^{(e)} \end{array}\right] \tag{115}$$

so that, accordingly,

$$\mathbf{M}_{1\mathrm{D}}^{(e)} = \big(\mathbf{R}_{1\mathrm{D}}^{(e)}\big)^{\mathsf{T}} \boldsymbol{M}_{1\mathrm{D}}^{(e)}\, \mathbf{R}_{1\mathrm{D}}^{(e)}, \tag{116}$$

where $\mathbf{M}_{1\mathrm{D}}^{(e)}$ becomes this mass matrix, transformed into a dodecahedral co-ordinate system $(\vec{\mathbf{E}}_1, \vec{\mathbf{E}}_2, \vec{\mathbf{E}}_3)$ with $\big[\{\vec{\mathbf{e}}_1\}\{\vec{\mathbf{e}}_2\}\{\vec{\mathbf{e}}_3\}\big]^{(e)} = \big[\{\vec{\mathbf{E}}_1\}\{\vec{\mathbf{E}}_2\}\{\vec{\mathbf{E}}_3\}\big]\big[\mathbf{Q}^{(e)}\big]$, cf. Fig. 9. Even though $\boldsymbol{M}_{1\mathrm{D}}^{(e)}$ is a constant mass matrix, $\mathbf{M}_{1\mathrm{D}}^{(e)}$ need not be, because $\mathbf{R}_{1\mathrm{D}}^{(e)}$ will typically vary over time in our analysis of alveoli subjected to shock waves.

We can now rewrite our example equation for $\boldsymbol{f} = \mathbf{M}\ddot{\boldsymbol{u}}$ as a block matrix equation

$$\begin{Bmatrix} \boldsymbol{f}_i \\ \boldsymbol{f}_j \end{Bmatrix} = \begin{bmatrix} \mathbf{M}_{1\mathrm{D}:ii}^{(e)} & \mathbf{M}_{1\mathrm{D}:ij}^{(e)} \\ \mathbf{M}_{1\mathrm{D}:ji}^{(e)} & \mathbf{M}_{1\mathrm{D}:jj}^{(e)} \end{bmatrix} \begin{Bmatrix} \ddot{\boldsymbol{u}}_i \\ \ddot{\boldsymbol{u}}_j \end{Bmatrix}$$

wherein $\boldsymbol{f}_i = f_1^{(i)}\vec{\mathbf{E}}_1 + f_2^{(i)}\vec{\mathbf{E}}_2 + f_3^{(i)}\vec{\mathbf{E}}_3$, etc., where i and j are the nodal numbers for the two nodes that establish this chord.

From this example, following standard procedures,[119] it becomes apparent how to assemble the overall mass matrix of our space truss when using the geometry of a dodecahedron to model an alveolus. This mass matrix will be a $20{\times}20$ block matrix, with each block element being a 3×3 matrix. Entries placed into this block matrix for each truss element are positioned into this matrix according to the element numbering scheme presented in Table 2.

6.1.2 Mass Matrix for a Triangle

Even though we need to know the shape functions and quadrature rule for triangles in our analysis, we do not need to construct their mass matrix for our specific application.

6.1.3 Mass Matrix for a Pentagon

The surface of a dodecahedron is tiled with 12 pentagons, and as such, an analysis to establish a mass matrix for a pentagon becomes the building block needed to be able to assemble a 2D mass matrix $\mathbf{M}_{\mathrm{2D}}$ representing the alveolar membranes that envelope an alveolar sac.

For an alveolar membrane, represented here as an irregular pentagon, the matrix of shape functions $\mathbf{N}(\xi, \eta)$ takes on the general form of

$$\mathbf{N} = \begin{bmatrix} N_1 & 0 & N_2 & 0 & N_3 & 0 & N_4 & 0 & N_5 & 0 \\ 0 & N_1 & 0 & N_2 & 0 & N_3 & 0 & N_4 & 0 & N_5 \end{bmatrix} \tag{117}$$

whose product $\mathbf{N}^{\mathsf{T}}\mathbf{N}(\xi, \eta)$ is a symmetric singular matrix with a banded structure

$$\mathbf{N}^{\mathsf{T}}\mathbf{N} = \begin{bmatrix} N_1^2 & 0 & N_1N_2 & 0 & N_1N_3 & 0 & N_1N_4 & 0 & N_1N_5 & 0 \\ 0 & N_1^2 & 0 & N_1N_2 & 0 & N_1N_3 & 0 & N_1N_4 & 0 & N_1N_5 \\ N_1N_2 & 0 & N_2^2 & 0 & N_2N_3 & 0 & N_2N_4 & 0 & N_2N_5 & 0 \\ 0 & N_1N_2 & 0 & N_2^2 & 0 & N_2N_3 & 0 & N_2N_4 & 0 & N_2N_5 \\ N_1N_3 & 0 & N_2N_3 & 0 & N_3^2 & 0 & N_3N_4 & 0 & N_3N_5 & 0 \\ 0 & N_1N_3 & 0 & N_2N_3 & 0 & N_3^2 & 0 & N_3N_4 & 0 & N_3N_5 \\ N_1N_4 & 0 & N_2N_4 & 0 & N_3N_4 & 0 & N_4^2 & 0 & N_4N_5 & 0 \\ 0 & N_1N_4 & 0 & N_2N_4 & 0 & N_3N_4 & 0 & N_4^2 & 0 & N_4N_5 \\ N_1N_5 & 0 & N_2N_5 & 0 & N_3N_5 & 0 & N_4N_5 & 0 & N_5^2 & 0 \\ 0 & N_1N_5 & 0 & N_2N_5 & 0 & N_3N_5 & 0 & N_4N_5 & 0 & N_5^2 \end{bmatrix} \tag{118}$$

that when summed along rows produces a diagonal matrix with elements

$$\sum_{\text{rows}} \mathbf{N}^{\mathsf{T}}\mathbf{N} = \operatorname{diag}\begin{pmatrix} N_1 & N_1 & N_2 & N_2 & N_3 & N_3 & N_4 & N_4 & N_5 & N_5 \end{pmatrix} \tag{119}$$

wherein N_i, $i = 1, \ldots, 5$, are the five shape functions that correspond with the five vertices of a pentagon, as established in Eq. 20. These shape functions are nonlinear functions of their co-ordinates (ξ, η), which is readily apparent in Fig. 12.

A consistent mass matrix $\mathbf{M}_{\mathrm{C2D}}$ is constructed by substituting the above matrix of shape functions into the following expression

$$\mathbf{M}_{\mathrm{C2D}} = \int_{\pentagon} \rho\, \mathbf{N}^{\mathsf{T}}\mathbf{N}\, |\mathbf{J}|\, H\, \mathrm{d}\xi\, \mathrm{d}\eta = |\mathbf{J}| \sum_{i=1}^{m} \rho_i H_i\, \mathbf{N}^{\mathsf{T}}\mathbf{N}(\xi_i, \eta_i)\, w_i, \tag{120}$$

where m is the number of Gauss points with (ξ_i, η_i) and w_i being their respective co-ordinates and weights of quadrature that, in our implementation, are provided by Eqs. 97 and 98. As with alveolar chords, alveolar membranes have mass densities ρ_i and heights H_i (thicknesses) that are not uniform across a membrane; hence, they are treated as properties of the Gauss point, and as such, are not pulled out in front of the above summation, as is typically done.

Here $|\mathbf{J}|$ is the Jacobian determinant of a 2×2 Jacobian matrix $\mathbf{J}$. In areal derivations, the Jacobian of a 2D transformation connects the physical x, y to the natural ξ, η co-ordinate systems involved. Components of this Jacobian matrix are calculated using derivatives of shape functions taken with respect to the local co-ordinates via (cf. Reddy[118] p. 424)

$$\mathbf{J} = \begin{bmatrix} \partial x/\partial\xi & \partial y/\partial\xi \\ \partial x/\partial\eta & \partial y/\partial\eta \end{bmatrix} = \begin{bmatrix} \sum_{i=1}^{5} N_{i,\xi}(\xi,\eta)\, x_i & \sum_{i=1}^{5} N_{i,\xi}(\xi,\eta)\, y_i \\ \sum_{i=1}^{5} N_{i,\eta}(\xi,\eta)\, x_i & \sum_{i=1}^{5} N_{i,\eta}(\xi,\eta)\, y_i \end{bmatrix} \tag{121}$$

where the shape function gradients $N_{i,\xi}$ and $N_{i,\eta}$ are provided by Eq. 24, with

$$|\mathbf{J}| = \frac{\partial x}{\partial \xi}\frac{\partial y}{\partial \eta} - \frac{\partial x}{\partial \eta}\frac{\partial y}{\partial \xi} \tag{122}$$

establishing the Jacobian determinant. It is proportional to the area of the pentagon $A_{\pentagon}$ because $A_{\pentagon} = \int_{\pentagon} \mathrm{d}x\,\mathrm{d}y = \int_{\pentagon} |\mathbf{J}|\,\mathrm{d}\xi\,\mathrm{d}\eta = |\mathbf{J}| \sum_{i=1}^{5} w_i = 2.378|\mathbf{J}|$ using the quadrature rule for pentagons given in Eq. 98, cf. Eq. 6.

From the consistent mass matrix of Eq. 120, its associated lumped mass matrix is readily computed via Eq. 107b that when averaged with Eq. 120 results in the 2D mass matrix $\mathbf{M}_{2\mathrm{D}}$ that we implement.

6.1.3.1 Assembly of Pentagonal Mass Matrices

In our alveolar model comprising septal membranes, there are 20 common nodes (vertices) whose numbering scheme and natural co-ordinates (those of a regular dodecahedron) are specified in Table 1. Subsets of these 20 nodes allow for the construction of 12 pentagons (septal membranes) whose numbering scheme and associated nodal numbers are specified in Table 3.

In the co-ordinate system of a pentagon $(\vec{\mathbf{e}}_1, \vec{\mathbf{e}}_2, \vec{\mathbf{e}}_3)^{(e)}$, $e \in \{1, 2, \ldots, 12\}$, a pentagon

has a mass matrix with a symmetric block structure of

$$\boldsymbol{M}_{\mathrm{2D}}^{(e)} = \begin{bmatrix} \boldsymbol{M}_{11}^{\mathrm{2D}} & \boldsymbol{M}_{12}^{\mathrm{2D}} & \boldsymbol{M}_{13}^{\mathrm{2D}} & \boldsymbol{M}_{14}^{\mathrm{2D}} & \boldsymbol{M}_{15}^{\mathrm{2D}} \\ \boldsymbol{M}_{21}^{\mathrm{2D}} & \boldsymbol{M}_{22}^{\mathrm{2D}} & \boldsymbol{M}_{23}^{\mathrm{2D}} & \boldsymbol{M}_{24}^{\mathrm{2D}} & \boldsymbol{M}_{25}^{\mathrm{2D}} \\ \boldsymbol{M}_{31}^{\mathrm{2D}} & \boldsymbol{M}_{32}^{\mathrm{2D}} & \boldsymbol{M}_{33}^{\mathrm{2D}} & \boldsymbol{M}_{34}^{\mathrm{2D}} & \boldsymbol{M}_{35}^{\mathrm{2D}} \\ \boldsymbol{M}_{41}^{\mathrm{2D}} & \boldsymbol{M}_{42}^{\mathrm{2D}} & \boldsymbol{M}_{43}^{\mathrm{2D}} & \boldsymbol{M}_{44}^{\mathrm{2D}} & \boldsymbol{M}_{45}^{\mathrm{2D}} \\ \boldsymbol{M}_{51}^{\mathrm{2D}} & \boldsymbol{M}_{52}^{\mathrm{2D}} & \boldsymbol{M}_{53}^{\mathrm{2D}} & \boldsymbol{M}_{54}^{\mathrm{2D}} & \boldsymbol{M}_{55}^{\mathrm{2D}} \end{bmatrix} \tag{123a}$$

with each element in this matrix being a 3×3 matrix with diagonal entries of

$$\boldsymbol{M}_{ij}^{\mathrm{2D}} = \begin{bmatrix} M_{ij}^{\mathrm{2D}} & 0 & 0 \\ 0 & M_{ij}^{\mathrm{2D}} & 0 \\ 0 & 0 & 0 \end{bmatrix} \tag{123b}$$

whose components have values of

$$M_{ii}^{\mathrm{2D}} = \frac{|\mathbf{J}_0|}{2} \sum_{k=1}^{5} \rho_{0k} H_{0k} N_i (1 + N_i)(\xi_k, \eta_k)\, w_k \quad i = 1, 2, \ldots, 5 \tag{124a}$$

$$M_{ij}^{\mathrm{2D}} = M_{ji}^{\mathrm{2D}} = \frac{|\mathbf{J}_0|}{2} \sum_{k=1}^{5} \rho_{0k} H_{0k} N_i N_j (\xi_k, \eta_k)\, w_k \qquad i \neq j \tag{124b}$$

with co-ordinates (ξ_i, η_i) and weights w_i of quadrature being given in Eqs. 97 and 98, and whose shape functions are defined according to Eq. 20. Because the mass of an alveolar membrane is conserved when exposed to a traveling shock wave, it follows that $\rho H |\mathbf{J}| = \rho_0 H_0 |\mathbf{J}_0|$, and as such, like the mass matrices $\boldsymbol{M}_{\mathrm{1D}}^{(e)}$ and $\boldsymbol{M}_{\mathrm{3D}}^{(e)}$ for chords and tetrahedra, the mass matrix $\boldsymbol{M}_{\mathrm{2D}}^{(e)}$ for each pentagon only needs to be evaluated once.

To rotate this mass matrix for element e, $e \in \{1, 2, \ldots, 12\}$, from its elemental co-ordinate system for the pentagon $(\vec{\mathbf{e}}_1, \vec{\mathbf{e}}_2, \vec{\mathbf{e}}_3)^{(e)}$ into a fixed co-ordinate system for the dodecahedron $(\vec{\mathbf{E}}_1, \vec{\mathbf{E}}_2, \vec{\mathbf{E}}_3)$, where it can be assembled with mass matrices from

the other 11 elements, one must apply the orthogonal transformation

$$\mathbf{R}_{2\mathrm{D}}^{(e)} = \begin{bmatrix} \mathbf{Q}^{(e)} & \mathbf{0} & \mathbf{0} & \mathbf{0} & \mathbf{0} \\ \mathbf{0} & \mathbf{Q}^{(e)} & \mathbf{0} & \mathbf{0} & \mathbf{0} \\ \mathbf{0} & \mathbf{0} & \mathbf{Q}^{(e)} & \mathbf{0} & \mathbf{0} \\ \mathbf{0} & \mathbf{0} & \mathbf{0} & \mathbf{Q}^{(e)} & \mathbf{0} \\ \mathbf{0} & \mathbf{0} & \mathbf{0} & \mathbf{0} & \mathbf{Q}^{(e)} \end{bmatrix} \tag{125a}$$

whose diagonal entries are themselves orthogonal matrices with components

$$\mathbf{Q}^{(e)} = \begin{bmatrix} Q_{11}^{(e)} & Q_{12}^{(e)} & Q_{13}^{(e)} \\ Q_{21}^{(e)} & Q_{22}^{(e)} & Q_{23}^{(e)} \\ Q_{31}^{(e)} & Q_{32}^{(e)} & Q_{33}^{(e)} \end{bmatrix} \tag{125b}$$

so that, accordingly,

$$\mathbf{M}_{2\mathrm{D}}^{(e)} = \big(\mathbf{R}_{2\mathrm{D}}^{(e)}\big)^{\mathsf{T}} \boldsymbol{M}_{2\mathrm{D}}^{(e)}\, \mathbf{R}_{2\mathrm{D}}^{(e)}, \tag{125c}$$

where $\mathbf{M}_{2\mathrm{D}}^{(e)}$ is its mass matrix transformed into the dodecahedral co-ordinate system $(\vec{\mathbf{E}}_1, \vec{\mathbf{E}}_2, \vec{\mathbf{E}}_3)$ according to the map $\big[\{\vec{\mathbf{e}}_1\}\{\vec{\mathbf{e}}_2\}\{\vec{\mathbf{e}}_3\}\big]^{(e)} = \big[\{\vec{\mathbf{E}}_1\}\{\vec{\mathbf{E}}_2\}\{\vec{\mathbf{E}}_3\}\big]\big[\mathbf{Q}^{(e)}\big]$, cf. Fig. 10. Even though $\boldsymbol{M}_{2\mathrm{D}}^{(e)}$ is a constant mass matrix, $\mathbf{M}_{2\mathrm{D}}^{(e)}$ need not be, because $\mathbf{R}_{2\mathrm{D}}^{(e)}$ will typically vary over time in our analysis of alveoli subjected to shock waves.

One can now take entries from mass matrix $\mathbf{M}_{2\mathrm{D}}^{(e)}$ for each nodal location in a pentagonal element e and sum them into their appropriate nodal locations in the overall mass matrix $\mathbf{M}_{2\mathrm{D}}$ for the structure, following standard procedures.[119]

6.1.4 Mass Matrix for a Tetrahedron

The volume of a dodecahedron is filled with 60 tetrahedra, whose centroid (the origin in its natural co-ordinate system) is a common vertex among these 60 tetrahedra. Hence, an analysis to find the mass matrix of a tetrahedron becomes the building block needed to be able to assemble a 3D mass matrix for modeling an alveolar sac.

The matrix of shape functions $\mathbf{N}(\xi, \eta, \zeta)$ for a tetrahedron has a general form of

$$\mathbf{N} = \begin{bmatrix} N_1 & 0 & 0 & N_2 & 0 & 0 & N_3 & 0 & 0 & N_4 & 0 & 0 \\ 0 & N_1 & 0 & 0 & N_2 & 0 & 0 & N_3 & 0 & 0 & N_4 & 0 \\ 0 & 0 & N_1 & 0 & 0 & N_2 & 0 & 0 & N_3 & 0 & 0 & N_4 \end{bmatrix} \tag{126}$$

whose product $\mathbf{N}^{\mathsf{T}}\mathbf{N}(\xi, \eta, \zeta)$ is a symmetric singular matrix with banded structure

$$\mathbf{N}^{\mathsf{T}}\mathbf{N} = \begin{bmatrix} N_1^2 & 0 & 0 & N_1N_2 & 0 & 0 & N_1N_3 & 0 & 0 & N_1N_4 & 0 & 0 \\ 0 & N_1^2 & 0 & 0 & N_1N_2 & 0 & 0 & N_1N_3 & 0 & 0 & N_1N_4 & 0 \\ 0 & 0 & N_1^2 & 0 & 0 & N_1N_2 & 0 & 0 & N_1N_3 & 0 & 0 & N_1N_4 \\ N_1N_2 & 0 & 0 & N_2^2 & 0 & 0 & N_2N_3 & 0 & 0 & N_2N_4 & 0 & 0 \\ 0 & N_1N_2 & 0 & 0 & N_2^2 & 0 & 0 & N_2N_3 & 0 & 0 & N_2N_4 & 0 \\ 0 & 0 & N_1N_2 & 0 & 0 & N_2^2 & 0 & 0 & N_2N_3 & 0 & 0 & N_2N_4 \\ N_1N_3 & 0 & 0 & N_2N_3 & 0 & 0 & N_3^2 & 0 & 0 & N_3N_4 & 0 & 0 \\ 0 & N_1N_3 & 0 & 0 & N_2N_3 & 0 & 0 & N_3^2 & 0 & 0 & N_3N_4 & 0 \\ 0 & 0 & N_1N_3 & 0 & 0 & N_2N_3 & 0 & 0 & N_3^2 & 0 & 0 & N_3N_4 \\ N_1N_4 & 0 & 0 & N_2N_4 & 0 & 0 & N_3N_4 & 0 & 0 & N_4^2 & 0 & 0 \\ 0 & N_1N_4 & 0 & 0 & N_2N_4 & 0 & 0 & N_3N_4 & 0 & 0 & N_4^2 & 0 \\ 0 & 0 & N_1N_4 & 0 & 0 & N_2N_4 & 0 & 0 & N_3N_4 & 0 & 0 & N_4^2 \end{bmatrix} \tag{127}$$

that when summed along each row produces a diagonal matrix with elements

$$\sum_{\text{rows}} \mathbf{N}^{\mathsf{T}}\mathbf{N} = \operatorname{diag}\begin{pmatrix} N_1 & N_1 & N_1 & N_2 & N_2 & N_2 & N_3 & N_3 & N_3 & N_4 & N_4 & N_4 \end{pmatrix} \tag{128}$$

in which the N_i, $i = 1, 2, 3, 4$, are the four shape functions corresponding to the four vertices of a tetrahedron that, along with their gradients, are described by

$$N_1 = 1 - \xi - \eta - \zeta \qquad N_{1,\xi} = -1 \qquad N_{1,\eta} = -1 \qquad N_{1,\zeta} = -1 \tag{129a}$$

$$N_2 = \xi \qquad N_{2,\xi} = 1 \qquad N_{2,\eta} = 0 \qquad N_{2,\zeta} = 0 \tag{129b}$$

$$N_3 = \eta \qquad N_{3,\xi} = 0 \qquad N_{3,\eta} = 1 \qquad N_{3,\zeta} = 0 \tag{129c}$$

$$N_4 = \zeta \qquad N_{4,\xi} = 0 \qquad N_{4,\eta} = 0 \qquad N_{4,\zeta} = 1 \tag{129d}$$

out of which consistent, lumped, and weighted mass matrices can be constructed.

Numerical integration is used to obtain a consistent mass matrix for a tetrahedron

$$\begin{aligned} \mathbf{M}_{\text{C3D}} &= \int_V \rho\, \mathbf{N}^{\mathsf{T}}\mathbf{N}\, \mathrm{d}\mathbf{z}\, \mathrm{d}\mathbf{y}\, \mathrm{d}\mathbf{x} \\ &= \int_0^1 \int_0^{1-\xi} \int_0^{1-\xi-\eta} \rho\, \mathbf{N}^{\mathsf{T}}\mathbf{N}\, |\mathbf{J}|\, \mathrm{d}\zeta\, \mathrm{d}\eta\, \mathrm{d}\xi \\ &= \rho\, |\mathbf{J}| \sum_{i=1}^{m} \mathbf{N}^{\mathsf{T}}\mathbf{N}(\xi_i, \eta_i, \zeta_i)\, w_i \end{aligned} \tag{130}$$

where $|\mathbf{J}|$ is the determinant of the Jacobian matrix $\mathbf{J}$, with m being the number of Gauss points used for spatial integration, which in our case is four. The co-ordinates (ξ_i, η_i, ζ_i) and weights w_i of quadrature used for integrating over the volume of a tetrahedron are found in Table 9.

The Jacobian is calculated from taking derivatives of the shape functions with respect to their local co-ordinates (ξ, η, ζ), as specified in Eq. 129, which associate with the current global co-ordinates (x_i, y_i, z_i) of its four vertices according to (cf. Reddy[118] p. 424)

$$\begin{aligned}
\mathbf{J} &= \begin{bmatrix} \partial x/\partial\xi & \partial y/\partial\xi & \partial z/\partial\xi \\ \partial x/\partial\eta & \partial y/\partial\eta & \partial z/\partial\eta \\ \partial x/\partial\zeta & \partial y/\partial\zeta & \partial z/\partial\zeta \end{bmatrix} \\
&= \begin{bmatrix} \sum_{i=1}^{4} N_{i,\xi}(\xi,\eta,\zeta)\, x_i & \sum_{i=1}^{4} N_{i,\xi}(\xi,\eta,\zeta)\, y_i & \sum_{i=1}^{4} N_{i,\xi}(\xi,\eta,\zeta)\, z_i \\ \sum_{i=1}^{4} N_{i,\eta}(\xi,\eta,\zeta)\, x_i & \sum_{i=1}^{4} N_{i,\eta}(\xi,\eta,\zeta)\, y_i & \sum_{i=1}^{4} N_{i,\eta}(\xi,\eta,\zeta)\, z_i \\ \sum_{i=1}^{4} N_{i,\zeta}(\xi,\eta,\zeta)\, x_i & \sum_{i=1}^{4} N_{i,\zeta}(\xi,\eta,\zeta)\, y_i & \sum_{i=1}^{4} N_{i,\zeta}(\xi,\eta,\zeta)\, z_i \end{bmatrix} \\
&= \begin{bmatrix} x_2 - x_1 & y_2 - y_1 & z_2 - z_1 \\ x_3 - x_1 & y_3 - y_1 & z_3 - z_1 \\ x_4 - x_1 & y_4 - y_1 & z_4 - z_1 \end{bmatrix}
\end{aligned} \tag{48c}$$

whose determinant $|\mathbf{J}|$ is proportional to the volume of this element when evaluated in the physical co-ordinate system $(\vec{\mathbf{E}}_1, \vec{\mathbf{E}}_2, \vec{\mathbf{E}}_3)$. Specifically, $|\mathbf{J}| = 6V_{tet}$ because $V_{tet} = \int_{V_{tet}} \mathrm{d}z\, \mathrm{d}y\, \mathrm{d}x = \int_0^1 \int_0^{1-\xi} \int_0^{1-\xi-\eta} |\mathbf{J}|\, \mathrm{d}\zeta\, \mathrm{d}\eta\, \mathrm{d}\xi = |\mathbf{J}| \sum_{i=1}^{m} w_i = \frac{1}{6}|\mathbf{J}|$.

Averaging this mass matrix based on Eq. 127 with its lumped version based on Eq. 128, according to Eq. 130, gives the 3D mass matrix $\mathbf{M}_{3\mathrm{D}}$ that we implement.

Because tetrahedra are used to model an alveolar sac, which will either be filled with air or fluid, their mass densities ρ are considered to be uniform over the domains of these elements, which is why ρ can be pulled out in front of the summation in Eq. 130.

6.1.4.1 Assembly of Tetrahedral Mass Matrices

In our finite element model for an alveolar sac, there are 21 nodes (20 vertices and the origin) whose numbering scheme and natural co-ordinates are given in Table 1. Filling this volume are 60 tetrahedra whose numbering scheme and associated nodal numbers are specified according to the following strategy. Using the element and

nodal numbering scheme for pentagons given in Table 3, begin with pentagon 1 and sequence to pentagon 12. Associated with any given pentagon are five tetrahedra. Nodes 1 and 4 of these five tetrahedra are the same. Node 1 is at the centroid of the pentagon, and node 4 is at the origin of the dodecahedron. Nodes 2 and 3 of the tetrahedron are also nodes of this pentagon, and are sequenced such that when traversing nodes $1 \rightarrow 2 \rightarrow 3$ of a tetrahedron one undergoes a counterclockwise path when viewed looking inward from outside of the dodecahedron. The first tetrahedron associated with a pentagon shares nodes 2 and 3 of its tetrahedron with nodes 1 and 2 of the pentagon. The second tetrahedron shares nodes 2 and 3 of its tetrahedron with nodes 2 and 3 of the pentagon, etc.

In the co-ordinate system of a tetrahedron $(\vec{\mathbf{e}}_1, \vec{\mathbf{e}}_2, \vec{\mathbf{e}}_3)^{(e)}$, a tetrahedron has a mass matrix with a symmetric block structure of

$$\boldsymbol{M}_{3\mathrm{D}}^{(e)} = \begin{bmatrix} \boldsymbol{M}_{11}^{3\mathrm{D}} & \boldsymbol{M}_{12}^{3\mathrm{D}} & \boldsymbol{M}_{13}^{3\mathrm{D}} & \boldsymbol{M}_{14}^{3\mathrm{D}} \\ \boldsymbol{M}_{21}^{3\mathrm{D}} & \boldsymbol{M}_{22}^{3\mathrm{D}} & \boldsymbol{M}_{23}^{3\mathrm{D}} & \boldsymbol{M}_{24}^{3\mathrm{D}} \\ \boldsymbol{M}_{31}^{3\mathrm{D}} & \boldsymbol{M}_{32}^{3\mathrm{D}} & \boldsymbol{M}_{33}^{3\mathrm{D}} & \boldsymbol{M}_{34}^{3\mathrm{D}} \\ \boldsymbol{M}_{41}^{3\mathrm{D}} & \boldsymbol{M}_{42}^{3\mathrm{D}} & \boldsymbol{M}_{43}^{3\mathrm{D}} & \boldsymbol{M}_{44}^{3\mathrm{D}} \end{bmatrix} \tag{131a}$$

with each element in this matrix being a 3×3 matrix with diagonal entries of

$$\boldsymbol{M}_{ij}^{3\mathrm{D}} = \begin{bmatrix} M_{ij}^{3\mathrm{D}} & 0 & 0 \\ 0 & M_{ij}^{3\mathrm{D}} & 0 \\ 0 & 0 & M_{ij}^{3\mathrm{D}} \end{bmatrix} \tag{131b}$$

whose components have values of

$$M_{ii}^{3\mathrm{D}} = \frac{\rho_0 |\mathbf{J}_0|}{2} \sum_{k=1}^{4} N_i (1 + N_i)(\xi_k, \eta_k, \zeta_k)\, w_k \qquad i = 1, 2, 3, 4 \tag{132a}$$

$$M_{ij}^{3\mathrm{D}} = M_{ji}^{3\mathrm{D}} = \frac{\rho_0 |\mathbf{J}_0|}{2} \sum_{k=1}^{4} N_i N_j (\xi_k, \eta_k, \zeta_k)\, w_k \qquad i \neq j \tag{132b}$$

with co-ordinates (ξ_i, η_i, ζ_i) and weights w_i of quadrature being given in Table 9, and whose shape functions are defined according to Eq. 129. Here we consider that mass is conserved over the volume of each element, and as such, $\rho |\mathbf{J}| = \rho_0 |\mathbf{J}_0|$. Specifically, there is insufficient time for the normal transport of air into and out of an alveolar sac to occur through breathing in the presence of a shock wave traversing

across the alveolus. Consequently, the mass matrix $\boldsymbol{M}_{3D}^{(e)}$ for each element only needs to be evaluated once.

To rotate this mass matrix for element e, $e \in \{1, 2, \ldots, 60\}$, from its elemental co-ordinate system for the tetrahedron $(\vec{\mathbf{e}}_1, \vec{\mathbf{e}}_2, \vec{\mathbf{e}}_3)^{(e)}$ into a fixed co-ordinate system for the dodecahedron $(\vec{\mathbf{E}}_1, \vec{\mathbf{E}}_2, \vec{\mathbf{E}}_3)$, where it can be assembled with mass matrices from the other 59 elements, one must apply the orthogonal transformation

$$\mathbf{R}_{3D}^{(e)} = \begin{bmatrix} \mathbf{Q}^{(e)} & \mathbf{0} & \mathbf{0} & \mathbf{0} \\ \mathbf{0} & \mathbf{Q}^{(e)} & \mathbf{0} & \mathbf{0} \\ \mathbf{0} & \mathbf{0} & \mathbf{Q}^{(e)} & \mathbf{0} \\ \mathbf{0} & \mathbf{0} & \mathbf{0} & \mathbf{Q}^{(e)} \end{bmatrix} \tag{133a}$$

whose diagonal entries are themselves orthogonal matrices with components

$$\mathbf{Q}^{(e)} = \begin{bmatrix} Q_{11}^{(e)} & Q_{12}^{(e)} & Q_{13}^{(e)} \\ Q_{21}^{(e)} & Q_{22}^{(e)} & Q_{23}^{(e)} \\ Q_{31}^{(e)} & Q_{32}^{(e)} & Q_{33}^{(e)} \end{bmatrix} \tag{133b}$$

so that, accordingly,

$$\mathbf{M}_{3D}^{(e)} = \left(\mathbf{R}_{3D}^{(e)}\right)^{\mathsf{T}} \boldsymbol{M}_{3D}^{(e)} \, \mathbf{R}_{3D}^{(e)} \tag{133c}$$

where $\mathbf{M}_{3D}^{(e)}$ is its mass matrix transformed into the dodecahedral co-ordinate system $(\vec{\mathbf{E}}_1, \vec{\mathbf{E}}_2, \vec{\mathbf{E}}_3)$ according to the map $\left[\{\vec{\mathbf{e}}_1\}\{\vec{\mathbf{e}}_2\}\{\vec{\mathbf{e}}_3\}\right]^{(e)} = \left[\{\vec{\mathbf{E}}_1\}\{\vec{\mathbf{E}}_2\}\{\vec{\mathbf{E}}_3\}\right]\left[\mathbf{Q}^{(e)}\right]$. Even though $\boldsymbol{M}_{3D}^{(e)}$ is a constant mass matrix, $\mathbf{M}_{3D}^{(e)}$ need not be, because $\mathbf{R}_{3D}^{(e)}$ will typically vary over time in our analysis of alveoli subjected to shock waves.

One can now take the mass matrix $\mathbf{M}_{3D}^{(e)}$ for each nodal location in a tetrahedral element e and sum them into their appropriate nodal locations in an overall mass matrix $\mathbf{M}_{3D}$ for the structure, following standard procedures.[119]

6.2 Constitutive Models for Finite Elements

In this study, we implement implicit, elastic, material models. Consequently, their elastic compliance $\boldsymbol{\mathcal{C}}$ and modulus $\boldsymbol{\mathcal{M}}$, where $\boldsymbol{\mathcal{M}} := \boldsymbol{\mathcal{C}}^{-1}$, are taken to be functions of both strain *and* stress in a manner that is consistent with thermodynamics, cf. Section 4 and the Appendix. Furthermore, the conjugate response between temperature and entropy is not incorporated into our finite element solution strategy,

because changes in entropy caused by elastic deformations have been shown to be negligible in our application, cf. Section 4.4.4.2. As such, one can write down the governing constitutive equations for use in finite elements as

$$\boldsymbol{E} = \boldsymbol{\mathcal{C}}^s(\boldsymbol{E}, \boldsymbol{T}) \cdot (\boldsymbol{T} - \boldsymbol{T}_0), \tag{134a}$$

$$\boldsymbol{T} = \boldsymbol{T}_0 + \boldsymbol{\mathcal{M}}^s(\boldsymbol{E}, \boldsymbol{T}) \cdot \boldsymbol{E}, \tag{134b}$$

where $\boldsymbol{T}_0$ is an initial (residual) stress at zero strain, and where $\boldsymbol{\mathcal{C}}^s$ and $\boldsymbol{\mathcal{M}}^s$ are the secant compliance and secant modulus, respectively, obeying $\boldsymbol{\mathcal{M}}^s = (\boldsymbol{\mathcal{C}}^s)^{-1}$. Written symbolically, $\boldsymbol{\mathcal{C}}^s = \boldsymbol{E}/(\boldsymbol{T} - \boldsymbol{T}_0)$ and $\boldsymbol{\mathcal{M}}^s = (\boldsymbol{T} - \boldsymbol{T}_0)/\boldsymbol{E}$.

Expressing these constitutive equations in differential form, one can write

$$\mathrm{d}\boldsymbol{E} = \boldsymbol{\mathcal{C}}^t(\boldsymbol{E}, \boldsymbol{T}) \cdot \mathrm{d}\boldsymbol{T}, \tag{134c}$$

$$\mathrm{d}\boldsymbol{T} = \boldsymbol{\mathcal{M}}^t(\boldsymbol{E}, \boldsymbol{T}) \cdot \mathrm{d}\boldsymbol{E}, \tag{134d}$$

where $\boldsymbol{\mathcal{C}}^t$ and $\boldsymbol{\mathcal{M}}^t$ are the tangent compliance and tangent modulus, respectively, obeying $\boldsymbol{\mathcal{M}}^t = (\boldsymbol{\mathcal{C}}^t)^{-1}$. Written symbolically, $\boldsymbol{\mathcal{C}}^t = \mathrm{d}\boldsymbol{E}/\mathrm{d}\boldsymbol{T}$ and $\boldsymbol{\mathcal{M}}^t = \mathrm{d}\boldsymbol{T}/\mathrm{d}\boldsymbol{E}$.

The components from these elastic compliance and moduli relate to one another via

$$\mathcal{C}^t_{ij} = \left(I_{ik} - \frac{\partial \mathcal{C}^s_{i\ell}}{\partial E_k} (T_\ell - T_{0\,\ell}) \right)^{-1} \left(\mathcal{C}^s_{kj} + \frac{\partial \mathcal{C}^s_{k\ell}}{\partial T_j} (T_\ell - T_{0\,\ell}) \right), \tag{134e}$$

$$\mathcal{M}^t_{ij} = \left(I_{ik} - \frac{\partial \mathcal{M}^s_{i\ell}}{\partial T_k} E_\ell \right)^{-1} \left(\mathcal{M}^s_{kj} + \frac{\partial \mathcal{M}^s_{k\ell}}{\partial E_j} E_\ell \right), \tag{134f}$$

that, because $\boldsymbol{\mathcal{M}}^t = (\boldsymbol{\mathcal{C}}^t)^{-1}$, enables one to write

$$\mathcal{M}^t_{ij} = \left(\mathcal{C}^s_{ik} + \frac{\partial \mathcal{C}^s_{i\ell}}{\partial T_k} (T_\ell - T_{0\,\ell}) \right)^{-1} \left(I_{kj} - \frac{\partial \mathcal{C}^s_{k\ell}}{\partial E_j} (T_\ell - T_{0\,\ell}) \right), \tag{134g}$$

and therefore we observe that if $\boldsymbol{\mathcal{C}}^s(\boldsymbol{E}, \boldsymbol{T})$ and $\boldsymbol{T}_0$ are known, then $\boldsymbol{\mathcal{M}}^s$, $\boldsymbol{\mathcal{C}}^t$, and $\boldsymbol{\mathcal{M}}^t$ can all be determined in terms of this secant compliance and initial stress. The tangent compliance will equate with its associated secant compliance only when all of its elastic parameters are constant valued. A like statement applies for the moduli. It is the moduli $\boldsymbol{\mathcal{M}}^s$ and $\boldsymbol{\mathcal{M}}^t$ that appear later in our finite element equations (Eq. 151).

In finite element implementations, strain $\boldsymbol{E}$ and stress $\boldsymbol{T}$ are treated as vectors of

size $\ell \times 1$ (Voigt components, typically, but not so in our case) while the compliance $\boldsymbol{\mathcal{C}}^s$ and $\boldsymbol{\mathcal{C}}^t$ and the moduli $\boldsymbol{\mathcal{M}}^s$ and $\boldsymbol{\mathcal{M}}^t$ are each matrices of size $\ell \times \ell$, where ℓ denotes the number of independent stress/strain attribute pairs that there are.

Equations 134a and 134b represent an implicit version of a Cauchy elastic material. Equations 134c and 134d represent an implicit version of a hypo-elastic material. Thermodynamically admissible compliance and moduli suitable for soft tissue analysis have been derived in Section 4 and the Appendix.

6.2.1 Moduli for a Chord

Alveolar chords comprise collagen and elastin fibers loaded in parallel.[54,91] Consequently, they are exposed to the same axial strain of $e = \ln(L/L_0)$ but carry different stresses s^c and s^e, where superscript c is for collagen and superscript e is for elastin. The rule of mixtures is used to average their individual responses into a collective chordal response. Specifically, the chordal, elastic, secant modulus is described by the averaged response

$$E^s := \phi\, E^c_s + (1-\phi) E^e_s, \tag{135a}$$

while the chordal, elastic, secant compliance is described by the averaged response

$$C^s = \frac{C^c_s\, C^e_s}{\phi\, C^e_s + (1-\phi) C^c_s}. \tag{135b}$$

Consequently, the chordal, elastic, secant modulus $\boldsymbol{\mathcal{M}}^s$ appearing in Eq. 134b, when described in terms of compliances C^c_s and C^e_s, becomes

$$\mathcal{M}^s = \phi/C^c_s + (1-\phi)/C^e_s. \tag{135c}$$

Given the constitutive equation $s = s_0 + E^s e$, it follows that the stresses average as

$$s_0 := \phi\, s^c_0 + (1-\phi) s^e_0, \tag{135d}$$

$$s := \phi\, s^c + (1-\phi) s^e \tag{135e}$$

because these fibers experience the same strain. The collagen, fiber, volume fraction ϕ that does this partitioning is established by

$$\phi := A^c_0/(A^c_0 + A^e_0), \tag{135f}$$

where the cross-sectional area of a chord is the sum of cross-sectional areas for its collagen A_0^c and elastin A_0^e fibers, here evaluated in a reference state. These areas are assigned via probability density functions according to Table 4. Assuming an isochoric fiber response, i.e., that volume is preserved, it necessarily follows that the homogenization parameter ϕ is a constant, i.e., it is independent of deformation.

The secant compliance C^s that we apply to the collagen and elastin fibers in an alveolar chord are derived in the Appendix, cf. Eq. A-9. This model, under isothermal conditions, describes an elastic secant compliance for collagen of

$$C_s^c(s^c) = \frac{e^c_{1_{\max}}}{s^c - s_0^c}\left(1 - \frac{\sqrt{E_1^c e^c_{1_{\max}}}}{\sqrt{E_1^c e^c_{1_{\max}} + 2(s^c - s_0^c)}}\right) + \frac{1}{E_2^c}, \tag{136a}$$

and an elastic secant compliance for elastin of

$$C_s^e(s^e) = \frac{e^e_{1_{\max}}}{s^e - s_0^e}\left(1 - \frac{\sqrt{E_1^e e^e_{1_{\max}}}}{\sqrt{E_1^e e^e_{1_{\max}} + 2(s^e - s_0^e)}}\right) + \frac{1}{E_2^e}, \tag{136b}$$

whose inverses, viz., $E_s^c \coloneqq 1/C_s^c$ and $E_s^e \coloneqq 1/C_s^e$, are their secant moduli, which are defined in accordance with Eqs. 134a and 134b, and as such, $s^c = s_0^c + E_s^c e$ and $s^e = s_0^e + E_s^e e$. The material properties associated with collagen fibers are a soft initial modulus E_1^c, a stiff terminal modulus E_2^c, and their strain of transition $e^c_{1_{\max}}$, with like material properties describing an elastin fiber, cf. Section 4 and the Appendix.

Whenever $s^c < s_0^c$, the elastic modulus for collagen is taken to be its modulus at zero strain, i.e., $E_s^c = E_1^c E_2^c/(E_1^c + E_2^c)$ so that $C_s^c = (E_1^c + E_2^c)/E_1^c E_2^c$, which helps to ensure numeric stability. Also, whenever a collagen fiber ruptures, $E_s^c \to 0$ and therefore $C_s^c \to \infty$. Like statements apply to the elastin fiber of an alveolar chord.

The elastic fiber compliance in Eq. 136 depend only upon stress, not upon strain, and as such the elastic tangent modulus $\boldsymbol{\mathcal{M}}^t$ of Eq. 134g, which is one of two moduli we use in our finite element implementation, reduces in this 1D case to

$$\mathcal{M}^t = \left(\mathcal{C}^s + \frac{\partial \mathcal{C}^s}{\partial s}(s - s_0)\right)^{-1}, \tag{137a}$$

where C^s is given by Eq. 135b, whose individual compliance C_s^c and C_s^e are described by Eq. 136, and whose derivatives are determined to be

$$\begin{aligned}\frac{\partial \mathcal{C}^s}{\partial s} &= \frac{\partial}{\partial s^c}\frac{\mathcal{C}_s^c(s^c)\,\mathcal{C}_s^e(s^e)}{\phi\,\mathcal{C}_s^e(s^e)+(1-\phi)\,\mathcal{C}_s^c(s^c)}\left(\frac{\partial s}{\partial s^c}\right)^{-1} \\ &\quad+\frac{\partial}{\partial s^e}\frac{\mathcal{C}_s^c(s^c)\,\mathcal{C}_s^e(s^e)}{\phi\,\mathcal{C}_s^e(s^e)+(1-\phi)\,\mathcal{C}_s^c(s^c)}\left(\frac{\partial s}{\partial s^e}\right)^{-1} \\ &= \frac{1}{\left(\phi C_s^e+(1-\phi)C_s^c\right)^2}\left((C_s^e)^2\,\frac{\partial C_s^c}{\partial s^c}+(C_s^c)^2\,\frac{\mathrm{d}C_s^e}{\mathrm{d}s^e}\right), \end{aligned} \tag{137b}$$

wherein

$$\begin{aligned}\frac{\mathrm{d}C_s^c}{\mathrm{d}s^c} &= \frac{e_{1_{\max}}^c}{s^c-s_0^c}\left(\frac{\sqrt{E_1^c e_{1_{\max}}^c}}{\left(E_1^c e_{1_{\max}}^c+2(s^c-s_0^c)\right)^{3/2}}\right. \\ &\quad\left.-\frac{1}{s^c-s_0^c}\left(1-\frac{\sqrt{E_1^c e_{1_{\max}}^c}}{\sqrt{E_1^c e_{1_{\max}}^c+2(s^c-s_0^c)}}\right)\right) \end{aligned} \tag{137c}$$

and

$$\begin{aligned}\frac{\mathrm{d}C_s^e}{\mathrm{d}s^e} &= \frac{e_{1_{\max}}^e}{s^e-s_0^e}\left(\frac{\sqrt{E_1^e e_{1_{\max}}^e}}{\left(E_1^e e_{1_{\max}}^e+2(s^e-s_0^e)\right)^{3/2}}\right. \\ &\quad\left.-\frac{1}{s^e-s_0^e}\left(1-\frac{\sqrt{E_1^e e_{1_{\max}}^e}}{\sqrt{E_1^e e_{1_{\max}}^e+2(s^e-s_0^e)}}\right)\right), \end{aligned} \tag{137d}$$

which follow from Eq. 136. The complexity here comes from the fact that an alveolar chord is a mixture of collagen and elastin fibers.

6.2.2 Moduli for a Pentagon

The secant response of an isothermal, isochoric, elastic pentagon can be written in terms of Eq. 134a, as established in Section 4.4.3, whose constitutive behavior is established via an elastic compliance $\boldsymbol{\mathcal{C}}^s$ defined through the matrix equation

$$\underbrace{\begin{Bmatrix}\xi\\ \varepsilon\\ \gamma\end{Bmatrix}}_{\boldsymbol{E}} = \underbrace{\begin{bmatrix}1/4M^s & 0 & 0\\ 0 & 3/4M^s & 0\\ 0 & 0 & 1/G^s\end{bmatrix}}_{\boldsymbol{\mathcal{C}}^s}\left(\underbrace{\begin{Bmatrix}s^\pi\\ s^\sigma\\ s^\tau\end{Bmatrix}}_{\boldsymbol{T}}-\underbrace{\begin{Bmatrix}s_0^\pi\\ 0\\ 0\end{Bmatrix}}_{\boldsymbol{T}_0}\right) \tag{138a}$$

or in terms of Eq. 134b, whose constitutive behavior is established through an elastic modulus $\boldsymbol{\mathcal{M}}^s$ such that

$$\underbrace{\begin{Bmatrix} s^\pi \\ s^\sigma \\ s^\tau \end{Bmatrix}}_{\boldsymbol{T}} = \underbrace{\begin{Bmatrix} s_0^\pi \\ 0 \\ 0 \end{Bmatrix}}_{\boldsymbol{T}_0} + \underbrace{\begin{bmatrix} 4M^s & 0 & 0 \\ 0 & 4M^s/3 & 0 \\ 0 & 0 & G^s \end{bmatrix}}_{\boldsymbol{\mathcal{M}}^s} \underbrace{\begin{Bmatrix} \xi \\ \varepsilon \\ \gamma \end{Bmatrix}}_{\boldsymbol{E}} \tag{138b}$$

which is used in our finite element implementation. This strain vector $\boldsymbol{E}$ has elements denoting dilation $\xi = \ln\sqrt{ab/a_0b_0}$, squeeze (pure shear) $\varepsilon = \ln\sqrt{ab_0/a_0b}$, and (simple) shear $\gamma = g - g_0$, which in turn are described in terms of two elongations a and b plus an in-plane shear g, with their reference values being a_0, b_0, and g_0. These stretch attributes are acquired via a **QR** decomposition of the deformation gradient $\mathbf{F}$, cf. Section 3.3.6. Dilation, squeeze, and shear are not coupled in this model.

The stress vector $\boldsymbol{T} = \{s^\pi, s^\sigma, s^\tau\}^\mathsf{T}$ conjugate to strain vector $\boldsymbol{E} = \{\xi, \varepsilon, \gamma\}^\mathsf{T}$ has elements of a surface tension $s^\pi = \mathcal{S}_{11} + \mathcal{S}_{22}$, a normal-stress difference $s^\sigma = \mathcal{S}_{11} - \mathcal{S}_{22}$, and a shear stress $s^\tau = \frac{a}{b}\,\mathcal{S}_{12}$. Only surface tension is considered to have a residual state of stress s_0^π, which is necessary for alveolar stability, and is caused, in part, by the presence of surfactant. In a reciprocal sense, the stress components are assigned via $\mathcal{S}_{11} = \frac{1}{2}(s^\pi + s^\sigma)$, $\mathcal{S}_{22} = \frac{1}{2}(s^\pi - s^\sigma)$, and $\mathcal{S}_{12} = \mathcal{S}_{21} = \frac{b}{a}s^\tau$ such that $\mathbf{S} = \mathbf{P}\boldsymbol{\mathcal{U}}^{-1}\boldsymbol{\mathcal{S}}\boldsymbol{\mathcal{U}}^{-\mathsf{T}}\mathbf{P}^\mathsf{T}$ with $\mathbf{S}$ being the second Piola–Kirchhoff stress evaluated in the co-ordinate system of a pentagon, while $\boldsymbol{\mathcal{U}}$ is Laplace stretch, and $\mathbf{P}$ is a re-indexer of co-ordinate labeling needed to ensure invariance under a transformation of Laplace stretch.

The elastic compliance governing an isothermal dilation response is

$$\frac{1}{4M^s(s^\pi)} = \frac{\xi_{1_{\max}}}{s^\pi - s_0^\pi}\left(1 - \frac{\sqrt{M_1\xi_{1_{\max}}}}{\sqrt{M_1\xi_{1_{\max}} + \frac{1}{2}(s^\pi - s_0^\pi)}}\right) + \frac{1}{4M_2}, \tag{139a}$$

where $M^s(s^\pi \leqslant s_0^\pi) = M_1M_2/(M_1 + M_2)$. The elastic compliance governing a shear response is

$$\frac{1}{G^s(s^\tau)} = \frac{\gamma_{1_{\max}}}{|s^\tau|}\left(1 - \frac{\sqrt{G_1\gamma_{1_{\max}}}}{\sqrt{G_1\gamma_{1_{\max}} + 2|s^\tau|}}\right) + \frac{1}{G_2}, \tag{139b}$$

where $G^s(s^\tau = 0) = G_1 G_2/(G_1 + G_2)$.

Only in the mode of dilation is membrane rupture considered to be possible. Nevertheless, whenever a rupture event does happen, both moduli vanish, i.e., $M^s \to 0$ and $G^s \to 0$. The membrane loses structural integrity upon rupture. The material parameters describing the various modes of a membrane are analogous to those used to describe a fiber.

Like the fiber compliance (Eq. 136) used to model an alveolar chord, the membrane compliance (Eq. 139) used to model alveolar septa has components that depend upon stress, but not upon strain. Consequently, the tangent modulus of Eq. 134g required of our finite element implementation has components of

$$\boldsymbol{\mathcal{M}}^t = \begin{bmatrix} \frac{1}{4M^s} + (s^\pi - s_0^\pi)\frac{\mathrm{d}(1/4M^s)}{\mathrm{d}s^\pi} & 0 & 0 \\ 0 & \frac{3}{4M^s} + (s^\pi - s_0^\pi)\frac{\mathrm{d}(3/4M^s)}{\mathrm{d}s^\pi} & 0 \\ 0 & 0 & \frac{1}{G^s} + s^\tau \frac{\mathrm{d}(1/G^s)}{\mathrm{d}s^\tau} \end{bmatrix}^{-1} \tag{140}$$

whose entries, taking into account Eq. 139, are determined to be

$$\frac{1}{4M^s} + (s^\pi - s_0^\pi)\frac{\mathrm{d}(1/4M^s)}{\mathrm{d}s^\pi} = \frac{\xi_{1_{\max}}\sqrt{M_1 \xi_{1_{\max}}}}{4\big(M_1 \xi_{1_{\max}} + \frac{1}{2}(s^\pi + s_0^\pi)\big)^{3/2}} + \frac{1}{4M_2} \tag{141a}$$

$$\frac{1}{G^s} + s^\tau \frac{\mathrm{d}(1/G^s)}{\mathrm{d}s^\tau} = \frac{\gamma_{1_{\max}}\sqrt{G_1 \gamma_{1_{\max}}}}{(G_1 \gamma_{1_{\max}} + 2|s^\tau|)^{3/2}} + \frac{1}{G_2} \tag{141b}$$

and as such, our implementation becomes quite straightforward.

6.2.3 Moduli for a Tetrahedron

The isothermal response of a volume element located within an alveolar sac will have a secant response governed by

$$\underbrace{\begin{Bmatrix} \Pi \\ \sigma_1 \\ \sigma_2 \\ \tau_1 \\ \tau_2 \\ \tau_3 \end{Bmatrix}}_{\boldsymbol{T}} = \underbrace{\begin{Bmatrix} \Pi_0 \\ 0 \\ 0 \\ 0 \\ 0 \\ 0 \end{Bmatrix}}_{\boldsymbol{T}_0} + \underbrace{\begin{bmatrix} 9K & 0 & 0 & 0 & 0 & 0 \\ 0 & 3N & -\frac{3}{2}N & 0 & 0 & 0 \\ 0 & -\frac{3}{2}N & 3N & 0 & 0 & 0 \\ 0 & 0 & 0 & G & 0 & 0 \\ 0 & 0 & 0 & 0 & G & 0 \\ 0 & 0 & 0 & 0 & 0 & G \end{bmatrix}}_{\boldsymbol{\mathcal{M}}^s} \underbrace{\begin{Bmatrix} \Xi \\ \varepsilon_1 \\ \varepsilon_2 \\ \gamma_1 \\ \gamma_2 \\ \gamma_3 \end{Bmatrix}}_{\boldsymbol{E}} \tag{142}$$

where, for air, only the bulk modulus K is non-zero; whereas, for blood, the bulk modulus K, the squeeze modulus N, and the shear modulus G are all non-zero. Blood is actually a nonlinear viscoelastic liquid, but for our application of studying pressure and shear waves traveling across a lung, blood will behave glassy elastic. Blood supports a normal-stress difference, hence $N \neq 0$, and blood supports a shear stress, hence $G \neq 0$.

The strain vector $\boldsymbol{E} = \{\Xi, \varepsilon_1, \varepsilon_2, \gamma_1, \gamma_2, \gamma_3\}^{\mathsf{T}}$ has elements that denote a dilatation $\Xi = \ln \sqrt[3]{abc/a_0b_0c_0}$, two separate squeezes (pure shears) $\varepsilon_1 = \ln \sqrt[3]{ab_0/a_0b}$ and $\varepsilon_2 = \ln \sqrt[3]{bc_0/b_0c}$, and three separate (simple) shears $\gamma_1 = \alpha - \alpha_0$, $\gamma_2 = \beta - \beta_0$, and $\gamma_3 = \gamma - \gamma_0$ whose stretch attributes come from a **QR** decomposition of the deformation gradient $\mathbf{F}$.

The stress vector $\boldsymbol{T} = \{\Pi, \sigma_1, \sigma_2, \tau_1, \tau_2, \tau_3\}^{\mathsf{T}}$ conjugate to strain $\boldsymbol{E}$ has elements that comprise a pressure $\Pi = \mathcal{S}_{11} + \mathcal{S}_{22} + \mathcal{S}_{33} = -3P$ where P denotes the common definition for pressure, two separate normal-stress differences $\sigma_1 = \mathcal{S}_{11} - \mathcal{S}_{22}$ and $\sigma_2 = \mathcal{S}_{22} - \mathcal{S}_{33}$, and three separate shear stresses $\tau_1 = \frac{b}{c}\mathcal{S}_{32}$, $\tau_2 = \frac{a}{c}\mathcal{S}_{31}$, and $\tau_3 = \frac{a}{b}\mathcal{S}_{21} - \alpha\tau_2$. Of these, only pressure has an initial value, viz., Π_0, which represents atmospheric pressure.

Moduli K, N, and G are considered to be constants in our modeling of an alveolar sac; therefore, $\boldsymbol{\mathcal{M}}^t = \boldsymbol{\mathcal{M}}^s$ when modeling alveolar volumes.

6.3 Stiffness Matrices

The solution strategy adopted here uses a secant modulus to determine the stress acquired over a past interval in time spanning from t_0 to t_i, i.e., from an initial to the current time, while a tangent modulus is used to determine an additional stress acquired over a future interval in time spanning from t_i to $t_{i+1} = t_i + \mathrm{d}t$ that is of infinitesimal extent. Here time t_i denotes time at the beginning of a solution step, where all fields are known, while time t_{i+1} denotes time at the end of a solution step, whereat all dependent fields are to be determined.

6.3.1 Strain-Displacement Matrices

Finite element techniques introduce a matrix $\mathbf{B}$ that transforms nodal displacements $\boldsymbol{u}^{(e)}$ for an element e into a vector of thermodynamic strains $\boldsymbol{E}$ located at a Gauss point via the mapping

$$\boldsymbol{E} = \mathbf{B}\,\boldsymbol{u}^{(e)}, \tag{143}$$

where $\boldsymbol{E}$ has size $\ell \times 1$, $\mathbf{B}$ has size $\ell \times nd$, and $\boldsymbol{u}^{(e)}$ has size $nd \times 1$. Here: d is the spatial dimension of an element (viz., $d = 1, 2$ or 3 that, in our case, associate with a chord, a pentagon, and a tetrahedron, respectively); ℓ is the number of conjugate pairs appropriate for an element (viz., $\ell = 1, 3$ or 6 that, in our case, associate with a chord, a pentagon, and a tetrahedron, respectively); while n is the number of nodes in an element (viz., $n = 2, 5$ or 4 that, in our case, associate with a chord, a pentagon, and a tetrahedron, respectively).

In order to make our computation more systematic, the strain-displacement matrix $\mathbf{B}$ is taken to additively decompose into linear and nonlinear constituents such that

$$\mathbf{B} = \mathbf{B}_L + \mathbf{B}_N, \tag{144a}$$

where the entries in $\mathbf{B}_L$ are constants (its strain-displacement relationship is linear in displacement), while the entries in $\mathbf{B}_N$ are functions of displacement (its strain-displacement relationship is nonlinear in displacement). Hence, in accordance with Eq. 143, this decomposition allows definitions for linear and nonlinear strain constituents to be introduced as

$$\boldsymbol{E}_L \coloneqq \mathbf{B}_L \, \boldsymbol{u}^{(e)}, \tag{144b}$$

$$\boldsymbol{E}_N \coloneqq \mathbf{B}_N \, \boldsymbol{u}^{(e)}, \tag{144c}$$

which add, i.e., $\boldsymbol{E} = \boldsymbol{E}_L + \boldsymbol{E}_N$. Their associated derivatives, taken with respect to displacement, produce the formulæ

$$\mathrm{d}\boldsymbol{E}_L = \mathbf{B}_L \, \mathrm{d}\boldsymbol{u}^{(e)} \quad \because \quad \mathrm{d}\mathbf{B}_L = \mathbf{0} \tag{144d}$$

$$\mathrm{d}\boldsymbol{E}_N = \mathbf{B}_N \, \mathrm{d}\boldsymbol{u}^{(e)} + \mathrm{d}\mathbf{B}_N \, \boldsymbol{u}^{(e)} \tag{144e}$$

which obey $\mathrm{d}\boldsymbol{E} = \mathrm{d}\boldsymbol{E}_L + \mathrm{d}\boldsymbol{E}_N$ and $\mathrm{d}\mathbf{B} = \mathrm{d}\mathbf{B}_N$ so that $\mathrm{d}\boldsymbol{E} = \mathbf{B} \, \mathrm{d}\boldsymbol{u}^{(e)} + \mathrm{d}\mathbf{B} \, \boldsymbol{u}^{(e)}$. This differential equation reduces to the classic result $\mathrm{d}\boldsymbol{E} = \mathbf{B} \, \mathrm{d}\boldsymbol{u}^{(e)}$ found in the finite element literature whenever the total displacements are infinitesimal in extent, under which conditions $\mathbf{B}_N \approx \mathbf{0}$ and $\mathbf{dB}_N \approx \mathbf{0}$.

It is advantageous for us to re-write this nonlinear strain-displacement relation $\mathbf{B}_N$ as a product between two matrices such that

$$\mathbf{B}_N = \mathbf{A} \, \mathbf{H}, \tag{145a}$$

where matrix $\mathbf{A}$ has size $\ell \times d$, while matrix $\mathbf{H}$ has size $d \times nd$, with $\mathbf{A}$ comprising various displacement gradients, and $\mathbf{H}$ comprising derivatives of shape functions taken in the element's co-ordinate system, and as such

$$\mathrm{d}\mathbf{B}_N = \mathrm{d}\mathbf{A} \cdot \mathbf{H} \quad \therefore \quad \mathrm{d}\mathbf{H} = \mathbf{0}. \tag{145b}$$

As a consequence of this definition, at least for the elements of interest to us, it turns out that one can establish another useful relationship, specifically

$$\mathrm{d}\mathbf{A}^{\mathsf{T}} \boldsymbol{T} = \mathbf{S}\,\mathbf{H}\,\mathrm{d}\boldsymbol{u}^{(e)}, \tag{145c}$$

wherein $\mathbf{S}$ is a symmetric matrix of size $d \times d$ whose components come from those of its conjugate stress vector $\boldsymbol{T}$ of size $\ell \times 1$. This representation follows whenever one adopts a triangular deconstruction of the deformation gradient $\mathbf{F}$ from which strain $\boldsymbol{E}$ is established, as addressed in Section 3.

6.3.2 Secant Stiffness Matrix

For nonlinear elastic materials, like soft tissues, stress/strain response curves generally become stiffer with increasing deformation.[31,120] Consequently, the slope of a line segment connecting the origin with its current stress/strain state, located somewhere along its response curve, will change with a change in stress and strain, and therefore, its secant modulus will necessarily be a function of stress and/or strain.

A variation in the residual energy R of a deformed elastic body is the difference between variations from two energy sources, assuming a simply connected body whose motion maps have sufficient smoothness, etc. These energies are a potential energy U that stores an internal strain energy, and a work done W that expends energy though an external loading, specifically

$$\delta R = \delta U - \delta W, \tag{146a}$$

such that for an element e one has[121]

$$\delta W = \sum\nolimits_e \boldsymbol{F} \cdot \delta \boldsymbol{u}^{(e)}, \tag{146b}$$

$$\delta U = \sum\nolimits_e \int_V \mathbf{B}^{\mathsf{T}} \boldsymbol{T}\,\mathrm{d}V \cdot \delta \boldsymbol{u}^{(e)}, \tag{146c}$$

or alternatively

$$\delta R = \sum\nolimits_e \boldsymbol{R} \cdot \delta \boldsymbol{u}^{(e)} = \sum\nolimits_e \left(\int_V \mathbf{B}^\mathsf{T} \boldsymbol{T} \, \mathrm{d}V - \boldsymbol{F} \right) \cdot \delta \boldsymbol{u}^{(e)}, \tag{146d}$$

where $\boldsymbol{F}$ and $\boldsymbol{R}$ are vectors denoting the external and residual forces, respectively, while $\boldsymbol{T}$ is a stress conjugate to strain $\boldsymbol{E}$, which are represented here as vector fields, with $\mathbf{B}$ being the well-known strain-displacement matrix found in Eq. 143.

In order to satisfy equilibrium, the internal and external forces of Eq. 146 must be in balance, and therefore, for each element[122]

$$\boldsymbol{R} = \int_V \mathbf{B}^\mathsf{T} \boldsymbol{T} \, \mathrm{d}V - \boldsymbol{F} = \mathbf{0} \tag{147a}$$

whose solution is typically achieved through an iterative process. Substituting the secant constitutive equation (Eq. 134b) along with the strain-displacement relationship of Eq. 143 into the above integral allows it to be rewritten as

$$\begin{aligned} \int_V \mathbf{B}^\mathsf{T} \boldsymbol{T} \, \mathrm{d}V &= \int_V \mathbf{B}^\mathsf{T} \boldsymbol{T}_0 \, \mathrm{d}V + \int_V \mathbf{B}^\mathsf{T} \boldsymbol{\mathcal{M}}^s \boldsymbol{E} \, \mathrm{d}V \\ &= \underbrace{\int_V \mathbf{B}^\mathsf{T} \boldsymbol{T}_0 \, \mathrm{d}V}_{\boldsymbol{F}_0} + \underbrace{\int_V \mathbf{B}^\mathsf{T} \boldsymbol{\mathcal{M}}^s \mathbf{B} \, \mathrm{d}V}_{\mathbf{K}^s} \boldsymbol{u}^{(e)}, \end{aligned} \tag{147b}$$

where $\mathbf{K}^s$ is a stiffness matrix built around the secant modulus $\boldsymbol{\mathcal{M}}^s$, and $\boldsymbol{F}_0$ is an internal force accounting for an initial residual stress of $\boldsymbol{T}_0$. Here $\mathbf{B}$ and $\boldsymbol{\mathcal{M}}^s$ are evaluated at current time t_i, i.e., at the beginning of an integration step.

6.3.3 Tangent Stiffness Matrix

Motivated by a definition for the tangent stiffness matrix being $\mathbf{C} \coloneqq \mathrm{d}\boldsymbol{R}/\mathrm{d}\boldsymbol{u}$ that, e.g., would be appropriate for an updated-Lagrangian finite element formulation,[116] we differentiate Eq. 146d to get $\mathrm{d}\delta R = \delta \mathrm{d}R = \mathrm{d}\boldsymbol{R} \cdot \delta \boldsymbol{u}^{(e)}$ from which one gets

$$\mathrm{d}\boldsymbol{R} = \int_V \mathrm{d}\mathbf{B}^\mathsf{T} \boldsymbol{T} \, \mathrm{d}V + \int_V \mathbf{B}^\mathsf{T} \, \mathrm{d}\boldsymbol{T} \, \mathrm{d}V \eqqcolon \mathbf{C} \, \mathrm{d}\boldsymbol{u}^{(e)}, \tag{148}$$

which follows because the external force $\boldsymbol{F}$ is considered to be a fixed boundary condition during a variation in its displacements. This equation establishes that a change in residual force $\mathrm{d}\boldsymbol{R}$ is needed to further deform an elastic body from an equilibrium condition $\boldsymbol{R} = \mathbf{0}$ that exists at current time t_i into another equilibrium

state associated with some future moment in time $t_{i+1} = t_i + \mathrm{d}t$. This differential force depends upon both the stress $\boldsymbol{T}$ at time t_i and its change $\mathrm{d}\boldsymbol{T}$ that occurs when advancing from t_i to t_{i+1}.

Substituting constitutive equation 134b for $\boldsymbol{T}$ into the first integral of Eq. 148, while incorporating Eq. 145, allows this integral to be rewritten as

$$\int_V \mathrm{d}\mathbf{B}^\mathsf{T}\,\boldsymbol{T}\,\mathrm{d}V = \int_V \mathrm{d}\mathbf{B}^\mathsf{T}\big(\boldsymbol{T}_0 + \boldsymbol{\mathcal{M}}^s\boldsymbol{E}\big)\,\mathrm{d}V = \underbrace{\int_V \mathbf{H}^\mathsf{T}\,\mathbf{S}\,\mathbf{H}\,\mathrm{d}V}_{\mathbf{C}^s}\;\mathrm{d}\boldsymbol{u}^{(e)} \tag{149}$$

where $\boldsymbol{T}_0 + \boldsymbol{\mathcal{M}}^s\boldsymbol{E} \mapsto \mathbf{S}$, and as such, $\mathbf{C}^s$ is that contribution to the tangent stiffness matrix $\mathbf{C}$ attributed to the secant modulus $\boldsymbol{\mathcal{M}}^s$ appearing in Eq. 134b, which is quadratic in $\mathbf{H}$ (not $\mathbf{B}$).

Now, substituting constitutive equation 134d for $\mathrm{d}\boldsymbol{T}$ into the second integral in Eq. 148, while employing Eqs. 144d and 144e to describe strain rate $\mathrm{d}\boldsymbol{E}$, this integral can be re-written as

$$\int_V \mathbf{B}^\mathsf{T}\,\mathrm{d}\boldsymbol{T}\,\mathrm{d}V = \int_V \mathbf{B}^\mathsf{T}\,\boldsymbol{\mathcal{M}}^t\,\mathrm{d}\boldsymbol{E}\,\mathrm{d}V \tag{150a}$$

$$= \underbrace{\int_V \mathbf{B}^\mathsf{T}\,\boldsymbol{\mathcal{M}}^t\,\mathbf{B}\,\mathrm{d}V}_{\mathbf{C}^t}\,\mathrm{d}\boldsymbol{u}^{(e)} + \underbrace{\int_V \mathbf{B}^\mathsf{T}\,\boldsymbol{\mathcal{M}}^t\,\mathrm{d}\mathbf{B}\,\mathrm{d}V}_{\mathbf{K}^t}\,\boldsymbol{u}^{(e)}, \tag{150b}$$

where the contribution to the secant stiffness can be expressed alternatively as

$$\mathbf{K}^t = \int_V \mathbf{H}^\mathsf{T}\,\mathrm{d}\mathbf{S}\,\mathbf{H}\,\mathrm{d}V \quad \text{given} \quad \mathrm{d}\mathbf{S} \coloneqq \mathbf{A}^\mathsf{T}\,\boldsymbol{\mathcal{M}}^t\,\mathrm{d}\mathbf{A} \tag{150c}$$

because of Eq. 145.

6.3.4 Equations of Motion

Pulling everything together, the equations of motion (Eq. 101), when written for an element, are given by

$$\boldsymbol{F} = \mathbf{K}\,\boldsymbol{u}^{(e)} + \mathbf{C}\,\dot{\boldsymbol{u}}^{(e)} + \mathbf{M}\,\ddot{\boldsymbol{u}}^{(e)}, \tag{151a}$$

which has a secant stiffness matrix of

$$\mathbf{K} = \mathbf{K}^s + \mathbf{K}^t, \tag{151b}$$

a tangent stiffness matrix of

$$\mathbf{C} = \mathbf{C}^s + \mathbf{C}^t, \tag{151c}$$

and a forcing function of

$$\boldsymbol{F} = \boldsymbol{F}_{BC} - \boldsymbol{F}_0, \tag{151d}$$

wherein

$$\mathbf{K}^s = \int_V \mathbf{B}^\mathsf{T} \boldsymbol{\mathcal{M}}^s \mathbf{B} \, \mathrm{d}V \tag{151e}$$

$$\mathbf{K}^t = \int_V \mathbf{H}^\mathsf{T} \, \mathrm{d}\mathbf{S}^t \, \mathbf{H} \, \mathrm{d}V \qquad \text{where} \qquad \mathrm{d}\mathbf{S}^t = \mathbf{A}^\mathsf{T} \boldsymbol{\mathcal{M}}^t \, \mathrm{d}\mathbf{A} \tag{151f}$$

$$\mathbf{C}^s = \int_V \mathbf{H}^\mathsf{T} \mathbf{S}^s \, \mathbf{H} \, \mathrm{d}V \qquad \text{where} \qquad \boldsymbol{T}_0 + \boldsymbol{\mathcal{M}}^s \boldsymbol{E} \mapsto \mathbf{S}^s \tag{151g}$$

$$\mathbf{C}^t = \int_V \mathbf{B}^\mathsf{T} \boldsymbol{\mathcal{M}}^t \mathbf{B} \, \mathrm{d}V \tag{151h}$$

$$\boldsymbol{F}_0 = \int_V \mathbf{B}^\mathsf{T} \boldsymbol{T}_0 \, \mathrm{d}V \tag{151i}$$

with $\boldsymbol{F}_{BC}$ being an external force associated with the boundary conditions evaluated at the end of a solution step. All other fields are evaluated at the beginning of this solution step. Superscript s implies that these matrices are evaluated using the secant modulus $\boldsymbol{\mathcal{M}}^s$, while superscript t implies that these matrices are evaluated using the tangent modulus $\boldsymbol{\mathcal{M}}^t$. There are contributions from both moduli in both stiffness matrices.

To minimize an accumulation of roundoff error, it is advantageous to compute $\mathbf{K}^s$ as four separate integrals, viz.,

$$\mathbf{K}^s = \int_V \mathbf{B}_L^\mathsf{T} \boldsymbol{\mathcal{M}}^s \mathbf{B}_L \, \mathrm{d}V + \int_V \mathbf{B}_L^\mathsf{T} \boldsymbol{\mathcal{M}}^s \mathbf{B}_N \, \mathrm{d}V + \int_V \mathbf{B}_N^\mathsf{T} \boldsymbol{\mathcal{M}}^s \mathbf{B}_L \, \mathrm{d}V + \int_V \mathbf{B}_N^\mathsf{T} \boldsymbol{\mathcal{M}}^s \mathbf{B}_N \, \mathrm{d}V$$

and to compute $\mathbf{C}^t$ as four separate integrals, too, viz.,

$$\mathbf{C}^t = \int_V \mathbf{B}_L^\mathsf{T} \boldsymbol{\mathcal{M}}^t \mathbf{B}_L \, \mathrm{d}V + \int_V \mathbf{B}_L^\mathsf{T} \boldsymbol{\mathcal{M}}^t \mathbf{B}_N \, \mathrm{d}V + \int_V \mathbf{B}_N^\mathsf{T} \boldsymbol{\mathcal{M}}^t \mathbf{B}_L \, \mathrm{d}V + \int_V \mathbf{B}_N^\mathsf{T} \boldsymbol{\mathcal{M}}^t \mathbf{B}_N \, \mathrm{d}V$$

while computing $\boldsymbol{F}_0$ as two separate integrals, viz.,

$$\boldsymbol{F}_0 = \int_V \mathbf{B}_L^\mathsf{T} \boldsymbol{T}_0 \, \mathrm{d}V + \int_V \mathbf{B}_N^\mathsf{T} \boldsymbol{T}_0 \, \mathrm{d}V,$$

where the first integral will only need to be evaluated once, as its argument is constant valued.

The vector and matrices established in Eq. 151 pertain to a single finite element. These arrays are to be assembled using standard techniques[119] when describing a finite element model. They will assemble into the form of Eq. 101, at which point these equations of motion can be solved.

6.4 Kinematic Matrices of Finite Elements

To implement our finite element discretization, it is necessary that we know the following matrices for a given element type: the linear strain-displacement matrix $\mathbf{B}_L$, the nonlinear strain-displacement matrix $\mathbf{B}_N$, and its decomposition $\mathbf{B}_N = \mathbf{AH}$, plus the differential rate $\mathrm{d}\mathbf{A}$. These matrices are acquired in the following sections for a chord, a pentagon, and a dodecahedron where **QR** kinematics have been adopted.

6.4.1 Kinematic Matrices for a Chord

The components of Laplace stretch $\boldsymbol{\mathcal{U}}$ can be obtained from a Cholesky factorization of the right, Cauchy–Green, deformation tensor $\mathbf{C} = \mathbf{F}^\mathsf{T}\mathbf{F} = \boldsymbol{\mathcal{U}}^\mathsf{T}\boldsymbol{\mathcal{U}}$,[63] which is a symmetric tensor. For a 1D chord, the only possible deformation is a stretch of the chord in its axial direction. Therefore, in this case, the deformation gradient, as well as the right Cauchy–Green tensor $\mathbf{C}$, have only one component. Consequently, the Laplace stretch $\boldsymbol{\mathcal{U}}$ also consists of only one component, which is denoted by a.

If u is the axial displacement of a chord, then its axial elongation a becomes

$$a = \mathcal{U}_{11} = \sqrt{C_{11}} \tag{152a}$$

with

$$C_{11} = 1 + 2\,\frac{\partial u}{\partial x} + \left(\frac{\partial u}{\partial x}\right)^2 \quad \text{given} \quad F_{11} = 1 + \frac{\partial u}{\partial x}. \tag{152b}$$

This chord is subjected to an axial strain defined as $e = \ln(a) = \ln(L/L_0)$, where L_0 and L are the initial and current lengths of the chord. Here we decompose the total strain into its linear and nonlinear components as

$$e = e_L + e_N \tag{153}$$

as determined by a Taylor expansion of $e = \ln\sqrt{C_{11}}$, which gives

$$e_L = \frac{\partial u}{\partial x} \quad \text{and} \quad e_N = -\frac{1}{2}\,\frac{\partial u}{\partial x}\,\frac{\partial u}{\partial x}, \tag{154}$$

where all contributions have been truncated beyond the quadratic term in this series expansion.

The linear strain-displacement matrix $\mathbf{B}_L$ can now be obtained by expressing the linear strain e_L in terms of its nodal displacements, viz.,

$$e_L = \frac{\partial u}{\partial x} = \sum\nolimits_{i=1}^{2} N_{i,x}\,u_i = \big[[\mathbf{b}_{L1}][\mathbf{b}_{L2}]\big]\big\{\mathbf{u}^{(e)}\big\} = \big[\mathbf{B}_L\big]\big\{\mathbf{u}^{(e)}\big\}, \tag{155a}$$

wherein

$$[\mathbf{b}_{Li}] = [N_{i,x}] = [N_{i,\xi}][\mathbf{J}]^{-1} \quad \text{and} \quad \mathbf{u}^{(e)} = \big\{u_1^{(e)} \quad u_2^{(e)}\big\}^{\mathsf{T}}, \tag{155b}$$

where $N_{i,\xi}$ is the gradient of shape function N_i evaluated in element e's natural co-ordinate system, which maps into gradient $N_{i,x}$ evaluated in the element's physical co-ordinate system via its Jacobian matrix $[\mathbf{J}]$, with $u_1^{(e)}$ and $u_2^{(e)}$ denoting the two nodal displacements of the chord. Shape functions N_i and their gradients $N_{i,\xi}$ for a chord are given in Eq. 15, whose Jacobian matrix $[\mathbf{J}]$ can be found in Eq. 110.

We now introduce machinery that is excessive for the chord, but becomes very useful when constructing the nonlinear strain-displacement matrices for a pentagon and a tetrahedron. Let nonlinear strain e_N be written as a product between some

matrix $\mathbf{A}$ and some vector $\boldsymbol{\theta}$; specifically, let

$$e_N = \tfrac{1}{2}\,[-\partial u/\partial x]\{\partial u/\partial x\} = \tfrac{1}{2}\,\mathbf{A}\,\boldsymbol{\theta} \tag{156}$$

where $\mathbf{A} = [-\partial u/\partial x]$ whose differential is

$$\mathrm{d}\mathbf{A} = \big\{-\partial \mathrm{d}u/\partial x\big\} = \big\{-\textstyle\sum_{i=1}^{2} N_{i,x}\,\mathrm{d}u_i\big\} = \big[[\mathbf{l}_1][\mathbf{l}_2]\big]\big[[\mathbf{d}_1][\mathbf{d}_2]\big]^{\mathsf{T}} = \mathbf{L}\,\mathbf{D} \tag{157a}$$

wherein

$$[\mathbf{l}_i] = [-N_{i,x}] = [-N_{i,\xi}][\mathbf{J}]^{-1} \quad \text{and} \quad [\mathbf{d}_i] = [\mathrm{d}u_i]. \tag{157b}$$

Furthermore, we consider that $\boldsymbol{\theta}$ can be expressed in terms of the nodal displacements as

$$\boldsymbol{\theta} = \big\{\partial u/\partial x\big\} = \big\{\textstyle\sum_{i=1}^{2} N_{i,x}\,u_i\big\} = \big[[\mathbf{h}_1][\mathbf{h}_2]\big]\big\{\mathbf{u}^{(e)}\big\} = \mathbf{H}\,\mathbf{u}^{(e)}, \tag{158a}$$

wherein

$$\mathbf{H} = \big[[\mathbf{h}_1][\mathbf{h}_2]\big] \quad \text{with} \quad [\mathbf{h}_i] = [N_{i,x}] = [N_{i,\xi}][\mathbf{J}]^{-1}, \tag{158b}$$

and we see that, for the chord, there is no difference between $\mathbf{b}_{Li}$ and $\mathbf{h}_i$, which will not be the case in higher-dimensional spaces. Hence, the nonlinear strain-displacement matrix $\mathbf{B}_N$ can be written as

$$\mathbf{B}_N = \mathbf{A}\,\mathbf{H} = \big[[\mathbf{b}_{N1}][\mathbf{b}_{N2}]\big], \tag{159}$$

where $\mathbf{b}_{Ni} = [-\partial u/\partial x][\mathbf{h}_i]$.

6.4.1.1 Tangent Stiffness Matrix $\mathbf{C}^s$

The tangent stiffness matrix $\mathbf{C}^s$ associated with $\boldsymbol{T}_0 + \boldsymbol{\mathcal{M}}^s\boldsymbol{E} \mapsto \mathbf{S}^s = [s_0 + E^s e]$, which is defined in Eq. 135, becomes

$$\mathbf{C}^s = \int_L \mathbf{H}^{\mathsf{T}}\,\mathbf{S}^s\,\mathbf{H}\,A\,\mathrm{d}L = |\mathbf{J}_0| \sum_{i=1}^{n} \mathbf{H}^{\mathsf{T}}\,\mathbf{S}^s(\xi_i)\,\mathbf{H}\,A_0(\xi_i)\,w_i, \tag{160}$$

where an isochoric response is assumed in that $A_0|\mathbf{J}_0| = A|\mathbf{J}|$. Here ξ_i and w_i are the co-ordinates and weights of quadrature for Gauss point i, and A_0 and A are the

initial and current cross-sectional areas of the chord with $A_0(\xi_i)$ being the initial cross-sectional area at Gauss point ξ_i.

6.4.1.2 Tangent Stiffness Matrix $\mathbf{C}^t$

The tangent stiffness matrix $\mathbf{C}^t$, as established in Eq. 150, becomes

$$\mathbf{C}^t = \int_L \mathbf{B}^\mathsf{T} \boldsymbol{\mathcal{M}}^t \mathbf{B}\, A\, \mathrm{d}L = |\mathbf{J}_0| \sum_{i=1}^{n} \mathbf{B}^\mathsf{T} \boldsymbol{\mathcal{M}}^t(\xi_i)\, \mathbf{B}\, A_0(\xi_i)\, w_i, \tag{161a}$$

where axial stress rate $\mathrm{d}s$ is described by a tangent modulus $\boldsymbol{\mathcal{M}}^t$ from Eq. 137.

6.4.1.3 Secant Stiffness Matrix $\mathbf{K}^s$

The secant stiffness matrix $\mathbf{K}^s$, as established in Eq. 147b, becomes

$$\mathbf{K}^s = \int_L \mathbf{B}^\mathsf{T} \boldsymbol{\mathcal{M}}^s \mathbf{B}\, A\, \mathrm{d}L = |\mathbf{J}_0| \sum_{i=1}^{n} \mathbf{B}^\mathsf{T} \boldsymbol{\mathcal{M}}^s(\xi_i)\, \mathbf{B}\, A_0(\xi_i)\, w_i, \tag{162a}$$

where axial stress s is described by a secant modulus $\boldsymbol{\mathcal{M}}^s$ from Eq. 135.

6.4.1.4 Secant Stiffness Matrix $\mathbf{K}^t$

Likewise, a secant stiffness matrix $\mathbf{K}^t$, also established in Eq. 150, becomes

$$\mathbf{K}^t = \int_L \mathbf{H}^\mathsf{T}\, \mathrm{d}\mathbf{S}^t\, \mathbf{H}\, A\, \mathrm{d}L = |\mathbf{J}_0| \sum_{i=1}^{n} \mathbf{H}^\mathsf{T}\, \mathrm{d}\mathbf{S}^t(\xi_i)\, \mathbf{H}\, A_0(\xi_i)\, w_i, \tag{163a}$$

where its stress rate is given by $\mathrm{d}\mathbf{S}^t \coloneqq \mathbf{A}^\mathsf{T} \boldsymbol{\mathcal{M}}^t\, \mathrm{d}\mathbf{A}$.

6.4.2 Kinematic Matrices for a Pentagon

For a planar membrane, components of Laplace stretch $\boldsymbol{\mathcal{U}}$, obtained from a Cholesky factorization of the right Cauchy–Green tensor $\mathbf{C} \coloneqq \mathbf{F}^\mathsf{T}\mathbf{F} = \boldsymbol{\mathcal{U}}^\mathsf{T}\boldsymbol{\mathcal{U}}$, cf. Eq. 34, such that[65]

$$\begin{aligned} \mathcal{U}_{11} = a = \sqrt{C_{11}} \qquad & \mathcal{U}_{12} = a\, g = C_{12}/\mathcal{U}_{11} \\ \mathcal{U}_{21} = 0 \qquad & \mathcal{U}_{22} = b = \sqrt{C_{22} - (\mathcal{U}_{12})^2} \end{aligned} \tag{164}$$

where a and b are elongations (stretches) in the 1- and 2-directions, respectively, and g is a magnitude for shear in the 12 plane, while C_{11}, $C_{12} = C_{21}$ and C_{22} are components of the right Cauchy–Green tensor $\mathbf{C}$. Furthermore, components from

this Cauchy–Green tensor can be expressed in terms of displacement gradients as

$$C_{11} = 1 + 2\,\frac{\partial u}{\partial x} + \left(\frac{\partial u}{\partial x}\right)^2 + \left(\frac{\partial v}{\partial x}\right)^2 \tag{165a}$$

$$C_{12} = \frac{\partial u}{\partial y} + \frac{\partial v}{\partial x} + \frac{\partial u}{\partial x}\frac{\partial u}{\partial y} + \frac{\partial v}{\partial x}\frac{\partial v}{\partial y} \tag{165b}$$

$$C_{22} = 1 + 2\,\frac{\partial v}{\partial y} + \left(\frac{\partial u}{\partial y}\right)^2 + \left(\frac{\partial v}{\partial y}\right)^2 \tag{165c}$$

which arise from the deformation gradient

$$\mathbf{F} = \begin{bmatrix} 1 + \partial u/\partial x & \partial u/\partial y \\ \partial v/\partial x & 1 + \partial v/\partial y \end{bmatrix} \tag{165d}$$

where u and v are displacements associated with the deformation of a planar membrane.

Gradients of shape functions are used to construct the above spatial gradients, viz.,

$$\begin{Bmatrix} N_{i,\xi} \\ N_{i,\eta} \end{Bmatrix} = \begin{bmatrix} \partial x/\partial \xi & \partial y/\partial \xi \\ \partial x/\partial \eta & \partial y/\partial \eta \end{bmatrix} \begin{Bmatrix} N_{i,x} \\ N_{i,y} \end{Bmatrix}$$

whose matrix is the non-singular Jacobian defined in Eq. 121, while $N_{i,\xi}$ and $N_{i,\eta}$ are gradients of the shape functions in their natural co-ordinates, as established in Eq. 24 for pentagons. These are evaluated at the i^{th} Gauss point for the quadrature rule used that, in our case, is found in Eqs. 97 and 98. It is necessary to invert this equation for it to become useful for us so that

$$\begin{Bmatrix} N_{i,x} \\ N_{i,y} \end{Bmatrix} = \begin{bmatrix} \partial x/\partial \xi & \partial y/\partial \xi \\ \partial x/\partial \eta & \partial y/\partial \eta \end{bmatrix}^{-1} \begin{Bmatrix} N_{i,\xi} \\ N_{i,\eta} \end{Bmatrix} \tag{166a}$$

from which one determines

$$\begin{Bmatrix} \partial u/\partial x \\ \partial u/\partial y \\ \partial v/\partial x \\ \partial v/\partial y \end{Bmatrix} = \begin{Bmatrix} \sum_{i=1}^{5} N_{i,x} u_i \\ \sum_{i=1}^{5} N_{i,y} u_i \\ \sum_{i=1}^{5} N_{i,x} v_i \\ \sum_{i=1}^{5} N_{i,y} v_i \end{Bmatrix} \tag{166b}$$

with $N_{i,x}$ and $N_{i,y}$ being employed below.

The thermodynamic strain attributes that we use are defined in Eq. 42 and can be expressed in terms of the components of Laplace stretch as

$$\xi = \ln\left(\sqrt{\frac{a}{a_0}\frac{b}{b_0}}\right), \quad \varepsilon = \ln\left(\sqrt{\frac{a}{a_0}\frac{b_0}{b}}\right), \quad \gamma = g - g_0. \tag{167}$$

Without loss of generality, we consider the membrane to be initially undeformed, which allows us to set a_0 and b_0 to one, while the initial shear g_0 is taken as zero. To gain computational advantage, we decompose these strain attributes into linear and nonlinear components; specifically, we consider

$$\xi = \xi_L + \xi_{N1} + \xi_{N2} + \xi_{N3}, \tag{168a}$$

$$\varepsilon = \varepsilon_L + \varepsilon_{N1} + \varepsilon_{N2} + \varepsilon_{N3}, \tag{168b}$$

$$\gamma = \gamma_L + \gamma_{N1} + \gamma_{N2} + \gamma_{N3}. \tag{168c}$$

Traditionally, finite element constructions decompose strain into a linear component and a nonlinear component. However, in our case, a further decomposition of the nonlinear strain component into three separate components makes our computation much easier, as is realized later.

Decomposition of strain attributes in Eq. 167 is achieved via Taylor expansions that retain terms through second-order. The linear and nonlinear components of these strain attributes, thus obtained, are given as

$$\xi_L = \frac{1}{2}\left(\frac{\partial u}{\partial x} + \frac{\partial v}{\partial y}\right) \tag{169a}$$

$$\xi_N = \frac{1}{4}\left(-\frac{\partial v}{\partial y}\frac{\partial v}{\partial y} - \frac{\partial u}{\partial x}\frac{\partial u}{\partial x} - 2\frac{\partial u}{\partial y}\frac{\partial v}{\partial x}\right) \tag{169b}$$

$$\varepsilon_L = \frac{1}{2}\left(\frac{\partial u}{\partial x} - \frac{\partial v}{\partial y}\right) \tag{169c}$$

$$\varepsilon_N = \frac{1}{4}\left(2\frac{\partial v}{\partial x}\frac{\partial v}{\partial x} + \frac{\partial v}{\partial y}\frac{\partial v}{\partial y} - \frac{\partial u}{\partial x}\frac{\partial u}{\partial x} + 2\frac{\partial u}{\partial y}\frac{\partial v}{\partial x}\right) \tag{169d}$$

$$\gamma_L = \frac{\partial u}{\partial y} + \frac{\partial v}{\partial x} \tag{169e}$$

$$\gamma_N = \frac{\partial v}{\partial x}\frac{\partial v}{\partial y} - 2\frac{\partial u}{\partial x}\frac{\partial v}{\partial x} - \frac{\partial u}{\partial x}\frac{\partial u}{\partial y} \tag{169f}$$

where the linear components of these strain attributes consist only of first-order derivatives in the displacements, while the nonlinear components contain the second-

order terms. (Recall that terms with third-order and higher derivatives in displacement have been truncated.) The nonlinear components of strain have been arranged in such a way that when represented in a set of base vectors, they can be written as the product of a matrix and a vector that contain these derivatives of displacement. To achieve that, for the dilatation ξ and squeeze ε strains, the nonlinear components contain squares of derivatives and products between different derivatives of displacement. Note that the nonlinear part of the total shear strain contains only products of different derivatives of displacements, i.e., no square term is present in its expression.

In terms of the nodal displacements, the vector containing the linear strain attributes, i.e., $\boldsymbol{E}_L$, can be written as

$$\begin{aligned}\boldsymbol{E}_L &= \begin{Bmatrix}\xi_L\\ \varepsilon_L\\ \gamma_L\end{Bmatrix} = \begin{Bmatrix}\frac{1}{2}\,u_{,x} + \frac{1}{2}\,v_{,y}\\ \frac{1}{2}\,u_{,x} - \frac{1}{2}\,v_{,y}\\ u_{,y} + v_{,x}\end{Bmatrix} = \sum_{i=1}^{5}\begin{bmatrix}\frac{1}{2}\,N_{i,x} & \frac{1}{2}\,N_{i,y}\\ \frac{1}{2}\,N_{i,x} & -\frac{1}{2}\,N_{i,y}\\ N_{i,y} & N_{i,x}\end{bmatrix}\begin{Bmatrix}u_i\\ v_i\end{Bmatrix}\\ &= \big[[\mathbf{b}_{L1}][\mathbf{b}_{L2}][\mathbf{b}_{L3}][\mathbf{b}_{L4}][\mathbf{b}_{L5}]\big]\big\{\mathbf{u}^{(e)}\big\} = \mathbf{B}_L\,\mathbf{u}^{(e)}\end{aligned} \tag{170a}$$

where

$$[\mathbf{b}_{Li}] = \begin{bmatrix}\frac{1}{2}\,N_{i,x} & \frac{1}{2}\,N_{i,y}\\ \frac{1}{2}\,N_{i,x} & -\frac{1}{2}\,N_{i,y}\\ N_{i,y} & N_{i,x}\end{bmatrix} \tag{170b}$$

$$\mathbf{u}^{(e)} = \big\{u_1 \quad v_1 \quad u_2 \quad v_2 \quad u_3 \quad v_3 \quad u_4 \quad v_4 \quad u_5 \quad v_5\big\}^{\mathsf{T}} \tag{170c}$$

for element e, whose matrix entries come from Eq. 166.

Now let nonlinear strain $\boldsymbol{E}_{N1}$ be written as a product between some matrix $\mathbf{A}_1$ and some vector $\boldsymbol{\theta}_1$; specifically, let

$$\begin{aligned}\mathbf{E}_{N1} &= \begin{Bmatrix}\xi_{N1}\\ \varepsilon_{N1}\\ \gamma_{N1}\end{Bmatrix} = \begin{Bmatrix}-\frac{1}{4}\,v_{,y}^2\\ -\frac{1}{4}\,u_{,x}^2 + \frac{1}{4}\,v_{,y}^2\\ v_{,x}\,v_{,y}\end{Bmatrix}\\ &= \frac{1}{2}\begin{bmatrix}0 & -\frac{1}{2}\,\partial v/\partial y\\ -\frac{1}{2}\,\partial u/\partial x & \frac{1}{2}\,\partial v/\partial y\\ 0 & 2\,\partial v/\partial x\end{bmatrix}\begin{Bmatrix}\partial u/\partial x\\ \partial v/\partial y\end{Bmatrix}\\ &= \tfrac{1}{2}\,\mathbf{A}_1\,\boldsymbol{\theta}_1\end{aligned}$$

with

$$\begin{aligned}
\mathrm{d}\mathbf{A}_1 &= \begin{bmatrix} 0 & -\frac{1}{2}\,\partial \mathrm{d}v/\partial y \\ -\frac{1}{2}\,\partial \mathrm{d}u/\partial x & \frac{1}{2}\,\partial \mathrm{d}v/\partial y \\ 0 & 2\,\partial \mathrm{d}v/\partial x \end{bmatrix} \\
&= \begin{bmatrix} 0 & -\frac{1}{2}\sum_{i=1}^{5} N_{i,y}\,\mathrm{d}v_i \\ -\frac{1}{2}\sum_{i=1}^{5} N_{i,x}\,\mathrm{d}u_i & \frac{1}{2}\sum_{i=1}^{5} N_{i,y}\,\mathrm{d}v_i \\ 0 & 2\sum_{i=1}^{5} N_{i,x}\,\mathrm{d}v_i \end{bmatrix} \\
&= \Big[[\mathbf{l}_1][\mathbf{l}_2][\mathbf{l}_3][\mathbf{l}_4][\mathbf{l}_5]\Big]\,\Big[[\mathbf{d}_1][\mathbf{d}_2][\mathbf{d}_3][\mathbf{d}_4][\mathbf{d}_5]\Big]^{\mathsf{T}} = \mathbf{L}_1\mathbf{D}_1
\end{aligned} \tag{171a}$$

wherein

$$[\mathbf{l}_i] = \begin{bmatrix} 0 & -\frac{1}{2}\,N_{i,y} \\ -\frac{1}{2}\,N_{i,x} & \frac{1}{2}\,N_{i,y} \\ 0 & 2\,N_{i,x} \end{bmatrix} \quad \text{and} \quad [\mathbf{d}_i] = \begin{bmatrix} \mathrm{d}u_i & 0 \\ 0 & \mathrm{d}v_i \end{bmatrix}. \tag{171b}$$

To obtain the nonlinear strain-displacement matrix, we require the nonlinear strain to be expressed in terms of the nodal displacements. This is achieved by expressing the elements of displacement gradient in terms of the nodal displacements by using the shape functions, specifically, the vector $\boldsymbol{\theta}_1$ can be written as

$$\boldsymbol{\theta}_1 = \begin{Bmatrix} \partial u/\partial x \\ \partial v/\partial y \end{Bmatrix} = \begin{Bmatrix} \sum_{i=1}^{5} N_{i,x}\,u_i \\ \sum_{i=1}^{5} N_{i,y}\,v_i \end{Bmatrix} = \Big[[\mathbf{h}_1][\mathbf{h}_2][\mathbf{h}_3][\mathbf{h}_4][\mathbf{h}_5]\Big]\,\{\mathbf{u}^{(e)}\} = \mathbf{H}_1\mathbf{u}^{(e)} \tag{172a}$$

where the components of $\mathbf{H}_1$ contains the derivatives of shape functions with respect to spatial variables, i.e.,

$$[\mathbf{h}_i] = \begin{bmatrix} N_{i,x} & 0 \\ 0 & N_{i,y} \end{bmatrix}. \tag{172b}$$

Therefore, the first nonlinear strain-displacement matrix $\mathbf{B}_{N1}$ can be written as

$$\mathbf{B}_{N1} = \mathbf{A}_1\,\mathbf{H}_1 = \Big[[\mathbf{b}_{N1}][\mathbf{b}_{N2}][\mathbf{b}_{N3}][\mathbf{b}_{N4}][\mathbf{b}_{N5}]\Big] \tag{173a}$$

where the components of $\mathbf{B}_{N1}$ are given as

$$[\mathbf{b}_{Ni}] = \begin{bmatrix} 0 & -\frac{1}{2}\,\partial v/\partial y \\ -\frac{1}{2}\,\partial u/\partial x & \frac{1}{2}\,\partial v/\partial y \\ 0 & 2\,\partial v/\partial x \end{bmatrix} \begin{bmatrix} N_{i,x} & 0 \\ 0 & N_{i,y} \end{bmatrix}. \tag{173b}$$

In a similar manner, the second nonlinear strain terms can be written as

$$\begin{aligned} \mathbf{E}_{N2} = \begin{Bmatrix} \xi_{N2} \\ \varepsilon_{N2} \\ \gamma_{N2} \end{Bmatrix} &= \begin{Bmatrix} -\frac{1}{2}\,u_{,y}\,v_{,x} \\ \frac{1}{2}\,u_{,y}\,v_{,x} \\ -2\,u_{,x}\,v_{,x} \end{Bmatrix} \\ &= \frac{1}{2} \begin{bmatrix} -\partial v/\partial x & 0 \\ \partial v/\partial x & 0 \\ 0 & -4\,\partial u/\partial x \end{bmatrix} \begin{Bmatrix} \partial u/\partial y \\ \partial v/\partial x \end{Bmatrix} = \tfrac{1}{2}\,\mathbf{A}_2\,\boldsymbol{\theta}_2 \end{aligned} \tag{174}$$

with

$$\begin{aligned} \mathrm{d}\mathbf{A}_2 &= \begin{bmatrix} -\partial \mathrm{d}v/\partial x & 0 \\ \partial \mathrm{d}v/\partial x & 0 \\ 0 & -4\,\partial \mathrm{d}u/\partial x \end{bmatrix} \\ &= \begin{bmatrix} -\sum_{i=1}^{5} N_{i,x}\,\mathrm{d}v_i & 0 \\ \sum_{i=1}^{5} N_{i,x}\,\mathrm{d}v_i & 0 \\ 0 & -4\,\sum_{i=1}^{5} N_{i,x}\,\mathrm{d}u_i \end{bmatrix} \\ &= \Big[[\mathbf{l}_1][\mathbf{l}_2][\mathbf{l}_3][\mathbf{l}_4][\mathbf{l}_5]\Big] \Big[[\mathbf{d}_1][\mathbf{d}_2][\mathbf{d}_3][\mathbf{d}_4][\mathbf{d}_5]\Big]^{\mathsf{T}} = \mathbf{L}_2\mathbf{D}_2 \end{aligned} \tag{175a}$$

wherein

$$[\mathbf{l}_i] = \begin{bmatrix} -N_{i,x} & 0 \\ N_{i,x} & 0 \\ 0 & -4\,N_{i,x} \end{bmatrix} \quad \text{and} \quad [\mathbf{d}_i] = \begin{bmatrix} \mathrm{d}v_i & 0 \\ 0 & \mathrm{d}u_i \end{bmatrix}. \tag{175b}$$

The vector $\boldsymbol{\theta}_2$ is expressed in terms of the nodal displacements with the use of shape

functions as

$$\boldsymbol{\theta}_2 = \begin{Bmatrix} \partial u/\partial y \\ \partial v/\partial x \end{Bmatrix} = \begin{Bmatrix} \sum_{i=1}^{5} N_{i,y}\, u_i \\ \sum_{i=1}^{5} N_{i,x}\, v_i \end{Bmatrix} = \Big[[\mathbf{h}_1][\mathbf{h}_2][\mathbf{h}_3][\mathbf{h}_4][\mathbf{h}_5] \Big] \left\{ \mathbf{u}^{(e)} \right\} = \mathbf{H}_2 \mathbf{u}^{(e)} \tag{176a}$$

where the elements of $\mathbf{H}_2$ are given as

$$[\mathbf{h}_i] = \begin{bmatrix} N_{i,y} & 0 \\ 0 & N_{i,x} \end{bmatrix}. \tag{176b}$$

Hence, the second nonlinear strain-displacement matrix $\mathbf{B}_{N2}$ becomes

$$\mathbf{B}_{N2} = \mathbf{A}_2\, \mathbf{H}_2 = \Big[[\mathbf{b}_{N1}][\mathbf{b}_{N2}][\mathbf{b}_{N3}][\mathbf{b}_{N4}][\mathbf{b}_{N5}] \Big] \tag{177a}$$

where its elements are given as

$$[\mathbf{b}_{Ni}] = \begin{bmatrix} -\partial v/\partial x & 0 \\ \partial v/\partial x & 0 \\ 0 & -4\, \partial u/\partial x \end{bmatrix} \begin{bmatrix} N_{i,y} & 0 \\ 0 & N_{i,x} \end{bmatrix}. \tag{177b}$$

In like manner, the third nonlinear strain terms can be written as

$$\mathbf{E}_{N3} = \begin{Bmatrix} \xi_{N3} \\ \varepsilon_{N3} \\ \gamma_{N3} \end{Bmatrix} = \begin{Bmatrix} -\frac{1}{4}\, u_{,x}^2 \\ \frac{1}{2}\, v_{,x}^2 \\ -u_{,y}\, u_{,x} \end{Bmatrix}$$

$$= \frac{1}{2} \begin{bmatrix} -\frac{1}{2}\, \partial u/\partial x & 0 \\ 0 & \partial v/\partial x \\ -2\, \partial u/\partial y & 0 \end{bmatrix} \begin{Bmatrix} \partial u/\partial x \\ \partial v/\partial x \end{Bmatrix} = \tfrac{1}{2}\, \mathbf{A}_3\, \boldsymbol{\theta}_3 \tag{178}$$

with

$$\begin{aligned}
\mathrm{d}\mathbf{A}_3 &= \begin{bmatrix} -\frac{1}{2}\,\partial \mathrm{d}u/\partial x & 0 \\ 0 & \partial \mathrm{d}v/\partial x \\ -2\,\partial \mathrm{d}u/\partial y & 0 \end{bmatrix} \\
&= \begin{bmatrix} -\frac{1}{2}\,\sum_{i=1}^{5} N_{i,x}\,\mathrm{d}u_i & 0 \\ 0 & \sum_{i=1}^{5} N_{i,x}\,\mathrm{d}v_i \\ -2\,\sum_{i=1}^{5} N_{i,y}\,\mathrm{d}u_i & 0 \end{bmatrix} \\
&= \Big[[\mathbf{l}_1][\mathbf{l}_2][\mathbf{l}_3][\mathbf{l}_4][\mathbf{l}_5]\Big]\,\Big[[\mathbf{d}_1][\mathbf{d}_2][\mathbf{d}_3][\mathbf{d}_4][\mathbf{d}_5]\Big]^{\mathsf{T}} = \mathbf{L}_3\mathbf{D}_3
\end{aligned} \tag{179a}$$

wherein

$$[\mathbf{l}_i] = \begin{bmatrix} -\frac{1}{2}\,N_{i,x} & 0 \\ 0 & N_{i,x} \\ -2\,N_{i,y} & 0 \end{bmatrix} \quad \text{and} \quad [\mathbf{d}_i] = \begin{bmatrix} \mathrm{d}u_i & 0 \\ 0 & \mathrm{d}v_i \end{bmatrix}. \tag{179b}$$

The vector $\boldsymbol{\theta}_3$ is expressed in terms of the nodal displacements with the use of shape functions as

$$\boldsymbol{\theta}_3 = \begin{Bmatrix} \partial u/\partial x \\ \partial v/\partial x \end{Bmatrix} = \begin{Bmatrix} \sum_{i=1}^{5} N_{i,x}\,u_i \\ \sum_{i=1}^{5} N_{i,x}\,v_i \end{Bmatrix} = \Big[[\mathbf{h}_1][\mathbf{h}_2][\mathbf{h}_3][\mathbf{h}_4][\mathbf{h}_5]\Big]\left\{\mathbf{u}^{(e)}\right\} = \mathbf{H}_3\mathbf{u}^{(e)} \tag{180a}$$

where the components of $\mathbf{H}_3$ contains the derivatives of shape functions with respect to spatial variables, i.e.,

$$[\mathbf{h}_i] = \begin{bmatrix} N_{i,x} & 0 \\ 0 & N_{i,x} \end{bmatrix}. \tag{180b}$$

Therefore, the first nonlinear strain-displacement matrix $\mathbf{B}_{N3}$ can be written as

$$\mathbf{B}_{N3} = \mathbf{A}_3\,\mathbf{H}_3 = \Big[[\mathbf{b}_{N1}][\mathbf{b}_{N2}][\mathbf{b}_{N3}][\mathbf{b}_{N4}][\mathbf{b}_{N5}]\Big] \tag{181a}$$

where the components of $\mathbf{B}_{N3}$ are given as

$$[\mathbf{b}_{Ni}] = \begin{bmatrix} -\frac{1}{2}\,\partial u/\partial x & 0 \\ 0 & \partial v/\partial y \\ -2\,\partial u/\partial y & 0 \end{bmatrix} \begin{bmatrix} N_{i,x} & 0 \\ 0 & N_{i,x} \end{bmatrix}. \tag{181b}$$

The total nonlinear strain-displacement matrix is evaluated as the summation of its components $\mathbf{B}_{N1}$, $\mathbf{B}_{N2}$, and $\mathbf{B}_{N3}$. Now, with all the strain-displacement matrices evaluated, we are ready to compute the stiffness matrix for a planar membrane.

To obtain the stiffness matrix for a planar membrane, we need to compute the four constituent strain-displacement matrices $\mathbf{C}^s$, $\mathbf{C}^t$, $\mathbf{K}^s$, and $\mathbf{K}^t$, as mentioned earlier. These strain-displacement matrices are obtained by expressing their corresponding strain components in terms of the five nodal displacements, with help from the shape functions.

6.4.2.1 Tangent Stiffness Matrix $\mathbf{C}^s$

The tangent stiffness matrix $\mathbf{C}^s$, as established in Eq. 149, becomes

$$\mathbf{C}^s = \int_{\pentagon} \mathbf{H}^\mathsf{T}\,\mathbf{S}^s\,\mathbf{H}\,H\,\mathrm{d}A = |\mathbf{J}_0| \sum_{i=1}^{n} \mathbf{H}^\mathsf{T}\,\mathbf{S}^s(\xi_i,\eta_i)\,\mathbf{H}\,H_{0\,i}\,w_i \tag{182a}$$

wherein

$$\mathbf{S}^s = \begin{bmatrix} \mathcal{S}_{11} & \mathcal{S}_{12} \\ \mathcal{S}_{21} & \mathcal{S}_{22} \end{bmatrix} \qquad \text{with} \qquad \mathcal{S}_{21} = \mathcal{S}_{12} \tag{182b}$$

where an isochoric response is assumed in that $H_0|\mathbf{J}_0| = H|\mathbf{J}|$. Here H_0 and H are the initial and current height or thickness of the septal membrane, and ξ_i, η_i, and w_i are the co-ordinates and weights of quadrature for Gauss point i whereat the membrane has an initial thickness of $H_{0\,i}$.

The stress vector $\boldsymbol{T} = \{s^\pi, s^\sigma, s^\tau\}^\mathsf{T}$ conjugate to strain vector $\boldsymbol{E} = \{\xi, \varepsilon, \gamma\}^\mathsf{T}$ has elements of a surface tension $s^\pi = \mathcal{S}_{11} + \mathcal{S}_{22}$, a normal-stress difference $s^\sigma = \mathcal{S}_{11} - \mathcal{S}_{22}$, and a shear stress $s^\tau = \frac{a}{b}\,\mathcal{S}_{12}$. Only surface tension is considered to have a residual state of stress s_0^π, which is necessary for alveolar stability, and is caused, in part, by the presence of surfactant. In a reciprocal sense, the stress components are assigned via

$$\mathcal{S}_{11} = \frac{1}{2}(s^\pi + s^\sigma), \quad \mathcal{S}_{22} = \frac{1}{2}(s^\pi - s^\sigma), \quad \text{and} \quad \mathcal{S}_{12} = \mathcal{S}_{21} = \frac{b}{a}s^\tau, \tag{183}$$

such that $\mathbf{S} = \mathbf{P}\boldsymbol{\mathcal{U}}^{-1}\boldsymbol{\mathcal{S}}\boldsymbol{\mathcal{U}}^{-\mathsf{T}}\mathbf{P}^\mathsf{T}$ with $\mathbf{S}$ being the second Piola–Kirchhoff stress evaluated in the co-ordinate system of a pentagon, while $\boldsymbol{\mathcal{U}}$ is the Laplace stretch, and $\mathbf{P}$ is a re-indexer of co-ordinate labeling needed to ensure invariance under a

transformation of Laplace stretch.

6.4.2.2 Tangent Stiffness Matrix $\mathbf{C}^t$

The tangent stiffness matrix $\mathbf{C}^t$, as established in Eq. 150, becomes

$$\mathbf{C}^t = \int_{\pentagon} \mathbf{B}^{\mathsf{T}}\, \boldsymbol{\mathcal{M}}^t\, \mathbf{B}\, |\mathbf{J}|\, H\, \mathrm{d}A = |\mathbf{J}_0| \sum_{i=1}^{n} \mathbf{B}^{\mathsf{T}}\, \boldsymbol{\mathcal{M}}^t(\xi_i, \eta_i)\, \mathbf{B}\, H_{0\,i}\, w_i, \tag{184}$$

where its associated stress rate is described by a tangent modulus $\boldsymbol{\mathcal{M}}^t$ that, for biologic membranes, is described by Eq. 140.

6.4.2.3 Secant Stiffness Matrix $\mathbf{K}^s$

The secant stiffness matrix $\mathbf{K}^s$, as established in Eq. 147b, becomes

$$\mathbf{K}^s = \int_{\pentagon} \mathbf{B}^{\mathsf{T}}\, \boldsymbol{\mathcal{M}}^s\, \mathbf{B}\, H\, \mathrm{d}A = |\mathbf{J}_0| \sum_{i=1}^{n} \mathbf{B}^{\mathsf{T}}\, \boldsymbol{\mathcal{M}}^s(\xi_i, \eta_i)\, \mathbf{B}\, H_{0\,i}\, w_i, \tag{185}$$

where its associated stress is described by a secant modulus $\boldsymbol{\mathcal{M}}^s$ that, for biologic membranes, is described by Eq. 138b.

6.4.2.4 Secant Stiffness Matrix $\mathbf{K}^t$

Likewise, a secant stiffness matrix $\mathbf{K}^t$, also established in Eq. 150, becomes

$$\mathbf{K}^t = \int_{\pentagon} \mathbf{H}^{\mathsf{T}}\, \mathrm{d}\mathbf{S}^t\, \mathbf{H}\, H\, \mathrm{d}A = |\mathbf{J}_0| \sum_{i=1}^{n} \mathbf{H}^{\mathsf{T}}\, \mathrm{d}\mathbf{S}^t(\xi_i, \eta_i)\, \mathbf{H}\, H_{0\,i}\, w_i, \tag{186}$$

where its associated stress rate is given by $\mathrm{d}\mathbf{S}^t := \mathbf{A}^{\mathsf{T}}\, \boldsymbol{\mathcal{M}}^t\, \mathrm{d}\mathbf{A}$.

6.4.3 Kinematic Matrices for a Tetrahedron

Let us consider a tetrahedron subjected to displacements of u, v, and w in its three spatial directions, respectively. In terms of these displacements, elements of the deformation gradient can be written as

$$\mathbf{F} = \begin{bmatrix} 1 + \partial u/\partial x & \partial u/\partial y & \partial u/\partial z \\ \partial v/\partial x & 1 + \partial v/\partial y & \partial v/\partial z \\ \partial w/\partial x & \partial w/\partial y & 1 + \partial w/\partial z \end{bmatrix}. \tag{187}$$

Therefore, components of the right Cauchy–Green deformation tensor, defined as $\mathbf{C} \coloneqq \mathbf{F}^{\mathsf{T}}\mathbf{F}$, can be expressed as

$$C_{11} = \left(\frac{\partial u}{\partial x}\right)^2 + \left(\frac{\partial v}{\partial x}\right)^2 + \left(\frac{\partial w}{\partial x}\right)^2 + 2\,\frac{\partial u}{\partial x} + 1 \tag{188a}$$

$$C_{22} = \left(\frac{\partial u}{\partial y}\right)^2 + \left(\frac{\partial v}{\partial y}\right)^2 + \left(\frac{\partial w}{\partial y}\right)^2 + 2\,\frac{\partial v}{\partial y} + 1 \tag{188b}$$

$$C_{33} = \left(\frac{\partial u}{\partial z}\right)^2 + \left(\frac{\partial v}{\partial z}\right)^2 + \left(\frac{\partial w}{\partial z}\right)^2 + 2\,\frac{\partial w}{\partial z} + 1 \tag{188c}$$

$$C_{12} = C_{21} = \frac{\partial u}{\partial y} + \frac{\partial v}{\partial x} + \frac{\partial u}{\partial x}\frac{\partial u}{\partial y} + \frac{\partial v}{\partial x}\frac{\partial v}{\partial y} + \frac{\partial w}{\partial x}\frac{\partial w}{\partial y} \tag{188d}$$

$$C_{13} = C_{31} = \frac{\partial u}{\partial z} + \frac{\partial w}{\partial x} + \frac{\partial u}{\partial x}\frac{\partial u}{\partial z} + \frac{\partial v}{\partial x}\frac{\partial v}{\partial z} + \frac{\partial w}{\partial x}\frac{\partial w}{\partial z} \tag{188e}$$

$$C_{23} = C_{32} = \frac{\partial v}{\partial z} + \frac{\partial w}{\partial y} + \frac{\partial u}{\partial y}\frac{\partial u}{\partial z} + \frac{\partial v}{\partial y}\frac{\partial v}{\partial z} + \frac{\partial w}{\partial y}\frac{\partial w}{\partial z}. \tag{188f}$$

The Laplace stretch associated with an alveolar volume is a 3×3 upper-triangular matrix whose elements have specific geometric interpretations. The Laplace stretch can be written in matrix form as[64]

$$\mathcal{U}_{ij} = \begin{bmatrix} a & a\gamma & a\beta \\ 0 & b & b\alpha \\ 0 & 0 & c \end{bmatrix}. \tag{189}$$

It is possible to express the components of Laplace stretch $\boldsymbol{\mathcal{U}}$ in terms of displacement gradients through a Cholesky factorization of the right Cauchy–Green tensor $\mathbf{C} = \boldsymbol{\mathcal{U}}^{\mathsf{T}}\boldsymbol{\mathcal{U}}$. Specifically, the elements of Laplace stretch are obtained as[63]

$$\begin{aligned} &\mathcal{U}_{11} = \sqrt{C_{11}} && \mathcal{U}_{12} = C_{12}/\mathcal{U}_{11} && \mathcal{U}_{13} = C_{13}/\mathcal{U}_{11} \\ &\mathcal{U}_{21} = 0 && \mathcal{U}_{22} = \sqrt{C_{22} - \mathcal{U}_{12}^2} && \mathcal{U}_{23} = \big(C_{23} - \mathcal{U}_{12}\mathcal{U}_{13}\big)/\mathcal{U}_{22} \\ &\mathcal{U}_{31} = 0 && \mathcal{U}_{32} = 0 && \mathcal{U}_{33} = \sqrt{C_{33} - \mathcal{U}_{13}^2 - \mathcal{U}_{23}^2} \end{aligned} \tag{190}$$

where C_{11}, C_{12}, C_{13}, C_{22}, C_{23}, and C_{33} are components of the right Cauchy–Green tensor $\mathbf{C}$.

Now, in order to obtain the stiffness matrix for an alveolar volume, first we need to derive the strain attributes and express them in terms of the nodal displacements. The strain attributes are defined in terms of the derived elements of Laplace stretch,

as mentioned earlier.

The dilatation ξ for an alveolar volume is

$$\xi := \ln \sqrt[3]{\frac{a}{a_0}\frac{b}{b_0}\frac{c}{c_0}} \tag{191a}$$

whereas the squeeze strains ε_i are defined as

$$\varepsilon_1 := \ln \sqrt[3]{\frac{a}{a_0}\frac{b_0}{b}} \qquad \varepsilon_2 := \ln \sqrt[3]{\frac{b}{b_0}\frac{c_0}{c}} \tag{191b}$$

and the shear strains γ_i are defined as

$$\gamma_1 := \alpha - \alpha_0 \qquad \gamma_2 := \beta - \beta_0 \qquad \gamma_3 := \gamma - \gamma_0 \tag{191c}$$

wherein a_0, b_0, and c_0 are their initial elongation ratios, and where α_0, β_0, and γ_0 are their initial shears. Without loss of generality, we can assume that the initial stretches a_0, b_0, and c_0 are one, whereas the initial shears α_0, β_0, and γ_0 are zero. There is a third squeeze, too, viz., $\varepsilon_3 = -\varepsilon_1 - \varepsilon_2$, but it is not an independent descriptor of strain.

For computational ease, these strain attributes are additively decomposed into one linear and five nonlinear components. The primary advantage of this decomposition is an emergence of a systematic structure in the strain-displacement matrix, which makes evaluation of the stiffness matrix much easier. The linear and nonlinear components for the strain attributes are obtained by applying a Taylor series expansion to these strain attributes, and then expressing their constituents in terms of gradients for the displacements with respect to the different spatial variables. Here only terms up to second-order have been retained. The linear and nonlinear components for the strain attributes, thus obtained, are given by

$$\xi = \xi_L + \xi_{N1} + \xi_{N2} + \xi_{N3} + \xi_{N4} + \xi_{N5}, \tag{192a}$$

$$\varepsilon_i = \varepsilon_{iL} + \varepsilon_{iN1} + \varepsilon_{iN2} + \varepsilon_{iN3} + \varepsilon_{iN4} + \varepsilon_{iN5}, \tag{192b}$$

$$\gamma_i = \gamma_{iL} + \gamma_{iN1} + \gamma_{iN2} + \gamma_{iN3} + \gamma_{iN4} + \gamma_{iN5}, \tag{192c}$$

where their linear and nonlinear components can be expressed in terms of elements

arising from a matrix representation of the displacement gradient as

$$\xi_L = \frac{1}{3}\left(\frac{\partial u}{\partial x} + \frac{\partial v}{\partial y} + \frac{\partial w}{\partial z}\right) \tag{193a}$$

$$\xi_N = \frac{1}{6}\Big(- \frac{\partial u}{\partial x}\frac{\partial u}{\partial x} + \frac{\partial u}{\partial z}\frac{\partial u}{\partial z} - \frac{\partial v}{\partial y}\frac{\partial v}{\partial y} - \frac{\partial v}{\partial z}\frac{\partial v}{\partial z} + \frac{\partial w}{\partial x}\frac{\partial w}{\partial x} - \frac{\partial w}{\partial y}\frac{\partial w}{\partial y} - \frac{\partial w}{\partial z}\frac{\partial w}{\partial z} - 2\frac{\partial u}{\partial y}\frac{\partial v}{\partial x} - 4\frac{\partial v}{\partial z}\frac{\partial w}{\partial y}\Big) \tag{193b}$$

$$\varepsilon_{1L} = \frac{1}{3}\left(\frac{\partial u}{\partial x} - \frac{\partial v}{\partial y}\right) \tag{193c}$$

$$\varepsilon_{1N} = \frac{1}{6}\left(2\frac{\partial v}{\partial x}\frac{\partial v}{\partial x} + \frac{\partial v}{\partial y}\frac{\partial v}{\partial y} - \frac{\partial u}{\partial x}\frac{\partial u}{\partial x} + \frac{\partial w}{\partial x}\frac{\partial w}{\partial x} - \frac{\partial w}{\partial y}\frac{\partial w}{\partial y} + 2\frac{\partial u}{\partial y}\frac{\partial v}{\partial x}\right) \tag{193d}$$

$$\varepsilon_{2L} = \frac{1}{3}\left(\frac{\partial v}{\partial y} - \frac{\partial w}{\partial z}\right) \tag{193e}$$

$$\varepsilon_{2N} = \frac{1}{6}\Big(- \frac{\partial v}{\partial x}\frac{\partial v}{\partial x} - \frac{\partial v}{\partial y}\frac{\partial v}{\partial y} - \frac{\partial u}{\partial z}\frac{\partial u}{\partial z} + \frac{\partial v}{\partial z}\frac{\partial v}{\partial z} + 3\frac{\partial w}{\partial y}\frac{\partial w}{\partial y} + \frac{\partial w}{\partial z}\frac{\partial w}{\partial z} - 2\frac{\partial u}{\partial y}\frac{\partial v}{\partial x} + 4\frac{\partial v}{\partial z}\frac{\partial w}{\partial y}\Big) \tag{193f}$$

$$\gamma_{1L} = \frac{\partial v}{\partial z} + \frac{\partial w}{\partial y} \tag{193g}$$

$$\gamma_{1N} = 2\frac{\partial u}{\partial x}\frac{\partial v}{\partial z} - \frac{\partial u}{\partial z}\frac{\partial v}{\partial x} + 2\frac{\partial u}{\partial x}\frac{\partial w}{\partial y} - \frac{\partial u}{\partial y}\frac{\partial w}{\partial x} - \frac{\partial v}{\partial y}\frac{\partial v}{\partial z} - 2\frac{\partial v}{\partial y}\frac{\partial w}{\partial y} + \frac{\partial w}{\partial y}\frac{\partial w}{\partial z} \tag{193h}$$

$$\gamma_{2L} = \frac{\partial v}{\partial z} + \frac{\partial w}{\partial y} \tag{193i}$$

$$\gamma_{2N} = \frac{\partial u}{\partial y}\frac{\partial u}{\partial z} - 2\frac{\partial u}{\partial x}\frac{\partial v}{\partial z} - 2\frac{\partial u}{\partial x}\frac{\partial w}{\partial y} + \frac{\partial v}{\partial y}\frac{\partial v}{\partial z} + \frac{\partial w}{\partial y}\frac{\partial w}{\partial z} \tag{193j}$$

$$\gamma_{3L} = \frac{\partial u}{\partial y} + \frac{\partial v}{\partial x} \tag{193k}$$

$$\gamma_{3N} = -\frac{\partial u}{\partial x}\frac{\partial u}{\partial y} - 2\frac{\partial u}{\partial x}\frac{\partial v}{\partial x} + \frac{\partial v}{\partial x}\frac{\partial v}{\partial y} + \frac{\partial w}{\partial x}\frac{\partial w}{\partial y} \tag{193l}$$

The total stiffness matrix can be obtained as a sum of the linear and five nonlinear stiffness matrices. Therefore, we first have to evaluate these components of the stiffness matrices by using the associated strain-displacement matrices. For all these cases, the strain-displacement matrices are obtained by expressing the strains in terms of the nodal displacements with the help of shape functions and their spatial derivatives.

First, the linear strain-displacement matrix $\mathbf{B}_L$ is obtained by expressing the strain attributes in terms of the nodal displacements through derivatives of the shape functions. Specifically, the linear strain-displacement matrix takes the form of

$$\begin{aligned}
\mathbf{E}_L &= \begin{Bmatrix} \xi_L \\ \varepsilon_{1L} \\ \varepsilon_{2L} \\ \gamma_{1L} \\ \gamma_{2L} \\ \gamma_{3L} \end{Bmatrix} = \begin{Bmatrix} \frac{1}{3}\,u_{,x} + \frac{1}{3}\,v_{,y} + \frac{1}{3}\,w_{,z} \\ \frac{1}{3}\,u_{,x} - \frac{1}{3}\,v_{,y} \\ \frac{1}{3}\,v_{,y} - \frac{1}{3}\,w_{,z} \\ v_{,z} + w_{,y} \\ v_{,z} + w_{,y} \\ u_{,y} + v_{,x} \end{Bmatrix} \\
&= \begin{bmatrix} \frac{1}{3}\sum_{i=1}^{4} N_{i,x} & \frac{1}{3}\sum_{i=1}^{4} N_{i,y} & \frac{1}{3}\sum_{i=1}^{4} N_{i,z} \\ \frac{1}{3}\sum_{i=1}^{4} N_{i,x} & \frac{-1}{3}\sum_{i=1}^{4} N_{i,y} & 0 \\ 0 & \frac{1}{3}\sum_{i=1}^{4} N_{i,y} & \frac{-1}{3}\sum_{i=1}^{4} N_{i,z} \\ 0 & \sum_{i=1}^{4} N_{i,z} & \sum_{i=1}^{4} N_{i,y} \\ 0 & \sum_{i=1}^{4} N_{i,z} & \sum_{i=1}^{4} N_{i,y} \\ \sum_{i=1}^{4} N_{i,y} & \sum_{i=1}^{4} N_{i,x} & 0 \end{bmatrix} \begin{Bmatrix} u_i \\ v_i \\ w_i \end{Bmatrix} \\
&= \Big[[\mathbf{b}_{L1}][\mathbf{b}_{L2}][\mathbf{b}_{L3}][\mathbf{b}_{L4}] \Big] \left\{ \mathbf{u}^{(e)} \right\} = \mathbf{B}_L \mathbf{u}^{(e)}
\end{aligned} \tag{194}$$

wherein each component of $\mathbf{B}_L$ is given by

$$[\mathbf{b}_{Li}] = \begin{bmatrix} \frac{1}{3}\,N_{i,x} & \frac{1}{3}\,N_{i,y} & \frac{1}{3}\,N_{i,z} \\ \frac{1}{3}\,N_{i,x} & -\frac{1}{3}\,N_{i,y} & 0 \\ 0 & \frac{1}{3}\,N_{i,y} & -\frac{1}{3}\,N_{i,z} \\ 0 & N_{i,z} & N_{i,y} \\ 0 & N_{i,z} & N_{i,y} \\ N_{i,y} & N_{i,x} & 0 \end{bmatrix} \tag{195a}$$

and the nodal displacement vector for element e is given as

$$\mathbf{u}^{(e)} = \begin{Big\{} u_1 & v_1 & w_1 & u_2 & v_2 & w_2 & u_3 & v_3 & w_3 & u_4 & v_4 & w_4 \end{Big\}^{\mathsf{T}}. \tag{195b}$$

Note that the linear strain-displacement matrix $\mathbf{B_L}$ consists only of derivatives for the shape functions, and thus, remains the same throughout a deformation process.

Now we establish the nonlinear strain-displacement matrices that will be used to obtain the nonlinear stiffness matrix. The nonlinear components of each strain attribute have been additively decomposed into five components to make our com-

putation easier. Components of each strain attribute are placed into an associated vector resulting in an additive decomposition of the total nonlinear strain $\mathbf{E}_N$. To obtain the nonlinear stiffness matrix corresponding to these nonlinear strain components, the nonlinear strains are written as a product of two quantities: a matrix $\mathbf{A}$ containing various components of the displacement gradient, and a vector $\boldsymbol{\theta}$ that contains the derivatives of displacement with respect to spatial location. The vector $\boldsymbol{\theta}$ essentially represents the slope of response resulting from the deformation process. The components of the displacement gradient are placed in the matrix $\mathbf{A}$ in such a way so that its product with the slope vector yields the corresponding contribution to the nonlinear strain.

The slope vector $\boldsymbol{\theta}$ can further be expressed in terms of the corresponding nodal displacements by using the derivatives of the shape functions. Thus, the nonlinear strain components $\mathbf{E}_{Ni}, i = 1, 2, 3, 4$, can be expressed in terms of the nodal displacements, with the nonlinear strain-displacement matrix $\mathbf{B}_{Ni}$ corresponding to these strain components. These strain-displacement matrices are used to obtain the corresponding nonlinear stiffness matrices in a way described earlier. Note that, unlike its linear counterpart, the nonlinear strain-displacement matrix varies with the deformation of a body, and hence, the matrices corresponding to it must be updated at each step along a solution path.

Now let us perform the procedure described above on all five nonlinear strain components.

For the first nonlinear strain, $\mathbf{E}_{N1}$, can be written as a product of the matrix $\mathbf{A}_1$ and

the slope vector $\boldsymbol{\theta}_1$ as

$$
\begin{aligned}
\mathbf{E}_{N1} &= \begin{Bmatrix} \xi_{1N} \\ \varepsilon_{1N} \\ \varepsilon_{2N} \\ \gamma_{1N} \\ \gamma_{2N} \\ \gamma_{3N} \end{Bmatrix} = \begin{Bmatrix} \frac{1}{6}\left(-u_{,x}^2 - v_{,y}^2 - w_{,z}^2\right) \\ \frac{1}{6}\left(-u_{,x}^2 + v_{,y}^2\right) \\ \frac{1}{6}\left(-v_{,y}^2 + w_{,z}^2\right) \\ -v_{,z}\, v_{,y} + w_{,y}\, w_{,z} \\ v_{,z}\, v_{,y} + w_{,y}\, w_{,z} \\ -u_{,x}\, u_{,y} + v_{,x}\, v_{,y} \end{Bmatrix} \\
&= \frac{1}{2} \begin{bmatrix} -\frac{1}{3}\,\partial u/\partial x & -\frac{1}{3}\,\partial v/\partial y & -\frac{1}{3}\,\partial w/\partial z \\ -\frac{1}{3}\,\partial u/\partial x & \frac{1}{3}\,\partial v/\partial y & 0 \\ 0 & -\frac{1}{3}\,\partial v/\partial y & \frac{1}{3}\,\partial w/\partial z \\ 0 & -2\,\partial v/\partial z & 2\,\partial w/\partial y \\ 0 & 2\,\partial v/\partial z & 2\,\partial w/\partial y \\ -2\,\partial u/\partial y & 2\,\partial v/\partial x & 0 \end{bmatrix} \begin{Bmatrix} \partial u/\partial x \\ \partial v/\partial y \\ \partial w/\partial z \end{Bmatrix} \\
&= \tfrac{1}{2}\,\mathbf{A}_1\,\boldsymbol{\theta}_1
\end{aligned}
\tag{196}
$$

with

$$
\begin{aligned}
\mathrm{d}\mathbf{A}_1 &= \begin{bmatrix} -\frac{1}{3}\,\partial \mathrm{d}u/\partial x & -\frac{1}{3}\,\partial \mathrm{d}v/\partial y & -\frac{1}{3}\,\partial \mathrm{d}w/\partial z \\ -\frac{1}{3}\,\partial \mathrm{d}u/\partial x & \frac{1}{3}\,\partial \mathrm{d}v/\partial y & 0 \\ 0 & -\frac{1}{3}\,\partial \mathrm{d}v/\partial y & \frac{1}{3}\,\partial \mathrm{d}w/\partial z \\ 0 & -2\,\partial \mathrm{d}v/\partial z & 2\,\partial \mathrm{d}w/\partial y \\ 0 & 2\,\partial \mathrm{d}v/\partial z & 2\,\partial \mathrm{d}w/\partial y \\ -2\,\partial \mathrm{d}u/\partial y & 2\,\partial \mathrm{d}v/\partial x & 0 \end{bmatrix} \\
&= \begin{bmatrix} -\frac{1}{3}\sum_{i=1}^4 N_{i,x}\,\mathrm{d}u_i & -\frac{1}{3}\sum_{i=1}^4 N_{i,y}\,\mathrm{d}v_i & -\frac{1}{3}\sum_{i=1}^4 N_{i,z}\,\mathrm{d}w_i \\ -\frac{1}{3}\sum_{i=1}^4 N_{i,x}\,\mathrm{d}u_i & \frac{1}{3}\sum_{i=1}^4 N_{i,y}\,\mathrm{d}v_i & 0 \\ 0 & -\frac{1}{3}\sum_{i=1}^4 N_{i,y}\,\mathrm{d}v_i & \frac{1}{3}\sum_{i=1}^4 N_{i,z}\,\mathrm{d}w_i \\ 0 & -2\sum_{i=1}^4 N_{i,z}\,\mathrm{d}v_i & 2\sum_{i=1}^4 N_{i,y}\,\mathrm{d}w_i \\ 0 & 2\sum_{i=1}^4 N_{i,z}\,\mathrm{d}v_i & 2\sum_{i=1}^4 N_{i,y}\,\mathrm{d}w_i \\ -2\sum_{i=1}^4 N_{i,y}\,\mathrm{d}u_i & 2\sum_{i=1}^4 N_{i,x}\,\mathrm{d}v_i & 0 \end{bmatrix} \\
&= \Big[[\mathbf{l}_1][\mathbf{l}_2][\mathbf{l}_3][\mathbf{l}_4]\Big]\,\Big[[\mathbf{d}_1][\mathbf{d}_2][\mathbf{d}_3][\mathbf{d}_4]\Big]^{\mathsf{T}} = \mathbf{L}_1\mathbf{D}_1
\end{aligned}
\tag{197a}
$$

wherein

$$[\mathbf{l}_i] = \begin{bmatrix} -\frac{1}{3}\,N_{i,x} & -\frac{1}{3}\,N_{i,y} & -\frac{1}{3}\,N_{i,z} \\ -\frac{1}{3}\,N_{i,x} & \frac{1}{3}\,N_{i,y} & 0 \\ 0 & -\frac{1}{3}\,N_{i,y} & \frac{1}{3}\,N_{i,z} \\ 0 & -2\,N_{i,z} & 2\,N_{i,y} \\ 0 & 2\,N_{i,z} & 2\,N_{i,y} \\ -2\,N_{i,y} & 2\,N_{i,x} & 0 \end{bmatrix} \quad \text{and} \quad [\mathbf{d}_i] = \begin{bmatrix} \mathrm{d}u_i & 0 & 0 \\ 0 & \mathrm{d}v_i & 0 \\ 0 & 0 & \mathrm{d}w_i \end{bmatrix}. \tag{197b}$$

Now, the derivative of displacement with respect to spatial variables x, y, and z can be related to the nodal parameters via

$$\boldsymbol{\theta}_1 = \begin{Bmatrix} \partial u/\partial x \\ \partial v/\partial y \\ \partial w/\partial z \end{Bmatrix} = \begin{Bmatrix} \sum_{i=1}^{4} N_{i,x}\,u_i \\ \sum_{i=1}^{4} N_{i,y}\,v_i \\ \sum_{i=1}^{4} N_{i,z}\,w_i \end{Bmatrix} = \Big[[\mathbf{h}_1][\mathbf{h}_2][\mathbf{h}_3][\mathbf{h}_4]\Big] \left\{\mathbf{u}^{(e)}\right\} = \mathbf{H}_1\,\mathbf{u}^{(e)} \tag{198}$$

for element e, where

$$[\mathbf{h}_i] = \begin{bmatrix} N_{i,x} & 0 & 0 \\ 0 & N_{i,y} & 0 \\ 0 & 0 & N_{i,z} \end{bmatrix}. \tag{199}$$

Hence, the strain-displacement matrix $\mathbf{B}_{N1}$ corresponding to the first nonlinear strain becomes

$$\mathbf{B}_{N1} = \mathbf{A}_1\,\mathbf{H}_1 = \Big[[\mathbf{b}_{N1}][\mathbf{b}_{N2}][\mathbf{b}_{N3}][\mathbf{b}_{N4}]\Big] \tag{200}$$

wherein the components of $\mathbf{B}_{N1}$ are given as

$$[\mathbf{b}_{Ni}] = \begin{bmatrix} -\frac{1}{3}\,\partial u/\partial x & -\frac{1}{3}\,\partial v/\partial y & -\frac{1}{3}\,\partial w/\partial z \\ -\frac{1}{3}\,\partial u/\partial x & \frac{1}{3}\,\partial v/\partial y & 0 \\ 0 & -\frac{1}{3}\,\partial v/\partial y & \frac{1}{3}\,\partial w/\partial z \\ 0 & -2\,\partial v/\partial z & 2\,\partial w/\partial y \\ 0 & 2\,\partial v/\partial z & 2\,\partial w/\partial y \\ -2\,\partial u/\partial y & 2\,\partial v/\partial x & 0 \end{bmatrix} \begin{bmatrix} N_{i,x} & 0 & 0 \\ 0 & N_{i,y} & 0 \\ 0 & 0 & N_{i,z} \end{bmatrix}. \tag{201}$$

In a similar manner, we can obtain the strain-displacement matrices corresponding to the other nonlinear strain components. The second nonlinear strain terms can be

written in terms of an $\mathbf{A}_2$ whose slope vector $\boldsymbol{\theta}_2$ is

$$\begin{aligned}
\mathbf{E}_{N2} &= \left\{\begin{array}{c} \xi_L \\ \varepsilon_{1N} \\ \varepsilon_{2N} \\ \gamma_{1N} \\ \gamma_{2N} \\ \gamma_{3N} \end{array}\right\} = \left\{\begin{array}{c} \frac{1}{6}\,\left(u_{,z}^2 - v_{,z}^2 - w_{,y}^2\right) \\ \frac{-1}{6}\,w_{,y}^2 \\ \frac{1}{6}\,\left(-u_{,z}^2 + v_{,z}^2 + 3\,w_{,y}^2\right) \\ 0 \\ u_{,y}\,u_{,z} \\ w_{,x}\,w_{,y} \end{array}\right\} \\
&= \frac{1}{2}\left[\begin{array}{ccc} \frac{1}{3}\,\partial u/\partial z & -\frac{1}{3}\,\partial v/\partial z & -\frac{1}{3}\,\partial w/\partial y \\ 0 & 0 & -\frac{1}{3}\,\partial w/\partial y \\ -\frac{1}{3}\,\partial u/\partial z & \frac{1}{3}\,\partial v/\partial z & \partial w/\partial y \\ 0 & 0 & 0 \\ 2\,\partial u/\partial y & 0 & 0 \\ 0 & 0 & 2\,\partial w/\partial x \end{array}\right] \left\{\begin{array}{c} \partial u/\partial z \\ \partial v/\partial z \\ \partial w/\partial y \end{array}\right\} \\
&= \tfrac{1}{2}\,\mathbf{A}_2\,\boldsymbol{\theta}_2
\end{aligned} \tag{202}$$

with

$$\begin{aligned}
\mathrm{d}\mathbf{A}_2 &= \left[\begin{array}{ccc} \frac{1}{3}\,\partial \mathrm{d}u/\partial z & -\frac{1}{3}\,\partial \mathrm{d}v/\partial z & -\frac{1}{3}\,\partial \mathrm{d}w/\partial y \\ 0 & 0 & -\frac{1}{3}\,\partial \mathrm{d}w/\partial y \\ -\frac{1}{3}\,\partial \mathrm{d}u/\partial z & \frac{1}{3}\,\partial \mathrm{d}v/\partial z & \partial \mathrm{d}w/\partial y \\ 0 & 0 & 0 \\ 2\,\partial \mathrm{d}u/\partial y & 0 & 0 \\ 0 & 0 & 2\,\partial \mathrm{d}w/\partial x \end{array}\right] \\
&= \left[\begin{array}{ccc} \frac{1}{3}\,\sum_{i=1}^4 N_{i,z}\,\mathrm{d}u_i & -\frac{1}{3}\,\sum_{i=1}^4 N_{i,z}\,\mathrm{d}v_i & -\frac{1}{3}\,\sum_{i=1}^4 N_{i,y}\,\mathrm{d}w_i \\ 0 & 0 & -\frac{1}{3}\,\sum_{i=1}^4 N_{i,y}\,\mathrm{d}w_i \\ -\frac{1}{3}\,\sum_{i=1}^4 N_{i,z}\,\mathrm{d}u_i & \frac{1}{3}\,\sum_{i=1}^4 N_{i,z}\,\mathrm{d}v_i & \sum_{i=1}^4 N_{i,y}\,\mathrm{d}w_i \\ 0 & 0 & 0 \\ 2\,\sum_{i=1}^4 N_{i,y}\,\mathrm{d}u_i & 0 & 0 \\ 0 & 0 & 2\,\sum_{i=1}^4 N_{i,x}\,\mathrm{d}w_i \end{array}\right] \\
&= \Big[[\mathbf{l}_1][\mathbf{l}_2][\mathbf{l}_3][\mathbf{l}_4]\Big]\,\Big[[\mathbf{d}_1][\mathbf{d}_2][\mathbf{d}_3][\mathbf{d}_4]\Big]^{\mathsf{T}} = \mathbf{L}_2\mathbf{D}_2
\end{aligned} \tag{203a}$$

wherein

$$[\mathbf{l}_i] = \begin{bmatrix} \frac{1}{3}\,N_{i,z} & -\frac{1}{3}\,N_{i,z} & -\frac{1}{3}\,N_{i,y} \\ 0 & 0 & -\frac{1}{3}\,N_{i,y} \\ -\frac{1}{3}\,N_{i,z} & \frac{1}{3}\,N_{i,z} & N_{i,y} \\ 0 & 0 & 0 \\ 2\,N_{i,y} & 0 & 0 \\ 0 & 0 & 2\,N_{i,x} \end{bmatrix} \quad \text{and} \quad [\mathbf{d}_i] = \begin{bmatrix} \mathrm{d}u_i & 0 & 0 \\ 0 & \mathrm{d}v_i & 0 \\ 0 & 0 & \mathrm{d}w_i \end{bmatrix}. \tag{203b}$$

The slope vector can further be expressed in terms of the nodal parameters via

$$\boldsymbol{\theta}_2 = \begin{Bmatrix} \partial u/\partial z \\ \partial v/\partial z \\ \partial w/\partial y \end{Bmatrix} = \begin{Bmatrix} \sum_{i=1}^{4} N_{i,z}\,u_i \\ \sum_{i=1}^{4} N_{i,z}\,v_i \\ \sum_{i=1}^{4} N_{i,y}\,w_i \end{Bmatrix} = \Big[[\mathbf{h}_1][\mathbf{h}_2][\mathbf{h}_3][\mathbf{h}_4]\Big] \left\{\mathbf{u}^{(e)}\right\} = \mathbf{H}_2\,\mathbf{u}^{(e)} \tag{204}$$

where

$$[\mathbf{h}_i] = \begin{bmatrix} N_{i,z} & 0 & 0 \\ 0 & N_{i,z} & 0 \\ 0 & 0 & N_{i,y} \end{bmatrix}. \tag{205}$$

Hence, the strain-displacement matrix $\mathbf{B}_{N2}$ becomes

$$\mathbf{B}_{N2} = \mathbf{A}_2\,\mathbf{H}_2 = \Big[[\mathbf{b}_{N1}][\mathbf{b}_{N2}][\mathbf{b}_{N3}][\mathbf{b}_{N4}]\Big]. \tag{206}$$

The components of this strain-displacement matrix are given as

$$[\mathbf{b}_{Ni}] = \begin{bmatrix} \frac{1}{3}\,\partial u/\partial z & -\frac{1}{3}\,\partial v/\partial z & -\frac{1}{3}\,\partial w/\partial y \\ 0 & 0 & -\frac{1}{3}\,\partial w/\partial y \\ -\frac{1}{3}\,\partial u/\partial z & \frac{1}{3}\,\partial v/\partial z & \partial w/\partial y \\ 0 & 0 & 0 \\ 2\,\partial u/\partial y & 0 & 0 \\ 0 & 0 & 2\,\partial w/\partial x \end{bmatrix} \begin{bmatrix} N_{i,z} & 0 & 0 \\ 0 & N_{i,z} & 0 \\ 0 & 0 & N_{i,y} \end{bmatrix}. \tag{207}$$

For the third nonlinear strain term, i.e., $\mathbf{E}_{N3}$, can be written as

$$\begin{aligned}
\mathbf{E}_{N3} &= \begin{Bmatrix} \xi_L \\ \varepsilon_{1N} \\ \varepsilon_{2N} \\ \gamma_{1N} \\ \gamma_{2N} \\ \gamma_{3N} \end{Bmatrix} = \begin{Bmatrix} \frac{1}{6}\left(-2\,v_{,x}\,u_{,y} - 4\,w_{,y}\,v_{,z} + w_{,x}^2\right) \\ \frac{1}{6}\left(2\,v_{,x}\,u_{,y} + w_{,x}^2\right) \\ \frac{1}{6}\left(-2\,v_{,x}\,u_{,y} + 4\,w_{,y}\,v_{,z}\right) \\ 0 \\ 0 \\ 0 \end{Bmatrix} \\
&= \frac{1}{2}\begin{bmatrix} -\frac{2}{3}\,\partial v/\partial x & -\frac{4}{3}\,\partial w/\partial y & \frac{1}{3}\,\partial w/\partial x \\ \frac{2}{3}\,\partial v/\partial x & 0 & \frac{1}{3}\,\partial w/\partial x \\ -\frac{2}{3}\,\partial v/\partial x & \frac{4}{3}\,\partial w/\partial y & 0 \\ 0 & 0 & 0 \\ 0 & 0 & 0 \\ 0 & 0 & 0 \end{bmatrix} \begin{Bmatrix} \partial u/\partial y \\ \partial v/\partial z \\ \partial w/\partial x \end{Bmatrix} \\
&= \tfrac{1}{2}\,\mathbf{A}_3\,\boldsymbol{\theta}_3
\end{aligned} \tag{208}$$

with

$$\begin{aligned}
\mathrm{d}\mathbf{A}_3 &= \begin{bmatrix} -\frac{2}{3}\,\partial \mathrm{d}v/\partial x & -\frac{4}{3}\,\partial \mathrm{d}w/\partial y & \frac{1}{3}\,\partial \mathrm{d}w/\partial x \\ \frac{2}{3}\,\partial \mathrm{d}v/\partial x & 0 & \frac{1}{3}\,\partial \mathrm{d}w/\partial x \\ -\frac{2}{3}\,\partial \mathrm{d}v/\partial x & \frac{4}{3}\,\partial \mathrm{d}w/\partial y & 0 \\ 0 & 0 & 0 \\ 0 & 0 & 0 \\ 0 & 0 & 0 \end{bmatrix} \\
&= \begin{bmatrix} -\frac{2}{3}\,\sum_{i=1}^4 N_{i,x}\,\mathrm{d}v_i & -\frac{4}{3}\,\sum_{i=1}^4 N_{i,y}\,\mathrm{d}w_i & \frac{1}{3}\,\sum_{i=1}^4 N_{i,x}\,\mathrm{d}w_i \\ \frac{2}{3}\,\sum_{i=1}^4 N_{i,x}\,\mathrm{d}v_i & 0 & \frac{1}{3}\,\sum_{i=1}^4 N_{i,x}\,\mathrm{d}w_i \\ -\frac{2}{3}\,\sum_{i=1}^4 N_{i,x}\,\mathrm{d}v_i & \frac{4}{3}\,\sum_{i=1}^4 N_{i,y}\,\mathrm{d}w_i & 0 \\ 0 & 0 & 0 \\ 0 & 0 & 0 \\ 0 & 0 & 0 \end{bmatrix} \\
&= \Big[[\mathbf{l}_1][\mathbf{l}_2][\mathbf{l}_3][\mathbf{l}_4]\Big]\,\Big[[\mathbf{d}_1][\mathbf{d}_2][\mathbf{d}_3][\mathbf{d}_4]\Big]^{\mathsf{T}} = \mathbf{L}_3\mathbf{D}_3
\end{aligned} \tag{209a}$$

wherein

$$[\mathbf{l}_i] = \begin{bmatrix} -\frac{2}{3}\,N_{i,x} & -\frac{4}{3}\,N_{i,y} & \frac{1}{3}\,N_{i,x} \\ \frac{2}{3}\,N_{i,x} & 0 & \frac{1}{3}N_{i,x} \\ -\frac{2}{3}\,N_{i,x} & \frac{4}{3}\,N_{i,y} & 0 \\ 0 & 0 & 0 \\ 0 & 0 & 0 \\ 0 & 0 & 0 \end{bmatrix} \quad \text{and} \quad [\mathbf{d}_i] = \begin{bmatrix} \mathrm{d}v_i & 0 & 0 \\ 0 & \mathrm{d}w_i & 0 \\ 0 & 0 & \mathrm{d}w_i \end{bmatrix}. \tag{209b}$$

Here the slope vector $\boldsymbol{\theta}_3$ contains derivatives of displacements with respect to spatial variables y, z, x that relate to the nodal parameters via

$$\boldsymbol{\theta}_3 = \begin{Bmatrix} \partial u/\partial y \\ \partial v/\partial z \\ \partial w/\partial x \end{Bmatrix} = \begin{Bmatrix} \sum_{i=1}^{4} N_{i,y}\,u_i \\ \sum_{i=1}^{4} N_{i,z}\,v_i \\ \sum_{i=1}^{4} N_{i,x}\,w_i \end{Bmatrix} = \Big[[\mathbf{h}_1][\mathbf{h}_2][\mathbf{h}_3][\mathbf{h}_4]\Big] \left\{\mathbf{u}^{(e)}\right\} = \mathbf{H}_3\mathbf{u}^{(e)} \tag{210}$$

where

$$[\mathbf{h}_i] = \begin{bmatrix} N_{i,y} & 0 & 0 \\ 0 & N_{i,z} & 0 \\ 0 & 0 & N_{i,x} \end{bmatrix}. \tag{211}$$

Therefore, the strain-displacement matrix $\mathbf{B}_{N3}$ becomes

$$\mathbf{B}_{N3} = \mathbf{A}_3\,\mathbf{H}_3 = \Big[[\mathbf{b}_{N1}][\mathbf{b}_{N2}][\mathbf{b}_{N3}][\mathbf{b}_{N4}]\Big] \tag{212}$$

whose components are given as

$$\mathbf{b}_{Ni} = \begin{bmatrix} -\frac{2}{3}\,\partial v/\partial x & -\frac{4}{3}\,\partial w/\partial y & \frac{1}{3}\,\partial w/\partial x \\ \frac{2}{3}\,\partial v/\partial x & 0 & \frac{1}{3}\,\partial w/\partial x \\ -\frac{2}{3}\,\partial v/\partial x & \frac{4}{3}\,\partial w/\partial y & 0 \\ 0 & 0 & 0 \\ 0 & 0 & 0 \\ 0 & 0 & 0 \end{bmatrix} \begin{bmatrix} N_{i,y} & 0 & 0 \\ 0 & N_{i,z} & 0 \\ 0 & 0 & N_{i,x} \end{bmatrix}. \tag{213}$$

For the fourth nonlinear strain term, viz., $\mathbf{E}_{N4}$, can be written as

$$\begin{aligned}
\mathbf{E}_{N4} &= \left\{\begin{array}{c} \xi_L \\ \varepsilon_{1N} \\ \varepsilon_{2N} \\ \gamma_{1N} \\ \gamma_{2N} \\ \gamma_{3N} \end{array}\right\} = \left\{\begin{array}{c} 0 \\ \frac{2}{6}\, v_{,x}^2 \\ -\frac{1}{6}\, v_{,x}^2 \\ 2\, v_{,z}\, u_{,x} + 2\, u_{,x}\, w_{,y} \\ -2\, v_{,z}\, u_{,x} - 2\, u_{,x}\, w_{,y} \\ -2\, v_{,x}\, u_{,x} \end{array}\right\} \\
&= \frac{1}{2} \left[\begin{array}{ccc} 0 & 0 & 0 \\ 0 & \frac{2}{3}\, \partial v/\partial x & 0 \\ 0 & -\frac{1}{3}\, \partial v/\partial x & 0 \\ 4\, \partial v/\partial z & 0 & 4\, \partial u/\partial x \\ -4\, \partial v/\partial z & 0 & -4\, \partial u/\partial x \\ -4\, \partial v/\partial x & 0 & 0 \end{array}\right] \left\{\begin{array}{c} \partial u/\partial x \\ \partial v/\partial x \\ \partial w/\partial y \end{array}\right\} \\
&= \tfrac{1}{2}\, \mathbf{A}_4\, \boldsymbol{\theta}_4
\end{aligned} \tag{214}$$

with

$$\begin{aligned}
\mathrm{d}\mathbf{A}_4 &= \left[\begin{array}{ccc} 0 & 0 & 0 \\ 0 & \frac{2}{3}\, \partial \mathrm{d}v/\partial x & 0 \\ 0 & -\frac{1}{3}\, \partial \mathrm{d}v/\partial x & 0 \\ 4\, \partial \mathrm{d}v/\partial z & 0 & 4\, \partial \mathrm{d}u/\partial x \\ -4\, \partial \mathrm{d}v/\partial z & 0 & -4\, \partial \mathrm{d}u/\partial x \\ -4\, \partial \mathrm{d}v/\partial x & 0 & 0 \end{array}\right] \\
&= \left[\begin{array}{ccc} 0 & 0 & 0 \\ 0 & \frac{2}{3}\, \sum_{i=1}^4 N_{i,x}\, \mathrm{d}v_i & 0 \\ 0 & -\frac{1}{3}\, \sum_{i=1}^4 N_{i,x}\, \mathrm{d}v_i & 0 \\ 4\, \sum_{i=1}^4 N_{i,z}\, \mathrm{d}v_i & 0 & 4\, \sum_{i=1}^4 N_{i,x}\, \mathrm{d}u_i \\ -4\, \sum_{i=1}^4 N_{i,z}\, \mathrm{d}v_i & 0 & -4\, \sum_{i=1}^4 N_{i,x}\, \mathrm{d}u_i \\ -4\, \sum_{i=1}^4 N_{i,x}\, \mathrm{d}v_i & 0 & 0 \end{array}\right] \\
&= \Big[[\mathbf{l}_1][\mathbf{l}_2][\mathbf{l}_3][\mathbf{l}_4]\Big]\, \Big[[\mathbf{d}_1][\mathbf{d}_2][\mathbf{d}_3][\mathbf{d}_4]\Big]^{\mathsf{T}} = \mathbf{L}_4 \mathbf{D}_4
\end{aligned} \tag{215a}$$

wherein

$$[\mathbf{l}_i] = \begin{bmatrix} 0 & 0 & 0 \\ 0 & \frac{2}{3}\,N_{i,x} & 0 \\ 0 & -\frac{1}{3}\,N_{i,x} & 0 \\ 4\,N_{i,z} & 0 & 4\,N_{i,x} \\ -4\,N_{i,z} & 0 & -4\,N_{i,x} \\ -4\,N_{i,x} & 0 & 0 \end{bmatrix} \quad \text{and} \quad [\mathbf{d}_i] = \begin{bmatrix} \mathrm{d}v_i & 0 & 0 \\ 0 & \mathrm{d}v_i & 0 \\ 0 & 0 & \mathrm{d}u_i \end{bmatrix}. \tag{215b}$$

Here the slope vector $\boldsymbol{\theta}_4$ contains derivatives of displacements with respect to the spatial variables x and y that relate to the nodal parameters via

$$\boldsymbol{\theta}_4 = \begin{Bmatrix} \partial u/\partial x \\ \partial v/\partial x \\ \partial w/\partial y \end{Bmatrix} = \begin{Bmatrix} \sum_{i=1}^4 N_{i,x}\,u_i \\ \sum_{i=1}^4 N_{i,x}\,v_i \\ \sum_{i=1}^4 N_{i,y}\,w_i \end{Bmatrix} = \Big[[\mathbf{h}_1][\mathbf{h}_2][\mathbf{h}_3][\mathbf{h}_4]\Big] \left\{\mathbf{u}^{(e)}\right\} = \mathbf{H}_4\mathbf{u}^{(e)} \tag{216}$$

where

$$[\mathbf{h}_i] = \begin{bmatrix} N_{i,x} & 0 & 0 \\ 0 & N_{i,x} & 0 \\ 0 & 0 & N_{i,y} \end{bmatrix}. \tag{217}$$

Therefore, the strain-displacement matrix $\mathbf{B}_{N4}$ becomes

$$\mathbf{B}_{N4} = \mathbf{A}_4\,\mathbf{H}_4 = \Big[[\mathbf{b}_{N1}][\mathbf{b}_{N2}][\mathbf{b}_{N3}][\mathbf{b}_{N4}]\Big] \tag{218}$$

whose components are given as

$$\mathbf{b}_{Ni} = \begin{bmatrix} 0 & 0 & 0 \\ 0 & \frac{2}{3}\,\partial v/\partial x & 0 \\ 0 & -\frac{1}{3}\,\partial v/\partial x & 0 \\ 4\,\partial v/\partial z & 0 & 4\,\partial u/\partial x \\ -4\,\partial v/\partial z & 0 & -4\,\partial u/\partial x \\ -4\,\partial v/\partial x & 0 & 0 \end{bmatrix} \begin{bmatrix} N_{i,x} & 0 & 0 \\ 0 & N_{i,x} & 0 \\ 0 & 0 & N_{i,y} \end{bmatrix}. \tag{219}$$

The last nonlinear strain term, i.e., $\mathbf{E}_{N5}$, can be written as

$$\begin{aligned}
\mathbf{E}_{N5} &= \begin{Bmatrix} \xi_L \\ \varepsilon_{1N} \\ \varepsilon_{2N} \\ \gamma_{1N} \\ \gamma_{2N} \\ \gamma_{3N} \end{Bmatrix} = \begin{Bmatrix} 0 \\ 0 \\ 0 \\ -v_{,x}\, u_{,z} - 2\, w_{,y}\, v_{,y} - u_{,y}\, w_{,x} \\ 0 \\ 0 \end{Bmatrix} \\
&= \frac{1}{2} \begin{bmatrix} 0 & 0 & 0 \\ 0 & 0 & 0 \\ 0 & 0 & 0 \\ -2\,\partial v/\partial x & -4\,\partial w/\partial y & -2\,\partial u/\partial y \\ 0 & 0 & 0 \\ 0 & 0 & 0 \end{bmatrix} \begin{Bmatrix} \partial u/\partial z \\ \partial v/\partial y \\ \partial w/\partial x \end{Bmatrix} \\
&= \tfrac{1}{2}\, \mathbf{A}_5\, \boldsymbol{\theta}_5
\end{aligned} \tag{220}$$

with

$$\begin{aligned}
\mathrm{d}\mathbf{A}_5 &= \begin{bmatrix} 0 & 0 & 0 \\ 0 & 0 & 0 \\ 0 & 0 & 0 \\ -2\,\partial \mathrm{d}v/\partial x & -4\,\partial \mathrm{d}w/\partial y & -2\,\partial \mathrm{d}u/\partial y \\ 0 & 0 & 0 \\ 0 & 0 & 0 \end{bmatrix} \\
&= \begin{bmatrix} 0 & 0 & 0 \\ 0 & 0 & 0 \\ 0 & 0 & 0 \\ -2\,\sum_{i=1}^{4} N_{i,x}\, \mathrm{d}v_i & -4\,\sum_{i=1}^{4} N_{i,y}\, \mathrm{d}w_i & -2\,\sum_{i=1}^{4} N_{i,y}\, \mathrm{d}u_i \\ 0 & 0 & 0 \\ 0 & 0 & 0 \end{bmatrix} \\
&= \Big[[\mathbf{l}_1][\mathbf{l}_2][\mathbf{l}_3][\mathbf{l}_4] \Big] \Big[[\mathbf{d}_1][\mathbf{d}_2][\mathbf{d}_3][\mathbf{d}_4] \Big]^{\mathsf{T}} = \mathbf{L}_5 \mathbf{D}_5
\end{aligned} \tag{221a}$$

wherein

$$[\mathbf{l}_i] = \begin{bmatrix} 0 & 0 & 0 \\ 0 & 0 & 0 \\ 0 & 0 & 0 \\ -2\,N_{i,x} & -4\,N_{i,y} & -2\,N_{i,y} \\ 0 & 0 & 0 \\ 0 & 0 & 0 \end{bmatrix} \quad \text{and} \quad [\mathbf{d}_i] = \begin{bmatrix} \mathrm{d}v_i & 0 & 0 \\ 0 & \mathrm{d}w_i & 0 \\ 0 & 0 & \mathrm{d}u_i \end{bmatrix}. \tag{221b}$$

Here the slope vector $\boldsymbol{\theta}_5$ contains derivatives of displacements with respect to the spatial variables z, y, and x that relate to the nodal parameters via

$$\boldsymbol{\theta}_5 = \begin{Bmatrix} \partial u/\partial z \\ \partial v/\partial y \\ \partial w/\partial x \end{Bmatrix} = \begin{Bmatrix} \sum_{i=1}^{4} N_{i,z}\, u_i \\ \sum_{i=1}^{4} N_{i,y}\, v_i \\ \sum_{i=1}^{4} N_{i,x}\, w_i \end{Bmatrix} = \Big[[\mathbf{h}_1][\mathbf{h}_2][\mathbf{h}_3][\mathbf{h}_4]\Big] \left\{\mathbf{u}^{(e)}\right\} = \mathbf{H}_5 \mathbf{u}^{(e)} \tag{222}$$

where

$$[\mathbf{h}_i] = \begin{bmatrix} N_{i,z} & 0 & 0 \\ 0 & N_{i,y} & 0 \\ 0 & 0 & N_{i,x} \end{bmatrix}. \tag{223}$$

Therefore, the strain-displacement matrix $\mathbf{B}_{N5}$ becomes

$$\mathbf{B}_{N5} = \mathbf{A}_5\, \mathbf{H}_5 = \Big[[\mathbf{b}_{N1}][\mathbf{b}_{N2}][\mathbf{b}_{N3}][\mathbf{b}_{N4}]\Big] \tag{224}$$

whose components are given as

$$\mathbf{b}_{Ni} = \begin{bmatrix} 0 & 0 & 0 \\ 0 & 0 & 0 \\ 0 & 0 & 0 \\ -2\,\partial v/\partial x & -4\,\partial w/\partial y & -2\,\partial u/\partial y \\ 0 & 0 & 0 \\ 0 & 0 & 0 \end{bmatrix} \begin{bmatrix} N_{i,z} & 0 & 0 \\ 0 & N_{i,y} & 0 \\ 0 & 0 & N_{i,x} \end{bmatrix}. \tag{225}$$

The total nonlinear strain-displacement matrix $\mathbf{B}_N$ can be obtained as a sum of its five components, i.e., $\mathbf{B}_N = \sum_{i=1}^{5} \mathbf{B}_{Ni}$.

With all the strain-displacement matrices evaluated, now we are able to find the total stiffness matrix.

To obtain the stiffness matrix for a tetrahedron, we need to compute the four constituent strain-displacement matrices $\mathbf{C}^s$, $\mathbf{C}^t$, $\mathbf{K}^s$, and $\mathbf{K}^t$, as mentioned earlier. These strain-displacement matrices are obtained by expressing their corresponding strain components in terms of the four nodal displacements, with help from the shape functions.

6.4.3.1 Tangent Stiffness Matrix $\mathbf{C}^s$

The tangent stiffness matrix $\mathbf{C}^s$, as established in Eq. 149, becomes

$$\mathbf{C}^s = \int_V \mathbf{H}^\mathsf{T}\,\mathbf{S}^s\,\mathbf{H}\,\mathrm{d}V = |\mathbf{J}| \sum_{i=1}^{n} \mathbf{H}^\mathsf{T}\,\mathbf{S}^s(\xi_i,\eta_i,\zeta_i)\,\mathbf{H}\,w_i, \tag{226a}$$

wherein ξ_i, η_i, ζ_i, and w_i are the co-ordinates and weights of quadrature at the i^{th} Gauss point, and

$$\mathbf{S}^s = \begin{bmatrix} \mathcal{S}_{11} & \mathcal{S}_{12} & \mathcal{S}_{13} \\ \mathcal{S}_{21} & \mathcal{S}_{22} & \mathcal{S}_{23} \\ \mathcal{S}_{31} & \mathcal{S}_{32} & \mathcal{S}_{33} \end{bmatrix}. \tag{226b}$$

The stress vector $\boldsymbol{T} = \{\pi, \sigma_1, \sigma_2, \tau_1, \tau_2, \tau_3\}^\mathsf{T}$ conjugate to strain $\boldsymbol{E}$ has elements that comprise a pressure $\pi = \mathcal{S}_{11} + \mathcal{S}_{22} + \mathcal{S}_{33} = -3P$ where P denotes the common definition for pressure, two separate normal-stress differences $\sigma_1 = \mathcal{S}_{11} - \mathcal{S}_{22}$ and $\sigma_2 = \mathcal{S}_{22} - \mathcal{S}_{33}$, and three separate shear stresses $\tau_1 = \frac{b}{c}\mathcal{S}_{32}$, $\tau_2 = \frac{a}{c}\mathcal{S}_{31}$, and $\tau_3 = \frac{a}{b}\mathcal{S}_{21} - \alpha\tau_2$. Of these, only pressure has an initial value, viz., Π_0, which represents atmospheric pressure. In a reciprocal sense, the stress components are assigned via

$$\mathbf{S}^s = \begin{bmatrix} \frac{1}{3}(\pi + 2\sigma_1 + \sigma_2) & \frac{b}{a}(\tau_3 + \alpha\,\tau_2) & \frac{c}{a}\,\tau_2 \\ \frac{b}{a}(\tau_3 + \alpha\,\tau_2) & \frac{1}{3}(\pi - \sigma_1 + \sigma_2) & \frac{c}{a}\tau_1 \\ \frac{c}{a}\,\tau_2 & \frac{c}{a}\tau_1 & \frac{1}{3}(\pi - \sigma_1 - 2\sigma_2) \end{bmatrix} \tag{227}$$

such that $\mathbf{S} = \mathbf{P}\boldsymbol{\mathcal{U}}^{-1}\boldsymbol{\mathcal{S}}\boldsymbol{\mathcal{U}}^{-\mathsf{T}}\mathbf{P}^\mathsf{T}$ with $\mathbf{S}$ being the second Piola–Kirchhoff stress, while $\boldsymbol{\mathcal{U}}$ is the Laplace stretch, and $\mathbf{P}$ is a re-indexer of co-ordinate labeling needed to ensure invariance under a transformation of Laplace stretch.

6.4.3.2 Tangent Stiffness Matrix $\mathbf{C}^t$

The tangent stiffness matrix $\mathbf{C}^t$, as established in Eq. 150, becomes

$$\mathbf{C}^t = \int_V \mathbf{B}^\mathsf{T}\, \boldsymbol{\mathcal{M}}^t\, \mathbf{B}\, \mathrm{d}V = |\mathbf{J}| \sum_{i=1}^{n} \mathbf{B}^\mathsf{T}\, \boldsymbol{\mathcal{M}}^t(\xi_i, \eta_i, \zeta_i)\, \mathbf{B}\, w_i, \tag{228}$$

where the stress rate is described by its tangent modulus $\boldsymbol{\mathcal{M}}^t$.

6.4.3.3 Secant Stiffness Matrix $\mathbf{K}^s$

The secant stiffness matrix $\mathbf{K}^s$, as established in Eq. 147b, becomes

$$\mathbf{K}^s = \int_V \mathbf{B}^\mathsf{T}\, \boldsymbol{\mathcal{M}}^s\, \mathbf{B}\, \mathrm{d}V = |\mathbf{J}| \sum_{i=1}^{n} \mathbf{B}^\mathsf{T}\, \boldsymbol{\mathcal{M}}^s(\xi_i, \eta_i, \zeta_i)\, \mathbf{B}\, w_i, \tag{229}$$

where the stress is described by its secant modulus $\boldsymbol{\mathcal{M}}^s$.

6.4.3.4 Secant Stiffness Matrix $\mathbf{K}^t$

Likewise, a secant stiffness matrix $\mathbf{K}^t$, also established in Eq. 150, becomes

$$\mathbf{K}^t = \int_V \mathbf{H}^\mathsf{T}\, \mathrm{d}\mathbf{S}^t\, \mathbf{H}\, \mathrm{d}V = |\mathbf{J}| \sum_{i=1}^{n} \mathbf{H}^\mathsf{T}\, \mathrm{d}\mathbf{S}^t(\xi_i, \eta_i, \zeta_i)\, \mathbf{H}\, w_i, \tag{230}$$

where its stress rate is given by $\mathrm{d}\mathbf{S}^t := \mathbf{A}^\mathsf{T}\, \boldsymbol{\mathcal{M}}^t\, \mathrm{d}\mathbf{A}$.

6.5 Force Vector

The principle of stationary potential energy via the Rayleigh–Ritz approach, i.e., Eq. 146, determines a basis for finite element stress analysis. The internal strain energy is balanced with the potential energy of applied internal and external loads on the body.

The virtual work done by external forces δW in Eq. 146 can be expressed as

$$\delta W = \int_S \mathbf{t}\, \delta\mathbf{u}\, \mathrm{d}S = \int_S \mathbf{t}\, \mathbf{N}\, \mathrm{d}\boldsymbol{\Delta}\, \mathrm{d}S = \left(\int_S \mathbf{N}^\mathsf{T}\, \mathbf{t}\, \mathrm{d}S \right)\, \mathrm{d}\boldsymbol{\Delta}, \tag{231a}$$

where $\mathrm{d}S$ denotes a surface element with $\mathbf{t}$ being its surface traction vector (per unit surface area) at current time. Hence, the external $\mathbf{F}_{BC}$ force vectors are

$$\mathbf{F}_{BC} = \int_S \mathbf{N}^\mathsf{T}\, \mathbf{t}\, \mathrm{d}S. \tag{231b}$$

The force needed to balance the residual stresses, i.e., $\boldsymbol{F}_0$, is evaluated as two separate integrals, viz.,

$$\boldsymbol{F}_0 = \int_V \mathbf{B}_L^{\mathsf{T}}\, \boldsymbol{T}_0 \,\mathrm{d}V + \int_V \mathbf{B}_N^{\mathsf{T}}\, \boldsymbol{T}_0 \,\mathrm{d}V, \tag{232}$$

where the first integral only needs to be evaluated once, as its argument is constant valued.

6.5.1 Force Vector for a Chord

Following the procedure described above, the force vector of a 1D alveolar chord is evaluated numerically in its natural co-ordinate system as

$$\mathbf{F}_{BC} = \int_L \mathbf{N}^{\mathsf{T}}\, \mathbf{t} \,\mathrm{d}L = \sum_{i=1}^{2} \mathbf{N}^{\mathsf{T}}\, \mathbf{t}\, |\mathbf{J}|\, w_i, \tag{233}$$

where w_i are the weighting coefficients of the Gauss integration rule, $\mathbf{N}$ is the shape function matrix for chord, and $\mathbf{t}$ is the traction on the septal chord that is selected so that the traction can be additively decomposed into that carried by the collagen and elastin fibers, i.e., $\mathbf{t} = \mathbf{t}^c + \mathbf{t}^e$.

The internal force $\boldsymbol{F}_0$ accounting for an initial residual stress of $\boldsymbol{T}_0$, expressed as two separate integrals, can be computed as

$$\boldsymbol{F}_0 = \int_L \mathbf{B}_L^{\mathsf{T}}\, \boldsymbol{T}_0\, A \,\mathrm{d}L + \int_L \mathbf{B}_N^{\mathsf{T}}\, \boldsymbol{T}_0\, A \,\mathrm{d}L \tag{234a}$$

$$= |\mathbf{J}| \sum_{i=1}^{2} \mathbf{B}_L^{\mathsf{T}}\, \boldsymbol{T}_0\, A_i\, w_i + |\mathbf{J}| \sum_{i=1}^{2} \mathbf{B}_N^{\mathsf{T}}\, \boldsymbol{T}_0\, A_i\, w_i, \tag{234b}$$

where the first integral will only need to be evaluated once, as the argument is constant valued. The cross-sectional areas of biologic chords need not be the same at both Gauss points; hence, it cannot be pulled outside the sum (integration). Here the initial stress $\mathbf{T}_0 = [s_0] \mapsto \mathbf{S}_0 = [s_0]$ contains the initial stress s_0 carried by the collagen and elastin fibers; specifically, from the rule of mixtures

$$s_0 = \left(\phi s_0^c + (1-\phi) s_0^e\right) \quad \text{where} \quad \phi \coloneqq A_0^c/(A_0^c + A_0^e) = A_0^c/A_0, \tag{234c}$$

where A_0 and A are the initial and current cross-sectional areas of the chord. The superscripts c and e designate collagen and elastin.

6.5.2 Force Vector for a Pentagon

The boundary of a 2D pentagon consists of line segments, which can be considered as 1D chords. Hence, an evaluation of the boundary integrals of a pentagon amounts to evaluating the line integrals along these boundary lines. Once the interpolation function for a pentagon are evaluated on the boundary of a pentagon, we can obtain the corresponding chordal interpolation functions.[118] Thus, the force vector $\mathbf{F}_{BC}$ for a pentagon can be obtained by integrating the traction vectors multiplied by appropriate shape functions over all sides of pentagon. Specifically, force along the boundary of a membrane can be obtained as

$$\begin{aligned}\mathbf{F}_{BC} = \oint_L \mathbf{N}^{\mathsf{T}}\,\mathbf{t}\,\mathrm{d}L &= \int_{L_{12}} \mathbf{N}^{\mathsf{T}}\,\mathbf{t}_{12}\,|\mathbf{J}|\,\mathrm{d}L + \int_{L_{23}} \mathbf{N}^{\mathsf{T}}\,\mathbf{t}_{23}\,|\mathbf{J}|\,\mathrm{d}L + \int_{L_{34}} \mathbf{N}^{\mathsf{T}}\,\mathbf{t}_{34}\,|\mathbf{J}|\,\mathrm{d}L \\ &\quad + \int_{L_{45}} \mathbf{N}^{\mathsf{T}}\,\mathbf{t}_{45}\,|\mathbf{J}|\,\mathrm{d}L + \int_{L_{51}} \mathbf{N}^{\mathsf{T}}\,\mathbf{t}_{51}\,|\mathbf{J}|\,\mathrm{d}L \\ &= |\mathbf{J}| \sum_{i=1}^{2} \mathbf{N}^{\mathsf{T}}\,\mathbf{t}_{12}\,w_i + |\mathbf{J}| \sum_{i=1}^{2} \mathbf{N}^{\mathsf{T}}\,\mathbf{t}_{23}\,w_i + |\mathbf{J}| \sum_{i=1}^{2} \mathbf{N}^{\mathsf{T}}\,\mathbf{t}_{34}\,w_i \\ &\quad + |\mathbf{J}| \sum_{i=1}^{2} \mathbf{N}^{\mathsf{T}}\,\mathbf{t}_{45}\,w_i + |\mathbf{J}| \sum_{i=1}^{2} \mathbf{N}^{\mathsf{T}}\,\mathbf{t}_{51}\,w_i,\end{aligned} \tag{235}$$

where $\mathbf{N}$ represents the shape function matrix of a chord, but with the matrix dimension of a pentagon, $|\mathbf{J}|$ is the determinant of the Jacobian for a 1D chord, w_i denotes the natural weight of the chord, $\mathrm{d}S$ is the arc-length of an infinitesimal line element along the boundary, and $\mathbf{t}$ is the traction vector on each edge of the pentagon defined as

$$\mathbf{t} = \mathbf{S}^{s\mathsf{T}} \cdot \mathbf{n}, \tag{236}$$

where $\mathbf{n}$ is the normal vector to each sides of pentagon on which the traction acts, and $\mathbf{S}^s$ are established in Eq. 182b.

The internal force $\boldsymbol{F}_0$ accounting for an initial residual stress of $\boldsymbol{T}_0$ becomes

$$\begin{aligned}\boldsymbol{F}_0 &= \int_V \mathbf{B}_L^{\mathsf{T}}\,\boldsymbol{T}_0\,\mathrm{d}V + \int_V \mathbf{B}_N^{\mathsf{T}}\,\boldsymbol{T}_0\,\mathrm{d}V \\ &= |\mathbf{J}| \sum_{i=1}^{5} \mathbf{B}_L^{\mathsf{T}}\,\boldsymbol{T}_0\,H_i\,w_i + |\mathbf{J}| \sum_{i=1}^{5} \mathbf{B}_N^{\mathsf{T}}\,\boldsymbol{T}_0\,H_i\,w_i,\end{aligned} \tag{237}$$

where $\mathbf{B}$ and $\mathbf{J}$ are the strain displacement and Jacobian matrix of pentagon, respec-

tively, whose thickness or height H_i can vary over the surface of the membrane, and as such, cannot be pulled outside the summation. Here the initial stress

$$\mathbf{T}_0 = \begin{Bmatrix} s_0^{\pi} \\ s_0^{\sigma} = 0 \\ s_0^{\tau} = 0 \end{Bmatrix} \mapsto \mathbf{S}_0 = \begin{bmatrix} \frac{1}{2} s_0^{\pi} & 0 \\ 0 & \frac{1}{2} s_0^{\pi} \end{bmatrix} \tag{238}$$

contains the initial surface tension s_0^{π} carried by the septal membrane.

6.5.3 Force Vector for a Tetrahedron

The force vector on the alveolar volume is computed by integrating the traction vector over the four boundary surfaces of the tetrahedron. Here the matrix of shape functions, given in Eq. 126, is used to obtain the force vector for tetrahedron. The force vector $\mathbf{F}_{BC}$ can be specified as

$$\begin{aligned} \mathbf{F}_{BC} &= \oint_A \mathbf{N}^{\mathsf{T}}\, \mathbf{t}\, \mathrm{d}A = \int_{\triangle_1} \mathbf{N}^{\mathsf{T}}\, \mathbf{t}_{\triangle_1}\, \mathrm{d}A + \int_{\triangle_2} \mathbf{N}^{\mathsf{T}}\, \mathbf{t}_{\triangle_2}\, \mathrm{d}A \\ &+ \int_{\triangle_3} \mathbf{N}^{\mathsf{T}}\, \mathbf{t}_{\triangle_3}\, \mathrm{d}A + \int_{\triangle_4} \mathbf{N}^{\mathsf{T}}\, \mathbf{t}_{\triangle_4}\, \mathrm{d}A \\ &= |\mathbf{J}| \sum_{i=1}^{3} \mathbf{N}^{\mathsf{T}}\, \mathbf{t}_{\triangle_1}\, w_i + |\mathbf{J}| \sum_{i=1}^{3} \mathbf{N}^{\mathsf{T}}\, \mathbf{t}_{\triangle_2}\, w_i \\ &+ |\mathbf{J}| \sum_{i=1}^{3} \mathbf{N}^{\mathsf{T}}\, \mathbf{t}_{\triangle_3}\, w_i + |\mathbf{J}| \sum_{i=1}^{3} \mathbf{N}^{\mathsf{T}}\, \mathbf{t}_{\triangle_4}\, w_i, \end{aligned} \tag{239}$$

where $\Delta_i, i = 1, 2, 3, 4$, represent the triangular boundary surfaces of a tetrahedron. Here $\mathbf{N}$ represents the shape function matrix for these associated triangular boundaries. $|\mathbf{J}|$ is the determinant of the Jacobian for triangle, n denotes the number of Gauss points, w_i is the natural weight of the triangle from Table 8, and $\mathbf{t}$ is the surface traction on the triangle surface. Integral $\oint$ denotes an integration over the surface boundary of a tetrahedron.

Note: Except for the base of the tetrahedron, the tractions on its other sides have equal and opposite contributions to the total force vector. Therefore, contributions from opposite boundary surfaces of the tetrahedron nullify each other. Hence, in order to obtain the total force vector for a tetrahedron, it is sufficient to only consider the contributions due to the traction on its base. Therefore, the total force vector

takes the form of

$$\mathbf{F}_{BC} = |\mathbf{J}| \sum_{i=1}^{3} \mathbf{N}^{\mathsf{T}} \, \mathbf{t}_{\triangle_1} \, w_i, \tag{240}$$

where $\mathbf{t}_{\triangle_1}$ is the traction vector on the surface of triangle defined as

$$\mathbf{t}_{\triangle_1} = \mathbf{S}^{s\mathsf{T}} \mathbf{n}, \tag{241}$$

wherein $\mathbf{n}$ is the normal vector to each sides of tetrahedron on which the traction acts, and $\mathbf{S}^s$ has been defined in Eq. 226b.

The internal force $\boldsymbol{F}_0$ accounting for an initial residual stress of $\boldsymbol{T}_0$ becomes

$$\boldsymbol{F}_0 = \int_V \mathbf{B}^{\mathsf{T}} \, \boldsymbol{T}_0 \, \mathrm{d}V \tag{242a}$$

$$= |\mathbf{J}| \sum_{i=1}^{4} \mathbf{B}_L^{\mathsf{T}} \, \boldsymbol{T}_0 \, w_i + |\mathbf{J}| \sum_{i=1}^{4} \mathbf{B}_N^{\mathsf{T}} \, \boldsymbol{T}_0 \, w_i, \tag{242b}$$

where $\mathbf{B}$ and $\mathbf{J}$ are the strain displacement and Jacobian matrices of a tetrahedron, respectively. Here the stress vector $\boldsymbol{T}_0 = \{\Pi, \sigma_1, \sigma_2, \tau_1, \tau_2, \tau_3\}^{\mathsf{T}}$ is conjugate to strain $\boldsymbol{E} = \{\Xi, \varepsilon_1, \varepsilon_2, \gamma_1, \gamma_2, \gamma_3\}^{\mathsf{T}}$, where

$$\mathbf{T}_0 = \begin{Bmatrix} \Pi_0 \\ \sigma_{1\,0} = 0 \\ \sigma_{2\,0} = 0 \\ \tau_{1\,0} = 0 \\ \tau_{2\,0} = 0 \\ \tau_{3\,0} = 0 \end{Bmatrix} \mapsto \mathbf{S}_0 = \begin{bmatrix} \frac{1}{3}\Pi_0 & 0 & 0 \\ 0 & \frac{1}{3}\Pi_0 & 0 \\ 0 & 0 & \frac{1}{3}\Pi_0 \end{bmatrix} \tag{243}$$

contains the residual pressure Π_0 inside a tetrahedron.

7. Conclusions

This report develops a microscopic alveolar model whose homogenized response describes the macroscopic behavior of parenchyma in lung. Such a model can be used in lieu of physical experiments to help develop and parameterize a better continuum lung model for use in finite element analyses. The need for such a model is to aid Army engineers in their development of improved PPE to better protect Soldiers from BABT and BLI when impacted by ballistic projectiles or blast waves.

The geometry of an individual alveolus is modeled as an irregular dodecahedron comprising 20 alveolar vertices, 30 1D alveolar chords, and 12 2D pentagonal alveolar septa, all enveloping a 3D alveolar sac. Implicit elastic constitutive equations are used to model these alveolar chords and septa. Alveolar chords are modeled as collagen and elastin fibers loaded in parallel. Damage is accounted for through the rupture of individual alveolar fibers and septa, and the tearing of capillaries that lead to blood and interstitial fluids leaking into its alveolar sac. Material properties for the individual fibers and septa are assigned through probability distribution functions to account for their biologic variability.

It is shown that geometric strains for the three physical dimensions that arise in this analysis are equivalent during uniform deformations when they are defined as $\ln(L/L_0)$ for 1D rods, $\ln\sqrt{A/A_0}$ for 2D membranes, and $\ln\sqrt[3]{V/V_0}$ for 3D volumes. Adopting Laplace stretch as our fundamental kinematic variable, thermodynamic conjugate pairs are established for these three geometric dimensions. These thermodynamic strains equate with the above geometric strains under conditions of uniform deformation, plus they allow for the handling of nonuniform deformations, in particular, pure and simple shears.

New to this report are the following: *i*) Sets of consistent interpolation/extrapolation procedures for 1D rods, 2D triangles and pentagons, and 3D tetrahedra, which allow physical fields to be mapped between the nodes and Gauss points of an element in a reproducible manner; *ii*) Shape functions and a Gauss integration formula suitable for constructing a pentagonal finite element, which is used to model alveolar septa; *iii*) Nonlinear strain-displacement matrices for 2D pentagons and 3D tetrahedra that employ Laplace stretch as their kinematic variable; and *iv*) A numerical algorithm that employs both secant and tangent stiffness matrices in its finite element solver.

8. References

1. Cannon LB. Behind armour blunt trauma—an emerging problem. Journal of the Royal Army Medical Corps. 2001;147:87–96.

2. Grimal Q, Gama B, Naili S, Watzky A, Gillespie J. Finite element study of high-speed blunt impact on thorax: linear elastic considerations. International Journal of Impact Engineering. 2004;30:665–683.

3. Cronin D. Investigation of lung response resulting from behind armor blunt trauma impact scenarios. In: Proceedings of the 2015 International Research Council on Biomechanics of Injury (IRCOBI) Conference; p. 722–723.

4. Hanlon E, Gillich P. Origin of the 44-mm behind-armor blunt trauma standard. Military Medicine. 2012;177:333–339.

5. Gibbons M, Dang X, Adkins M, Powell B, Chan P. Finite element modeling of blast lung injury in sheep. Journal of Biomechanical Engineering. 2015;137:041002.

6. Zhou H, Ma G. Stress amplification effect of lung. Medical Hypotheses. 2010;74:37–38.

7. Clayton J, Freed A. A continuum mechanical model of the lung. DEVCOM Army Research Laboratory; 2019 November. Report No.: ARL-TR-8859.

8. Clayton J, Freed A. Viscoelastic-damage theory based on a QR decomposition of deformation gradient. DEVCOM Army Research Laboratory; 2019 October. Report No.: ARL-TR-8840.

9. Clayton JD, Freed AD. A constitutive model for lung mechanics and injury applicable to static, dynamic, and shock loading. Mechanics of Soft Materials. 2020;2:3.

10. Clayton J, Freed A. A constitutive framework for finite viscoelasticity and damage based on the Gram-Schmidt decomposition. Acta Mechanica. 2020;231:3319–3362.

11. Clayton J, Banton R, Freed A. A nonlinear thermoelastic-viscoelastic continuum model of lung mechanics for shock wave analysis. In: Shock compres-

sion of condensed matter; Vol. 2272. Lane J, editor. AIP Conference Proceedings; 2020. p. 040001.

12. Clayton J. Modeling lung tissue dynamics and injury under pressure and impact loading. Biomechanics and Modeling in Mechanobiology. 2020;19:2603–2626.

13. Clayton J, Banton R, Goertz A. A continuum model of the human lung: implementation and parameterization. DEVCOM Army Research Laboratory; 2021 January. Report No.: ARL-TR-9138.

14. Josey T. Investigation of Blast Load Characteristics on Lung Injury [master's thesis]. University of Waterloo; 2010.

15. Stuhmiller JH. Blast injury: Translating research into operational medicine. TMM Publications; 2008. (Borden Institute Monograph Series).

16. Stitzel JD, Gayzik FS, Hoth JJ, Mercier J, Gage HD, Morton KA, Duma SM, Payne RM. Development of a finite element-based injury metric for pulmonary contusion, Part I: Model development and validation. Stapp Car Crash Journal. 2005;49:271–289.

17. Stuhmiller JH, Chuong CJ, Phillips YY, Dodd KT. Computer modeling of thoracic response to blast. Journal of Trauma. 1988;28:S132–S139.

18. Vlessis AA, Trunkey DD. Non-penetrating injury of the thorax. In: Scientific Foundations of Trauma. Cooper GJ, Dudley HAF, Gann DS, Little RA, Maynard RL, editors. Butterworth Heinemann; 1997. p. 127–143.

19. Fung YC, Patitucci P, Tong P. Stress and strain in the lung. ASCE Journal of Engineering Mechanics. 1978;104:201–223.

20. Vawter DL, Fung YC, West JB. Constitutive equation of lung tissue elasticity. Journal of Biomechanical Engineering. 1979;101:38–45.

21. Vawter DL. A finite element model for macroscopic deformation of the lung. Journal of Biomechanical Engineering. 1980;102:1–7.

22. Gayzik FS, Hoth JJ, Daly M, Meredith JW, Stitzel JD. A finite element based injury metric for pulmonary contusion: investigation of candidate metrics through correlation with computed tomography. Stapp Car Crash Journal. 2007;51:189–209.

23. Gayzik FS, Hoth JJ, Stitzel J. Finite element-based injury metrics for pulmonary contusion via concurrent model optimization. Biomechanics and Modeling in Mechanobiology. 2011;10:505–520.

24. Yuen K, Cronin DS, Deng YC. Lung response and injury in side impact conditions. In: Proceedings of the 2008 International Research Council on Biomechanics of Injury (IRCOBI) Conference; p. 87–98.

25. Freed AD, Einstein DR, Carson JP, Jacob RE. Viscoelastic model for lung parenchyma for multi-scale modeling of respiratory system, Phase II: Dodecahedral micro-model. Pacific Northwest National Laboratory; 2012 March. Report No.: PNNL-21287.

26. Tsokos M, Paulsen F, Petri S, Madea B, Püschel K, Türk EE. Histologic, immunohistochemical, and ultrastructural findings in human blast lung injury. American Journal of Respiratory and Critical Care Medicine. 2003;168:549–555.

27. Butler JP, Miki H, Squarcia S, Rogers RA, Lehr JL. Effect of macroscopic deformation on lung microstructure. Journal of Applied Physiology. 1996;81:1792–1799.

28. Nemat-Nasser S, Hori M. Micromechanics: overall properties of heterogeneous materials. Elsevier; 1999.

29. Clayton J. Nonlinear mechanics of crystals. Springer; 2011.

30. Roan E, Waters CM. What do we know about mechanical strain in lung alveoli?. American Journal of Physiology–Lung Cellular and Molecular Physiology. 2011;301:L625–L635.

31. Fung YC. Biomechanics: Motion, flow, stress, and growth. Springer-Verlag; 1990.

32. Fung YC. Stress, deformation, and atelectasis of the lung. Circulation Research. 1975;37:481–496.

33. Fung YC. A model of the lung structure and its validation. Journal of Applied Physiology. 1988;64:2132–2141.

34. Hoppin, Jr. FG, Hildebrandt J. Mechanical properties of the lung. In: Bioengineering Aspects of the Lung; Vol. 3. West JB, editor. Marcel Dekker; 1977. p. 83–162.

35. Frankus A, Lee GC. A theory for distortion studies of lung parenchyma based on alveolar membrane properties. Journal of Biomechanics. 1974;7:101–107.

36. de Ryk J, Thiesse J, Namati E, McLennan G. Stress distribution in a three dimensional, geometric alveolar sac under normal and emphysematous conditions. International Journal of COPD. 2007;2:81–91.

37. Dale PJ, Matthews FL, Schroter RC. Finite element analysis of lung alveolus. Journal of Biomechanics. 1980;13:865–873.

38. Denny E, Schroter RC. The mechanical behavior of a mammalian lung alveolar duct model. Journal of Biomechanical Engineering. 1995;117:254–261.

39. Denny E, Schroter RC. Relationships between alveolar size and fibre distribution in mammalian lung alveolar duct model. Journal of Biomechanical Engineering. 1997;119:289–297.

40. Denny E, Schroter RC. Viscoelastic behavior of a lung alveolar duct model. Journal of Biomechanical Engineering. 2000;122:143–151.

41. Kowe R, Schroter RC, Matthews FL, Hitchings D. Analysis of elastic and surface tension effects in the lung alveolus using finite element methods. Journal of Biomechanics. 1986;19(7):541–549.

42. Chen G, Zhang ZS, Mei YH, Li X, Yu DJ, Wang L, Chen X. Applying viscoplastic constitutive models to predict ratcheting behavior of sintered nanosilver lap-shear joint. Mechanics of Materials. 2014;2014:61–71.

43. Kimmel E, Kamm RD, Shapiro AH. A cellular model of lung elasticity. Journal of Biomechanical Engineering. 1987;109:126–131.

44. Budiansky B, Kimmel E. Elastic moduli of lungs. Journal of Applied Mechanics. 1987;54:351–358.

45. Kimmel E, Budiansky B. Surface tension and the dodecahedron model for lung elasticity. Journal of Biomechanical Engineering. 1990;112:160–167.

46. Weed B, Patnaik S, Rougeau-Browning M, Brazile B, Liao J, Prabhu R, Williams LN. Experimental evidence of mechanical isotropy in porcine lung parenchyma. Materials. 2015;8:2454–2466.

47. Hughes JMB, Hoppin FG, Mead J. Effect of lung inflation on bronchial length and diameter in excised lungs. Journal of Applied Physiology. 1972;32(1):25–35.

48. Mead J. Respiration: pulmonary mechanics. Annual Review of Physiology. 1973;35:169–192.

49. West JB. Respiratory physiology: The essentials. eighth ed. Lippincott Williams & Wilkins; 2007.

50. Denny E, Schroter RC. A model of non-uniform lung parenchyma distortion. Journal of Biomechanics. 2006;39:652–663.

51. McLellan AG. The classical thermodynamics of deformable materials. Cambridge University Press; 1980. (Cambridge Monographs in Physics).

52. Freed AD, Zamani S. On the use of convected coordinate systems in the mechanics of continuous media derived from a **QR** factorization of **F**. International Journal of Engineering Science. 2018;127:145–161.

53. Paul S, Freed AD, Clayton JD. Coordinate indexing: On the use of Eulerian and Lagrangian Laplace stretches. Applications in Engineering Science. 2021;5:100029.

54. Sobin SS, Fung YC, Tremer HM. Collagen and elastin fibers in human pulmonary alveolar walls. Journal of Applied Physiology. 1988;64(4):1659–1675.

55. Freed AD, Zamani S, Szabó L, Clayton JD. Laplace stretch: Eulerian and Lagrangian formulations. Zeitschrift für angewandte Mathematik und Physik. 2020;71:157.

56. Freed AD, le Graverend JB, Rajagopal KR. A decomposition of Laplace stretch with applications in inelasticity. Acta Mechanica. 2019;230:3423–3429.

57. Wachspress EL. A rational finite element basis. Academic Press; 1975.

58. Wachspress E. Rational bases and generalized barycentrics: Applications to finite elements and graphics. Springer; 2016.

59. Hughes TJR. The finite element method: Linear static and dynamic finite element analysis. Prentice-Hall; 1987.

60. Sukumar N, Malsch EA. Recent advances in the construction of polygonal finite element interpolants. Archives of Computational Methods in Engineering. 2006;13:129–163.

61. Dasgupta G. Interpolants within convex polygons: Wachspress' shape functions. Journal of Aerospace Engineering. 2003;16:1–8.

62. Clayton JD. Differential geometry and kinematics of continua. World Scientific; 2014.

63. Srinivasa AR. On the use of the upper triangle (or **QR**) decomposition for developing constitutive equations for Green-elastic materials. International Journal of Engineering Science. 2012;60:1–12.

64. Freed AD, Srinivasa AR. Logarithmic strain and its material derivative for a **QR** decomposition of the deformation gradient. Acta Mechanica. 2015;226:2645–2670.

65. Freed AD, Erel V, Moreno MR. Conjugate stress/strain base pairs for planar analysis of biological tissues. Journal of Mechanics of Materials and Structures. 2017;12:219–247.

66. Freed AD, Zamani S. Elastic Kelvin-Poisson-Poynting solids described through scalar conjugate stress/strain pairs derived from a **QR** factorization of **F**. Journal of the Mechanics and Physics of Solids. 2019;129:278–293.

67. McLellan AG. Finite strain coordinate and the stability of solid phases. Journal of Physics C: Solid State Physics. 1976;9:4083–4094.

68. Rosakis P. Ellipticity and deformations with discontinuous gradients in finite elastostatics. Archives for Rational Mechanics and Analysis. 1990;109:1–37.

69. Souchet R. Concerning the polar decomposition of the deformation gradient. International Journal of Engineering Science. 1993;31:1499–1506.

70. Leon SJ, Björck Å, Gander W. Gram-Schmidt orthogonalization: 100 years and more. Numerical Linear Algebra with Applications. 2013;20:492–532.

71. Clayton J. Compatibility conditions from a Gram-Schmidt decomposition of deformation gradient in two dimensions. Mechanics Research Communications. 2020;104:103498.

72. Paul S, Freed AD. A simple and practical representation of compatibility condition derived using a **QR** decomposition of the deformation gradient. Acta Mechanica. 2020;231:3289-3304.

73. Freed AD. A note on stress/strain conjugate pairs: explicit and implicit theories of thermoelasticity for anisotropic materials. International Journal of Engineering Science. 2017;120:155–171.

74. Carathéodory C. Untersuchungen über die Grundlagen der Thermodynamik. Mathematische Annalen. 1909;67:355–386.

75. Perlman CE, Bhattacharya J. Alveolar expansion imaged by optical sectioning microscopy. Journal of Applied Physiology. 2007;103:1037–1044.

76. Treloar LRG. The physics of rubber elasticity. third ed. Clarendon Press; 1975.

77. Suki B, Ito S, Stamenović D, Lutchen KR, Ingenito EP. Biomechanics of the lung parenchyma: critical roles of collagen and mechanical forces. Journal of Applied Physiology. 2005;98:1892–1899.

78. Suki B, Stamenović D, Hubmayr R. Lung parenchymal mechanics. Comprehensive Physiology. 2011;1:1317–1351.

79. Weinhold F. Metric geometry of equilibrium thermodynamics. III. Elementary formal structure of a vector-algebraic representation of equilibrium thermodynamics. The Journal of Chemical Physics. 1975;63:2488–2495.

80. Gilmore R. Length and curvature in the geometry of thermodynamics. Physical Review A. 1984;30:1994–1997.

81. Truesdell C. Hypoelasticity. Journal of Rational Mechanics and Analysis. 1955;4:83–133.

82. Lai-Fook SJ. Elastic properties of lung parenchyma: the effect of pressure-volume hysteresis on the behavior of large blood vessels. Journal of Biomechanics. 1979;12:757–764.

83. Jahed M, Lai-Fook SJ, Bhagat PK. Effect of vascular volume and edema on wave propagation in canine lungs. Journal of Applied Physiology. 1990;68:2171–2176.

84. Saraf H, Ramesh KT, Lennon AM, Merkle AC, Roberts JC. Mechanical properties of soft human tissues under dynamic loading. Journal of Biomechanics. 2007;40:1960–1967.

85. Hajji MA, Wilson TA, Lai-Fook SJ. Improved measurements of shear modulus and pleural membrane tension of the lung. Journal of Applied Physiology. 1979;47:175–181.

86. Hildebrandt J. Comparison of mathematical models for cat lung and viscoelastic balloon derived by Laplace transform methods from pressure-volume data. Bulletin of Mathematical Biophysics. 1969;31:651-667.

87. Ames Research Staff. Equations, tables, and charts for compressible flow. National Advisory Committee for Aeronautics; 1953. Report No.: NACA 1135.

88. Stamenović D. Micromechanical foundations of pulmonary elasticity. Physiological Reviews. 1990;70(4):1117–1134.

89. Hills BA. An alternative view of the role(s) of surfactant and the alveolar model. Journal of Applied Physiology. 1999;87:1567–1583.

90. Bates JHT. A recruitment model of quasi-linear power-law stress adaptation in lung tissue. Annals of Biomedical Engineering. 2007;35:1165–1174.

91. Matsuda M, Fung YC, Sobin SS. Collagen and elastin fibers in human pulmonary alveolar mouths and ducts. Journal of Applied Physiology. 1987;63(3):1185–1194.

92. Kastelic J, Galeski A, Baer E. The multicomposite structure of tendon. Connective Tissue Research. 1978;6:11–23.

93. Freed AD, Doehring TC. Elastic model for crimped collagen fibrils. Journal of Biomechanical Engineering. 2005;127:587–593.

94. Aaron BB, Gosline JM. Elastin as a random-network elastomer: a mechanical and optical analysis of single elastin fibers. Biopolymers. 1981;20:1247–1260.

95. Urry DW. Physicochemical properties of elastin and constituent peptides. In: Physicochemical properties of elastin and constituent peptides; Vol. 1; CRC Press; 1989. Chapter 10, p. 141–173.

96. Freed AD, Rajagopal KR. A promising approach for modeling biological fibers. Acta Mechanica. 2016;227:1609–1619; Errata: **229** (2018), pg. 3573.

97. Hörmann H, Schlebusch H. Reversible and irreversible denaturation of collagen fibers. Biochemistry. 1971;10(6):932–937.

98. Fels IG. Hydration and density of collagen and gelatin. Journal of Applied Polymer Science. 1964;8:1813–1824.

99. Kanagy JR. Specific heats of collagen and leather. Journal of Research of the National Bureau of Standards. 1955;55:191–195.

100. Weir CE. Effect of temperature on the volume of leather and collagen in water. Journal of Research of the National Bureau of Standards. 1948;41:279–285.

101. Lillie MA, Gosline JM. Unusual swelling of elastin. Biopolymers. 2002;64:115–126.

102. Shadwick RE, Gosline JM. Physical and chemical properties of rubber-like elastic fibres from the octopus aorta. Journal of Experimental Biology. 1985;114:239–257.

103. Kakivaya SR, Hoeve CAJ. The glass point of elastin. Proceedings of the National Academy of Sciences, USA. 1975;72:3505–3507.

104. Lillie MA, Gosline JM. Mechanical properties of elastin along the thoracic aorta in the pig. Journal of Biomechanics. 2007;40:2214–2221.

105. Svensson RB, Hassenkam T, Grant CA, Magnusson SP. Tensile properties of human collagen fibrils and fascicles are insensitive to environmental salts. Biophysical Journal. 2010;99:4020–4027.

106. Davison L. Fundamentals of shock wave propagation in solids. Springer; 2008. (Shock Wave and High Pressure Phenomena).

107. Birzle AM, Hobrack SMK, Martin C, Uhlig S, Wall WA. Constituent-specific material behavior of soft biological tissue: experimental quantification and numerical identification for lung parenchyma. Biomechanics and Modeling in Mechanobiology. 2019;18:1383–1400.

108. Freed AD. A technical note: Two-step PECE methods for approximating solutions to first- and second-order ODEs. Texas A&M University; 2017. Report No.: arXiv:1707.02125 [cs.NA].

109. Noll W. On the continuity of the solid and fluid states. Journal of Rational Mechanics and Analysis. 1955;4:3–81.

110. Newmark NM. A method of computation for structural dynamics. Journal of the Engineering Mechanics Division, Proceedings of the American Society of Civil Engineers. 1959;EM 3:67–94.

111. Oñate E. Structural analysis with the finite element method. linear statics. Springer; 2009. (Lecture Notes on Numerical Methods in Engineering and Sciences; vol. 1. Basis and Solids).

112. Mousavi SE, Xiao H, Sukumar N. Generalized Gaussian quadrature rules on arbitrary polygons. International Journal for Numerical Methods in Engineering. 2010;82:99–113.

113. Chakraborty S, Natarajan S, Singh S, Mahapatra DR, Bordas SPA. Optimal numerical integration schemes for a family of polygonal finite elements with Schwarz-Christoffel conformal mapping. International Journal for Computational Methods in Engineering Science and Mechanics. 2018;19:283–304.

114. Saraf H, Ramesh K, Lennon A, Merkle A, Roberts J. Mechanical properties of soft human tissues under dynamic loading. Journal of Biomechanics. 2007;40:1960–1967.

115. Sanborn B, Nie X, Chen W, Weerasooriya T. High strain rate pure shear and axial compressive response of porcine lung tissue. Journal of Applied Mechanics. 2013;80:011029.

116. Belytschko T, Liu WK, Moran B. Nonlinear Finite Elements for Continua and Structures. Wiley; 2000.

117. Archer JS. Consistent matrix formulations for structural analysis using finite-element techniques. AIAA Journal. 1965;3:1910–1918.

118. Reddy JN. An introduction to the finite element method. 2nd ed. McGraw.Hill series in mechanical engineering; 1993.

119. Clayton JD, Chung PW. Applied finite element methods: Lecture notes on principles and procedures. CreateSpace; 2018.

120. Freed AD. Soft solids: A primer to the theoretical mechanics of materials. Birkhäuser; 2014. (Modeling and Simulation in Science, Engineering and Technology).

121. Yang XY, Zhao JC, Gong JH. Stiffness matrix derivation of space beam element at elevated temperature. J. Shanghai Jiaotong Univ. 2010;4:492–497.

122. Elseifi M. A new scheme for the optimum design of stiffened composite panels with geometric imperfections [thesis]. Virginia Polytechnic Institute and State University; 1998.

123. Green G. On the propagation of light in crystallized media. Transactions of the Cambridge Philosophical Society. 1841;7:121–140.

124. Rajagopal KR. On implicit constitutive theories. Applications of Mathematics. 2003;48(4):279–319.

125. Akintunde AR, Miller KS. Evaluation of microstructurally motivated constitutive models to describe age-dependent tendon healing. Biomechanics and Modeling in Mechanobiology. 2018;17:793–814.

126. Robbins AB, Freed AD, Moreno MR. Characterizing the non-linear mechanical behavior of native and biomimetic engineered tissues in 1d with physically meaningful parameters. Journal of the Mechanical Behavior of Biomedical Materials. 2020;102:103509.

127. Freed AD, Rajagopal KR. A viscoelastic model for describing the response of biological fibers. Acta Mechanica. 2016;227:3367–3380.

Appendix. Implicit Elasticity

Both explicit (i.e., Green[123]) and implicit (i.e., Rajagopal[124]) elastic material models are put forward in this appendix for one's consideration when choosing a material model to represent biologic fibers and membranes. We discuss thermoelastic fibers first, and then thermoelastic membranes. We have no need to address thermoelastic bodies in 3D for our application, beyond what has been presented in Section 4.4.4. In this appendix, we employ Gibbs free-energy potential $\mathcal{G}$ instead of the internal energy potential U, which we employ in the body of this report. These potentials relate to one another through a well-known Legendre transformation. A Gibbs energy approach implies that a change in the intensive variables (thermodynamic forces) will cause a response in the extensive variables (thermodynamic displacements), which is the exact opposite cause-and-effect arising from an internal energy approach. Causality is correct whenever one uses a Gibbs approach, from a physics perspective. Nevertheless, applications often find other approaches to be more useful, especially that of Helmholtz. Here we present both secant and tangent moduli formulations for biologic fibers and membranes, as both are required by our variational formulation.

A.1 Alveolar Chords as Green (Explicit) Thermoelastic Fibers

For a 1D fiber with a mass density of ρ per unit length, the thermodynamic conjugate fields are temperature θ and entropy η, plus force F and length L, whose initial values in some reference configuration are denoted as θ_0, η_0, F_0, and L_0. In our construction, it is insightful to use $\ln(\theta/\theta_0)$ and $\ln(L/L_0)$ as measures for change in temperature and length, with the former changing how we interpret thermal strain, but not specific heat, while the latter is commonly referred to as mechanical strain, viz., $e \coloneqq \ln(L/L_0)$.

A Green thermoelastic fiber has a Gibbs free-energy potential described by an explicit function of state, viz., $\mathcal{G}(\theta, F)$ where $\mathrm{d}\mathcal{G} = -\eta\,\mathrm{d}\theta - \frac{1}{\rho}e\,\mathrm{d}F$ (cf. Eq. 56a), out of which one derives the governing thermoelastic constitutive equations, viz., for entropy

$$\eta = -\partial_\theta \mathcal{G}(\theta, F), \tag{A-1a}$$

and for strain

$$e \coloneqq \ln(L/L_0) = -\rho\,\partial_F \mathcal{G}(\theta, F). \tag{A-1b}$$

Providing an energy function establishes a material model.

A.1.1 Hookean Fibers

Herein we consider a Gibbs free-energy potential suitable for describing a Hookean fiber, i.e.,

$$\mathcal{G}(\theta, F) = -\eta_0(\theta - \theta_0) - C\left(\theta \ln\left(\frac{\theta}{\theta_0}\right) - (\theta - \theta_0)\right) - \frac{F - F_0}{\rho}\left(\alpha \ln\left(\frac{\theta}{\theta_0}\right) + \frac{F - F_0}{2E}\right) \quad \text{(A-2)}$$

normalized so that $\mathcal{G}(\theta_0, F_0) = 0$ with initial conditions of $\eta_0 = -\partial_\theta \mathcal{G}(\theta_0, F_0)$ and $e_0 = -\rho\, \partial_F \mathcal{G}(\theta_0, F_0) = 0$ in our reference state associated with fields θ_0 and F_0. Introducing $\ln(\theta/\theta_0)$ presumes that temperature θ is absolute, i.e., it is measured in Kelvin, not centigrade, so in our application $\theta_0 = 310$ K is body temperature.

The model's material properties are a specific heat C, a thermal strain coefficient α, and an elastic compliance $1/E$ or modulus E. These properties are interpreted from the perspective of both secant and tangent functions of state in this appendix.

In vivo, biologic fibers operate under cyclic loading conditions where, typically, $0 < F_{\min} < F < F_{\max} < F_{\text{ult}}$ that, under normal physiologic conditions, finds force F traversing between $F_{\min}$ and $F_{\max}$ with F_{ult} designating ultimate rupture strength. Here we take F_0 to associate with $F_{\min}$. Consequently, strain is assigned to be zero in this reference state of $F_0 > 0$. Similarly, physicians will reference against some physiologic state of relevance; however, their reference states usually associate with $F_{\max}$, not $F_{\min}$, e.g., total lung capacity for pulmonary applications, and max systole for cardiac applications. *Ex vivo*, one typically selects $F_0 = 0$ for biologic fibers.

A.1.2 Secant Material Properties

Substituting the Gibbs free-energy function (Eq. A-2) into the constitutive equations (Eqs. A-1a and A-1b) governing entropy and strain, respectively, results in the matrix expression

$$\begin{Bmatrix} \eta - \eta_0 \\ \ln(L/L_0) \end{Bmatrix} = \begin{bmatrix} C_s & \alpha_s/\rho\theta \\ \alpha_s & 1/E_s \end{bmatrix} \begin{Bmatrix} \ln(\theta/\theta_0) \\ F - F_0 \end{Bmatrix}$$

which rearranges into a form that is more suitable for our needs, specifically

$$\begin{Bmatrix} \eta - \eta_0 \\ F - F_0 \end{Bmatrix} = \begin{bmatrix} C_s - \alpha_s^2 E_s/\rho\theta & \alpha_s E_s/\rho\theta \\ -\alpha_s E_s & E_s \end{bmatrix} \begin{Bmatrix} \ln(\theta/\theta_0) \\ \ln(L/L_0) \end{Bmatrix} \tag{A-3a}$$

with material properties: a specific heat (evaluated at some reference force F_0) of

$$C_s := \left.\frac{\eta - \eta_0}{\ln(\theta/\theta_0)}\right|_{F=F_0}, \tag{A-3b}$$

with $C_s - \alpha_s^2 E_s/\rho\theta$ being a heat capacity (evaluated at some reference length L_0), plus a thermal strain coefficient (evaluated at some reference force F_0) of

$$\alpha_s := \left.\frac{\ln(L/L_0)}{\ln(\theta/\theta_0)}\right|_{F=F_0}, \tag{A-3c}$$

and an elastic compliance (evaluated at some reference temperature θ_0) of

$$\frac{1}{E_s} := \left.\frac{\ln(L/L_0)}{F - F_0}\right|_{\theta=\theta_0}. \tag{A-3d}$$

These are *secant* material properties, hence the subscript s, which can be measured through appropriate experiments. The curves that they trace through state space are then to be approximated via a model.

Note: Thermal elongation is typically modeled as $\alpha(\theta - \theta_0)$, wherein α is referred to as the coefficient for thermal expansion. Our thermal strain coefficient α_s, which is dimensionless, and the coefficient for thermal expansion α, which has dimensions of reciprocal temperature, relate via $\alpha_s = \alpha\theta_0 + \mathcal{O}\big(((\theta - \theta_0)/\theta_0)^2\big)$ because $\ln(\theta/\theta_0) = (\theta - \theta_0)/\theta_0 - (\theta - \theta_0)^2/\theta_0^2 + (\theta - \theta_0)^3/\theta_0^3 - \cdots$.

A.1.3 Tangent Material Properties

Upon differentiating the constitutive equations for entropy and strain found in Eqs. A-1a and A-1b, respectively, assuming that they are both sufficiently differentiable functions of state, while adopting the expression for Gibbs free energy found in Eq. A-2, results in the following constitutive equation

$$\begin{Bmatrix} \mathrm{d}\eta \\ L^{-1}\,\mathrm{d}L \end{Bmatrix} = -\begin{bmatrix} \partial_{\theta\theta}\mathcal{G} & \partial_{\theta F}\mathcal{G} \\ \rho\,\partial_{F\theta}\mathcal{G} & \rho\,\partial_{FF}\mathcal{G} \end{bmatrix} \begin{Bmatrix} \mathrm{d}\theta \\ \mathrm{d}F \end{Bmatrix} = \begin{bmatrix} C_t & \alpha_t/\rho\theta \\ \alpha_t & 1/E_t \end{bmatrix} \begin{Bmatrix} \theta^{-1}\,\mathrm{d}\theta \\ \mathrm{d}F \end{Bmatrix}$$

where we observe that the intensive and extensive variables now appear in rate or differential form; hence, this formulation is hypo-elastic.[81] This matrix equation can be rearranged into an expression that is more suitable for our needs, viz.,

$$\begin{Bmatrix} \mathrm{d}\eta \\ \mathrm{d}F \end{Bmatrix} = \begin{bmatrix} C_t - \alpha_t^2 E_t/\rho\theta & \alpha_t E_t/\rho\theta \\ -\alpha_t E_t & E_t \end{bmatrix} \begin{Bmatrix} \theta^{-1}\,\mathrm{d}\theta \\ L^{-1}\,\mathrm{d}L \end{Bmatrix} \tag{A-4a}$$

whose material properties are a specific heat (at constant force) of

$$C_t \coloneqq \left.\frac{\mathrm{d}\eta}{\theta^{-1}\,\mathrm{d}\theta}\right|_{\mathrm{d}F=0} = C_s - \frac{\alpha_s(F-F_0)}{\rho\,\theta} = -\theta\,\partial_{\theta\theta}\,\mathcal{G}(\theta,F), \tag{A-4b}$$

where the tangent response for specific heat C_t relates to the secant response for specific heat C_s via $C_t = C_s - \alpha_s(F-F_0)/\rho\theta$, with $C_t - \alpha_t^2 E_t/\rho\theta$ being a heat capacity (at constant strain), plus a thermal strain coefficient (at constant force) of

$$\alpha_t \coloneqq \left.\frac{L^{-1}\,\mathrm{d}L}{\theta^{-1}\,\mathrm{d}\theta}\right|_{\mathrm{dF}=0} = -\rho\theta\,\partial_{F\theta}\,\mathcal{G}(\theta,F) = -\rho\theta\,\partial_{\theta F}\,\mathcal{G}(\theta,F), \tag{A-4c}$$

where, typically, $\alpha_t \equiv \alpha_s$, and an elastic compliance (at constant temperature) of

$$\frac{1}{E_t} \coloneqq \left.\frac{L^{-1}\,\mathrm{d}L}{\mathrm{d}F}\right|_{\mathrm{d}\theta=0} = -\rho\,\partial_{FF}\,\mathcal{G}(\theta,F), \tag{A-4d}$$

which is distinct from its secant compliance for the biologic fiber model that follows. These are *tangent* material properties, hence the subscript t, whose values can be measured through appropriate experiments.

Matrix equation A-4a is expressed in terms of Helmholtz causality, but is derived out of Gibbs causality to ensure that Maxwell's condition present in Eqs. A-4a and A-4c is satisfied.

It turns out that these tangent material properties correspond directly with components acquired from the Laplacian of one's Gibbs free-energy potential.

A.2 Alveolar Chords as Rajagopal (Implicit) Thermoelastic Fibers

In 2003, Rajagopal[124] introduced the idea of an implicit elastic solid. In 2016, Freed and Rajagopal[96] constructed an elastic fiber model that convolves an explicit energy with an implicit energy. In their approach, they decomposed fiber strain $e \coloneqq \ln(L/L_0)$ into a sum of two strains, viz., $e = e_1 + e_2$ wherein $e_1 \coloneqq \ln(L_1/L_0)$ and $e_2 \coloneqq \ln(L/L_1)$. Length L_0 is a reference fiber length, viz., its length whereat $F = F_0$. Length L_1 can be thought of as the fiber's length caused solely by a molecular reconfiguration under an applied load of F (e.g., an unraveling of crimp in collagen, a network reorientation in elastin, a reconformation in structural proteins, etc.). The state associated with length L_1 is non-physical in that one cannot unravel molecules without also stretching some of their bonds to a certain extent. Final length L is the actual fiber length under an applied load F caused by both a reconfiguration and a stretching of its molecular network. Here we present their ideas in terms of a Gibbs free-energy function, which leads naturally to additive compliances, instead of working with moduli, which do not add.*

Let the Gibbs free-energy potential be described by a function of the form†

$$\mathcal{G}(\theta, e, F) \coloneqq \mathcal{G}_1(e_1, F) + \mathcal{G}_2(\theta, F) \quad \text{with} \quad \mathrm{d}\mathcal{G} = -\eta\,\mathrm{d}\theta - \tfrac{1}{\rho} e\,\mathrm{d}F, \tag{A-5}$$

where $\mathcal{G}_1$ is an implicit potential (a configuration energy) and $\mathcal{G}_2$ is an explicit potential (a strain energy). This energy function leads to the same constitutive equation displayed in Eq. A-4a, but whose material properties from Eqs. A-4b–A-4d are now interpreted according to the following formulæ

$$C_t \coloneqq \left.\frac{\mathrm{d}\eta}{\theta^{-1}\,\mathrm{d}\theta}\right|_{\mathrm{d}F=0} = -\theta\,\partial_{\theta\theta}\,\mathcal{G}(\theta, e, F) = -\theta\,\partial_{\theta\theta}\,\mathcal{G}_2(\theta, F) \tag{A-6a}$$

$$\alpha_t \coloneqq \left.\frac{L^{-1}\,\mathrm{d}L}{\theta^{-1}\,\mathrm{d}\theta}\right|_{\mathrm{dF}=0} = -\rho\theta\,\partial_{F\theta}\,\mathcal{G}(\theta, e, F) = -\rho\theta\,\partial_{F\theta}\,\mathcal{G}_2(\theta, F) \tag{A-6b}$$

$$\begin{aligned}\frac{1}{E_t} \coloneqq \left.\frac{L^{-1}\,\mathrm{d}L}{\mathrm{d}F}\right|_{\mathrm{d}\theta=0} &= -\big(\rho\,\partial_{e_1}\mathcal{G}_1(e_1, F)\big)^{-1}\big(e + \rho\,\partial_F\,\mathcal{G}(\theta, e, F)\big) \\ &\quad - \rho\,\partial_{FF}\,\mathcal{G}_2(\theta, F)\end{aligned} \tag{A-6c}$$

*Freed and Rajagopal[96] originally used a Helmholtz free-energy function.

†One might be tempted to consider an implicit energy function of the form $\mathcal{G} = \mathcal{G}_1(\theta, e, F) + \mathcal{G}_2(\theta, F)$, but this would lead to a non-symmetric susceptibility matrix. Consequently, it would not satisfy Maxwell's thermodynamic constraint, a.k.a. Sylvester's condition for integrability of a Pfaffian form. Hence, it is an inadmissible functional dependence for a Gibbs potential.

where mass density ρ is a mass per unit length of line. Elastic compliance $1/E_t$ is now found to be a sum of two compliances, independent of the functional forms that one might select for $\mathcal{G}_1(e_1, F)$ and $\mathcal{G}_2(\theta, F)$. One compliance is explicit in origin, i.e., $e_2 = -\rho\,\partial_F \mathcal{G}_2$ with rate $\mathrm{d}e_2 = -\rho\,\partial_{F\theta}\mathcal{G}_2\,\mathrm{d}\theta - \rho\,\partial_{FF}\mathcal{G}_2\,\mathrm{d}F$. It comprises the second row in Eq. A-6c. The other compliance is implicit in origin, viz., $\mathrm{d}e_1 = -(\rho\,\partial_{e_1}\mathcal{G}_1)^{-1}(e_1 + \rho\,\partial_F\mathcal{G}_1)\mathrm{d}F \equiv -(\rho\,\partial_{e_1}\mathcal{G}_1)^{-1}(e + \rho\,\partial_F\mathcal{G})\mathrm{d}F$. It comprises the first row in Eq. A-6c. Also, $\partial_{F\theta}\mathcal{G} = \partial_{\theta F}\mathcal{G}$ because of Maxwell's thermodynamic constraint.

The material properties of Eq. A-6 apply to matrix equation A-4a, just as those for a Hookean material do, viz., Eqs. A-4b–A-4d. The specific heat C_t and thermal strain coefficient α_t have the same interpretations for both explicit and implicit fiber theories. It is with respect to their compliances through which they differ.

Derivation: Because Gibbs free energy is a state function, its differential describes a Pfaffian form, and as such, the left-hand side of the thermodynamic expression $\mathrm{d}\mathcal{G} = -\eta\,\mathrm{d}\theta - \frac{1}{\rho}e\,\mathrm{d}F$ becomes $\mathrm{d}\mathcal{G} = \partial_{e_1}\mathcal{G}_1\,\mathrm{d}e_1 + \partial_F\mathcal{G}_1\,\mathrm{d}F + \partial_\theta\mathcal{G}_2\,\mathrm{d}\theta + \partial_F\mathcal{G}_2\,\mathrm{d}F$. Recalling that $e = e_1 + e_2$, the explicit (hyper-elastic like) terms combine to produce constitutive equations

$$\eta = -\partial_\theta\mathcal{G}_2(\theta, F) \quad \text{and} \quad e_2 = -\rho\,\partial_F\mathcal{G}_2(\theta, F)$$

while the remaining implicit terms collect to yield a differential constitutive equation of the form

$$\rho\,\partial_{e_1}\mathcal{G}_1(e_1, F)\,\mathrm{d}e_1 = -\big(e_1 + \rho\,\partial_F\mathcal{G}_1(e_1, F)\big)\mathrm{d}F.$$

Differentiating the constitutive equation for entropy with respect to state leads directly to expressions for the specific heat C_t and the thermal expansion coefficient α_t stated in Eqs. A-6a and A-6b. Recalling that the strains add, i.e., $e = e_1 + e_2$, and therefore so do their rates, viz., $\mathrm{d}e = \mathrm{d}e_1 + \mathrm{d}e_2$, a direct consequence of them being logarithmic in construction, it follows that upon rearranging the implicit constitutive equation to solve for $\mathrm{d}e_1$, while differentiating the explicit constitutive equation for e_2, and finally adding these strain increments to get $\mathrm{d}e$, one obtains the elastic compliance function stated in Eq. A-6c. □

A.2.1 Biologic Fibers with Tangent Material Properties

The fiber model of Freed and Rajagopal[96] imposes a limiting constraint $e_{1_{\max}}$ onto the internal strain of reconfiguration e_1, viz., $e_1 \leqslant e_{1_{\max}}$. Their model, when cast in terms of a Gibbs free-energy function in the form of Eq. A-5, is described by an implicit energy contribution of*

$$\mathcal{G}_1(e_1, F) = -\frac{1}{\rho}\Big(e_{1_{\max}}\big(E_1 e_1 - (F - F_0)\big) + 2e_1(F - F_0)\Big) \tag{A-7a}$$

and explicit energy contribution of

$$\begin{aligned}\mathcal{G}_2(\theta, F) = &-\eta_0(\theta - \theta_0) - C\left(\theta \ln\left(\frac{\theta}{\theta_0}\right) - (\theta - \theta_0)\right) \\ &- \frac{F - F_0}{\rho}\left(\alpha \ln\left(\frac{\theta}{\theta_0}\right) + \frac{F - F_0}{2E_2}\right)\end{aligned} \tag{A-7b}$$

that, collectively, depend upon temperature θ, force F, and an internal strain e_1, whose free energy is normalized so that $\mathcal{G}_1(e_{1,0}, F_0) = 0$ and $\mathcal{G}_2(\theta_0, F_0) = 0$ with initial conditions $e_{1,0} = 0$, $e_{2,0} = -\rho\,\partial_F \mathcal{G}_2(\theta_0, F_0) = 0$ and $\eta_0 = -\partial_\theta \mathcal{G}_2(\theta_0, F_0)$. In fact, the explicit contribution to the free energy adopted here is Hookean, cf. Eq. A-2. The resulting constitutive responses for entropy η and force F are therefore described by the following differential matrix equation

$$\begin{Bmatrix} \mathrm{d}\eta \\ \mathrm{d}F \end{Bmatrix} = \begin{bmatrix} C_t - \alpha_t^2 E_t/\rho\theta & \alpha_t E_t/\rho\theta \\ -\alpha_t E_t & E_t \end{bmatrix} \begin{Bmatrix} \theta^{-1}\,\mathrm{d}\theta \\ L^{-1}\,\mathrm{d}L \end{Bmatrix} \tag{A-4a}$$

whose elastic tangent compliance is now described by

$$\frac{1}{E_t(\theta, e, F)} = \frac{e_{1_{\max}} - e_1}{E_1 e_{1_{\max}} + 2(F - F_0)} + \frac{1}{E_2} \tag{A-7c}$$

wherein

$$e_1 = e - \alpha \ln\left(\frac{\theta}{\theta_0}\right) - \frac{F - F_0}{E_2} \tag{A-7d}$$

*In the paper of Freed and Rajagopal,[96] they adopted a Helmholtz free-energy potential of the form $Ee_1 - F + \beta e_1 F$ where β is a material parameter that relates to a limiting state of strain. Here we adopt a Gibbs free-energy potential of like form, specifically $e_{1_{\max}}(Ee_1 - F) + 2e_1 F$ where $e_{1_{\max}}$ is this limiting state of internal strain e_1. We point out that an exponential response akin to Fung's material models will result whenever the energy of reconfiguration takes on a form of $Ee_1 - F$.

and whose initial tangent modulus $E_t(\theta_0, e_0, F_0)$ is $E_1E_2/(E_1 + E_2)$ ($\approx E_1$ whenever $E_2 \gg E_1 > 0$) while its terminal tangent modulus $E_t(e_1 = e_{1_{\max}})$ is E_2. A transition strain occurs at $e_{1_{\max}}$ (> 0), which establishes the limiting state for internal strain e_1, i.e., $e_1 \leqslant e_{1_{\max}}$. This is a strain whereat the fiber's molecular configuration becomes completely unraveled. The 2 in term $2e_1(F - F_0)$ of Eq. A-7a leads to the desired numerator for the implicit contribution to compliance established in Eq. A-7c, viz., $e_{1_{\max}} - e_1$, which is the source of the strain limiting quality of the model. This fiber model has been found to be superior to other models commonly employed in the literature for modeling biologic fibers.[125,126]

Both the explicit and implicit models have the same hypo-elastic structure, viz., Eq. A-4a. Furthermore, their thermal properties C_t and α_t have the same physical interpretations. Only their elastic compliances/moduli are interpreted differently. Even so, they are related because $1/E_s = \int_{F_0}^{F} (1/E_t)\,\mathrm{d}F$.

The sum of implicit and explicit fiber compliances, as established in Eq. A-7c, was originally a conjecture by Freed and Rajagopal.[96] Here it is shown to be a thermodynamic consequence, provided that $\mathcal{G}(\theta, e, F) = \mathcal{G}_1(e_1, F) + \mathcal{G}_2(\theta, F)$ and that $e = e_1 + e_2$ with $e_2 = -\rho\,\partial_F \mathcal{G}_2$. This follows because a Gibbs free energy is used here; whereas, Freed and Rajagopal employed a Helmholtz free energy.

Biologic fibers, per our application, are long and slender. Consequently, they will buckle under compression. Buckling is not accounted for in our modeling of alveolar chords. Rather, it is assumed that the compliant response at F_0, with a modulus of $E_1E_2/(E_1 + E_2)$, continues over the non-physiologic loading range of $0 < F \leqslant F_{\min} = F_0$, which is the body's way of ensuring structural integrity of its biologic fibers.

The above methodology would allow us to construct a suite of thermodynamically admissible, elastic, compliance functions, but we will only have need for the simple fiber model put forward in Eq. A-7.

A.2.2 Biologic Fibers with Secant Material Properties

Material properties C_t, α_t, and E_t for the above model, viz., those of Eq. A-7, describe tangents to material response functions. For the thermal properties, their secant counterparts C_s and α_s relate to their tangent properties C_t and α_t just as they do for a Green elastic fiber. Only the elastic compliance needs to be addressed.

The tangent modulus E_t is established through the relationship

$$\frac{1}{E_t} \coloneqq \left.\frac{\mathrm{d}e}{\mathrm{d}F}\right|_{\mathrm{d}\theta=0} = \left.\frac{\mathrm{d}e_1}{\mathrm{d}F}\right|_{\mathrm{d}\theta=0} + \left.\frac{\mathrm{d}e_2}{\mathrm{d}F}\right|_{\mathrm{d}\theta=0} \eqqcolon \frac{1}{E_{1t}} + \frac{1}{E_{2t}} \tag{A-8a}$$

so that a fiber's elastic compliance is described by

$$\mathrm{d}e = \frac{\mathrm{d}F}{E_t} \quad \text{where} \quad \frac{1}{E_t} = \frac{1}{E_{1t}} + \frac{1}{E_{2t}} \tag{A-8b}$$

and, consequently, its elastic modulus is described by

$$\mathrm{d}F = E_t\,\mathrm{d}e \quad \text{where} \quad E_t = \frac{E_{1t}E_{2t}}{E_{1t} + E_{2t}}. \tag{A-8c}$$

The implicit free-energy function introduced through Eq. A-7 produces a tangent compliance of

$$\frac{1}{E_t} = \frac{e_{1_{\max}} - e_1}{E_1 e_{1_{\max}} + 2(F - F_0)} + \frac{1}{E_2} \tag{A-8d}$$

whose internal strain caused by molecular reconfiguration comes from

$$e_1 = e - \alpha_t \ln\left(\frac{\theta}{\theta_0}\right) - \frac{F - F_0}{E_2}. \tag{A-8e}$$

The material properties of this model are: $E_1E_2/(E_1 + E_2)$ (> 0) is the initial tangent modulus, E_2 $(\gg E_1 > 0)$ is the terminal tangent modulus, $e_{1_{\max}}$ is the maximum strain that can arise from a molecular reconfiguration, and α_t is the thermal strain coefficient, all quantified against a reference state described by θ_0 and F_0.

It follows then that its associated secant compliance obeys

$$\frac{1}{E_s} \coloneqq \left.\frac{e}{F - F_0}\right|_{\theta=\theta_0} = \left.\frac{e_1}{F - F_0}\right|_{\theta=\theta_0} + \left.\frac{e_2}{F - F_0}\right|_{\theta=\theta_0} \eqqcolon \frac{1}{E_{1s}} + \frac{1}{E_{2s}} \tag{A-9a}$$

so the fiber's compliance representation is described by

$$e = \frac{F - F_0}{E_s} \quad \text{where} \quad \frac{1}{E_s} = \frac{1}{E_{1s}} + \frac{1}{E_{2s}} \tag{A-9b}$$

and, therefore, its modulus representation is described by

$$F = F_0 + E_s\, e \quad \text{where} \quad E_s = \frac{E_{1s} E_{2s}}{E_{1s} + E_{2s}}. \tag{A-9c}$$

Upon integrating Eq. A-8d by separation of variables, one arrives at a secant compliance comprising a sum between

$$\frac{1}{E_{1s}} = \frac{e_{1_{\max}}}{F - F_0} \left(1 - \frac{\sqrt{E_1 e_{1_{\max}}}}{\sqrt{E_1 e_{1_{\max}} + 2(F - F_0)}} \right) \tag{A-9d}$$

and

$$\frac{1}{E_{2s}} = \frac{1}{E_2} \tag{A-9e}$$

with $E_s(F \leqslant F_0) = E_1 E_2/(E_1 + E_2)$.

A.2.3 Viscoelastic Biologic Fibers

Freed and Rajagopal[127] have shown that realistic viscoelastic responses for biologic fibers can be based upon the above thermoelastic fiber model by retaining the implicit contribution to the compliance, i.e., $1/E_1$, as elastic, while only extending the explicit contribution to the compliance, viz., $1/E_2$, into the viscoelastic domain. This finding is significant! It allows one to model the viscoelastic response of nonlinear biologic fibers by employing a *linear* theory for viscoelasticity. Effectively, elastic compliance $1/E_2$ in Eq. A-7c becomes a viscoelastic function of state. This is a topic for future work.

A.3 Alveolar Septa as Green (Explicit) Thermoelastic Membranes

For a 2D membrane with a mass density of ρ per unit area, its response comprises uniform and non-uniform contributions. The thermodynamic conjugate fields pertaining to uniform behaviors are temperature θ and entropy η, and surface tension π and dilation ξ, cf. Eq. 69a. While the conjugate fields pertaining to non-uniform behaviors are normal stress difference σ and squeeze strain ε, and shear stress τ and shear strain γ, cf. Eq. 69b.

We observed in Section 4.1.3 that the uniform and non-uniform contributions of an alveolar membrane are not coupled. Consequently, their Gibbs free energies add in such a manner that $\mathcal{G}(\theta, \pi, \sigma, \tau) = \mathcal{G}_u(\theta, \pi) + \mathcal{G}_n(\sigma, \tau)$, with $\mathcal{G}_u$ being the uniform

contribution of $\mathcal{G}$, and $\mathcal{G}_n$ being the non-uniform contribution of $\mathcal{G}$.

A Green thermoelastic membrane has a Gibbs free-energy potential described by $\mathcal{G}(\theta,\pi,\sigma,\tau) = \mathcal{G}_u(\theta,\pi)+\mathcal{G}_n(\sigma,\tau)$ where $\mathrm{d}\mathcal{G} = -\eta\,\mathrm{d}\theta-\frac{1}{\rho}\big(\xi\,\mathrm{d}\pi+\varepsilon\,\mathrm{d}\sigma+\gamma\,\mathrm{d}\tau\big)$ from which one derives its governing thermoelastic constitutive equations; specifically, for entropy

$$\eta = -\partial_\theta\,\mathcal{G}(\theta,\pi,\sigma,\tau) = -\partial_\theta\,\mathcal{G}_u(\theta,\pi), \tag{A-10a}$$

for dilation

$$\xi = -\rho\,\partial_\pi\,\mathcal{G}(\theta,\pi,\sigma,\tau) = -\rho\,\partial_\pi\,\mathcal{G}_u(\theta,\pi), \tag{A-10b}$$

for squeeze

$$\varepsilon = -\rho\,\partial_\sigma\,\mathcal{G}(\theta,\pi,\sigma,\tau) = -\rho\,\partial_\sigma\,\mathcal{G}_n(\sigma,\tau), \tag{A-10c}$$

and for shear

$$\gamma = -\rho\,\partial_\tau\,\mathcal{G}(\theta,\pi,\sigma,\tau) = -\rho\,\partial_\tau\,\mathcal{G}_n(\sigma,\tau) \tag{A-10d}$$

whereby specifying energies $\mathcal{G}_u$ and $\mathcal{G}_n$ produces a material model for membranes.

A.3.1 Hookean Membranes

In this appendix, we consider a function for the Gibbs free-energy potential that is suitable for describing biologic Hookean membranes; specifically, for governing their uniform response, let

$$\begin{aligned}\mathcal{G}_u(\theta,\pi) = -\eta_0(\theta-\theta_0) - C\left(\theta\ln\left(\frac{\theta}{\theta_0}\right)-(\theta-\theta_0)\right)\\ -\frac{\pi-\pi_0}{2\rho}\left(2\alpha\ln\left(\frac{\theta}{\theta_0}\right)+\frac{\pi-\pi_0}{4M}\right)\end{aligned} \tag{A-11a}$$

and for governing their non-uniform response, let

$$\mathcal{G}_n(\sigma,\tau) = -\frac{1}{2\rho}\left(\frac{\sigma^2}{2N}+\frac{\tau^2}{G}\right), \tag{A-11b}$$

where symmetries $\mathcal{G}_n(\sigma,\tau) = \mathcal{G}_n(-\sigma,\tau) = \mathcal{G}_n(\sigma,-\tau) = \mathcal{G}_n(-\sigma,-\tau)$ must hold because the squeeze and shear variables can take on either sign. These free energies

are normalized so that $\mathcal{G}_u(\theta_0, \pi_0) = 0$ and $\mathcal{G}_n(\sigma_0, \tau_0) = 0$ with initial conditions of $\eta_0 = -\partial_\theta \mathcal{G}_u(\theta_0, \pi_0)$, $\xi_0 = -\rho\, \partial_\pi \mathcal{G}_u(\theta_0, \pi_0) = 0$, $\varepsilon_0 = -\rho\, \partial_\sigma \mathcal{G}_n(0, 0) = 0$, and $\gamma_0 = -\rho\, \partial_\tau \mathcal{G}_n(0, 0) = 0$ for a reference state with fields θ_0, π_0, $\sigma_0 = 0$ and $\tau_0 = 0$.

Here we presume that the reference values for the non-uniform stresses, viz., σ_0 and τ_0, are both zero, i.e., $\sigma_0 = 0$ and $\tau_0 = 0$. This follows because these fields can be either positive or negative in their values; whereas, surface tension π is a positive only field, and as such, the notion of a non-zero reference value π_0 is physiologically sound; it is nature's way of helping to stabilize a membrane.

A.3.2 Secant Material Properties

A.3.2.1 Uniform Response

Substituting the Gibbs free-energy function of Eq. A-11a into the constitutive equations governing entropy (Eq. A-10a) and dilation (Eq. A-10b) results in a matrix expression of

$$\begin{Bmatrix} \eta - \eta_0 \\ \ln\sqrt{A/A_0} \end{Bmatrix} = \begin{bmatrix} C_s & \alpha_s/\rho\theta \\ \alpha_s & 1/4M_s \end{bmatrix} \begin{Bmatrix} \ln(\theta/\theta_0) \\ \pi - \pi_0 \end{Bmatrix}$$

where $\xi := \ln\sqrt{A/A_0}$. This matrix equation can be rearranged into a form that is more suitable for our needs, viz.,

$$\begin{Bmatrix} \eta - \eta_0 \\ \pi - \pi_0 \end{Bmatrix} = \begin{bmatrix} C_s - 4\alpha_s^2 M_s/\rho\theta & 4\alpha_s M_s/\rho\theta \\ -4\alpha_s M_s & 4M_s \end{bmatrix} \begin{Bmatrix} \ln(\theta/\theta_0) \\ \ln\sqrt{A/A_0} \end{Bmatrix} \tag{A-12a}$$

whose material properties are a specific heat (evaluated at a reference surface tension π_0) of

$$C_s := \left.\frac{\eta - \eta_0}{\ln(\theta/\theta_0)}\right|_{\pi=\pi_0} \tag{A-12b}$$

with $C_s - 4\alpha_s^2 M_s/\rho\theta$ being a heat capacity in an absence of dilation, plus a thermal strain coefficient (evaluated at a reference surface tension π_0) of

$$\alpha_s := \left.\frac{\ln(L/L_0)}{\ln(\theta/\theta_0)}\right|_{\pi=\pi_0} = \frac{1}{2}\left.\frac{\ln(A/A_0)}{\ln(\theta/\theta_0)}\right|_{\pi=\pi_0}, \tag{A-12c}$$

where $\ln(A/A_0) = 2\ln(L/L_0)$ is the surface dilation, with L/L_0 being the stretch between any two points on its surface, plus an elastic membrane compliance (evaluated at a reference temperature θ_0) of

$$\frac{1}{M_s} \coloneqq \left.\frac{\ln(A/A_0)}{T - T_0}\right|_{\theta=\theta_0} = 4 \left.\frac{\xi}{\pi - \pi_0}\right|_{\theta=\theta_0}, \tag{A-12d}$$

where $T \coloneqq \frac{1}{2}(\sigma_{11} + \sigma_{22}) =: \frac{1}{2}\,\pi$ is the surface tension, with σ_{ij} being components of the Cauchy stress in this 2D space. These are *secant* material properties, hence the subscript s, whose values can be measured in experiments.

Note: Thermal strain is typically modeled as $\alpha(\theta - \theta_0)$, wherein α is referred to as the coefficient for lineal thermal expansion. Our thermal strain coefficient α_s and the coefficient for lineal thermal expansion α relate via $\alpha_s = \alpha\theta_0 + \mathcal{O}\big(((\theta - \theta_0)/\theta_0)^2\big)$ because $\ln(\theta/\theta_0) = (\theta - \theta_0)/\theta_0 - (\theta - \theta_0)^2/\theta_0^2 + (\theta - \theta_0)^3/\theta_0^3 - \cdots$.

A.3.2.2 Non-Uniform Response

Substituting the Gibbs free-energy function of Eq. A-11b into the constitutive equations governing squeeze (Eq. A-10c) and shear (Eq. A-10d) leads to the following matrix equation

$$\begin{Bmatrix} \varepsilon \\ \gamma \end{Bmatrix} = \begin{bmatrix} 1/2N_s & 0 \\ 0 & 1/G_s \end{bmatrix} \begin{Bmatrix} \sigma \\ \tau \end{Bmatrix}$$

that when inverted becomes

$$\begin{Bmatrix} \sigma \\ \tau \end{Bmatrix} = \begin{bmatrix} 2N_s & 0 \\ 0 & G_s \end{bmatrix} \begin{Bmatrix} \varepsilon \\ \gamma \end{Bmatrix} \tag{A-13a}$$

whose material properties are a squeeze compliance (in an absence of shear γ) of

$$\frac{1}{N_s} \coloneqq \left.\frac{\ln(\Gamma/\Gamma_0)}{\sigma_{11} - \sigma_{22}}\right|_{g=g_0} = 2 \left.\frac{\varepsilon}{\sigma}\right|_{\gamma=0} \tag{A-13b}$$

where $\Gamma \coloneqq a/b$ and $\Gamma_0 = a_0/b_0$ are the current and reference stretches of squeeze, with $\varepsilon \coloneqq \ln\sqrt{\Gamma/\Gamma_0}$ being the squeeze strain, and where $\sigma \coloneqq \sigma_{11} - \sigma_{22}$ establishes a normal stress difference, plus a shear compliance (in an absence of squeeze ε) of

$$\frac{1}{G_s} \coloneqq \left.\frac{g - g_0}{\Gamma\sigma_{21}}\right|_{\Gamma=\Gamma_0} = \left.\frac{\gamma}{\tau}\right|_{\varepsilon=0} \tag{A-13c}$$

where g and g_0 are the current and reference magnitudes of shear, with $\gamma \coloneqq g - g_0$ denoting shear strain, and where $\tau \coloneqq \Gamma\sigma_{21}$ establishes the thermodynamic shear stress. These are *secant* material properties, hence the subscript s, whose values can be measured in experiments.

A.3.3 Tangent Material Properties

A.3.3.1 Uniform Response

Differentiating the constitutive equations for entropy and dilation found in Eqs. A-10a and A-10b, respectively, assuming they are both sufficiently differentiable functions of state, while adopting the Gibbs free energy from Eq. A-11a, results in the following matrix constitutive equation

$$\begin{Bmatrix} \mathrm{d}\eta \\ \mathrm{d}\xi \end{Bmatrix} = -\begin{bmatrix} \partial_{\theta\theta}\,\mathcal{G}_u & \partial_{\theta\pi}\,\mathcal{G}_u \\ \rho\,\partial_{\pi\theta}\,\mathcal{G}_u & \rho\,\partial_{\pi\pi}\,\mathcal{G}_u \end{bmatrix} \begin{Bmatrix} \mathrm{d}\theta \\ \mathrm{d}\pi \end{Bmatrix} = \begin{bmatrix} C_t & \alpha_t/\rho\theta \\ \alpha_t & 1/4M_t \end{bmatrix} \begin{Bmatrix} \theta^{-1}\,\mathrm{d}\theta \\ \mathrm{d}\pi \end{Bmatrix}$$

which is hypo-elastic in its construction.[81] This expression can be rearranged into

$$\begin{Bmatrix} \mathrm{d}\eta \\ \mathrm{d}\pi \end{Bmatrix} = \begin{bmatrix} C_t - 4\alpha_t^2 M_t/\rho\theta & 4\alpha_t M_t/\rho\theta \\ -4\alpha_t M_t & 4M_t \end{bmatrix} \begin{Bmatrix} \theta^{-1}\,\mathrm{d}\theta \\ \frac{1}{2}A^{-1}\,\mathrm{d}A \end{Bmatrix} \tag{A-14a}$$

recalling that $\mathrm{d}\xi = \mathrm{d}A/2A$, and with material properties defined accordingly: a specific heat (at constant surface tension) of

$$C_t \coloneqq \left.\frac{\mathrm{d}\eta}{\theta^{-1}\,\mathrm{d}\theta}\right|_{\mathrm{d}\pi=0} = C_s - \alpha_s(\pi - \pi_0)/\rho\theta = -\theta\,\partial_{\theta\theta}\,\mathcal{G}_u \tag{A-14b}$$

with $C_t - 4\alpha_t^2 M_t/\rho\theta$ denoting a heat capacity at constant dilation, and a lineal thermal strain coefficient (at constant surface tension) of

$$\alpha_t \coloneqq \left.\frac{L^{-1}\,\mathrm{d}L}{\theta^{-1}\,\mathrm{d}\theta}\right|_{\mathrm{d}\pi=0} = \frac{1}{2}\left.\frac{A^{-1}\,\mathrm{d}A}{\theta^{-1}\,\mathrm{d}\theta}\right|_{\mathrm{d}\pi=0} = \begin{cases} -\rho\theta\,\partial_{\pi\theta}\,\mathcal{G}_u \\ -\rho\theta\,\partial_{\theta\pi}\,\mathcal{G}_u \end{cases} \tag{A-14c}$$

plus a compliance (at constant temperature) of

$$\frac{1}{M_t} \coloneqq \left.\frac{A^{-1}\,\mathrm{d}A}{\mathrm{d}T}\right|_{\mathrm{d}\theta=0} = 4\left.\frac{\mathrm{d}\xi}{\mathrm{d}\pi}\right|_{\mathrm{d}\theta=0} = -4\rho\,\partial_{\pi\pi}\,\mathcal{G}_u. \tag{A-14d}$$

These are *tangent* material properties, hence the subscript t, whose values can be measured in experiments.

A.3.3.2 Non-Uniform Response

From $\mathrm{d}\mathcal{G} = \mathrm{d}\mathcal{G}_u + \mathrm{d}\mathcal{G}_n$ with $\mathrm{d}\mathcal{G}_u = -\eta\,\mathrm{d}\theta - \frac{1}{\rho}\xi\,\mathrm{d}\pi$ comes $\mathrm{d}\mathcal{G}_n = -\frac{1}{\rho}(\varepsilon\,\mathrm{d}\sigma + \gamma\,\mathrm{d}\tau)$ out of which one obtains the constitutive equations governing non-uniform responses in a Green elastic membrane, viz., $\varepsilon = -\rho\,\partial_\sigma\,\mathcal{G}_n$ and $\gamma = -\rho\,\partial_\tau\,\mathcal{G}_n$, that, assuming they are continuous and differentiable functions of state, can be expressed as the matrix differential equation

$$\begin{Bmatrix} \mathrm{d}\varepsilon \\ \mathrm{d}\gamma \end{Bmatrix} = -\rho \begin{bmatrix} \partial_{\sigma\sigma}\,\mathcal{G}_n & \partial_{\sigma\tau}\,\mathcal{G}_n \\ \partial_{\tau\sigma}\,\mathcal{G}_n & \partial_{\tau\tau}\,\mathcal{G}_n \end{bmatrix} \begin{Bmatrix} \mathrm{d}\sigma \\ \mathrm{d}\tau \end{Bmatrix} = \begin{bmatrix} 1/2N_t & 0 \\ 0 & 1/G_t \end{bmatrix} \begin{Bmatrix} \mathrm{d}\sigma \\ \mathrm{d}\tau \end{Bmatrix}$$

where $\partial_{\sigma\tau}\,\mathcal{G}_n = \partial_{\tau\sigma}\,\mathcal{G}_n = 0$, because the modes of squeeze and shear are taken to be decoupled. The resulting matrix is readily inverted into a form that is more useful for us, namely

$$\begin{Bmatrix} \mathrm{d}\sigma \\ \mathrm{d}\tau \end{Bmatrix} = \begin{bmatrix} 2N_t & 0 \\ 0 & G_t \end{bmatrix} \begin{Bmatrix} \mathrm{d}\varepsilon \\ \mathrm{d}\gamma \end{Bmatrix} \tag{A-15a}$$

whose associated material properties are established via

$$\frac{1}{N_t} \coloneqq \left.\frac{\Gamma^{-1}\,\mathrm{d}\Gamma}{\mathrm{d}(\sigma_{11}-\sigma_{22})}\right|_{\mathrm{d}\gamma=0} = 2\left.\frac{\mathrm{d}\varepsilon}{\mathrm{d}\sigma}\right|_{\mathrm{d}\gamma=0} = -2\rho\,\partial_{\sigma\sigma}\,\mathcal{G}_n \tag{A-15b}$$

and

$$\frac{1}{G_t} \coloneqq \frac{1}{\Gamma}\left.\frac{\mathrm{d}g}{\mathrm{d}\sigma_{21}}\right|_{\mathrm{d}\Gamma=0} = \left.\frac{\mathrm{d}\gamma}{\mathrm{d}\tau}\right|_{\mathrm{d}\varepsilon=0} = -\rho\,\partial_{\tau\tau}\,\mathcal{G}_n \tag{A-15c}$$

where the conjugate stresses are defined as $\sigma \coloneqq \sigma_{11} - \sigma_{22}$ and $\tau \coloneqq \Gamma\sigma_{21}$ with $\Gamma \coloneqq a/b$ being the stretch of squeeze from which it follows that $\Gamma^{-1}\mathrm{d}\Gamma = 2\,\mathrm{d}\varepsilon$ because the strain of squeeze is given by $\varepsilon = \ln\sqrt{\Gamma/\Gamma_0}$. The squeeze compliance $1/N_t = 2\,\mathrm{d}\varepsilon/\mathrm{d}\sigma|_\gamma$ is evaluated at a constant shear γ, while the shear compliance $1/G_t = \mathrm{d}\gamma/\mathrm{d}\tau|_\varepsilon$ is evaluated at a constant squeeze ε.

A.4 Alveolar Septa as Rajagopal (Implicit) Thermoelastic Membranes

We employ implicit elasticity here to derive a constitutive theory suitable for describing biologic membranes.

A.4.1 Tangent Material Properties

A.4.1.1 Uniform Response

Like the implicit elastic fiber introduced in Eq. A-7, the uniform response of an implicit elastic membrane with a strain-limiting dilation can be modeled using a Gibbs free energy of the form $\mathcal{G}_u(\theta, \xi, \pi) \coloneqq \mathcal{G}_1(\xi_1, \pi) + \mathcal{G}_2(\theta, \pi)$ where our definition for dilation $\xi \coloneqq \ln\sqrt{A/A_0}$ decomposes into a sum of two dilations: $\xi_1 \coloneqq \ln\sqrt{A_1/A_0}$ and $\xi_2 \coloneqq \ln\sqrt{A/A_1}$ so that $\xi = \xi_1 + \xi_2$, with like interpretations as those from their 1D fiber counterparts, viz., e, e_1, and e_2. Such a membrane's tangent material properties are then given by

$$C_t \coloneqq -\theta\,\partial_{\theta\theta}\,\mathcal{G}_u(\theta,\xi,\pi) = -\theta\,\partial_{\theta\theta}\,\mathcal{G}_2(\theta,\pi) \tag{A-16a}$$

$$\alpha_t \coloneqq -\rho\theta\,\partial_{\pi\theta}\,\mathcal{G}_u(\theta,\xi,\pi) = -\rho\theta\,\partial_{\pi\theta}\,\mathcal{G}_2(\theta,\pi) = -\rho\theta\,\partial_{\theta\pi}\,\mathcal{G}_2(\theta,\pi) \tag{A-16b}$$

$$1/4M_t \coloneqq -\big(\rho\,\partial_{\xi_1}\mathcal{G}_1(\xi_1,\pi)\big)^{-1}\big(\xi + \rho\,\partial_{\pi}\,\mathcal{G}_u(\theta,\xi,\pi)\big) - \rho\,\partial_{\pi\pi}\,\mathcal{G}_2(\theta,\pi) \tag{A-16c}$$

whose derivations are analogous to those for the implicit fiber derived in Eq. A-6.

A.4.1.2 Uniform Biologic Membrane Model

Like our model for a biologic fiber, we consider a Gibbs free-energy function for describing the uniform response of a biologic membrane whose implicit energy function takes on the form of

$$\mathcal{G}_1(\xi_1,\pi) = -\frac{1}{\rho}\Big(\xi_{1_{\max}}\big(4M_1\xi_1 - (\pi-\pi_0)\big) + 2\xi_1(\pi-\pi_0)\Big) \tag{A-17a}$$

and whose explicit energy function is

$$\begin{aligned}\mathcal{G}_2(\theta,\pi) = &-\eta_0(\theta-\theta_0) - C_t\left(\theta\ln\left(\frac{\theta}{\theta_0}\right) - (\theta-\theta_0)\right)\\ &- \frac{\pi-\pi_0}{2\rho}\left(2\alpha_t\ln\left(\frac{\theta}{\theta_0}\right) + \frac{\pi-\pi_0}{4M_2}\right),\end{aligned} \tag{A-17b}$$

thereby resulting an elastic tangent compliance, as established in Eq. A-16c, of

$$\frac{1}{4M_t(\theta,\xi,\pi)} = \frac{\xi_{1_{\max}} - \xi_1}{4M_1\xi_{1_{\max}} + 2(\pi - \pi_0)} + \frac{1}{4M_2}, \tag{A-17c}$$

wherein

$$\xi_1 = \xi - \alpha_t \ln\left(\frac{\theta}{\theta_0}\right) - \frac{\pi - \pi_0}{4M_2}, \tag{A-17d}$$

with $\xi_{1_{\max}} > 0$ being an upper bound on strain ξ_1, i.e., $\xi_1 \leqslant \xi_{\max}$. Such a membrane has an initial tangent stiffness $M_t(\theta_0, \xi_0, \pi_0)$ of $M_1M_2/(M_1+M_2)$ ($\approx M_1$ whenever $M_2 \gg M_1 > 0$) and it has a terminal tangent stiffness $M_t(\xi_1 = \xi_{1_{\max}})$ of M_2.

Membranes will wrinkle under states of negative surface tension (or dilation). In alveolar mechanics, surfactant helps to prevent this, and a possible ensuing alveolar collapse. Wrinkling is not accounted for in our modeling of alveolar septa. Rather, like fibers, it is assumed that the compliant response at π_0, with modulus $M_1M_2/(M_1 + M_2)$, continues over the non-physiologic regime of loading $0 < \pi \leqslant \pi_0$, which is a body's way of ensuring structural stability in its membranes.

The difference between a Green and Rajagopal thermoelastic membrane undergoing a dilation is in their definitions for elastic compliance. There is no difference in their properties for the specific heat or the thermal strain coefficient. The above model has been successfully applied to a visceral pleura membrane.[65]

A.4.1.3 Non-Uniform Response

We seek an energetic construction that is consistent with the Freed and Rajagopal[96] fiber model, but which is applicable to the non-uniform responses that planar membranes can support. A Rajagopal elastic solid is implicit. Therefore, we choose a Gibbs free-energy function for governing non-uniform behavior that looks like

$$\mathcal{G}_n(\varepsilon,\gamma,\sigma,\tau) = \mathcal{G}_1(\varepsilon_1,\sigma) + \mathcal{G}_2(\sigma) + \mathcal{G}_3(\gamma_1,\tau) + \mathcal{G}_4(\tau) \tag{A-18}$$

which depend upon three squeeze strains $\varepsilon := \ln\sqrt{\Gamma/\Gamma_0}$, $\varepsilon_1 := \ln\sqrt{\Gamma_1/\Gamma_0}$, and $\varepsilon_2 := \ln\sqrt{\Gamma/\Gamma_1}$, and three shear strains $\gamma := g - g_0$, $\gamma_1 := g_1 - g_0$, and $\gamma_2 := g - g_1$, both of which are additive in the sense that $\varepsilon = \varepsilon_1 + \varepsilon_2$ and $\gamma = \gamma_1 + \gamma_2$, and as such, so are their differential rates of change $\mathrm{d}\varepsilon = \mathrm{d}\varepsilon_1 + \mathrm{d}\varepsilon_2$ and $\mathrm{d}\gamma =$

$\mathrm{d}\gamma_1 + \mathrm{d}\gamma_2$. Strains ε_1 and γ_1 may be thought of as describing an unraveling of molecular configuration, analogous to e_1 in the fiber model of Eq. A-7, and ξ_1 in the uniform membrane model of Eq. A-17. No coupling between squeeze and shear is assumed in this energy function.* Energies $\mathcal{G}_1$ and $\mathcal{G}_3$ are Rajagopal elastic (they have implicit dependencies upon state), while energies $\mathcal{G}_2$ and $\mathcal{G}_4$ are Green elastic (they have explicit dependencies upon state).

From the thermodynamic expression $-\rho\,\mathrm{d}\mathcal{G}_n = \varepsilon\,\mathrm{d}\sigma + \gamma\,\mathrm{d}\tau$, the non-uniform Gibbs free energy $\mathcal{G}_n$, when expressed in the form of Eq. A-18, and given the definitions for squeeze $1/N$ and shear $1/G$ compliances put forward in Eqs. A-15b and A-15c, one determines that the tangent squeeze compliance is described by

$$\frac{1}{2N_t} \coloneqq \frac{\mathrm{d}\varepsilon}{\mathrm{d}\sigma} = -\big(\rho\,\partial_{\varepsilon_1}\mathcal{G}_1\big)^{-1}\big(\varepsilon + \rho\,\partial_\sigma(\mathcal{G}_1 + \mathcal{G}_2)\big) - \rho\,\partial_{\sigma\sigma}\mathcal{G}_2 \tag{A-19a}$$

and that the tangent shear compliance is described by

$$\frac{1}{G_t} \coloneqq \frac{\mathrm{d}\gamma}{\mathrm{d}\tau} = -\big(\rho\,\partial_{\gamma_1}\mathcal{G}_3\big)^{-1}\big(\gamma + \rho\,\partial_\tau(\mathcal{G}_3 + \mathcal{G}_4)\big) - \rho\,\partial_{\tau\tau}\mathcal{G}_4 \tag{A-19b}$$

whose mathematical structure is similar to that of the Freed–Rajagopal fiber model presented in Eq. A-7. The first collection of terms on the right-hand side of both formulæ is Rajagopal elastic; the second is Green elastic.

Derivation: The First and Second Laws of Thermodynamics, as they pertain to non-uniform contributions of stress power, have energetic components described in Eq. A-18 so that $\rho\,\mathrm{d}\mathcal{G}_n = \rho\,\partial_{\varepsilon_1}\mathcal{G}_1(\varepsilon_1,\sigma)\,\mathrm{d}\varepsilon_1 + \rho\,\partial_\sigma\mathcal{G}_1(\varepsilon_1,\sigma)\,\mathrm{d}\sigma + \rho\,\partial_\sigma\mathcal{G}_2(\sigma)\,\mathrm{d}\sigma + \rho\,\partial_{\gamma_1}\mathcal{G}_3(\gamma_1,\tau)\,\mathrm{d}\gamma_1 + \rho\,\partial_\tau\mathcal{G}_3(\gamma_1,\tau)\,\mathrm{d}\tau + \rho\,\partial_\tau\mathcal{G}_4(\tau)\,\mathrm{d}\tau$ that associate with the conjugate pairings $-\varepsilon_1\,\mathrm{d}\sigma - \varepsilon_2\,\mathrm{d}\sigma - \gamma_1\,\mathrm{d}\tau - \gamma_2\,\mathrm{d}\tau$ because of the prescribed additivity in strains. These follow from a Legendre transformation of the internal energy. Gathering like terms result in a pair of Green elastic formulæ that describe two of the four internal strains

$$\varepsilon_2 = -\rho\,\partial_\sigma\mathcal{G}_2(\sigma) \quad \text{and} \quad \gamma_2 = -\rho\,\partial_\tau\mathcal{G}_4(\tau)$$

*The Poynting effect is a consequence of a coupling between squeeze and shear.[66] This is a second-order effect that can be neglected when modeling biologic tissues.

and two Rajagopal elastic formulæ whose ODEs describe the other internal strains

$$\mathrm{d}\varepsilon_1 = -\big(\rho\,\partial_{\varepsilon_1}\mathcal{G}_1(\varepsilon_1,\sigma)\big)^{-1}\big(\varepsilon_1 + \rho\,\partial_\sigma\,\mathcal{G}_1(\varepsilon_1,\sigma)\big)\mathrm{d}\sigma$$
$$\mathrm{d}\gamma_1 = -\big(\rho\,\partial_{\gamma_1}\mathcal{G}_3(\gamma_1,\tau)\big)^{-1}\big(\gamma_1 + \rho\,\partial_\tau\,\mathcal{G}_3(\gamma_1,\tau)\big)\mathrm{d}\tau$$

that when combined as rates become the constitutive formulæ in Eq. A-19. □

A.4.1.4 Non-Uniform Biologic Membrane Model

We now specify the Gibbs free-energy functions of Eq. A-18 such that they produce tangent compliances $1/N_t$ and $1/G_t$ with like mathematical structure to Eq. A-17c for dilation, viz., $1/M_t$. Specifically, we consider Gibbs free-energy functions of the form

$$-\rho\,\mathcal{G}_1(\varepsilon_1,\sigma) = \mathrm{sgn}(\varepsilon_1)\,\varepsilon_{1_{\max}}\big(2N_1\varepsilon_1 - \sigma\big) + 2\varepsilon_1\sigma \tag{A-20a}$$
$$-\rho\,\mathcal{G}_2(\sigma) = \sigma^2/4N_2 \tag{A-20b}$$
$$-\rho\,\mathcal{G}_3(\gamma_1,\tau) = \mathrm{sgn}(\gamma_1)\,\gamma_{1_{\max}}\big(G_1\gamma_1 - \tau\big) + 2\gamma_1\tau \tag{A-20c}$$
$$-\rho\,\mathcal{G}_4(\tau) = \tau^2/2G_2 \tag{A-20d}$$

where these energy functions have the same mathematical structure as the energies for biologic fibers (Eq. A-7) and uniform membranes (Eq. A-17), less their temperature dependence, and less their states of pre-stress, i.e., $\sigma_0 = 0$ and $\tau_0 = 0$.

The sign functions, viz., $\mathrm{sgn}(\varepsilon_1)$ and $\mathrm{sgn}(\gamma_1)$, account for the fact that squeeze and shear strains can be of either sign, but the Gibbs energy must remain negative. In effect, the sign functions flip the limiting state between tension and compression, i.e., they change the signs of $\varepsilon_{1_{\max}}$ and $\gamma_{1_{\max}}$ depending upon the respective signs of ε_1 and γ_1. As a consequence, $\mathcal{G}_1(\varepsilon_1,\sigma) = \mathcal{G}_1(-\varepsilon_1,-\sigma)$, $\mathcal{G}_2(\sigma) = \mathcal{G}_2(-\sigma)$, $\mathcal{G}_3(\gamma_1,\tau) = \mathcal{G}_3(-\gamma_1,-\tau)$, and $\mathcal{G}_4(\tau) = \mathcal{G}_4(-\tau)$.

When substituted into Eq. A-19, these energy functions produce the following thermoelastic compliances

$$\frac{1}{2N(\varepsilon,\sigma)} = \frac{\mathrm{sgn}(\varepsilon_1)\,\varepsilon_{1_{\max}} - \varepsilon_1}{2N_1\,\mathrm{sgn}(\varepsilon_1)\,\varepsilon_{1_{\max}} + 2\sigma} + \frac{1}{2N_2} \qquad \varepsilon_1 = \varepsilon - \frac{\sigma}{2N_2} \tag{A-21a}$$
$$\frac{1}{G(\gamma,\tau)} = \frac{\mathrm{sgn}(\gamma_1)\,\gamma_{1_{\max}} - \gamma_1}{G_1\,\mathrm{sgn}(\gamma_1)\,\gamma_{1_{\max}} + 2\tau} + \frac{1}{G_2} \qquad \gamma_1 = \gamma - \frac{\tau}{G_2} \tag{A-21b}$$

which provide the tangent operators that we use to describe the non-uniform behav-

ior of a biologic membrane.

Like our other biologic models, the tangent squeeze compliance $1/N_t$ is described by three material properties: an asymptotic modulus at the reference state of $N_1N_2/(N_1+N_2)$ ($\approx N_1$ whenever $N_2 \gg N_1 > 0$) where N_1 may be thought of as the stiffness of an unstretched molecular network, and a terminal modulus N_2 designating a stiffness after its molecular network has been stretched out at a limiting state of configurational squeeze $\varepsilon_{1_{\max}}$. The tangent shear compliance $1/G_t$ is also described by three material properties: an asymptotic modulus at the reference state of $G_1G_2/(G_1+G_2)$ ($\approx G_1$ whenever $G_2 \gg G_1 > 0$), a terminal modulus G_2, and a limiting state of configurational shear $\gamma_{1_{\max}}$.

In soft biological tissues, the shear moduli G_1 and G_2 will be several orders in magnitude smaller than their respective squeeze moduli N_1 and N_2. Classical theories cannot make such a distinction.

A.4.2 Secant Material Properties

A.4.2.1 Uniform Response

Through a separation of variables, the tangent compliance governing dilation found in Eq. A-17c can be integrated to produce a secant compliance of

$$\frac{1}{4M_s(\pi)} = \frac{\xi_{1_{\max}}}{\pi-\pi_0}\left(1-\frac{\sqrt{M_1\xi_{1_{\max}}}}{\sqrt{M_1\xi_{1_{\max}}+\frac{1}{2}(\pi-\pi_0)}}\right)+\frac{1}{4M_2} \tag{A-22}$$

where $M_s(\pi \leqslant \pi_0) = M_1M_2/(M_1+M_2)$. This compliance applies to the thermodynamic equations governing the uniform secant response of our membranes, as established in Eq. A-12a.

A.4.2.2 Non-Uniform Response

Integrating by separating variables, the tangent compliance governing squeeze in Eq. A-21a integrates to a secant compliance of

$$\frac{1}{2N_s(\sigma)} = \frac{\varepsilon_{1_{\max}}}{|\sigma|}\left(1-\frac{\sqrt{N_1\varepsilon_{1_{\max}}}}{\sqrt{N_1\varepsilon_{1_{\max}}+|\sigma|}}\right)+\frac{1}{2N_2}, \tag{A-23}$$

where $N_s(\sigma = 0) = N_1 N_2/(N_1 + N_2)$, while integrating the tangent compliance governing shear in Eq. A-21b results in its secant compliance of

$$\frac{1}{G_s(\tau)} = \frac{\gamma_{1_{\max}}}{|\tau|}\left(1 - \frac{\sqrt{G_1\gamma_{1_{\max}}}}{\sqrt{G_1\gamma_{1_{\max}} + 2|\tau|}}\right) + \frac{1}{G_2}, \tag{A-24}$$

where $G_s(\tau = 0) = G_1 G_2/(G_1 + G_2)$. These compliances apply to the thermodynamic equations governing the non-uniform secant response of our membranes, as established in Eq. A-13a.

List of Symbols, Abbreviations, and Acronyms

Symbols

A, D, H, L, V	area, diameter, height or thickness, length, volume
E, G, M, N	elastic moduli
U, $\mathcal{G}$	internal energy and Gibbs free energy
a, b, c	elongation attributes of Laplace stretch
α, β, γ	shear attributes of Laplace stretch
ξ, ε, γ	thermodynamic strain attributes
π, σ, τ	thermodynamic stress attributes
$(\vec{\boldsymbol{\imath}}, \vec{\boldsymbol{\jmath}}, \vec{\boldsymbol{k}})$	base vectors: user
$(\vec{\mathbf{E}}_1, \vec{\mathbf{E}}_2, \vec{\mathbf{E}}_3)$	base vectors: dodecahedron
$(\vec{\mathbf{e}}_1, \vec{\mathbf{e}}_2, \vec{\mathbf{e}}_3)$	base vectors: elements (chord, pentagon, tetrahedron)
(u, v, w)	nodal displacements
(x, y, z)	nodal positions or locations
(ξ, η, ζ)	natural co-ordinates of a finite element
$\mathbf{B}_L$, $\mathbf{B}_N$, $\mathbf{B}$	linear, nonlinear, and total strain-displacement matrices
$\mathbf{C}$, $\mathbf{K}$, $\mathbf{M}$	tangent stiffness, secant stiffness, and mass matrices
$\boldsymbol{F}$	force vector
$\mathbf{F}$	deformation gradient
$\mathbf{J}$	Jacobian matrix of a finite element
$\mathbf{N}$	matrix of shape functions
$\mathbf{P}$	pivoting or co-ordinate re-indexing matrix
$\mathbf{Q}$, $\mathcal{R}$	orthogonal matrices
$\mathcal{U}$	Laplace stretch

Abbreviations and Acronyms

1D, 2D, 3D	spatial dimensions
BABT	behind armor blunt trauma
BDF2	backward difference formula of second order
BLI	blast lung injury
ODE	ordinary differential equation
PBI	primary blast injury
PECE	predict evaluate correct evaluate
PPE	personal protective equipment
RVE	representative volume element

1 (PDF) DEFENSE TECHNICAL INFORMATION CTR DTIC OCA

1 (PDF) DEVCOM ARL FCDD RLD DCI TECH LIB

2 (PDF) MEDCOM USAMRMC R GUPTA C STEELE

1 (PDF) DEVCOM DAC FCDD DAD OP N EBERIUS

1 (PDF) US ARMY ITC-CANADA D SCOOLER

1 (PDF) CARLETON UNIV O PETEL

1 (PDF) TEXAS A&M UNIV A FREED

1 (PDF) UNIV COLORADO R REGUEIRO

ABERDEEN PROVING GROUND

35 (PDF) DEVCOM ARL
FCDD RLC HC
J KNAP
FCDD RLW
S KARNA
A RAWLETT
S SCHOENFELD
J ZABINSKI
FCDD RLW MB
G GAZONAS
FCDD RLW PB
R BANTON
T BAUMER
A BROWN
A DAGRO
A EIDESMORE
A GOERTZ
C HOPPEL
M KLEINBERGER
K RAFAELS
S SATAPATHY
S WOZNIAK
FCDD RLW PC
R BECKER
J BERRY
D CASEM
J CAZAMIAS
J CLAYTON
M FERMEN-COKER
A FREED
M GREENFIELD
R LEAVY
J LLOYD
C MEREDITH
R REGUEIRO
S SEGLETES
L SHANNAHAN
A TONGE
S TURNAGE
C WILLIAMS
FCDD RLW PE
P GILLICH